INCLUSION BEHAVIOUR IN STEEL FLOWS THROUGH CONVERGENT NOZZLES

by

John Trevor Duncombe

Submitted to the Council of National Academic Awards
in partial fulfilment of the requirements
for the Degree of

DOCTOR OF PHILOSOPHY

at Sheffield City Polytechnic in collaboration with the
British Steel plc, Swinden Laboratories.

March 1989

For Richard and Elaine

ACKNOWLEDGEMENTS

I am indebted to the following for their assistance during the work for this thesis:-

SERC for the financial support.

Dr. A. W. D. Hills for his supervision and help, particularly during the latter stages of the work,

Mr. N. Dzmeiko for his help and assistance throughout all the model building and experiments.

Dr. J. Rawson and his staff at B.S.C. Swinden Laboratories for helpful discussions.

Dr. I. G. Davies and the staff at B.S.C. Stocksbridge Works for their help with plant data.

Mr. D. Latimer for his guidance throughout, and to all the members of the Process Section.

Mr. P. Fisher and Mr. N. Cooper for the photography.

Mr. B. Palmer and Mr. B. Taylor for the instrumentation and electrics.

Mr. M. Furness for the loan of the pulse generator.

Mr. P. Haley of the Stainless Steel Wire Company, (Sheffield) for supplying the electrode wires.

The research assistants in the Department for their help at various stages of the work.

Mr. B. Naylor for his advice on the electrical safety.

For evidence of their help, it's all there in the thesis.

And finally to my wife Christine for her patience and understanding through it all.

INCLUSION BEHAVIOUR IN STEEL FLOWS THROUGH CONVERGENT NOZZLES

by

J. T. Duncombe

ABSTRACT

It is well established that nozzle blockage in Al-killed continuously cast steels is caused by the deposition of pre-existing Al_2O_3 inclusions at the narrowest part of the nozzle. These adhere strongly at the wall by interfacial forces. The theory examined in this thesis is that during the curved flow path through the nozzle, inclusions move towards the nozzle wall by the action of centripetal force. A mathematical model has been developed which takes account of centripetal, gravitational, and drag forces. A computer programme has been written to predict particle behaviour in nozzle flows.

To study the behaviour of second phase particles, a water model using a perspex tundish and an interchangeable glass nozzle has been built. Turbulence has been almost completely removed from the experimental tundish. Hydrogen bubbles electrolytically generated in water have been used to simulate the inclusions in steel and their flow paths through the nozzle have been recorded by cine photography. With frame by frame analysis of the films, the effects of bubble size, (50 µm to 1000 µm), and flow velocity have been studied. Two experimental nozzles have been tested which have demonstrated the importance of limiting the centripetal force.

It has been shown that there is a good relationship between hydrogen bubble behaviour and model predictions. This has been particularly true of small bubbles near the nozzle wall. By comparing the results with other experimental work it has been shown that centripetal forces can have a significant effect on the rate of blocking.

Practical suggestions for reducing the turbulent behaviour in steel tundishes and nozzles are made. The merits of an improved nozzle design which takes advantage of the results of the model work are discussed.

TABLE OF CONTENTS

FIGURE CAPTIONS

SYMBOLS USED IN THE THESIS

Hydrogen flow visualisation

h = height from the surface (m)

σ = surface tension (N m^{-1})

d = bubble diameter (um)

Z = electrochemical equivalent (kg $coulomb^{-1}$)

I = current (A)

Q = volume of hydrogen liberated (m^3)

T = temperature (^{o} K)

P = pressure (Pa)

N = number of bubbles

V_b = volume of a single bubble (m^3)

Theory

ρ_f = density of fluid (kg m^{-3})

ρ_p = density of particle (kg m^{-3})

ω = angular velocity (radians.s^{-1})

f = frequency (Hz)

k = particle drag factor

x_e = radial position of a bubble in the eddy

d = particle diameter (m)

μ = dynamic viscosity (kg s^{-1} m^{-1})

V = volume of particle (m^3)

n = number of revolutions of the eddy

t = time taken for particle to reach the centre of the eddy (s)

A = constant used in the calculations (m^{-2} s)

u = radial velocity of the particle (m s^{-1})

v = fluid velocity (m s^{-1})

x, θ = particle coordinates

ω_f = angular velocity of the fluid (radians.s^{-1})

ω_p = angular velocity of the particle (radians.s^{-1})

ν = kinematic viscosity (m^2 s^{-1})

$B = \rho_p / \rho_f$

$\alpha = 12\ k \nu / d^2(2\ B + 1\ )$ (s^{-1})

$G = (\ \alpha\ /\ 2\ \omega_f))^2$ (s)

$\Omega = \omega_p / \omega_f$

F_{drag} = drag force on the particle (N)

F_{cent} = centripetal force on the particle (N)

F_{buoy} = buoyant force on the particle (N)

F_{res} = resultant force on the particle (N)

g = acceleration due to gravity (m s^{-2})

ζ = streamline curvature (m^{-1})

V_p = velocity of the particle relative to the moving fluid (m s^{-1})

Re_p = particle Reynolds Number $(\ v\ \rho_f\ d\ )\ / \mu_f$

C_d = friction factor

A_p = the projected area of the particle in the direction of flow (m^2)

θ, α = angles

Similarity criteria

S = scale of the model

v_{exit} = exit velocity (m s^{-1})

W = width (m)

z = thickness (m)

suffixes

suffixes

p = plant

m = model

h = height

Experimental work

Re = flow Reynolds Number

D_h = hydraulic diameter (2 a b / a+b) (m)

ρ_a = density of liquid A (kg m^{-3})

ρ_b = density of liquid B (kg m^{-3})

V_a = volume of A (m^3)

V_b = volume of B (m^3)

R = radius of curvature of the nozzle (m)

W = nozzle width (m)

W_{eff} = effective nozzle width in nozzle 2 (m)

R_n = radius of nozzle 2 (m)

p = number of particles

y = total number of particle hits

v_{cine} = cine film framing speed

Potential flow

R = wire diameter (m)

$$\left.\begin{aligned} r_1 &= \\ r_2 &= \end{aligned}\right\}$$ distances from $(-x_o, 0)$ and $(x_o, 0)$ to a given point on the potential line (m)

x_o = distance from the origin to the point of intersection of the lines of force (m)

y_o = distance from the origin to the centre of curvature of the potential line (m)

$k = (r_1/r_2)^2$

r_{pot} = radius of potential line (m)

θ = angle subtended by the streamline tangent

α = angle subtended by the nozzle tangent

v_{local} = local fluid velocity (m s^{-1})

v_{exit} = exit velocity (m s^{-1})

Empirical flow

x_{act} = actual x coordinate of small particle pathline

x_{st} = x coordinate of the potential flow streamline

y_{entry} = y coordinate at the starting position on the entry arc

y_{act} = actual y coordinate of small particle pathline

k_{entry} = streamline constant at the starting position on the entry arc

Errors

e(A) = absolute error in variable A

r(A) = relative error in variable A

σ = standard deviation

1. INTRODUCTION

When aluminium killed steels are continuously cast, a serious problem is the blocking of the tundish nozzles. This restricts the flow of liquid steel and may eventually lead to the cast being aborted. The most operational damage is caused in metering nozzles where the flow of liquid steel is controlled by the constant ferrostatic head that is maintained in the tundish. Any blockage will cause the flow to reduce unless the height of steel in the tundish is increased. Any increase is obviously limited by the dimensions of the tundish.

It has been shown in a study of the literature that blockage is caused by the accumulation of pre-existing alumina inclusions at the narrowest part of the nozzle. The inclusions are not wetted by the steel and adhere strongly on the surface of the nozzle as well as forming a strong adherent network.

No theory as yet explains how the inclusion move to the surface. The work described in this thesis examines the suggestion that it is centripetal forces in the curved converging liquid steel flow paths that drive the inclusions to the nozzle wall. This examination is carried out by model studies, in which hydrogen bubbles in water replicate inclusion is steel, and theoretically.

2. LITERATURE SURVEY

2.1. NOZZLE BLOCKAGE

2.1.1. BACKGROUND

Although nozzle blockage is a major problem today in continuous casting tundishes, blockage of other nozzles has been known for over 30 years. In 1956 Kokin (ref.1) reported the clogging of nozzles in teeming ladles caused by mullite, which could be cured by avoiding simultaneous deoxidation by Al and Si. Earlier, in 1949, Snow and Shea (ref.2) observed the accumulation of alumina tufts in the nozzles of open-hearth teeming ladles during a study of ladle errosion. They did not, however, pursue this observation. Chigrinov (ref.3) in 1963 reported the clogging in steel teeming ladles in a continuous casting plant by deposition of alumina. A lowering of the aluminium to <0.2 kg/tonne was suggested.

With the widespread development of continuous casting the blocking of tundish nozzles became a serious operational problem causing a reduction in casting speed and eventual aborting of the cast. The varying sizes of nozzles used indicates the main problem relating to Al-killed steels. Fig. 2.1, (ref.4) shows the highest Al contents that can easily be cast at different nozzle diameters. The smaller nozzle, used for small mould sizes, is more easily blocked.

Most work on nozzle blockage concerns plain Al-killed steels, both carbon steels and alloy steels. There are, however, references to blockage by rare-earth oxides (refs 5,6) and by strong deoxidisers, Al,Zr,Ti, (refs 7,8).

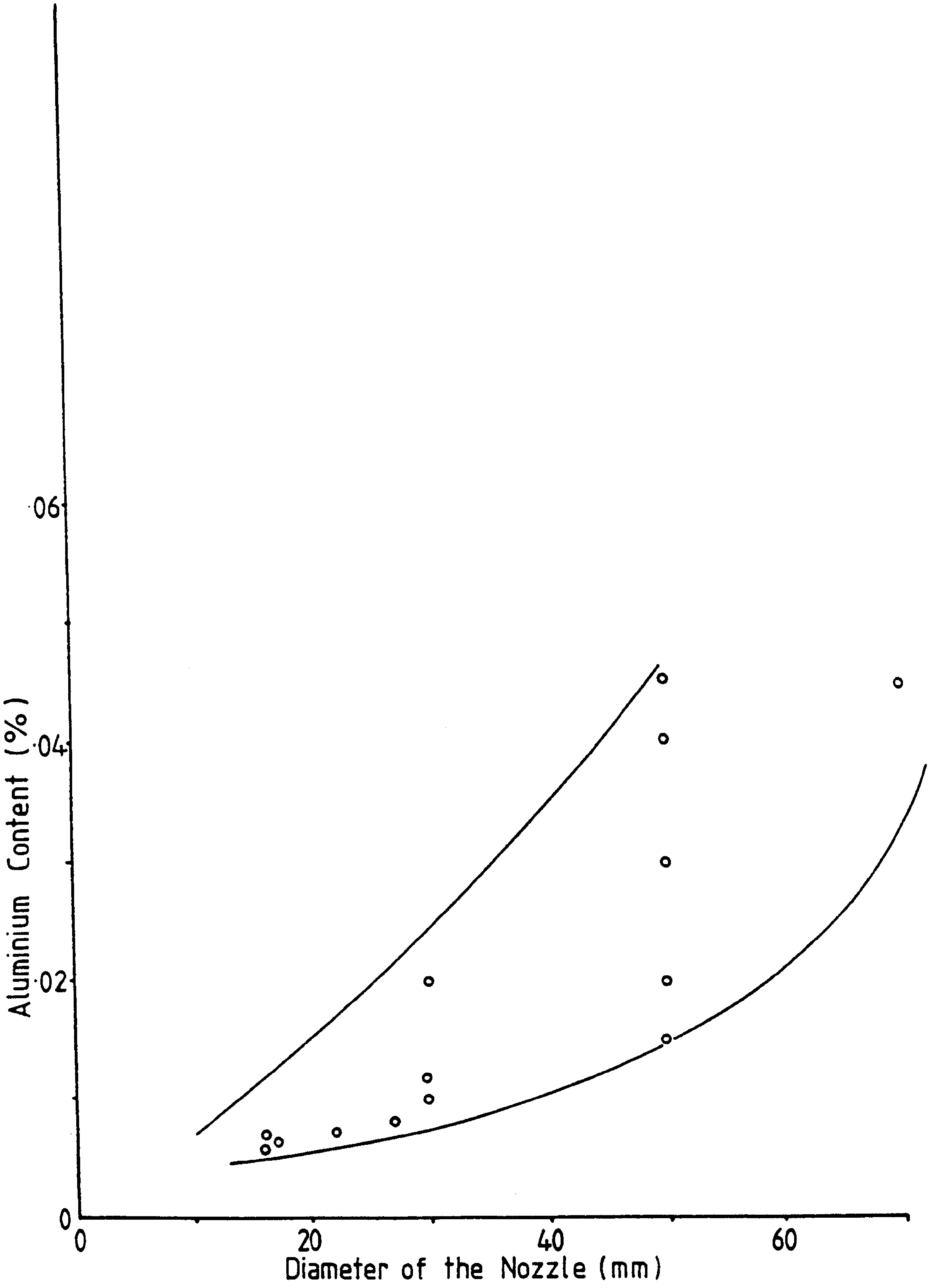

EFFECT OF NOZZLE DIAMETER ON
THE LIMITING ALUMINIUM CONTENT
FOR CONTINUOUSLY CAST BILLETS

FIG. 2.1

Titanium is important in the blocking of nozzles in casting stainless steels, (refs 9,10,11,12). The effect here is that alumina serves to bind the particles of titanium nitride in an adherent network, (ref.10). There is, however, some evidence that increase in aluminium content in titanium-containing stainless steel increases the weight of steel passing through an experimental nozzle, (ref. 13).

Nozzle blocking occurs in lances used for high rate injection processes, silica and nitrogen to liquid lead, (ref.14), and soda-ash and nitrogen to liquid steel, (ref.15). The clogging, however, is associated with too low a rate of transfer which results in freezing of the liquid at the nozzle exit. This is not something which is likely to occur in modern continuous casting processes.

2.1.2. THEORIES OF THE BLOCKAGE MECHANISM

Considering only Al-killed steels, four main theories have been put forward to explain the mechanism of nozzle blockage.

1) Chemical reaction between the aluminium in steel and the refractory, (refs 16,17,).

This involves the formation of high melting point alumina rich inlusions at the refractory surface, and a balance between the rate of build-up and the rate of removal by the fast flowing steel.

2) Reoxidation by air through the porous refractory (ref. 18).

Like the first theory this involves a reaction at the steel/refractory interface between Al in the steel and oxygen picked-up from the air through the porous refractory.

Both these theories have proved unsatisfactory since the reaction should be self limiting as the new material on the refractory surface will tend to prevent further reaction, (ref.7).

3) A temperature drop at the nozzle surface, (refs. 19,20).

When the temperature of the steel drops at the interface with the nozzle there will be a reduced solubility of aluminium and oxygen in steel causing precipitation of alumina at the nozzle surface. This is of course is thermodynamicly logical, but evidence (ref. 7) of an alumina deposit on the hottest part of the nozzle surface suggests that some other mechanism is dominant.

4) Many more investigators explain the blockage by the deposition and build-up of indigenous deoxidation products in the steel, (refs 3,7,21,22,23). There is some support for the view that the deposit in the nozzle is formed in the tundish by reaction of the steel with the tundish refractory, (ref.24). Also the freezing of steel at the refractory surface has been reported to be significant in trapping the alumina deposit, (ref.25).

Deposition of alumina is now accepted as the cause of nozzle blockage. It is well documented that solid alumina at steelmaking temperatures is highly adherent to the refractory, (ref.26), because of its high contact angle with steel. This favours the exclusion of steel from inclusion/inclusion interfaces and inclusion/refractory interfaces, causing a strong adherent network to form at the nozzle surface. The main question is how the inclusions are transported to the surface.

Singh (ref.7) has developed a theory which assumes that inclusions moving through the slow moving boundary layer attach themselves to the nozzle surface. Transport into the boundary layer is facilitated by turbulent eddies near the boundary layer. These eddies also increase the inclusion/inclusion collisions.

Liquid silicates found in Si or Si/Al killed steels are wetted by the steel and do not adhere to the refractory surface. Therefore there is not the concern with blocking nozzles in Si-killed steels.

2.1.3. MEANS OF PREVENTION

As already stated, the first means developed for control of nozzle blockage was the reduction in aluminium content of the steel, (refs 5,9,10,21,27,28). This is not, however, an option in steels which necessarily contain large amounts of Al for strong deoxidation or for grain refinement. A variety of other methods have therefore been used.

1) Use of larger nozzle diameters, possibly with stopper control, (refs 21,27). This obviously becomes more difficult at small mould sizes.

2) Addition of Al in the mould, (refs 29,30). This is effective but makes operation difficult. It also gives less time for dissolution of Al and less time for the removal of the alumina formed. Segregation is also more likely to occur.

3) Introduction of argon gas, (refs 31,32,33,34, 35). If this is introduced through the nozzle wall it should form a barrier between the steel and the refractory. It should also improve the removal of inclusions from the surface region. There is some evidence (ref 36) that indicates in bifurcated nozzles the alumina deposits at the base of the nozzle rather than in the upper convergent section (fig. 2.2).

4) With continued build-up of the deposit in nozzles it has been the practice to burn out the deposit with an oxygen lance, (ref.37). This can not remove all the deposit and continued lancing leads to cleanness problems in the cast product.

5) Redesign of the nozzle. There is particular emphasis on increasing the diameter of the nozzle in the part most prone to build-up (ref.20), though little evidence of how effective these new designs are. One new design, however, has been reported by Singh (ref.39). This is the annular nozzle (fig. 2.3). Use is made of the vena-contracta to separate the flowing steel from the refractory at the section of smallest diameter.

6) The surface properties of deoxidation products can be used to advantage by the addition of calcium to the

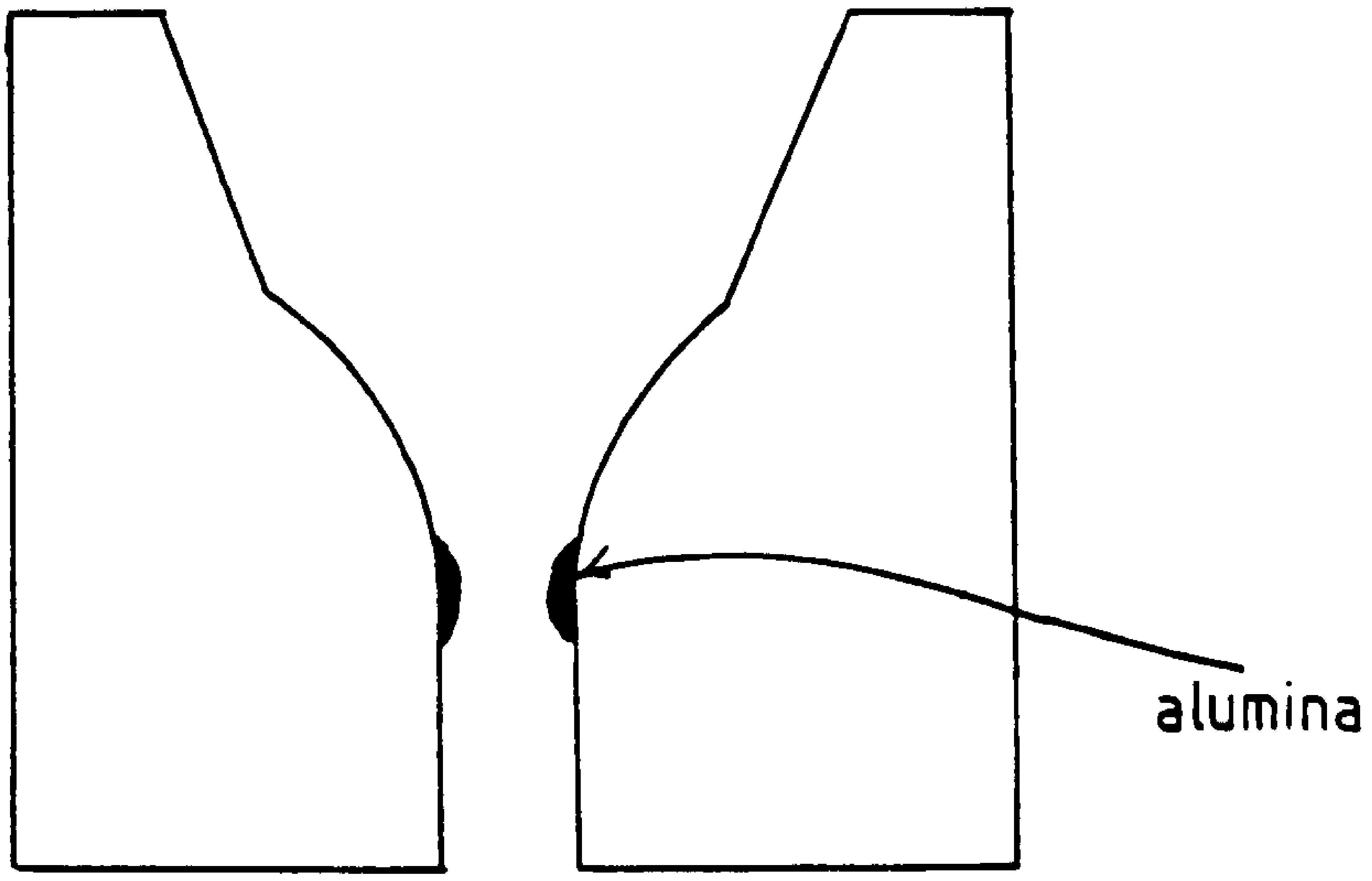

a) Location of deposit in Stocksbridge nozzle

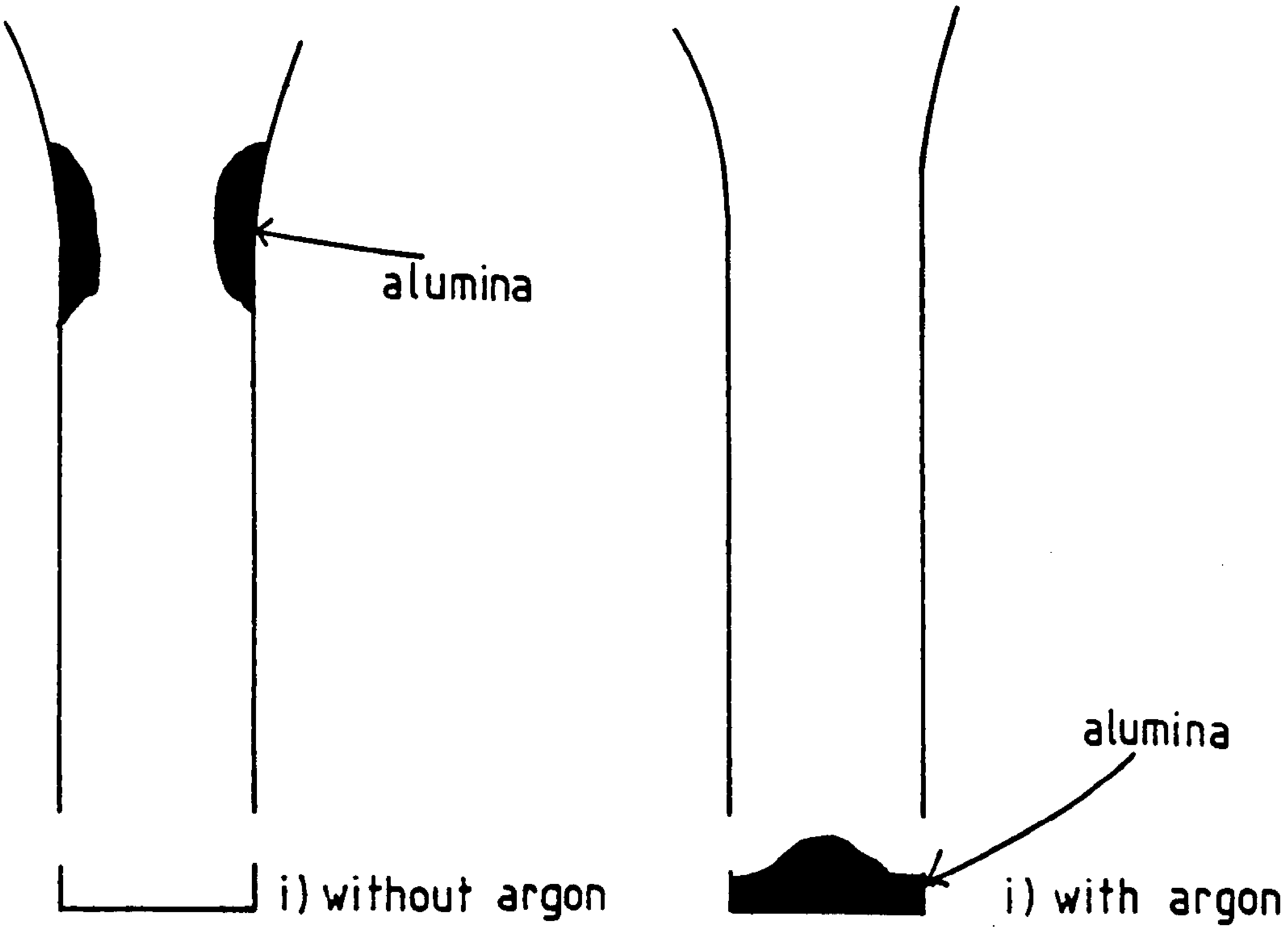

i) without argon

i) with argon

b) Alumina deposits in bifurcated nozzles

LOCATION OF ALUMINA DEPOSITS LEADING TO NOZZLE BLOCKAGE

FIG. 2.2

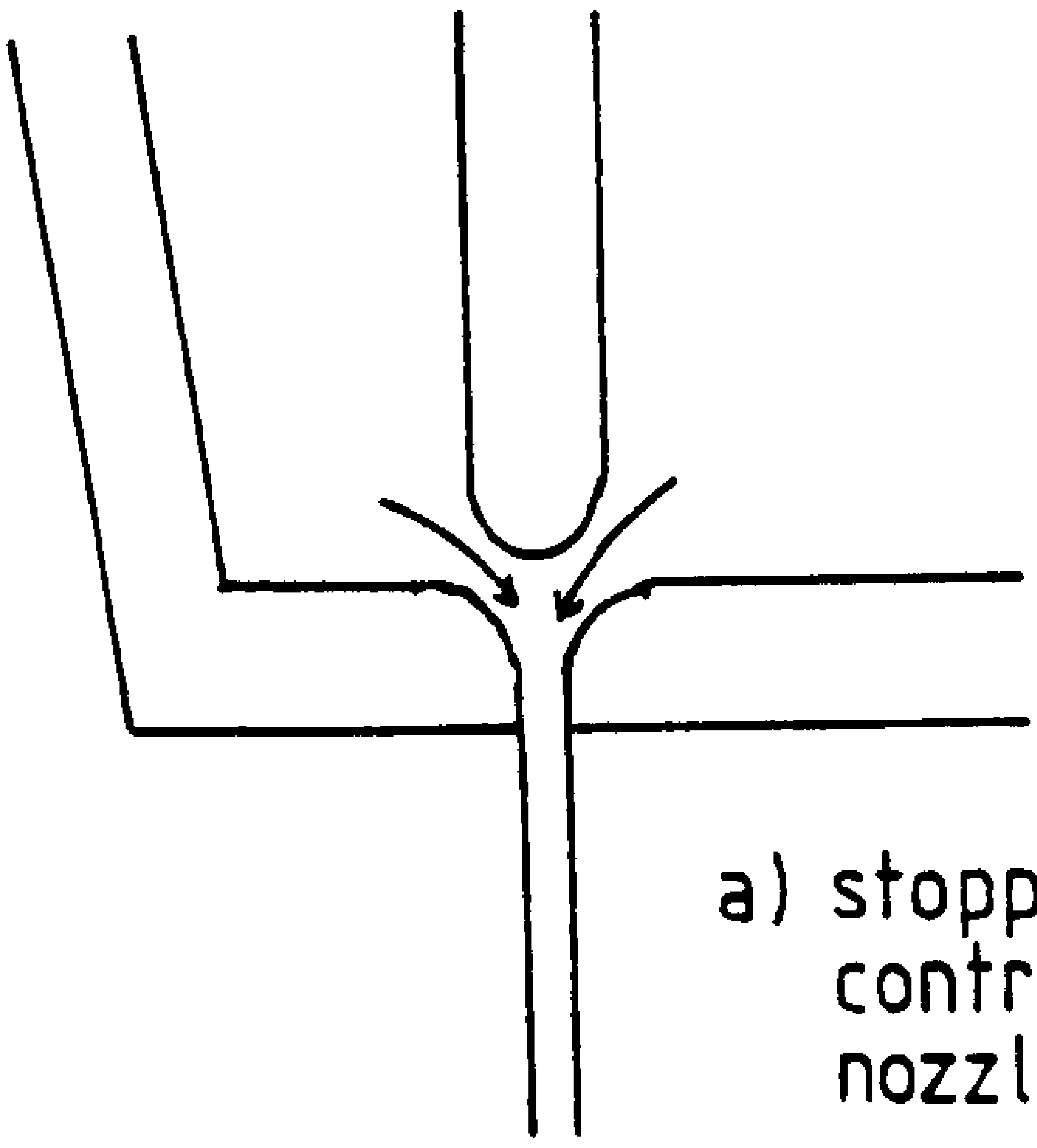

a) stopper controlled nozzle

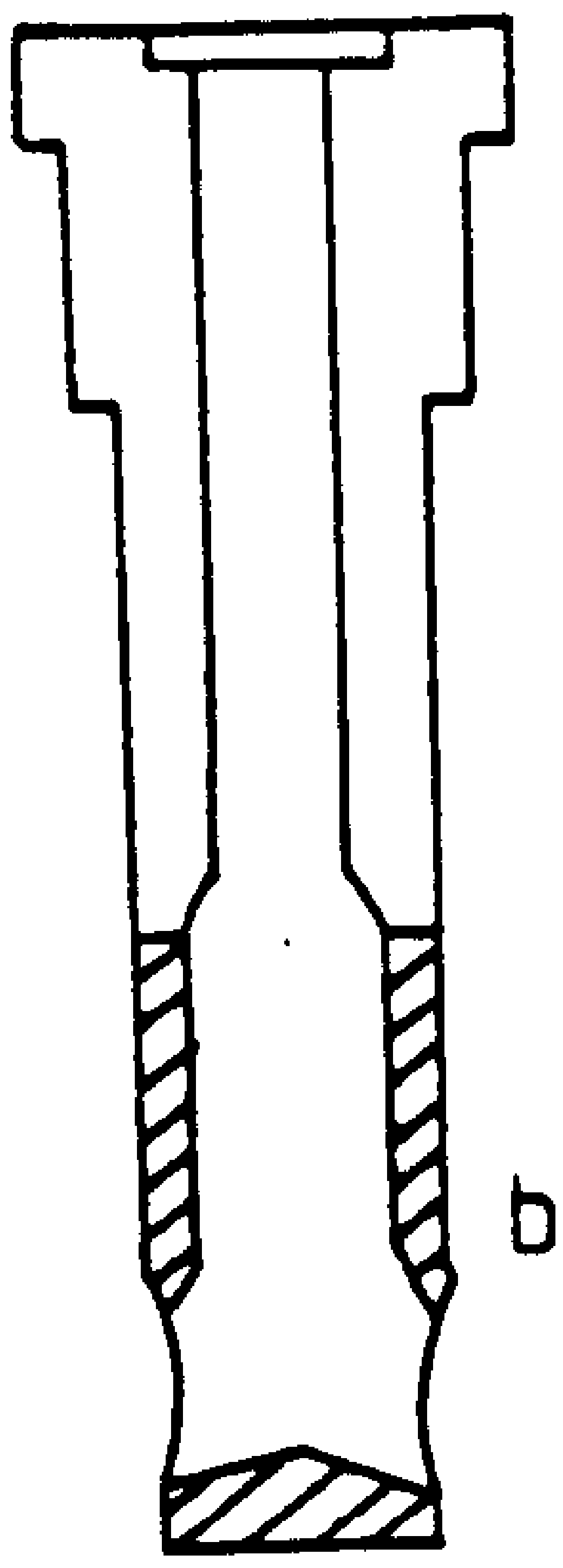

b) stepped nozzle (ref. 20)

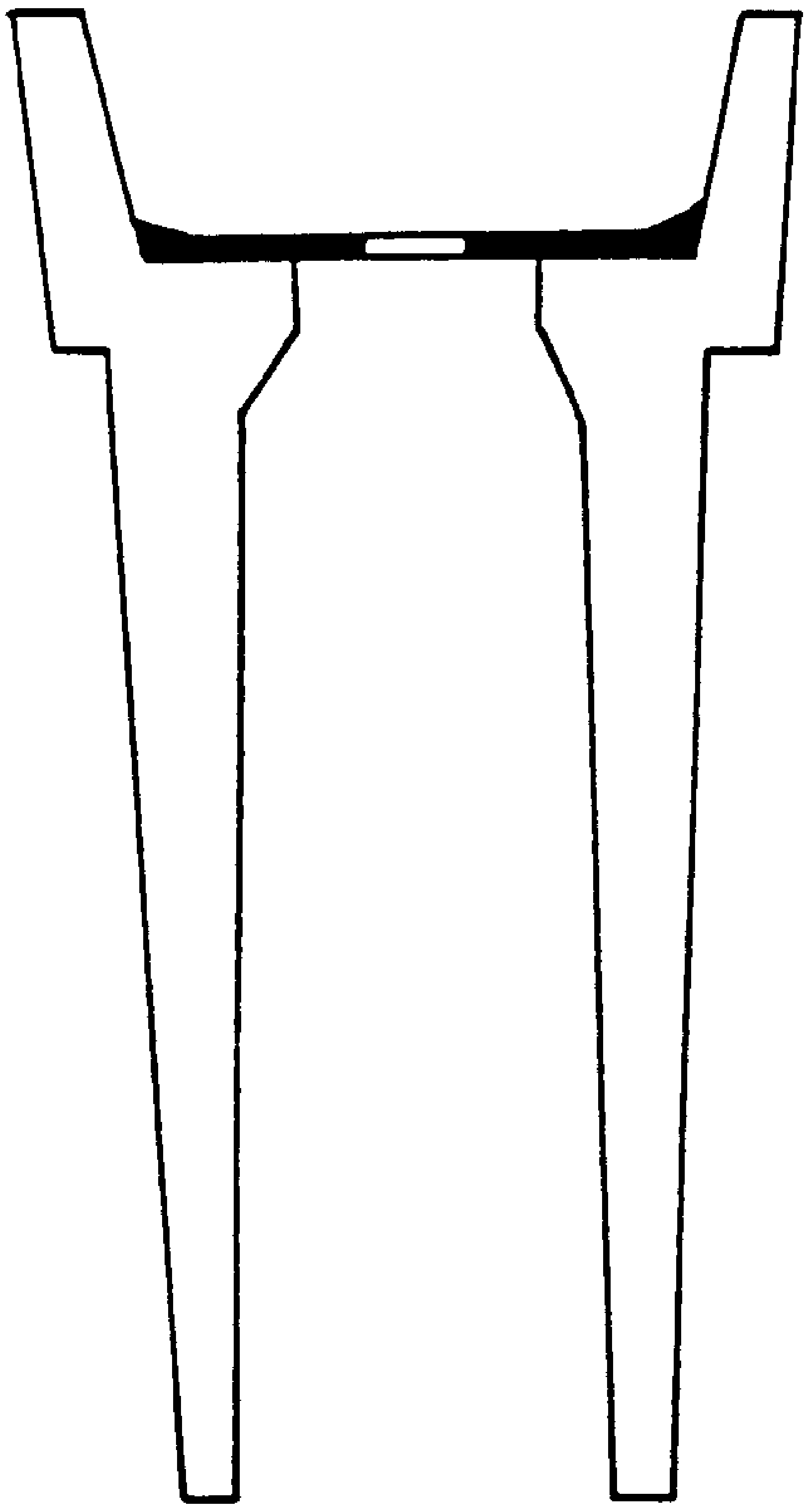

c) disc nozzle for inclusion collection and to prevent blockage (ref. 38)

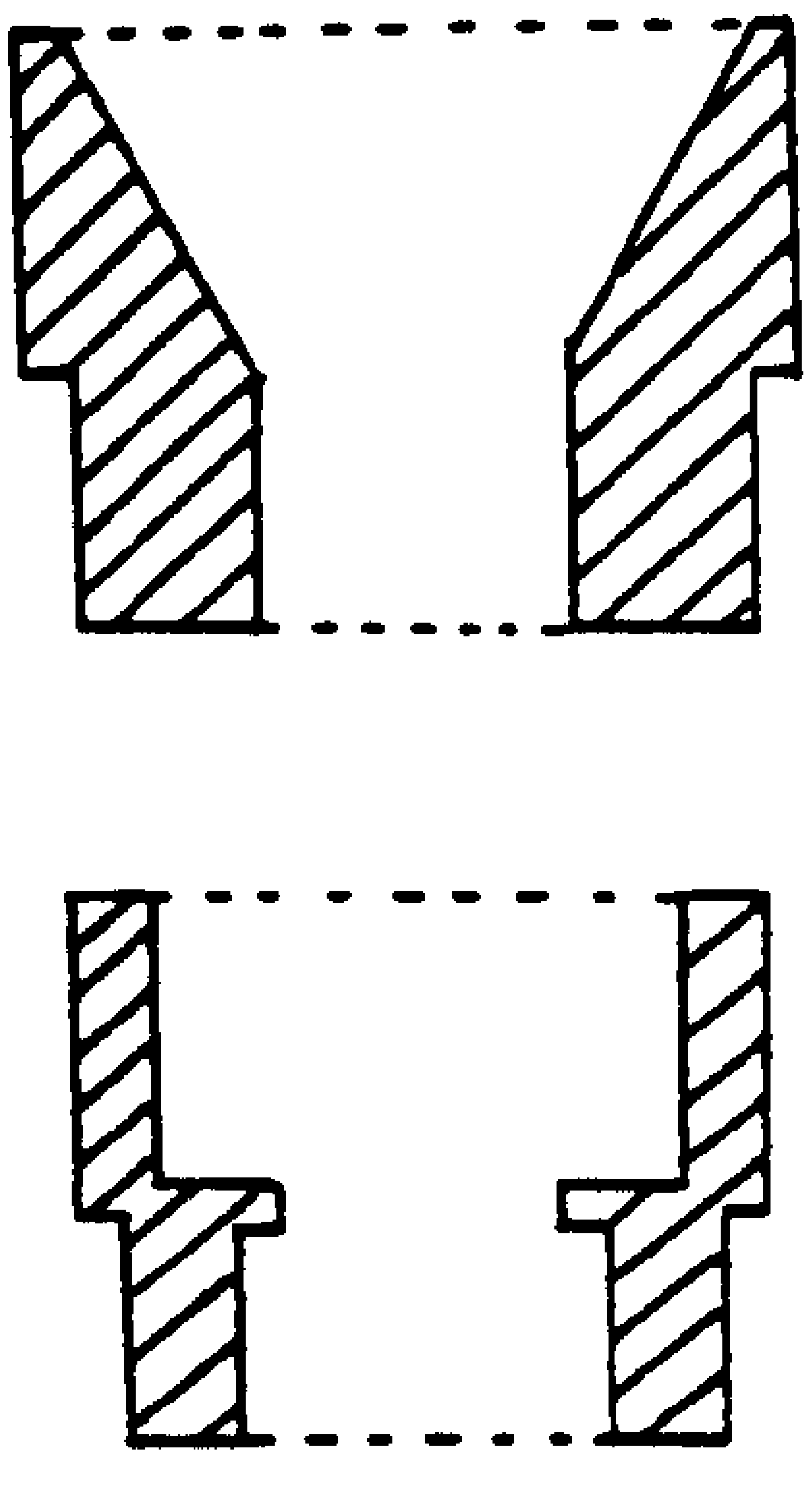

d) annular nozzle (ref. 39)

DIFFERENT NOZZLE DESIGNS

FIG. 2.3

steel, (refs 23,29,40,41,42). Here liquid $CaO.Al_2O_3$ or $CaO.2(Al_2O_3)$ is formed on deoxidation. Unlike alumina this does not adhere to the refractory surface to cause blocking. The calcium addition should be sufficient to prevent the formation of solid $CaO.6Al_2O_3$. i.e. $Ca/Al > 0.14$ (ref.40). If the calcium is too high, solid products such as CaO-rich CaO/Al_2O_3 /SiO_2 , CaS, or Al_2O_3 -rich calcium aluminates can again lead to blockage. There are therefore upper and lower limits between which the calcium addition is effective. The effectiveness is reduced by any reoxidation that fluxes the inclusions back to high melting point $Cao.6Al_2O_3$, (ref.23). Magnesium also reduces the effect of calcium because of the formation of $MgO.Al_2O_3$, (ref.40).

Calcium is the most widely used method for control of nozzle blockage.

7) Some success has been achieved by using a boron nitride based nozzle, (ref. 43). It appears that the surface of the nozzle is now wetted by the liquid steel and as a result inclusions are prevented from adhering to the surface.

8) A significant development in calcium treatment has been the use of a lime nozzle, (refs 44,45). These are produced by high temperature treament of $Ca(OH)_2$, which has been stabilised with TiO_2 ,ZrO_2 type oxides or salts such as $CaCl_2$, to prevent reaction with atmospheric moisture. Alumina inclusions that come in contact with the nozzle surface are fluxed by the lime in the same way as with normal calcium additions, and washed away. A recent design of this lime nozzle is one with an outer part of zirconia and

magnesite, and an inner part of lime based refractory which is in contact with the steel, (ref. 46)

2.1.4. CONCLUSIONS

1) Use of Ca/Al provides a very narrow range of control.

2) use of lime nozzles introduces extra non-metallic inclusions into steel.

Given the experimental and theoretical evidence that the adherence characteristics of alumina and refractories are important, the area that is most in need of study is how the inclusions travel to the nozzle surface.

2.2. FLOW VISUALISATION

2.2.1 THEORETICAL BACKGROUND

In the electrolysis of water hydrogen is generated at the cathode and oxygen at the anode.

$$H_2O = 2H^+ + O^-$$

If the bubbles are generated in the path of flowing water they will be swept along and can then act as flow tracers. Hydrogen is preferred to oxygen as the flow tracer because the volume produced is twice that of oxygen. The cathode can be any required size or shape and positioned where the flow is to be studied. The anode should be positioned downstream of the visualisation area.

The first reported use of hydrogen for fluid flow visualisation was by Kolin in 1953,(ref.47), to show the parobolic velocity profile across a circular pipe. Geller (ref.48) used a wire of 25 um and a pulsed current to give discrete lines of bubbles in studying boundary layers. Since then the development of the hydrogen bubble method has been reviewed in a number of papers,(refs 49,50,51,52,53,54,55, 56,57).

The electrochemistry of hydrogen evolution based upon Faradays Laws is detailed by Thompson (ref 58).
The volume of bubbles produced per second is expressed as follows:-

$$Q = \frac{43.1 \cdot T \cdot I}{P \cdot Hd} \qquad (2.2)$$

where T = temp ($^{\circ}$ K)

I = cathode current (amps)

P = hydrostatic pressure (Pa)

$= 1.013 \times 10^{5} + 9.81\, h$

h = hydrostatic head (m)

Hd = excess pressure due to surface tension

$$= 4\,\sigma / d \qquad (2.3)$$

σ for water = 0.072 N/m

d = diameter of bubbles (m)

Now the mass of hydrogen liberated = $I\ z$

where z = electrochemical equivalent of hydrogen

(1.04×10^{-8} kg/coulomb)

therefore mass of hydrogen liberated

$= 1.04 \times 10^{-8}\ I$ kg/s

Since the density of hydrogen at S.T.P. $= 0.08987\ \mathrm{kg/m^3}$

the volume of hydrogen liberated (Q) is given by,

$$Q = \frac{1.04 \times 10^{-8}\quad T\quad I}{0.08987\quad P}\ \mathrm{m^3/s} \qquad (2.4)$$

$$Q = \frac{4.3 \times 10^{-5}\quad T\quad I}{(1.013 \times 10^{5} + 9.81\ h) + (0.288/d)} \qquad (2.5)$$

To find the number of bubbles produced, $Q = N\ V_b$

where N = number of bubbles produced per second

and V_b = volume of a single bubble ($\pi d^3/6$)

$$\text{therefore}\quad N = \frac{4.3 \times 10^{-5}\quad T\quad I}{(1.013 \times 10^{5} + 9.81h) + (0.288/d)\ \pi d^3/6} \qquad (2.6)$$

If $T = 293$ K and $h = 0.5$ m

$$N = \frac{4.3 \times 10^{-5}\quad \times 293\quad I}{(1.013 \times 10^{5} + 9.81(0.5)) + 0.288/d\quad \times \pi d^3/6} \qquad (2.7)$$

$$N = \frac{0.024\ I}{4.97 \times 10^{5} + (0.288/d) \times d^3} \qquad (2.8)$$

If $I = 50$ mA (0.05 A) and $d = 25\ \mu m$ (25×10^{-6} m)

then $N = 1.5 \times 10^{5}\ s^{-1}$

If $I = 50$ mA and $d = 100\ \mu m$

then $N = 2.4 \times 10^{3}\ s^{-1}$

2.2.2 EXPERIMENTAL CONDITIONS FOR GOOD BUBBLE GENERATION

The voltage required for good visualisation of the bubbles is up to 600 V as described by Clutter et al (ref.54), depending on the size of the water model and the water flow speed. They also state that the generation of bubbles can vary from day to day under apparently identical conditions. There is evidence that at a water velocity of 7m/s the cathode voltage may need to be as high as 2 kV, (ref 59). Various electrical circuits have been used (refs 48, 50,52,54,56). Most convert an a.c. supply to d.c. which can then be used with a variable voltage. A reversing switch allows the regular alternation of anode and cathode, necessary for cleaning of the cathode (ref.48). There are references, however, to using an a.c. supply to produce alternate pulses of hydrogen and oxygen. The frequency is then fixed by the a.c. supply. If, however, the bubbles are produced at a high enough rate for good visualisation the method is safer than when using a d.c. source. The range of frequencies and pulse widths needed with a d.c. curcuit depend on the water flow velocity. If a large range of water flow rates are to be studied, wide ranges of frequencies and pulse widths are necessary. The effect of wire material, wire diameter, type of electrolyte, and temperature have been studied by Tory and Haywood (ref.60), although the addition of solute to water has been to increase the conductivity and not to increase the size of bubbles. Work by Blandamer et al (ref.61), showed that the size of hydrogen bubbles liberated in aqueous solution is decreased by the addition of sodium bromide and increased by the addition of ammonium bromide. This is a result of changes in the contact angle between the liquid and the cathode.

2.2.3. TYPE OF CATHODE

The most common type of material used for cathodes is platinum because of its corrosion resistance, particularly when using salt solutions for increased conductivity (refs 48,49,56,59,62,63,64,65). Steel piano wire (ref.49), stainless steel (ref.49), and Nichrome (ref.58) have been used for increased strength. Tungsten (refs 50,66) and copper (refs 47,67 have also been used. A particular problem occurs with stainless steel wire. Dirt accumulating on the wire has to be removed by reversing the current so that oxygen is liberated from the experimental wire, which would then be the anode. The oxygen causes oxidation and disintegration of the wire (ref. 60). For this reason current reversal is not a viable means of cleaning stainless steel electrodes.

The diameter of the cathode has varied from 5 or 10 µm in low speed flows (ref.66) to 300 µm at flow speeds of 7m/s (ref. 59) where good visualisation is necessary.

Using a straight cathode with a pulsed current can produce a series of velocity profiles (fig. 2.4a). A development to a 'kinked' wire (ref.54) allows discrete particle streaklines to be observed (fig. 2.4b). For a greater optical density of bubbles a cathode in the form of a

a) Straight pulsed cathode

b) Kinked cathode

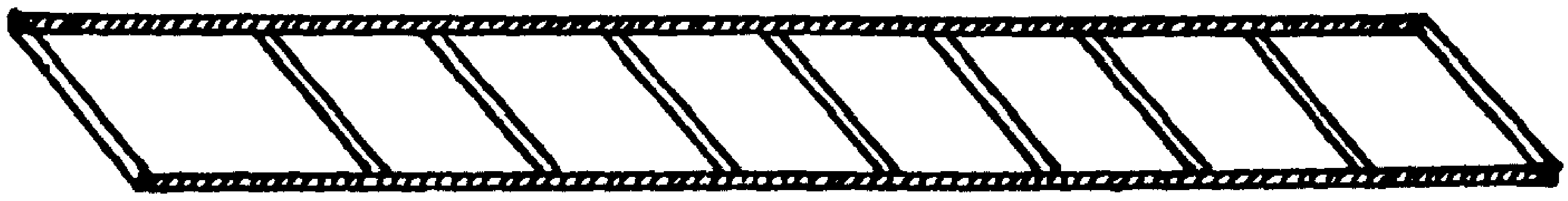

b) Ladder type cathode

VARIOUS FORMS OF CATHODE

FIG. 2.4

ladder (ref.49) was developed (fig. 2.4c). The combination of kinked or ladder type cathode producing streaklines on film, which gives a time dependent picture allows for good interpretation of unsteady flow patterns (ref.49).

2.2.4. LIGHTING AND PHOTOGRAPHY

The best lighting configuration is from a collimated source to the rear of the model. The angle of the incident light to the viewing axis should be about 65° (ref.49). Powerful lighting of up to 800 W from mercury vapour lamps (ref.54) or quartz-iodine (ref.58) is found to be necessary.

Electronic flash is required to freeze the bubble motion on film and clearly define the bubble rows (ref.54). Streaklines of bubbles can be produced with camera shutter speeds of about 1/500 s (ref.58). For motion photography, if it is necessary to freeze the bubble motion, framing speeds of 25 frames/s have been found satisfactory for flow speeds up to 1.5m/s (ref.56).

2.2.5. USES OF THE HYDROGEN BUBBLE METHOD

The method has been widely used for studying flows in boundary layers (refs.62,68,69,70,71). It is ideally suited to observing the turbulent flow in the wake of objects in a flowing stream, (ref.72). Also separated flows (refs 64,73) and unsteady flows in pipes (ref.65) are easily studied. Hydrogen bubble patterns have been investigated in 3-d flows and good 3-d patterns have been produced with the aid of computer interpretation (ref.74). An interesting development is the use of water/glycerine mixtures (refs 75, 76) which allows the investigation of more viscous fluids.

In the literature studied, no evidence has been found of previous attempts to use hydrogen or other gas bubbles to simulate the behaviour of inclusions in steel.

2.2.6. ADVANTAGES

The advantages of the method are well covered by Clutter (ref.54):-

1) The quantity of bubbles is easily controlled, and the bubbles easily placed in the desired location.

2) Bubbles do not contaminate the water in the same way as dyes.

3) The bubbles do not lose their identity in turbulent flows.

4) No special ducting is required.

2.2.7. ERRORS AND UNCERTAINTIES

The main sources of uncertainty arise in the measurement of local velocity and are fully analysed by Schraub (ref.49). Briefly, these are:-

1) Uncertainty of distance measurement on film.

2) Averaging uncertainty because a group of bubbles is followed rather than individual bubbles.

3) Displacement of bubbles out of a specific plane perpendicular to the viewing path.

4) Response uncertainty because bubbles do not reach the velocity of the fluid instantaneously.

5) Resolution uncertainty because of fluctuations

in the fluid, smaller than the bubble diameter.

6) Uncertainties because of bubble buoyancy.

7) There is a velocity defect behind the bubble generating wire as a result of the viscous wake behind the wire. For most investigations, however, the bubble velocity reaches the free stream velocity in less than 70 wire diameters. Also in order to avoid turbulence and separation behind the wire, the wire Reynolds Number should be less than 40 (ref.77).

In rapidly accelerating flows there may be an appreciable difference in the fluid flow path and the bubble flow path. These are, of course, errors in the flow path of the fluid as estimated by the flow path of a gas bubble. For the purpose of the present thesis these errors can be rationalised and used to advantage, because it is the flow path of the particle that is important.

2.2.8 OTHER GASES USED FOR VISUALISATION

Although hydrogen has been the gas most used for water flow visualisation, other gases have been tried with success. Compressed air has been introduced through a punctured rubber tube under water, (ref.78). The bubbles were not, however, uniformly distributed. A more uniform distibution of air bubbles was achieved by adding a surface activator to reduce the surface tension, (ref.79). When agitated an emulsion of tiny air bubbles is produced, the size of bubbles being dependent on the surface tension. Soap bubbles filled with helium gas have also been used to study both 2-d and 3-d flows, (ref.80). The problem with these methods is that the bubbles are ramdomly distributed throughout the volume and not confined to a specific plane as is possible with electrically generated hydrogen.

2.3. MATHEMATICAL BACKGROUND AND THEORY

2.3.1. THEORETICAL MODEL

The design of the Stocksbridge continuous casting nozzle is shown in Fig. 2.5. Streamlines estimated from a flow net have been superimposed. The proposed physical model is a constant thickness two-dimensional slice of the tundish and nozzle such that the width in the model is equivalent to the diameter in the actual nozzle. As a basis for further mathematical analysis we can consider the dynamics of a particle in a stable eddy, (ref.81). The analysis equates the centripetal force, first with particle inertia, and second with the friction. A comparison of the two approaches is then made.

The following assumptions are made:-

1) the terms, solid particle, inclusion, liquid drop, and gas bubble are used to denote specific second phases in the fluid. The term particle is used to denote any non-specific second phase. These definitions will apply throughout the thesis,

2) the fluid rotates with constant angular velocity,

3) the angular velocity of the particle is the same as that of the fluid.

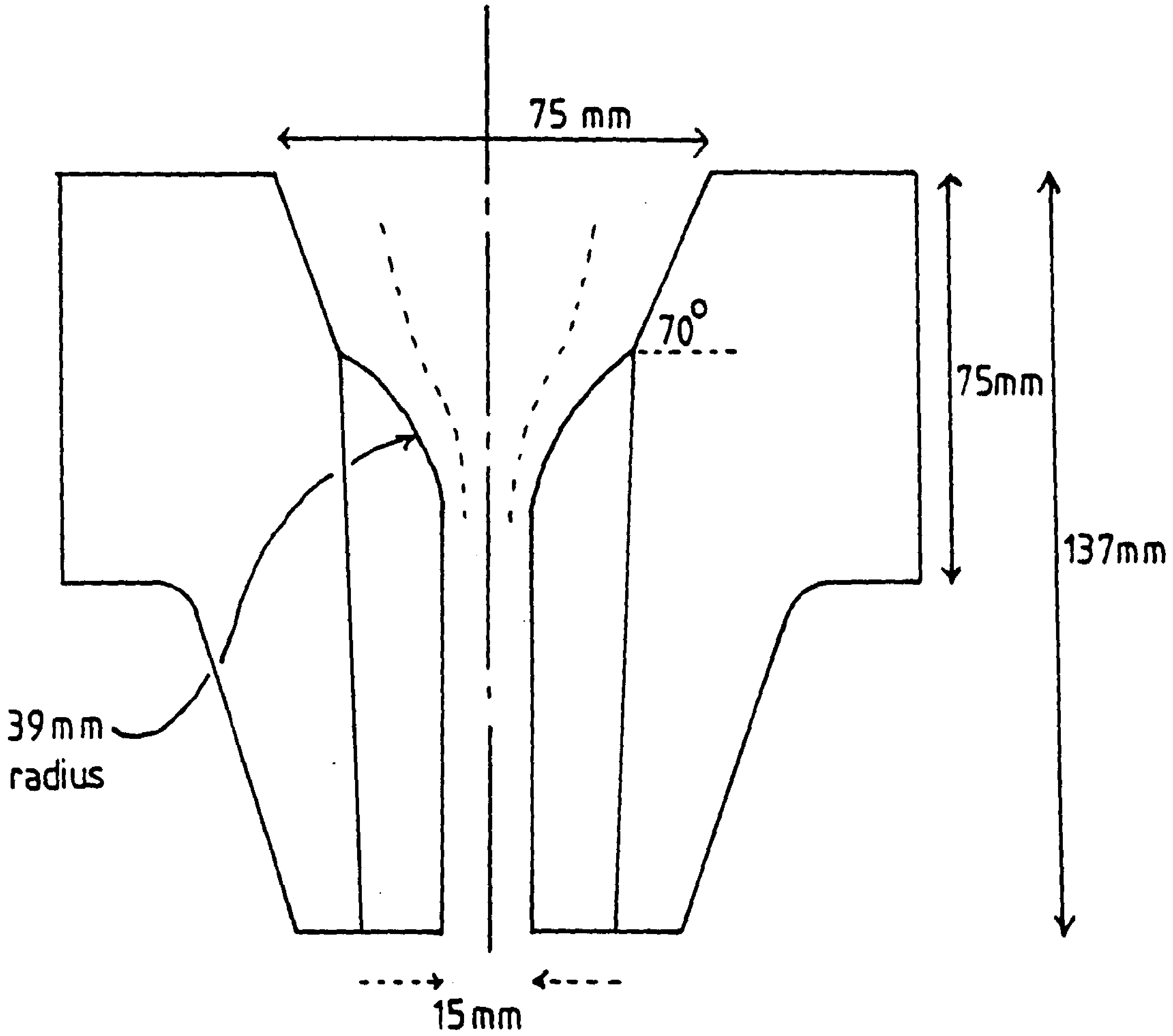

THE STOCKSBRIDGE NOZZLE

FIG. 2.5

4) the effects of buoyancy are neglected.

The forces involved are as shown:-

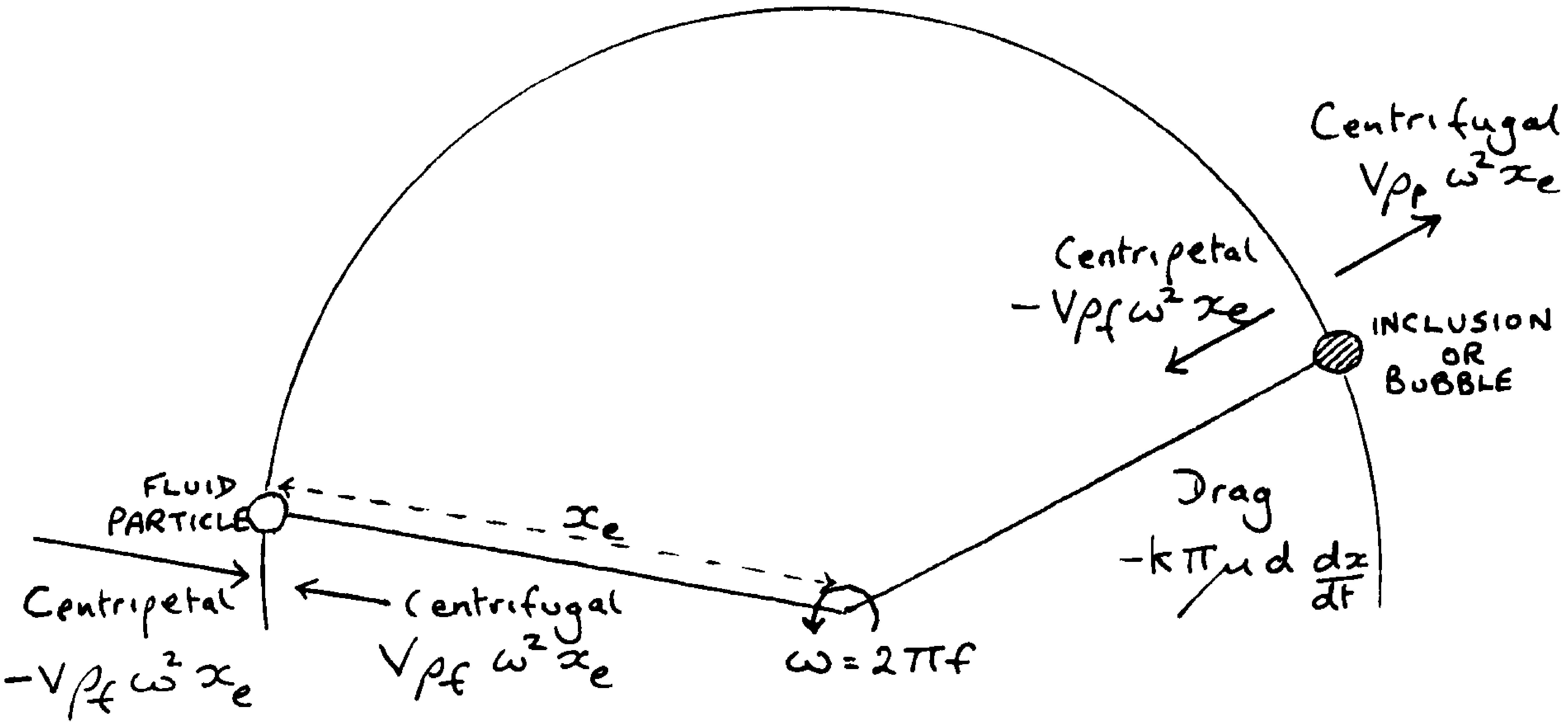

Where,

V = volume of particle

ρ_f = density of fluid

ρ_p = density of particle

x = radius of eddy

k = particle drag factor, (ref.82).

μ = viscosity of fluid

d = particle diameter

f = frequency of rotation

dx/dt = radial velocity of particle

Ignoring friction between the fluid and the particle

$$V\ (\rho_p + \rho_f/2)\ \frac{d^2x}{dt^2} = V\omega^2\ (\rho_f - \rho_p)\ x \qquad (2.9)$$

Where $V(\rho_f/2)$ is the added mass because of fluid which must be accelerated with the particle.

$$\frac{d^2x}{dt^2} = \left[\frac{\rho_f - \rho_p}{\rho_p + \rho_f/2}\right]\omega^2 x \qquad (2.10)$$

This is the equation of Simple Harmonic Motion where x varies from x_o at t=0 to zero at t, i.e. the quarter period. Therefore, t is the time taken for a particle to reach the centre of a stable eddy.

$$t = \frac{\pi}{2\omega}\sqrt{\frac{\rho_p + \rho_f/2}{\rho_f - \rho_p}} \qquad (2.11)$$

$$t = \frac{\pi}{2(2\pi f)}\sqrt{\frac{\rho_p + \rho_f/2}{\rho_f - \rho_p}} \qquad (2.12)$$

$$t = \frac{1}{4\ f}\sqrt{\frac{\rho_p + \rho_f/2}{\rho_f - \rho_p}} \qquad (2.13)$$

The frictionless motion is then independent of the size of the particle.

For an alumina inclusion in liquid steel,

ρ_p = 3810 kg/m^3

ρ_f = 7200 kg/m^3

$$t = \frac{1}{4\ f}\sqrt{\frac{3810+7200/2}{7200-3810}} \qquad (2.14)$$

$$t = \frac{1}{4\ f} \sqrt{2.186} \qquad (2.15)$$

$$\underline{\underline{t = \frac{0.37}{f}}} \qquad (2.16)$$

Since t = n/f (where n is the number of revolutions of the eddy),

$$n = 0.37$$

Therefore, if the fluid friction were unimportant, the particle would reach the centre of the eddy in less than half a revolution.

Similarly, for an hydrogen bubble in water,

$\rho_p \sim$ zero

$\rho_f = 998.2\ \mathrm{kg/m^3}$

$$t = \frac{1}{4\ f} \sqrt{\frac{998.2/2}{998.2}} \qquad (2.17)$$

$$t = \frac{1}{4\ f} \sqrt{0.5} \qquad (2.18)$$

$$\underline{\underline{t = \frac{0.177}{f}}} \qquad (2.19)$$

Therefore $n = 0.177$

so that, were friction unimportant, the hydrogen bubble would reach the centre of an eddy in less than a fifth of a revolution.

If we ignore inertia, but consider fluid friction, the force balance becomes:-

$$-\frac{4}{3}\pi r^3 (\rho_f - \rho_p)\omega^2 x = k\pi\mu(2r)\frac{dx}{dt} \tag{2.20}$$

where dx/dt is the radial velocity of the particle

$$\frac{dx}{dt} = \frac{-2 r^3 (\rho_f - \rho_p)(2\pi f)^2 x}{3 k \mu r} \tag{2.21}$$

$$\frac{dx}{dt} = \frac{-2 r^2 (\rho_f - \rho_p)(2\pi f)^2 x}{3\mu k} \tag{2.22}$$

$$\frac{dx}{x} = \frac{-2 r^2 (\rho_f - \rho_p)(2\pi f)^2 dt}{3\mu k} \tag{2.23}$$

$$\Big[\ln(x)\Big]_{x=x_o}^{x=0} = \frac{-2 r^2 (\rho_f - \rho_p)(2\pi f)^2}{3\mu k} \tag{2.24}$$

where r = radius of particle

t = time

μ = dynamic viscosity

since $\ln x - \ln x_o = \ln (x / x_o)$ (2.25)

and $t = n/f$ (2.26)

$$\ln x/x_o = \frac{-2 \; r^2 \; (\rho_f - \rho_p) \; (2 \pi f)^2 \; n/f}{3 \mu k} \tag{2.27}$$

$$x/x_o = \exp \left\{ \frac{-2 \; r^2 \; (\rho_f - \rho_p) \; (2 \pi f)^2 \; n/f}{3 \mu k} \right\} \tag{2.28}$$

$$x/x_o = \exp \left\{ \frac{-8 \; r^2 \; (\rho_f - \rho_p) \; \pi^2 \; f \; n}{3 \mu k} \right\} \tag{2.29}$$

$$x/x_o = \exp \left\{ \frac{-8 \; (\rho_f - \rho_p) \; \pi^2 \; f \; n \; r^2}{3 \mu k} \right\} \tag{2.30}$$

$$x/x_o = \exp \left(- A \; f \; n \; r^2 \right) \tag{2.31}$$

where $A = \frac{8 \pi^2 (\rho_f - \rho_p)}{3 k \mu}$ (2.32) for alumina in steel,

$$A = \frac{8 \cdot 3390 \ \pi^2}{3 \cdot 3 \cdot 6 \ 10^{-3}} \quad m^{-2} \ s \qquad (2\cdot33)$$

$$\underline{\underline{A = 4.957 \times 10^6 \ m^{-2} \ s}} \qquad (2\cdot34)$$

for hydrogen in water,

$$A = \frac{8 \cdot 998.2 \quad \pi}{3 \cdot 3 \cdot 1.005 \ 10^{-3}} \quad m^{-2} \ s \quad (2\cdot35)$$

k is taken as being the same as for a solid particle at small bubble sizes, (ref.83).

$$\underline{\underline{A = 8.71 \times 10^6 \ m^{-2} \ s}} \qquad (2\cdot36)$$

Considering an eddy of frequency 150 Hz fig. 2.6 shows the friction controlled movement of various sizes of alumina inclusions to the centre of the eddy. Fig. 2.7 shows the same for hydrogen in a water eddy. Compared to the frictionless movement, when the particle reaches the centre in a fraction of a revolution, it is evident that small particles take many revolutions to reach the centre. Thus the behaviour of the inertial effects can be ignored, particles being dominated by frictional effects.

With steel flow through a nozzle a maximum exit velocity of 4.5 m/s is possible. Taking the nozzle radius of curvature at 0.04 m gives an angular velocity of 112 radians.s^{-1} and a frequency of 18 Hz. A more typical exit velocity would be 2.5 m/s giving a frequency of 10 Hz. This is a more

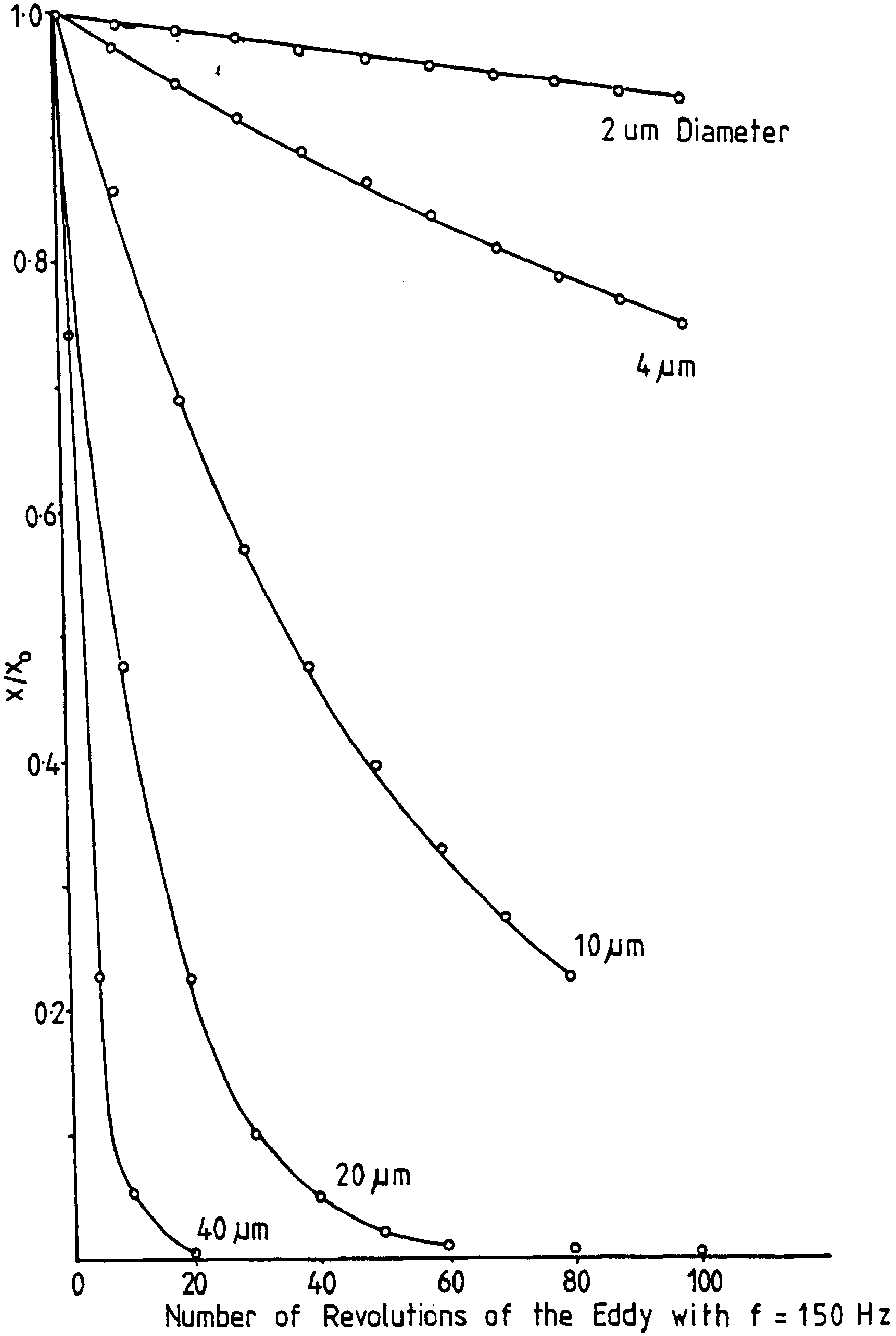

EFFECT OF THE NUMBER OF
EDDY REVOLUTIONS ON THE
RADIAL POSITION OF AN
ALUMINA INCLUSION

FIG. 2.6

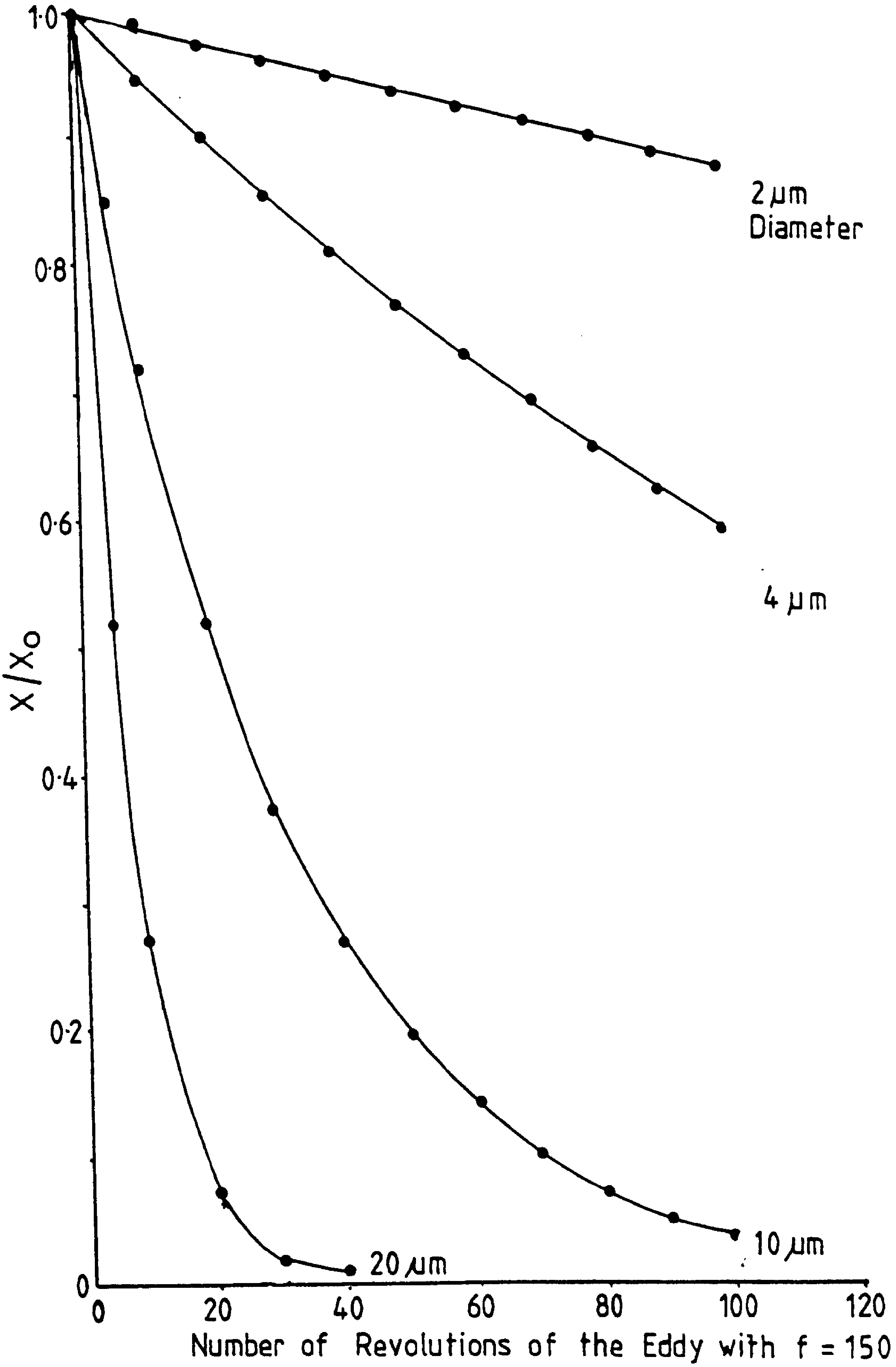

EFFECT OF THE NUMBER OF EDDY REVOLUTIONS ON THE RADIAL POSITION OF A HYDROGEN BUBBLE

FIG. 2.7

reasonable value to consider since a value of 18 Hz would only apply at the exit and not higher in the nozzle. To compare the effects of friction and inertia the effect of size on the radial movement of alumina particles is shown in fig. 2.8. At 10 Hz, (typical of flow through a convergent nozzle), a particle of diameter 250 μm is only about 20% of the distance to the centre with frictional flow.

An almost identical result is obtained for hydrogen in water, (fig. 2.9).

2.3.2. ALTERNATIVE APPROACHES

In the literature on hydrogen bubble flow visualisation a number of references are made to the errors obtained in curved flows by the movement of hydrogen to the centre of curvature. Okamoto et al (ref.84) considered the movement to be a balance of drag force and centripetal force, then expressed the difference in flow path as:-

$$\tan \theta = \frac{u}{v} \qquad (2.37)$$

where u = radial velocity of the bubble

v = fluid velocity

Ciobanu et al (ref.85) studying the retention of inclusions in cenrifugal slag collectors considered the inertial force. The formula obtained is the same as that derived by Hills except that the acceleration of fluid is not included in the inertial term. He also considered the effects of buoyancy. This, however, acted at right angles to

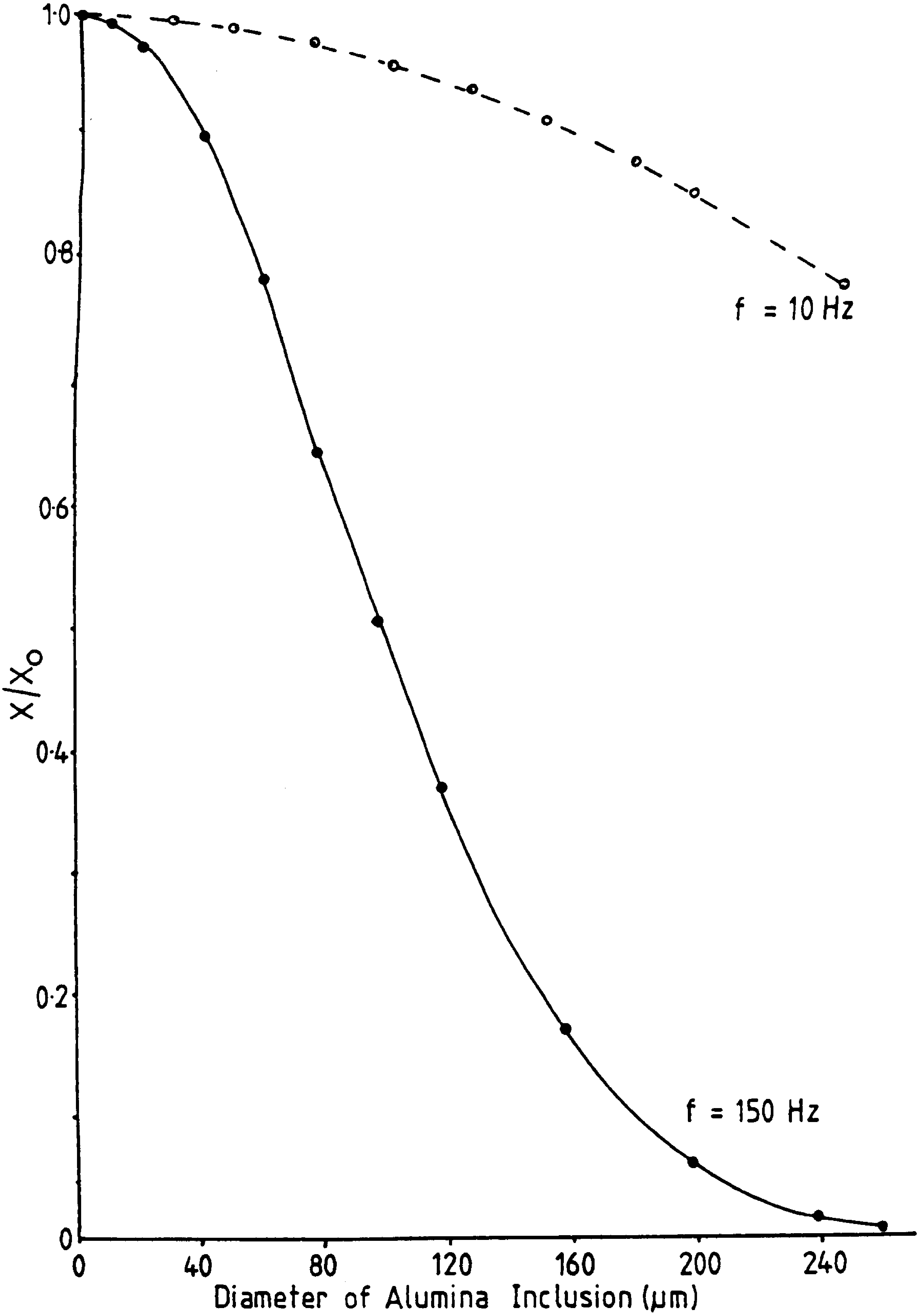

EFFECT OF INCLUSION SIZE
ON THE RADIAL POSITION
IN A STEEL EDDY

FIG. 2.8

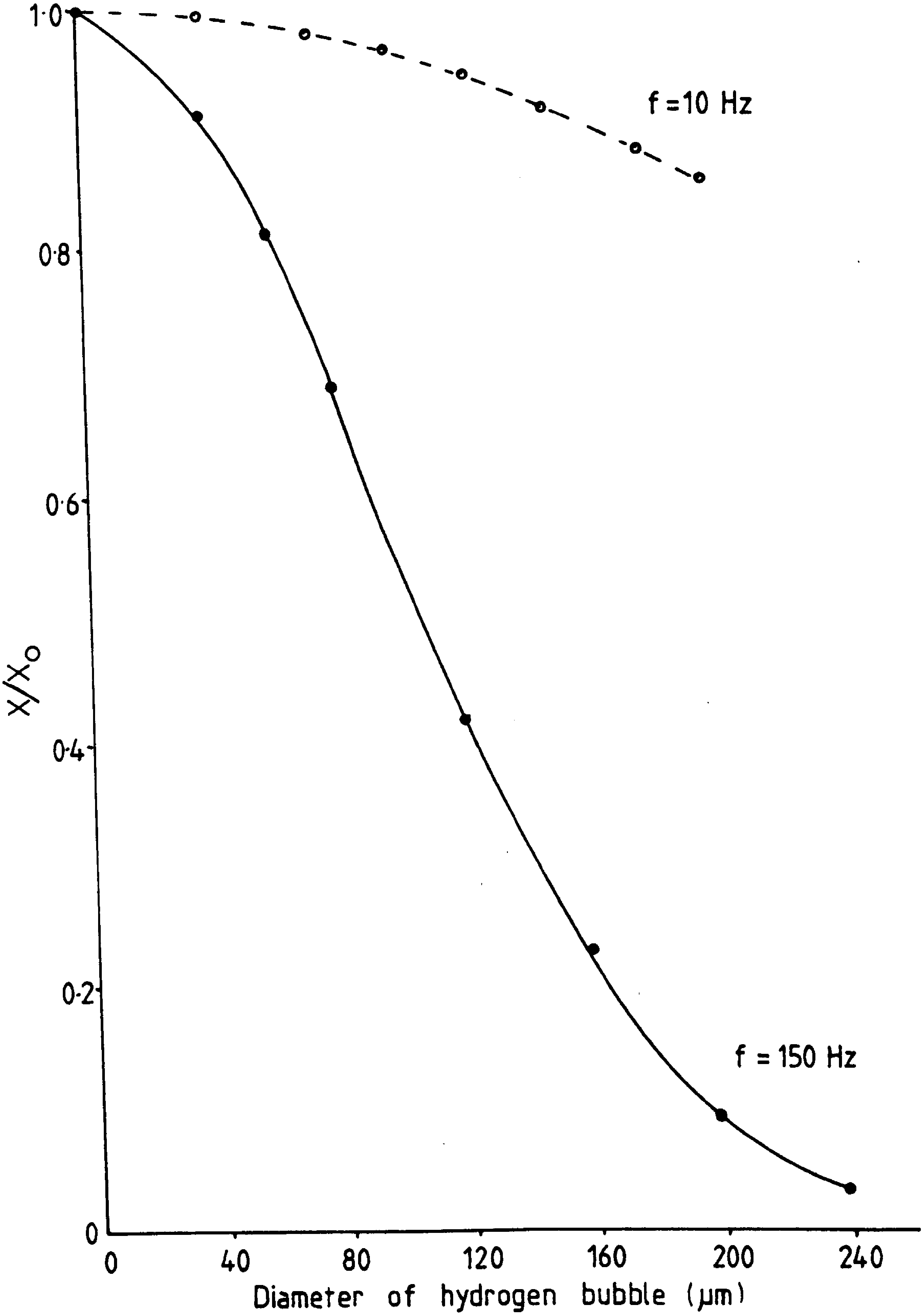

EFFECT OF HYDROGEN BUBBLE
SIZE ON THE RADIAL POSITION
IN A WATER EDDY

FIG. 2.9

the centripetal movement, and the two could be considered separately.

A comprehensive treatment by Langford (ref.86), considers the changing angular velocity of small sedimenting particles as they move away from the centre of curvature. This treatment has been applied to hydrogen bubbles in water by Thompson (ref.58). The equations of motion are expressed in tangential and radial form:-

$$\frac{d^2x}{dt^2} = x\left[\left(\frac{d\theta}{dt}\right)^2 - \beta\omega^2\right] - \frac{dx}{dt} \qquad (2.38)$$

$$\frac{d^2\theta}{dt^2} = \alpha\left[\omega_f - \frac{d\theta}{dt}\right] - \frac{2}{x}\frac{dx}{dt}\frac{d\theta}{dt} \qquad (2.39)$$

where x and θ are the particle coordinates

ω_f = angular velocity of the fluid

$$\alpha = \frac{12\,k\,\nu}{d^2\,(2B+1)} \qquad (2.40)$$

$B = \rho_p / \rho_f$ (the ratio of densities)

k = drag coefficient

ν = kinematic viscosity

d = bubble diameter

It was assumed that d^2x/dt^2 and $d^2\theta/dt^2$ were both zero and that $d\theta/dt = \omega_p$, $dx/dt = u$ (particle radial velocity). Thompson expressed the solution to these equations as:-

$$\Omega = \frac{\omega_p}{\omega_f} = \left\{ 1/2 \left[\sqrt{(G-\beta)^2 + 4G} - (G-\beta) \right] \right\}^{1/2} \qquad (2.41)$$

$$\text{where} \quad G = \left(\frac{\alpha}{2\,\omega_f} \right)^2 \qquad (2.42)$$

$$\text{and } u/v = \frac{\alpha}{2\,\omega_f} \left(\frac{1}{\Omega} - 1 \right) \qquad (2.43)$$

Therefore the particle radial velocity can be calculated.

2.3.2.1 COMPARISON OF RADIAL VELOCITY CALCULATIONS

Comparisons have been made between the radial velocity calculations of Hills and of Langford, to establish the area of agreement.

2.3.2.1.1 BEHAVIOUR OF ALUMINA IN STEEL

Again the effect of particle size on radial velocity at different steel flow rates is shown in fig. 2.10. The theory predicts a maximum radial velocity of 10.9% of the steel velocity. The inclusion size at which this occurs decreases with increasing steel velocity, (600 µm dia. at 1.0m/s and 300 µm dia. at 4.0m/s). Up to steel velocities of 4.0 m/s there is no predicted difference below diameters of 150 µm.

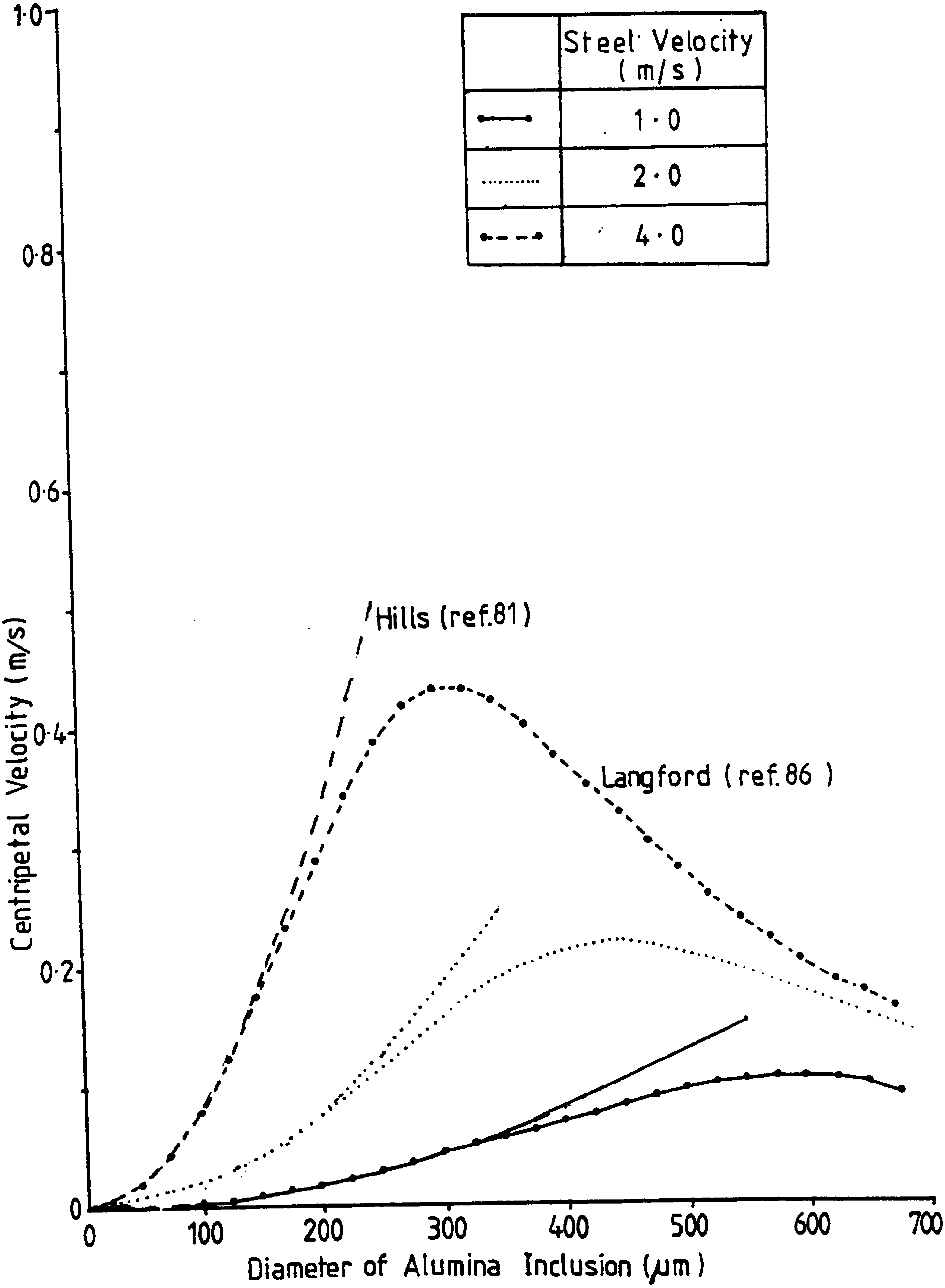

EFFECT OF INCLUSION SIZE ON
CENTRIPETAL VELOCITY IN STEEL

FIG. 2.10

2.3.2.1.2 BEHAVIOUR OF HYDROGEN IN WATER

The effect of bubble size on radial velocity is shown in fig. 2.11. The two theories predict identical radial velocity at small bubble sizes but the Langford theory gives a maximum velocity at a specific bubble size. The bubble size at which the maximum occurs is smaller with increasing water velocity, (1800 µm dia. at 1.0m/s and 1000 µm dia. at 4.0m/s). The maximum radial velocity is 41.6% of the water velocity. At all water velocities up to 4.0 m/s there is no difference in the two predictions for bubble diameters below 400 µm.

2.3.3 CONSIDERATION OF GRAVITATIONAL FORCES ON THE PARTICLE

Fig. 2.12 shows the parallelogram of forces acting on the particle in the absence of inertial forces. The drag force (F_{drag}) acts in opposition to F_{res},the resultant of the centripetal force, (F_{cent}) and the buoyant force, (F_{buoy}).

Using the cosine rule,

$$(F_{res})^2 = (F_{cent})^2 + (F_{buoy})^2 - 2 \cdot F_{cent} \cdot F_{buoy} \cdot \cos(90-\theta)$$

but $\cos(90-\theta) = \sin\theta$

therefore

$$(F_{res})^2 = (F_{cent})^2 + (F_{buoy})^2 - 2 \cdot F_{cent} \cdot F_{buoy} \cdot \sin\theta$$

also $F_{bouy} = V \cdot g \cdot \rho$

where V is the volume of the particle

and $F_{cent} = V \cdot v^2 \cdot \zeta \cdot \Delta\rho$

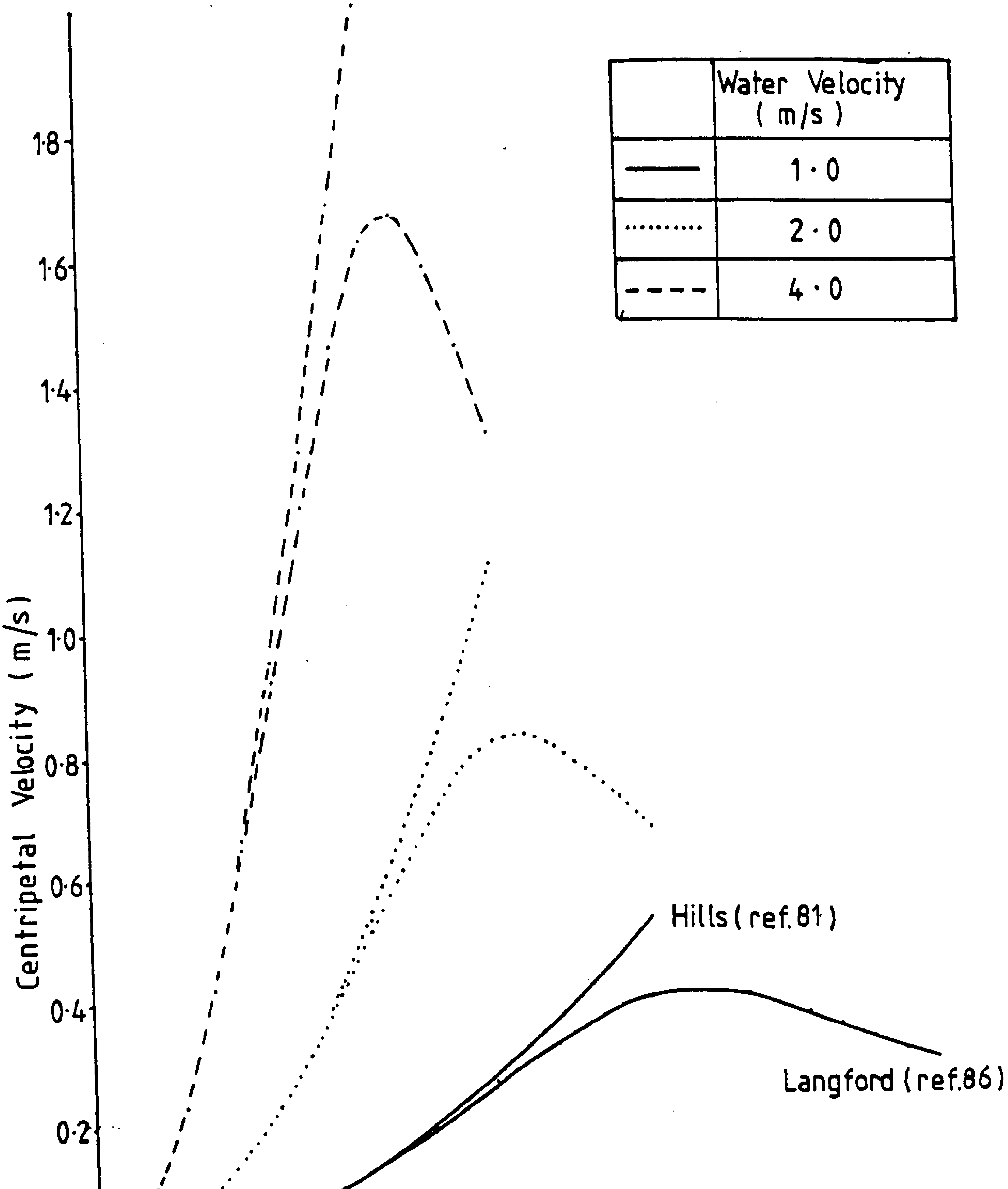

EFFECT OF HYDROGEN BUBBLE SIZE ON THE CENTRIPETAL VELOCITY IN WATER

FIG. 2.11

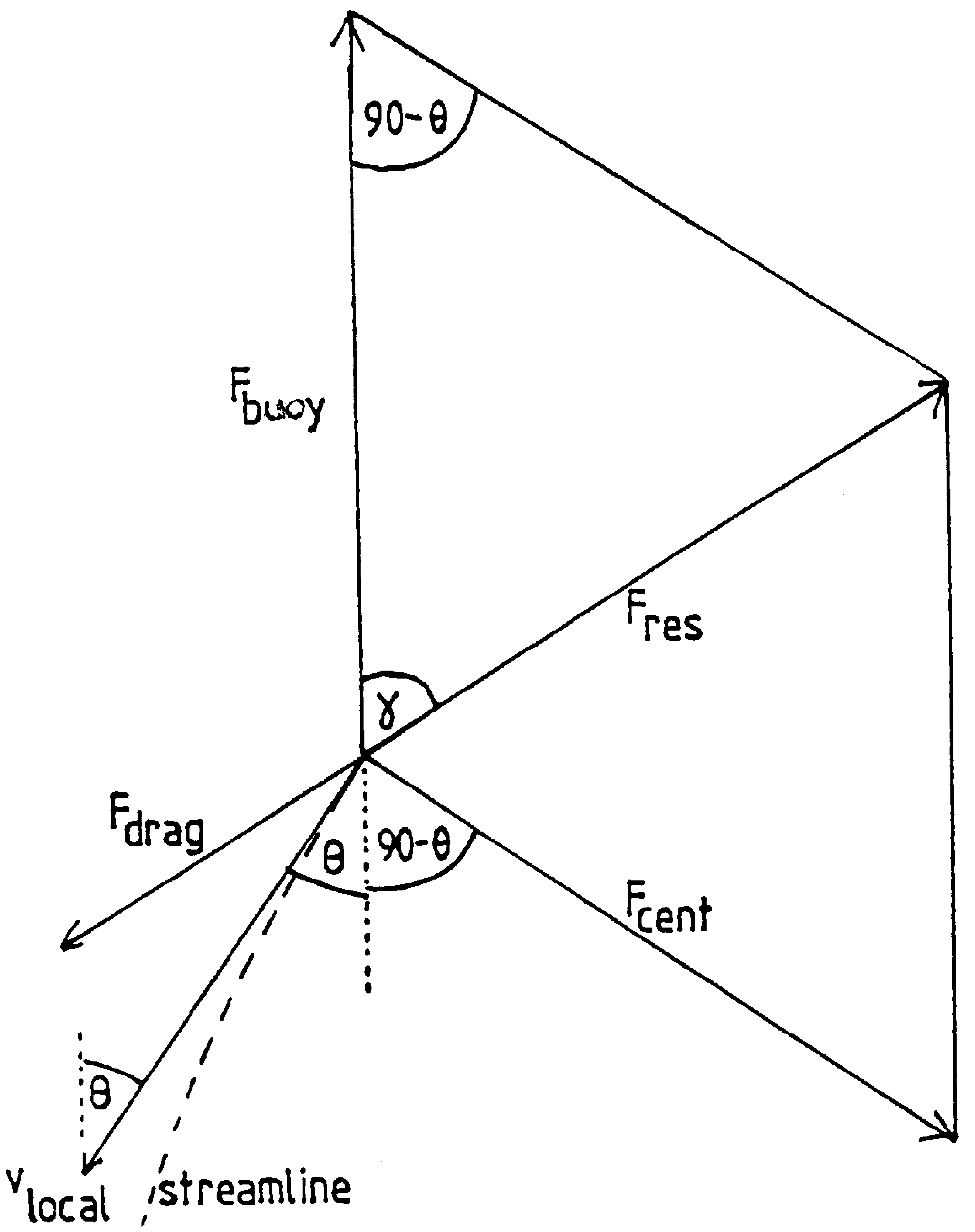

FORCES ACTING ON A PARTICLE IN THE FLUID FLOWING THROUGH THE NOZZLE

FIG. 2.12

where ζ = streamline curvature

in the absence of inertia the resultant force can be equated to the drag force on the particle.

therefore $F_{res} = F_{drag} = 3 \,.\, \pi \,.\, K \,.\, d \,.\, V_p$ (2.48)

where V_p is the velocity of the particle relative to the moving fluid.

therefore $V_p = F_{res} / (3 \,.\, \pi \,.\, K \,.\, d)$ (2.49)

To find the direction of the resultant force we can apply the sine rule on the force vectors.

$$\frac{F_{cent}}{\sin \gamma} = \frac{F_{res}}{\sin (90-\theta)} \quad (2.50)$$

but $\sin (90-\theta) = \cos \theta$

therefore $\sin \gamma = (F_{cent}/F_{res}) \,.\, \cos \theta$ (2.51)

2.3.4 TURBULENCE MODELS

Whilst work in this thesis has concentrated on two-dimensional potential flow, some work has been carried out on the solution to the Navier-Stoke's Equations involving turbulence. Two such models have been considered in work by Wilson et al, (ref.87). A model FFABS has been used to predict flow patterns through a nozzle. A model FLUENT is available commercially from CREARE Research and Development in the USA. This has the ability to model second phase particles.

The work by Wilson et al considered the conditions in a simple nozzle consisting of a straight conical section and a parallel section. This nozzle was used in the upright position, (fig. 2.13a), and inverted, (fig. 2.13b) positions.

a) upright

b) inverted

EXPERIMENTAL NOZZLE USED IN REF. 87

FIG. 2.13

As predicted by the FLUENT model, for a steel exit velocity of 2.0 m/s, turbulence is a maximum at the entrance to the parallel section of the upright nozzle and at the entrance of the inverted nozzle. By studying the random motion of different size inclusions from the nozzle axis the model predicted two regimes of inclusion movement.

1) For alumina inclusions <35 μm diameter radial movement was by turbulence only.

2) For inclusions >35 μm diameter, movement was a result of the centripetal forces with turbulence being less significant.

The degree of turbulence exhibited in the nozzle depends on the specific experimental conditions. Given good entry conditions to the nozzle as stated by Hinze, (ref.88) laminar flow at Reynolds Numbers up to 10^6, (ref.89) are possible. Any means of preventing or limiting the turbulence in the critical parts of the nozzle will assist the casting of aluminium-killed steels. Two other consequences of turbulence may also be important. First, pre-existing turbulence in the tundish will consist of a rotating or swirl component. As the steel travels through a convergent nozzle the swirl will be enhanced, leading to a rotation or vortex. The effect of this will be to move the inclusions towards the centre of the nozzle and away from the walls. Second, in turbulent eddies, inclusions will move towards the centre, when they may tend to agglomerate, and again be less likely to reach the nozzle surface. These effects make experimental model work difficult under fully turbulent conditions.

Therefore, means of establishing non-turbulent conditions are important.

2.3.5. RELATIONSHIP OF WATER MODEL TO REAL TUNDISH NOZZLE

2.3.5.1 SIMILARITY CRITERIA

For dynamic similarity of fluid flow path to be established between the real fluid and the model fluid equivalence of the Reynolds Number is necessary. In the circumstances of radial particle movement through a convergent nozzle, similarity of hydrogen in water with alumina in steel is satisfied if the ratio of centripetal force and drag force is the same in model and plant. Geometric similarity is assumed.

Therefore:-

$$\left(\frac{\text{centripetal force}}{\text{drag force}}\right)_p = \left(\frac{\text{centripetal force}}{\text{drag force}}\right)_m \qquad (2.52)$$

$$\left(\frac{V \; \Delta\rho \; v}{k \, \pi \, \mu \, d \; R \; u}\right)_{\text{plant}} = \left(\frac{V \; \Delta\rho \; v}{k \, \pi \, \mu \, d \; R \; u}\right)_{\text{model}} \qquad (2.53)$$

where μ = dynamic viscosity of fluid

V = volume of particle

$\Delta\rho$ = density difference (fluid - particle)

v = tangential velocity of fluid at radius of curvature R

u = radial velocity of particle

k = drag factor (2 for gas, 2.5 for liquid, 3 for solid).

As indicated before, for small gas bubbles that behave as solid particles, k = 3

d = diameter of particle

suffixes, p = plant, m = model

hence
$$\frac{d_p^3 \; \Delta\rho_p \; v_p^2}{6 \; k_p \mu_p \; d_p \; R_p \; u_p} = \frac{d_m^3 \; \Delta\rho_m \; v_m}{6 \; k_m \mu_m \; d_m \; R_m \; u_m} \qquad (2.54)$$

for geometric similarity $R_m = S\,R_p$ (where S = scale of model)

for similar particle movement $u_m = S\,u_p$

$$\frac{d_p^2 \; \Delta\rho_p \; v_p}{6 \; k_p \; \mu_p \; R_p \; u_p} = \frac{d_m^2 \; \Delta\rho_m \; v_m}{6 \; k_m \mu_m \; S \; R_p \; S \; u_p} \qquad (2.55)$$

$$\frac{d_p^2 \; \Delta\rho_p \; \mu_m \; k_m \; S^2}{d_m^2 \; \Delta\rho_m \; \mu_p \; k_p} = \left(\frac{v_m}{v_p}\right)^2 \qquad (2.56)$$

substituting the physical constants,

$\mu_p = 6 \times 10^{-3}$ kg m^{-1} s^{-1}

$\mu_m = 1.005 \times 10^{-3}$ kg m^{-1} s^{-1}

$\Delta\rho_p$ = 7200-3810 kg m^{-3}

$\Delta\rho_m$ = 998.2 - zero kg m^{-3}

k_m = 3

k_p = 3

$$\left(\frac{d_p}{d_m}\right)^2 \frac{3390}{998.2} \; \frac{3}{3} \; \frac{1.005 \times 10^{-3}}{6 \times 10^{-3}} \; S^2 = \left(\frac{v_m}{v_p}\right)^2 \qquad (2.57)$$

$$\left(\frac{d_p}{d_m}\right)^2 0.569 \; S^2 = \left(\frac{v_m}{v_p}\right)^2 \qquad (2.58)$$

$$\underline{\left(\frac{d_p}{d_m}\right) 0.754 \; S = \left(\frac{v_m}{v_p}\right)} \qquad (2.59)$$

Given a certain scale of the water model therefore, the movement of an alumina inclusion of specific size, at known fluid flow speeds can be modelled by adjusting the water flow velocity. This analysis ignores the effect of buoyancy, which in gravity flow through a convergent nozzle will act at a varying angle to the fluid flow direction and therefore to the direction of the centripetal force.

Fig. 2.14 shows the relationship between diameter ratios and the fluid velocity ratios at a scale of x2. As an example, if the steel exit velocity is 3.0 m/s and the water exit velocity is 2.0 m/s, a 50 µm diameter alumina inclusion would be modelled by a hydrogen bubble of 110 µm diameter.

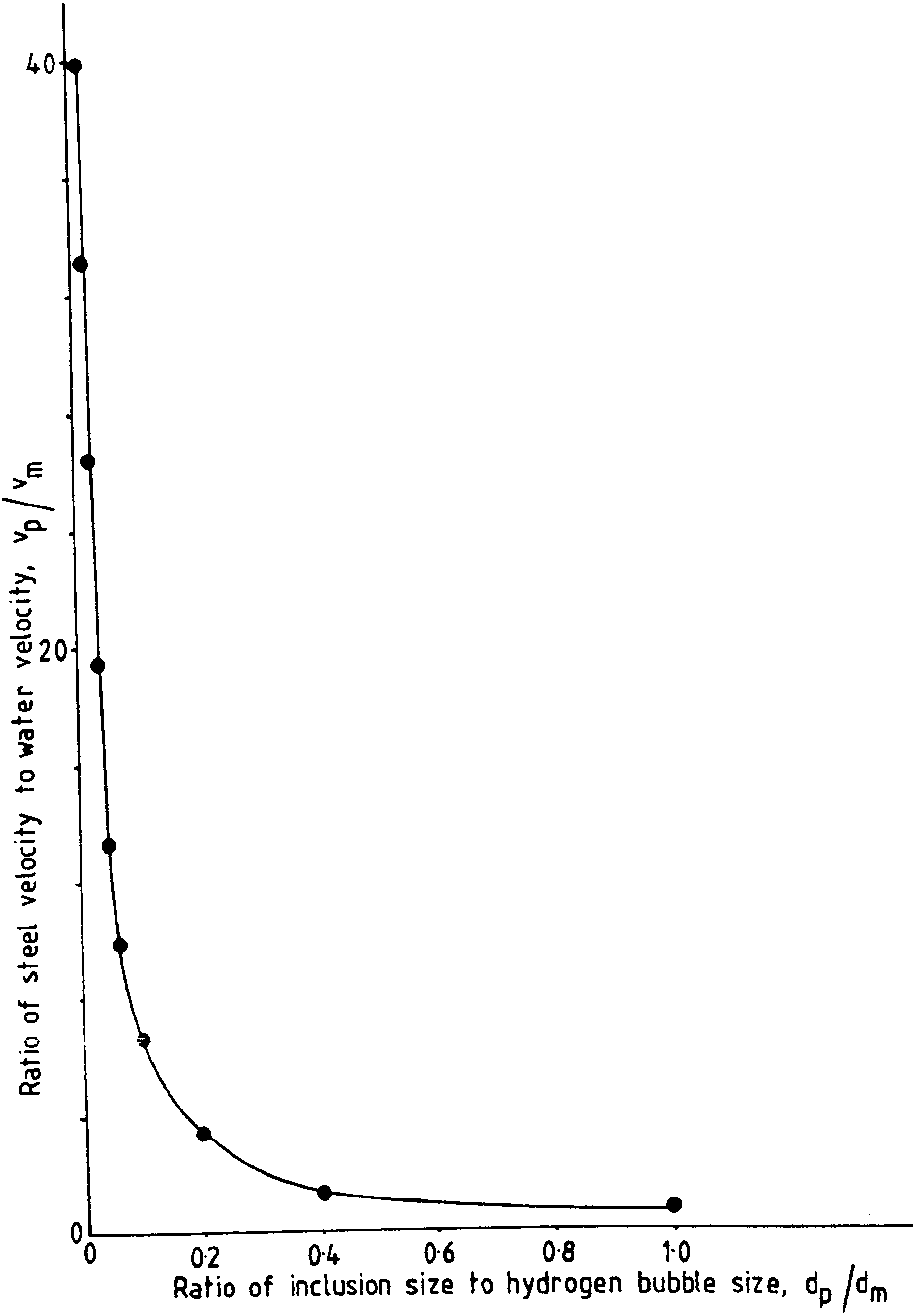

INFLUENCE OF ALUMINA : HYDROGEN
SIZE RATIO FOR MODELLING
CENTRIPETAL MOVEMENT AT A
SCALE OF x2

FIG. 2.14

2.3.5.2 TWO-DIMENSIONAL NATURE OF THE MODEL

The two-dimensional nature of a model nozzle will give a different pressure and velocity profile than that for three-dimensional convergence. A comparison of 2-d with 3-d flow can be made using the Steady Flow Energy Equation at the nozzle exit and at varying heights above the exit with a constant head of fluid. Varying diameter and width in the nozzle can both be expressed as 'w'.

The variation of mean velocity with height can be calculated as follows:-

1) Three-dimensions

Volumetric flow rate (V_{3-d}) = v_{exit} . area at exit

$$V_{3-d} = v_{exit} \cdot \pi (w_{exit}/2)^2$$

the same volumetric flow rate applies at each height 'h' because of the equation of continuity $m_1 v_1 = m_2 v_2$

Volumetric flow rate at 'h' = $V_h = v_h \cdot \pi (w/2)^2$

where v_h is the mean velocity at 'h'.

therefore $v_h \cdot (w/2)^2 = v_{exit} \cdot (w_{exit}/2)^2$

$$v_h = v_{exit} \quad \frac{w^2/_{exit}{}^4}{w^2/4}$$

$$v_h = v_{exit} \left(\frac{w_{exit}}{w_h}\right)^2 \qquad (2.65)$$

2) Two-dimensions

Volumetric flow rate $V_{2d} = v_{exit} \cdot$ area of exit

$$V_{2d} = v_{exit} \cdot w_{exit} \cdot z \qquad (2.66)$$

where 'z' is the internal thickness of the model

for equality of flow rates at height 'h'

$$V_h = v_{exit} \cdot w_h \cdot z \qquad (2.67)$$

therefore $v_h \cdot w_h \cdot z = v_{exit} \cdot w_{exit} \cdot z$ (2.68)

$$v_h = v_{exit} \frac{w_{exit} \cdot z}{w_h \cdot z} \qquad (2.69)$$

$$\underline{\underline{v_h = v_{exit} \frac{w_{exit}}{w_h}}} \qquad (2.70)$$

For a constant hydrostatic head v_{exit} is the same in two dimensions as in three dimensions. There will also be a difference in the pressure variation with height as follows, from applying the Steady Flow Energy Equation between the nozzle exit and height 'h'.

$$\rho \frac{v_h^2}{2} + P_h + \rho g h = \rho \frac{v_{exit}^2}{2} + P_{exit} + \rho g h_{exit} \quad (2.71)$$

divide throughout by ρ

$$\frac{v_h^2}{2} + \frac{P_h}{\rho} + g h = \frac{v_{exit}^2}{2} + \frac{P_{exit}}{\rho} + g h_{exit} \quad (2.72)$$

$$\frac{P_h - P_{exit}}{\rho} = \frac{v_{exit}^2}{2} - \frac{v_h^2}{2} - g(h - h_{exit}) \quad (2.73)$$

v_h can be replaced by the relevant expression derived above.

1) Three dimensions

$$\frac{P_h - P_{exit}}{\rho} = \frac{v_{exit}^2}{2} - \left[\frac{v_{exit}^2}{2} \left(\frac{d}{x}\right)^4\right] - g(h - h_{exit}) \quad (2.74)$$

2) Two dimensions

$$\frac{P_h - P_{exit}}{\rho} = \frac{v_{exit}}{2} - \left[\frac{v_{exit}}{2} \left(\frac{d}{x}\right)^2\right] - g(h - h_{exit}) \quad (2.75)$$

Velocity profiles for 2-d and 3-d flow are shown for steel flow through a Stocksbridge nozzle, (fig. 2.15), experimental nozzle 1, (fig. 2.16), and experimental nozzle 2, (fig. 2.17). The channel velocity is always higher in 2-d than 3-d flows at geometrically equivalent positions.

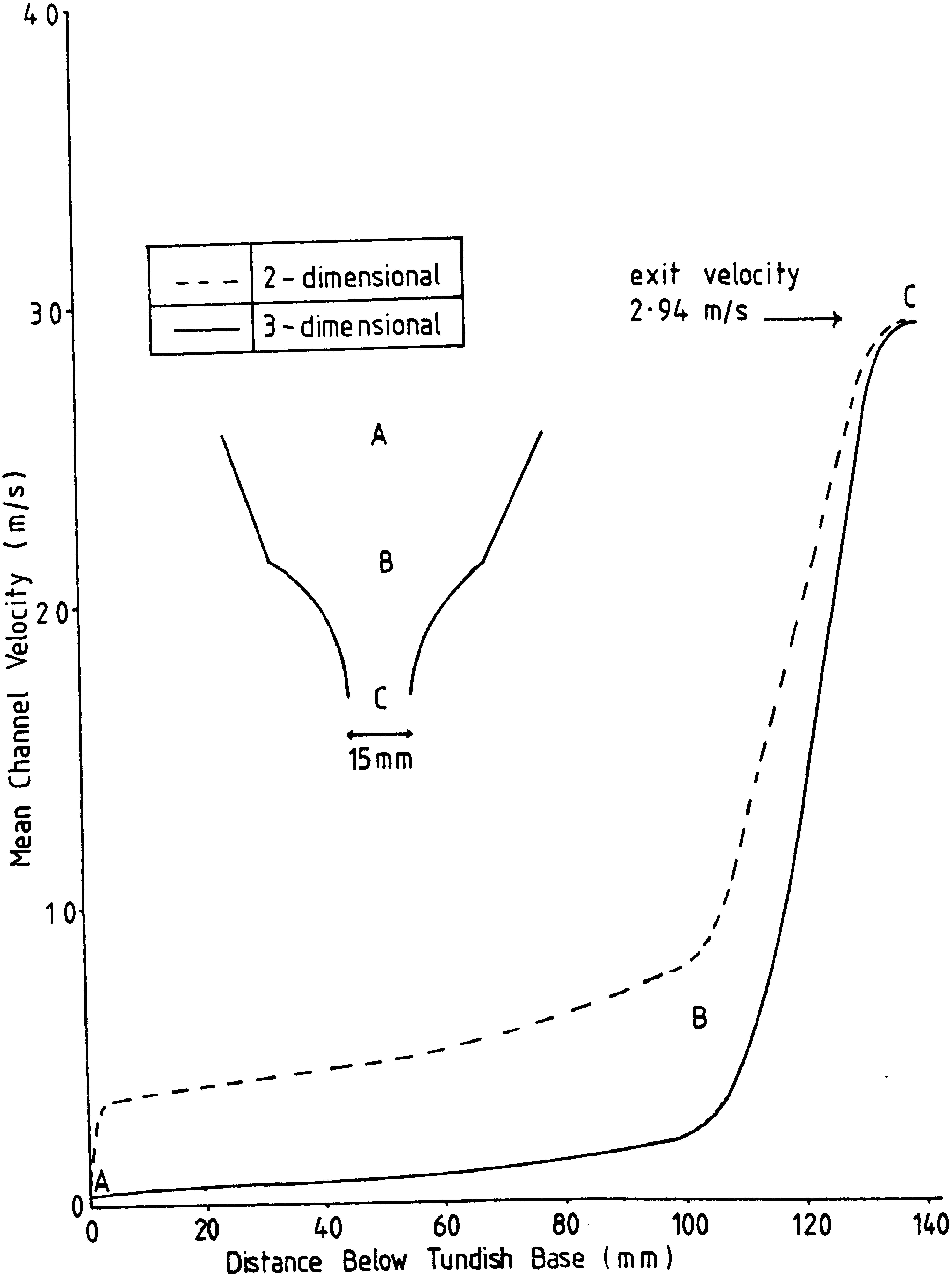

VELOCITY PROFILES IN THE EXPERIMENTAL STOCKSBRIDGE NOZZLE USED IN THE PROTOTYPE MODEL

FIG. 2.15

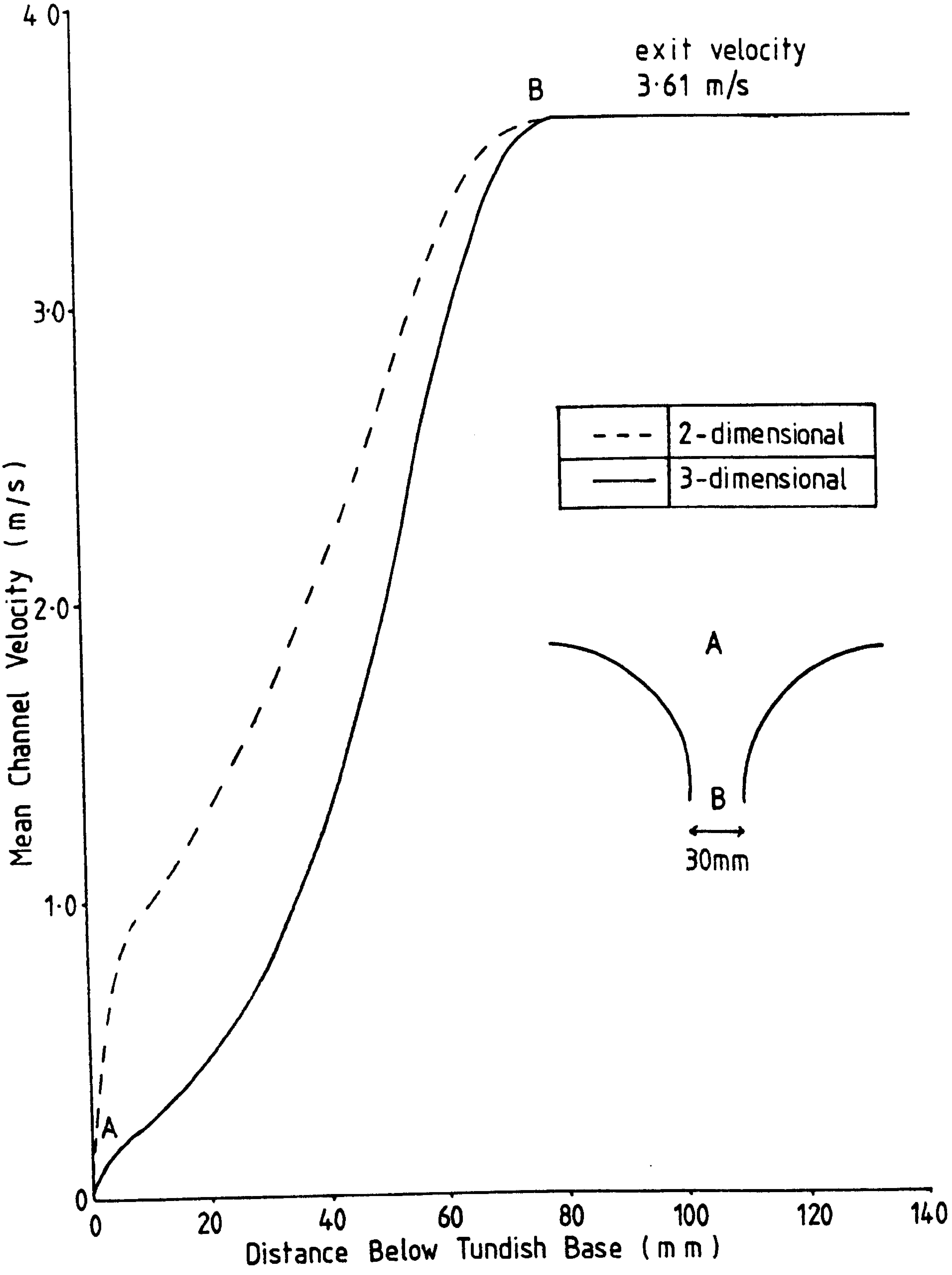

VELOCITY PROFILES IN
EXPERIMENTAL NOZZLE 1

FIG. 2.16

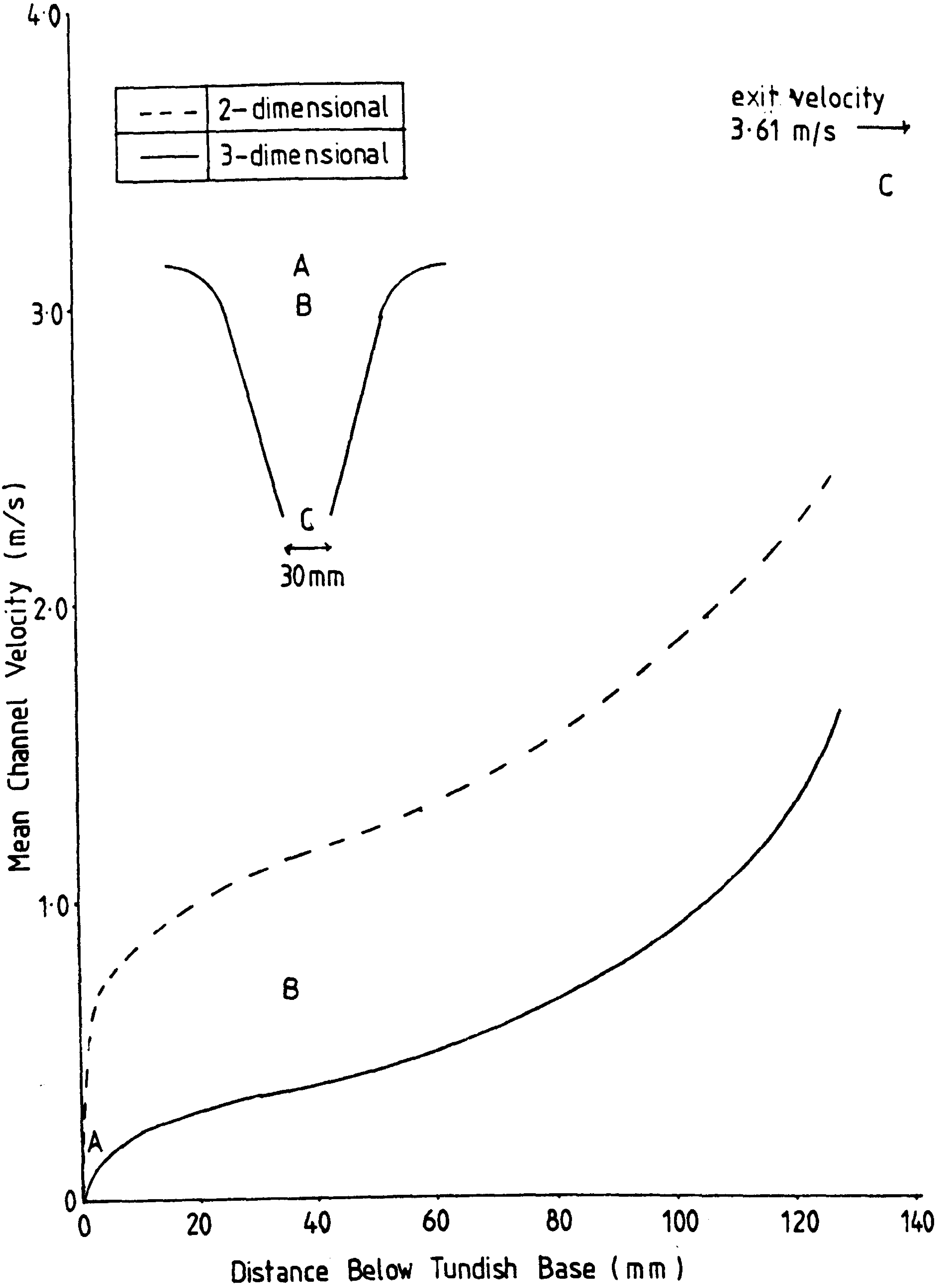

VELOCITY PROFILES IN
EXPERIMENTAL NOZZLE 2

FIG. 2.17

3. EXPERIMENTAL APPARATUS

3.1. DESIGN AND DEVELOPMENT OF THE MODEL

The experimental model to be used for observing hydrogen bubbles flowing through a nozzle was to be a two-dimensional slice model. Initially, however, it was uncertain what design would be most suitable. The final design was achieved by means of work on a prototype slice model.

Before describing the model development it is important to specify two experimental variables, the water exit velocity and the Reynolds Number at exit.

The exit velocity from the nozzle was calculated from the Steady Flow Energy Equation,

$$v_{exit} = \sqrt{2\ g\ h} \qquad (3.1)$$

where g = acceleration due to gravity

and h = the total head of water from the water level in the tundish to the exit at the flow constrictor.

All calculations of the flow Reynolds Number (R_e) use the hydraulic diameter such that;

$$Re = \frac{D_h\ v}{\nu} \qquad (3.2)$$

where v = mean flow velocity

ν = kinematic viscosity

D_h = hydraulic diameter, $2\ a\ b\ /\ (\ a + b\ )$

where a and b are the sides of the rectangular section.

3.1.1. THE PROTOTYPE MODEL

A model designed for some initial feasibilty studies was built in two dimensions to model the actual nozzle used at Stocksbridge Works. This model was extensively modified to gain the maximum possible information about the design requirements of the final model.

The model of internal thickness 15 mm is shown diagramatically in fig. 3.1a and as modified for electrolysis in fig. 3.1b

The various parts of the model are described below:-

3.1.1.1. TUNDISH

A tundish section maintained the head of water and controlled the flow of water to the nozzle. Two pairs of grooves on each side of the tundish allowed the introduction of dams to direct the flow of water. Wire gauze could also be added from the top of the dam to the water surface to limit the surface turbulence. Flow streamliners were inserted to prevent the formation of separated regions of flow in the nozzle section.

The nozzle section was a fixed part of the tundish section. The exit width of the nozzle was 16 mm, (a standard size used at Stocksbridge Works).

3.1.1.2. FEEDER BOX

A feeder box above the tundish distributed the water from three mains taps, through two outlet ports, into the tundish. Water from the mains was introduced from three inlets at the top of the box. However, this was modified because of the high air entrainment so that water could be

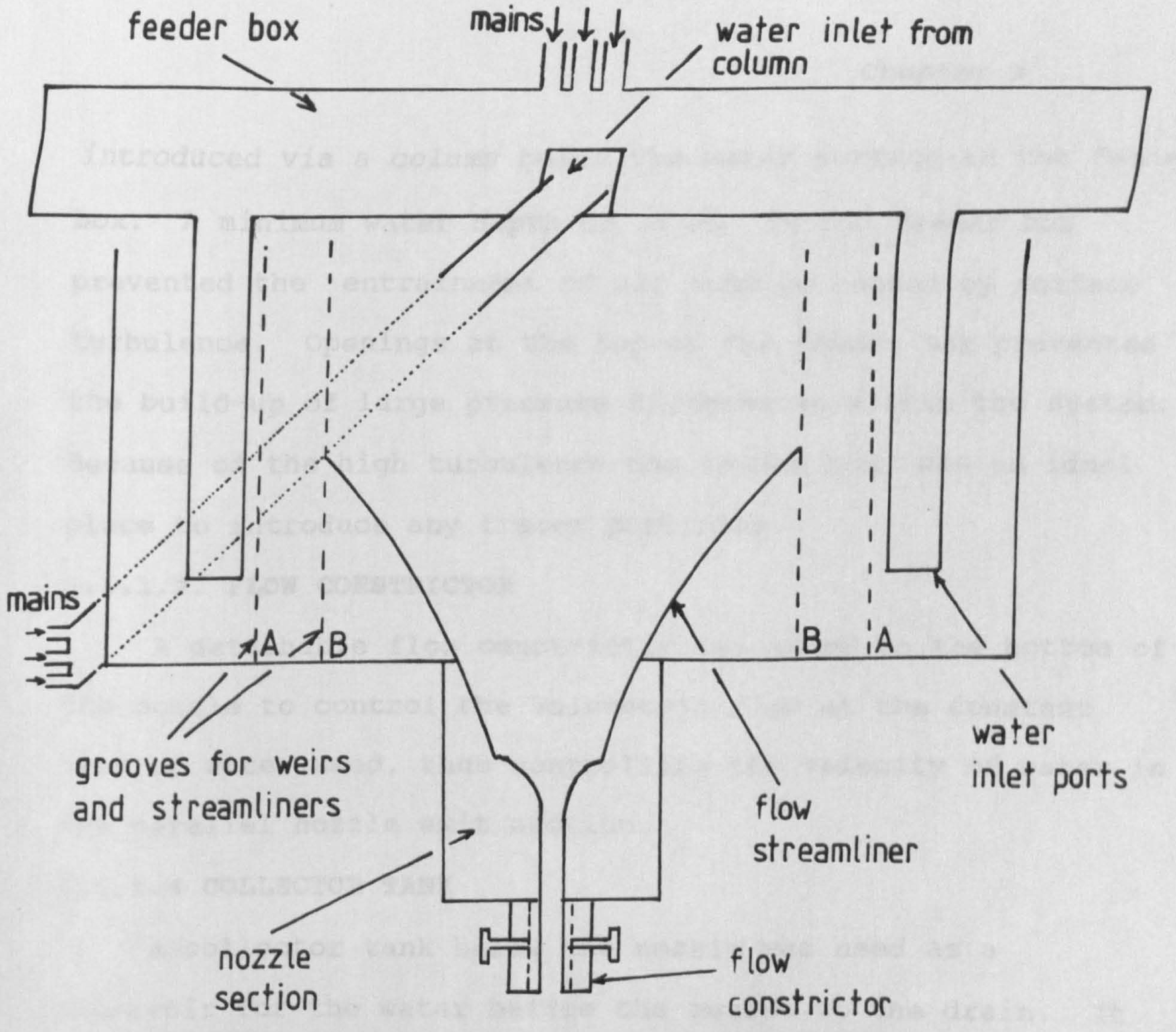

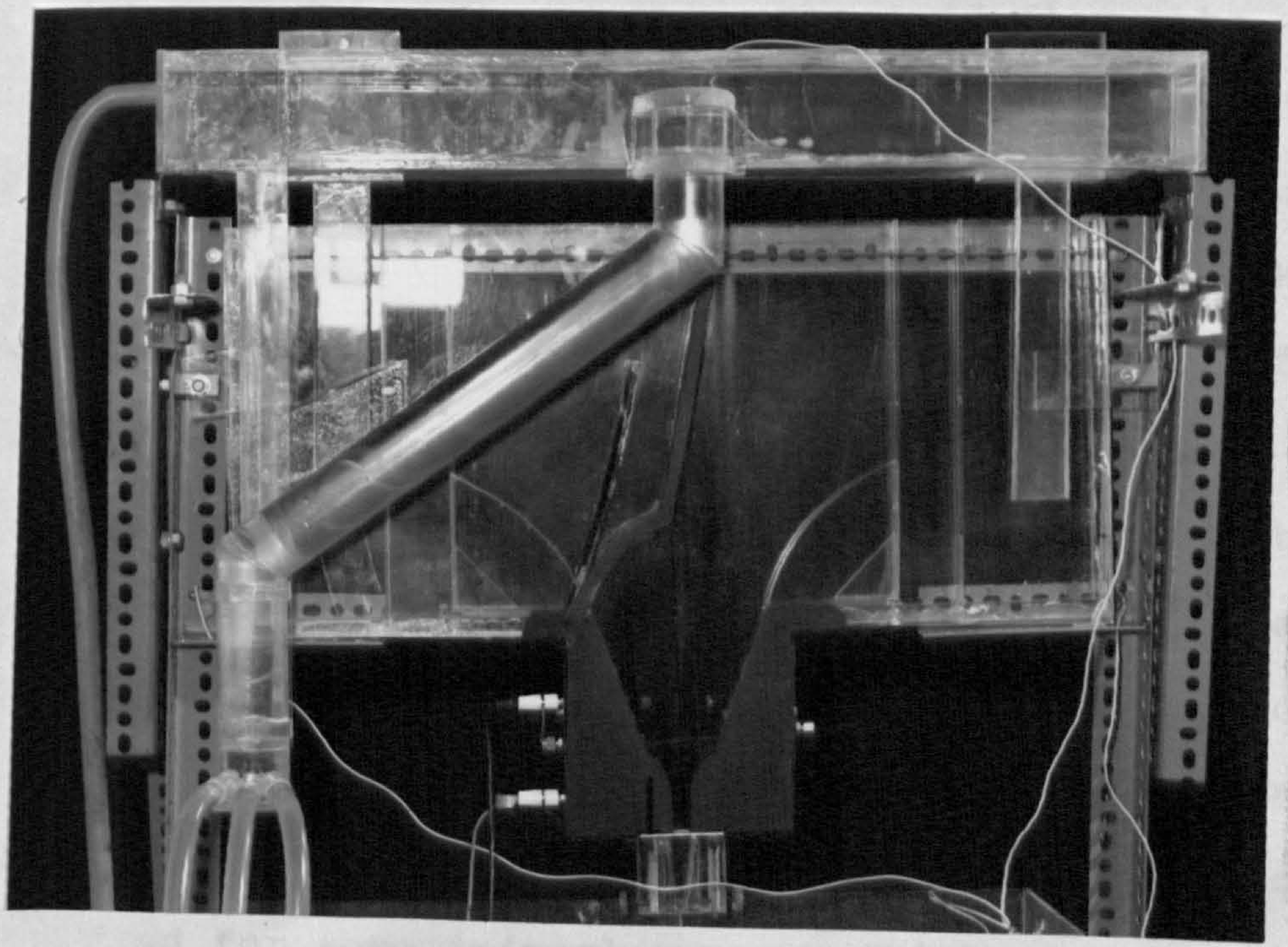

THE INITIAL MODEL

FIG. 3.1.

introduced via a column below the water surface in the feeder box. A minimum water depth of 25 mm in the feeder box prevented the entrainment of air bubbles caused by surface turbulence. Openings at the top of the feeder box prevented the build-up of large pressure differences within the system. Because of the high turbulence the feeder box was an ideal place to introduce any tracer particles.

3.1.1.3. FLOW CONSTRICTOR

A detachable flow constrictor was added to the bottom of the nozzle to control the volumetric flow at the constant head of water used, thus controlling the velocity of water in the parallel nozzle exit section.

3.1.1.4 COLLECTOR TANK

A collector tank below the nozzle was used as a reservoir for the water before the outlet to the drain. It was also used to measure the volumetric flow rate. Two marks on the tank, both above the normal water level, indicated a difference of 2 litres. By closing a gate at the outlet side of the tank the time for water to pass the two marks could be measured. The gate was opened again immediately after the measurement.

The maximum total head of water achievable with this model was 388 mm. This allowed a maximum mean water exit velocity of 2.76 m/s, and a maximum Re of 4.25×10^4.

To gain information about the electrical generation of hydrogen bubbles in flowing water, the prototype model was modified for some initial experiments.

Holes were drilled in the straight convergent nozzle section, to allow connection of a stainless wire cathode. In order to introduce a kinked wire, the hole in the nozzle needed to be 3 mm diameter. Although attempts were made to seal off this hole smoothly, the inside surface was prone to turbulence.

3.1.1.5. TUNDISH FLOW PATTERNS

Knowledge of the flow patterns in the tundish was essential to the model work, particularly as they influenced flow through the nozzle. Reynold's Numbers up to 42000 were expected in the prototype.

Polystyrene beads are often used as tracer particles in large water models for flow studies (ref.90). These, however, have a density slightly higher than that of water. Silica glass spheres have been reported (ref.91) at sizes below 100 μm, but these were not readily available. To meet the requirements of iso-density a mixture of two liquids was considered to be the most satisfactory, one liquid with a density higher than water and one with a density lower. Two such liquids are xylene (density = 860 kg/m^3) and di-butyl phthalate (density = 1045 kg/m^3), used by Macagno (ref.51). They are completely miscible with each other and the mixture is immiscible in water. White oil based paint can be added for easier visualisation.

If the density of water is assumed to be 1000 kg/m^3 ,the proportion of xylene (A) and di-butyl phthalate (B) to give the same density can be calculated as follows:-

density of A = ρ_a

density of B $= \rho_b$

1000 kg of A + B occupies 1 m^3

1000 kg of A + B occupies V_a m^3 of A + V_b m^3 of B

V_a m^3 of A weighs $\rho_a V_a$ kg

V_b m^3 of B weighs $\rho_b V_b$ kg

$V_a + V_b = 1$

$$\rho_a V_a + \rho_b V_b = 1000 \qquad (3.3)$$

$$\rho_a + V_b(\rho_b - \rho_a) = 1000 \qquad (3.4)$$

$$V_b = \frac{1000 - \rho_a}{\rho_b - \rho_a} \qquad (3.5)$$

and $V_a = 1 - V_b$

Substituting the values of density

$\underline{V_b = 0.757}$ and $\underline{V_a = 0.243}$

Therefore an iso-density mixture contains 75.6% by volume of di-butyl phthalate and 24.3% by volume of xylene.

A mixture of the above composition was prepared and droplets tested in water sank slowly. As a result the composition was adjusted to 69% di-butyl phthalate. Tests with the new composition in fully run tap water showed the particles to be stationary in the water after 2 minutes. After one hour there was no obvious change. Left to stand overnight, however, some particles rose to the surface and some particles sank. Approximately 10% of the particles remained in suspension. This suggests incomplete mixing or a gradual separation of the two liquids. Also there may have been some effect of the paint.

For addition to the water model the xylene/di-butyl phthalate was mixed with about the same volume of water and shaken in a sqeeze bottle. The turbulence in the feeder box ensured break-up into small droplets.

Two features of the model were considered to be crucial. First, conditions in the tundish entry ports meant that dams were necessary to prevent flow along the tundish base. Second, the sharp change in section at the nozzle entry made it imperative to insert streamliners. There was insufficient water flowing through the slice model to allow the water level to be controlled by the dam height, in contrast to a three dimensional model. The most satisfactory dams were 50mm in height in the position furthest away from the nozzle. Dams taller than 100mm left too little distance between their top and the surface, making air entrainment at the water surface more likely.

Whether or not dams were used, there tended to be a separated region of flow in the nozzle section. This is shown in fig. 3.2a where no dams were used. When dams were used this separated region did not extend so far down the nozzle. Because flow at the surface was to be investigated it was important to remove this separated region.

Streamliners were inserted into each of the grooves nearer the nozzle section, those with heights 50 mm, 100 mm,

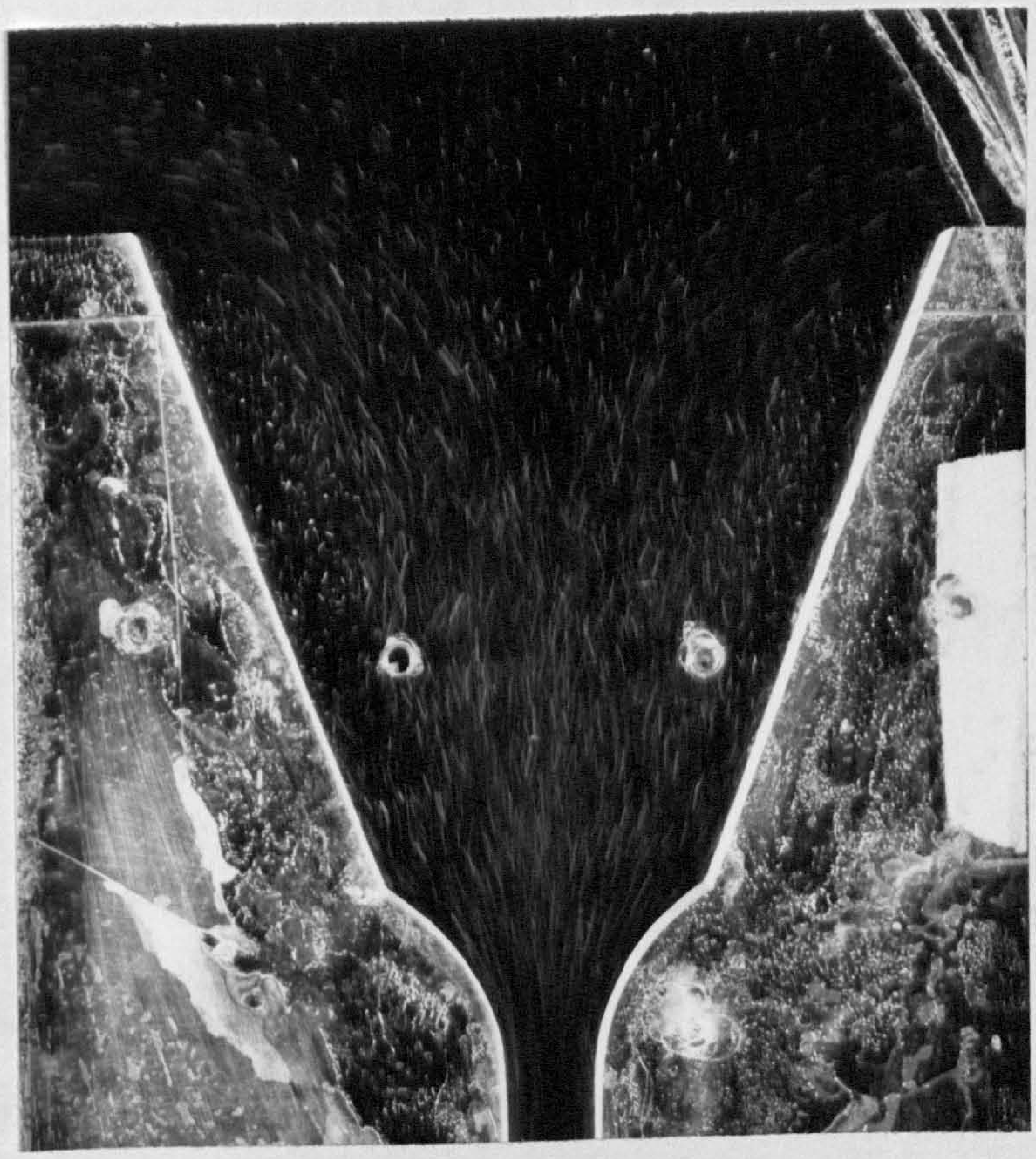

a) no streamliner

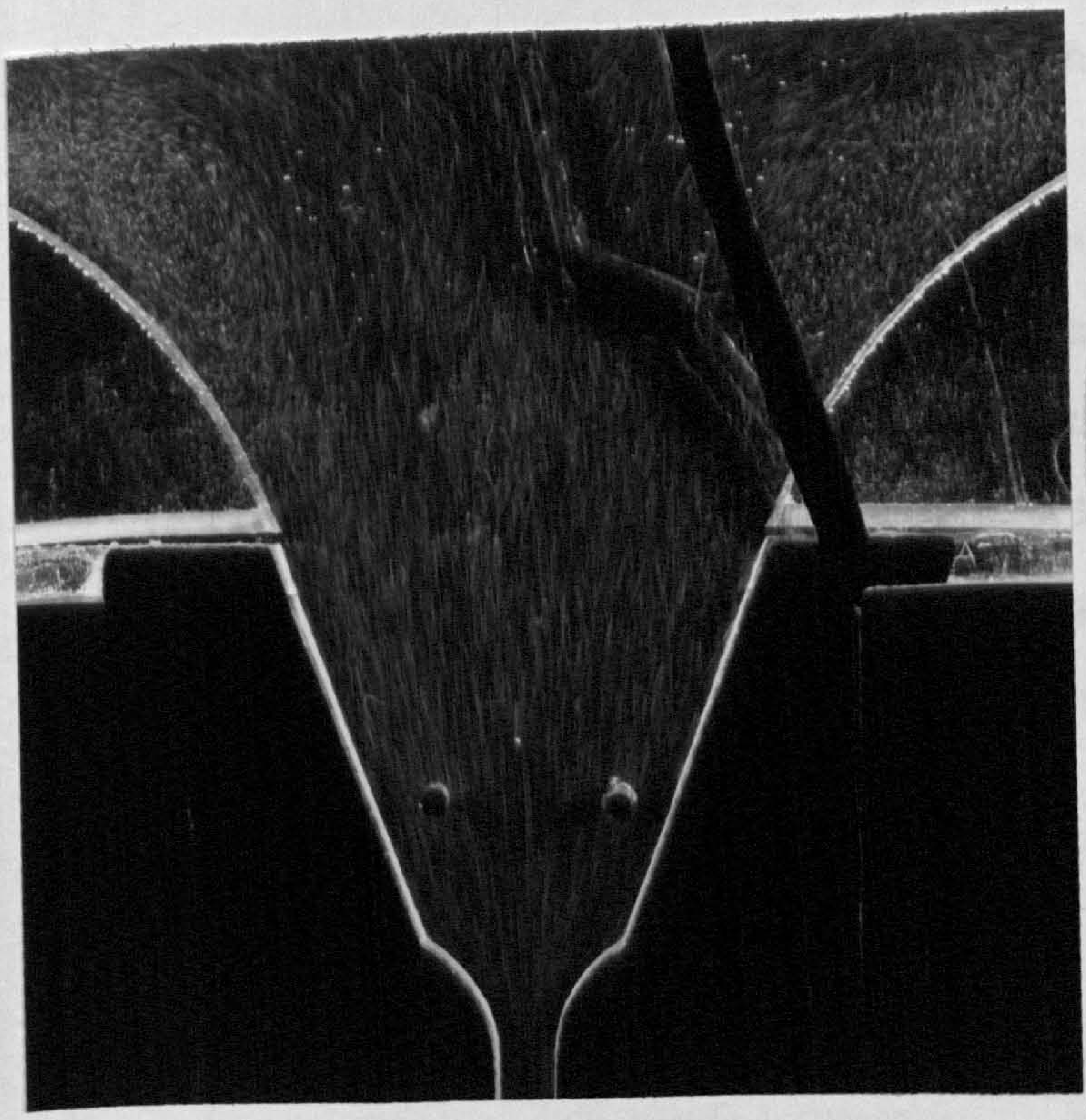

b) with 100 mm tall streamliner

EFFECT OF STREAMLINERS ON THE SEPARATED REGION FORMED IN THE PROTOTYPE MODEL

FIG. 3.2.

and 150 mm being tried. The most effective at removing the separated region away from the nozzle was a 100 mm tall streamliner combined with a 50 mm tall dam near the entry port, (fig. 3.2b). A wire gauze in the groove above the streamliner reduced the surface turbulence.

3.1.2. THE FINAL MODEL

A diagram of the final model is shown in fig. 3.3 drawn to the scale of x 1/10 and photographs in fig. 3.4 a and b. It was built on the same principle as the prototype model but was designed as a recirculating system. The details of the various parts of the model are described below.

3.1.2.1. THE TUNDISH

The tundish was made with 15 mm thick perspex. The internal model thickness was 21.15 mm. Internal grooves were machined as in the prototype model to allow the possible insertion of dams or streamliners. A high volume reservoir and overflow section was added to the top, first to enable a constant head of water to be maintained, and secondly to prevent the danger of water overflowing on to the electrical apparatus. A gap in the base allowed an interchangeable nozzle to be inserted. Two 50 mm x 28 mm beams each 218 mm long were firmly attached to bottom of the tundish for the watertight attachment of the nozzle.

The nominal total head of water obtained was 665 mm. This was the maximum that could be maintained given the height of the room, the need to be able to remove the distibuter tank and entry ports, and still have enough height to collect water below the nozzle.

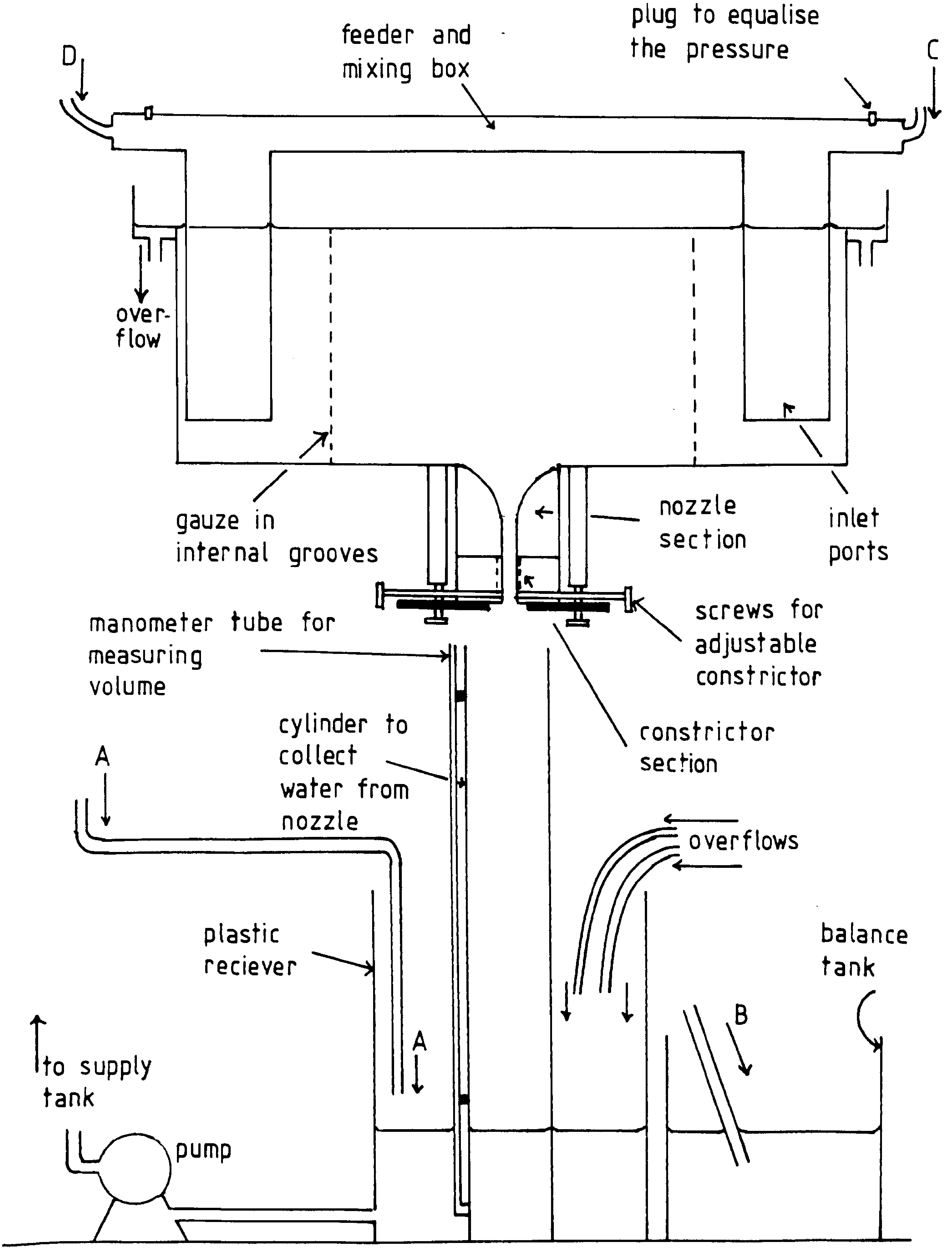

THE FINAL MODEL (scale = 1/10)

FIG. 3. 3.

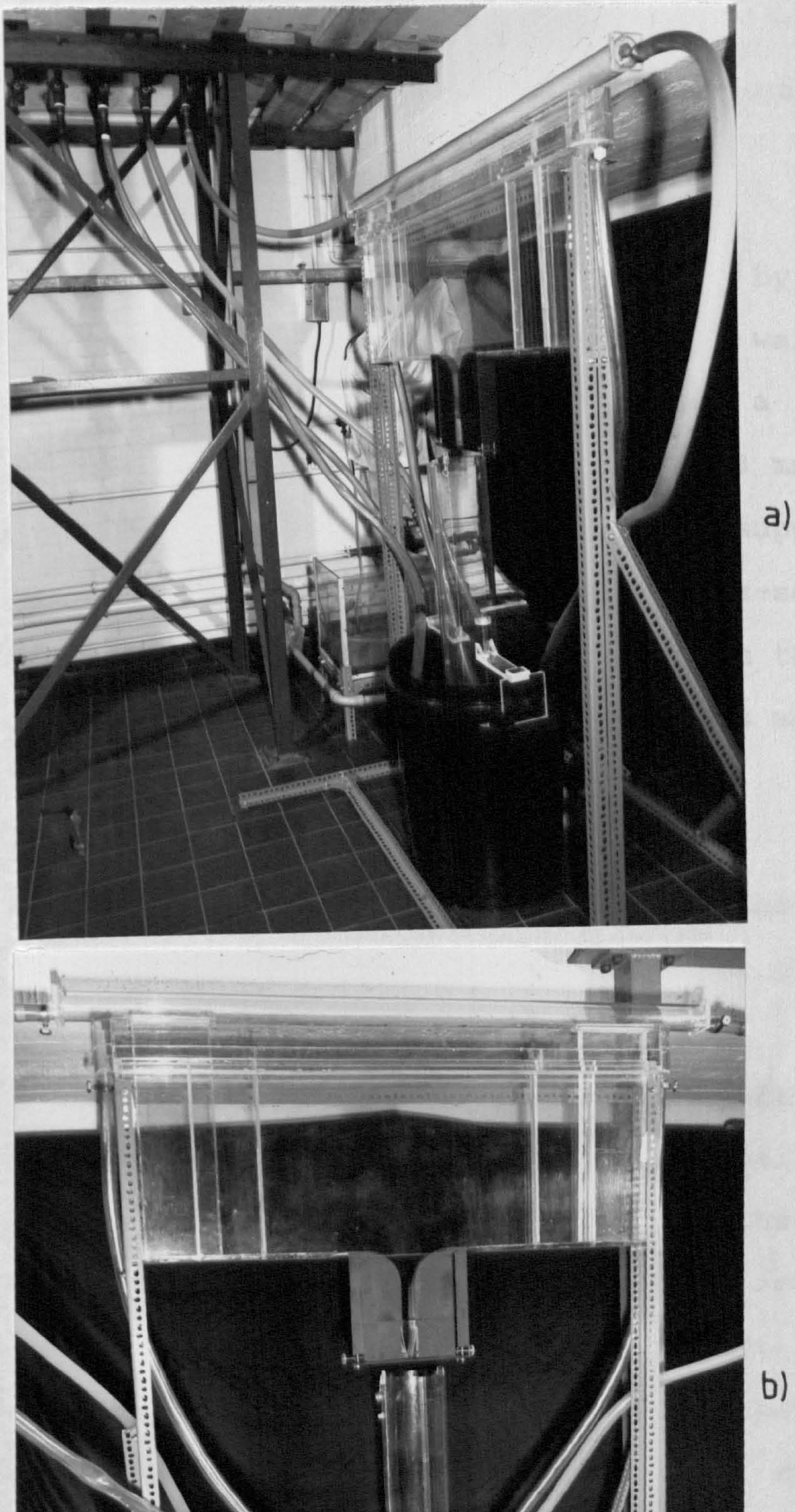

THE FINAL MODEL

FIG. 3.4.

3.1.2.2. THE DISTRIBUTOR TANK

Water from the supply tank was piped by flexible tubing of 27 mm internal diameter and 3.5 mm wall thickness to each end of a distributor tank. This was a cylindrical perspex tube of 53 mm internal diameter and 3 mm wall thickness. Two rectangular exit ports then supplied water to each side of the tundish. The internal cross-section of the ports was 156 mm x 12 mm. Two bleed plugs on the top of the tube helped to prevent any pressure build-ups when filling or emptying the model.

3.1.2.3. THE NOZZLE

The nozzle block was designed to be completely interchangeable and to allow fixing of the wire electrodes before insertion into the tundish.

The model of the Stocksbridge tundish nozzle used in the prototype was difficult to analyse mathematically because of the reverse in curvature of the surface and the point of singularity in the convergent section. As a result, two simpler experimental nozzle designs were used. The first, (nozzle 1), had an exit width of 30 mm. The convergent surface was a quarter circle of radius 80 mm, such that the tundish base formed a continuing tangent at the top, and an 80 mm long parellel exit section was tangential below, as seen in the full size diagram,(fig. 3.5). The total length of the nozzle from the tundish base to the exit was 160 mm.

A second nozzle, (nozzle 2), was designed on the same principle and is also shown at full size in fig. 3.5. The

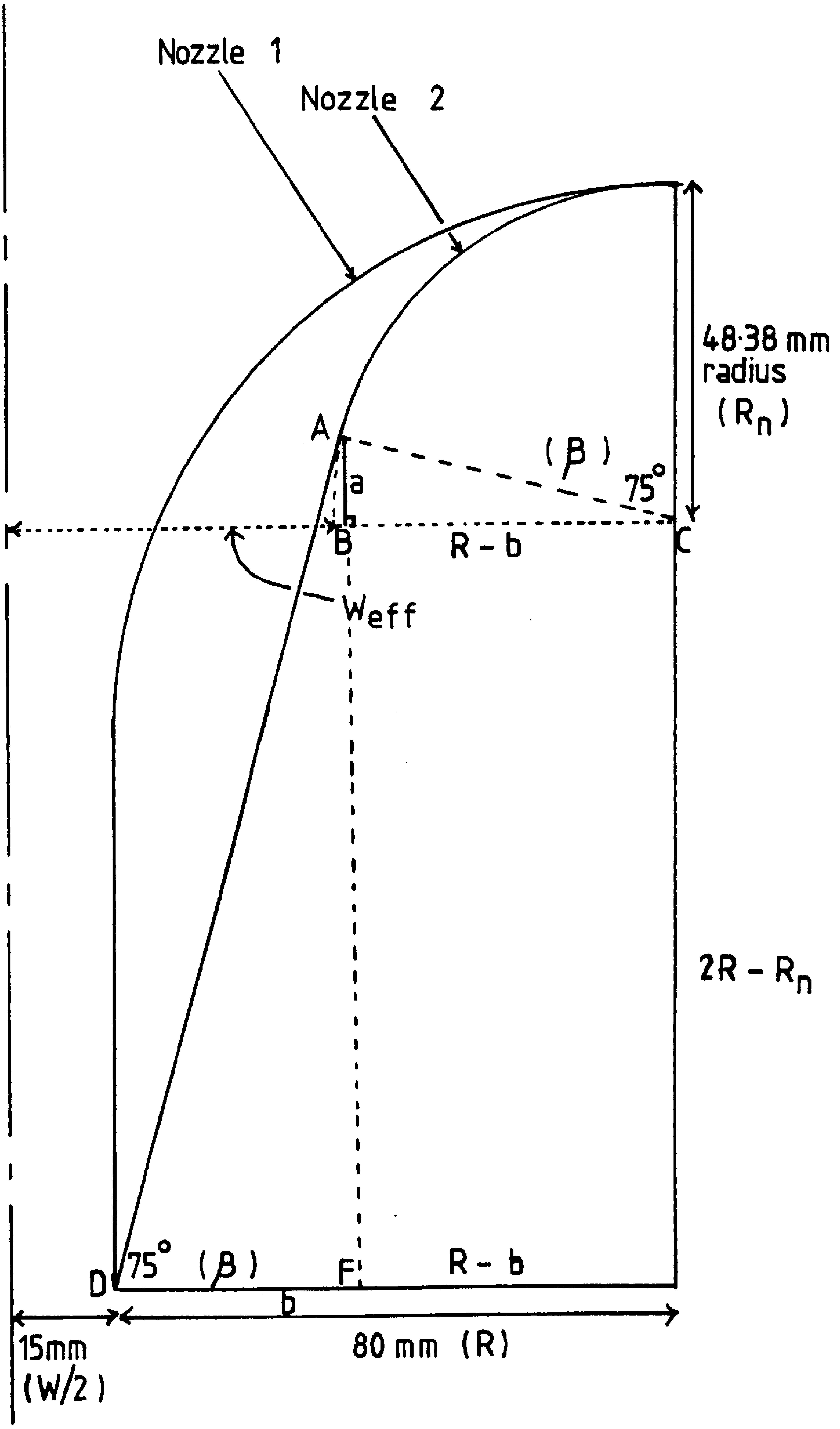

THE EXPERIMENTAL NOZZLE DESIGNS
USED IN THE FINAL MODEL

FIG. 3.5.

curved surface was to be an arc of less than $\pi/2$, the remaining surface to the exit being linear. This was to take advantage of linear streamlines in the lower part of the nozzle when no centripetal force would be exerted. The total length of this nozzle was kept at 160 mm so that the total head of water remained the same, and to use the same fittings. The radius of nozzle 2, (Rn) is equivalent to but smaller than the radius of nozzle 1, (R). The geometric equivalent of the nozzle width (W) is, however, the width obtained when the surface arc is $\pi/2$. It was designated as the effective nozzle width (W_{eff}).

$$\text{Here,} \quad R + W/2 = Rn + W_{eff}/2 \qquad (3.6)$$

Referring to fig. 3.5,

To Find the Nozzle Radius (Rn)

from ABC

$$\sin\beta = (R - b)/Rn \qquad (3.7)$$

$$\text{therefore} \quad b = R - Rn\sin\beta \qquad (3.8)$$

$$\text{and} \quad \cos\beta = a/Rn \qquad (3.9)$$

$$\text{therefore} \quad a = Rn\cos\beta \qquad (3.10)$$

from ADF

$$\tan\beta = \frac{a + (R + W/2) - Rn}{b} \qquad (3.11)$$

therefore substituting for a and b,

$$\tan\beta = \frac{Rn\cos\beta + (R + W/2) - Rn}{R - Rn\sin\beta} \tag{3.12}$$

$$R\tan\beta - Rn\tan\beta\sin\beta = Rn\cos\beta + (R + W/2) - Rn \tag{3.13}$$

$$Rn + Rn\tan\beta\sin\beta - Rn\cos\beta = (R + W/2) - R\tan\beta \tag{3.14}$$

$$Rn\,(1 + \tan\beta\sin\beta - \cos\beta) = R - R\tan\beta + W/2 \tag{3.15}$$

$$Rn = \frac{R\,(1 - \tan\beta) + W/2}{1 + \tan\beta\sin\beta - \cos\beta} \tag{3.16}$$

If R = 80 mm and W = 30 mm

then

$$Rn = \frac{80\,(2 - \tan\beta)}{1 + \tan\beta\sin\beta - \cos\beta}\ \text{mm} \tag{3.17}$$

With the given experimental constants $\beta = \pi/2$ when Rn = 80mm (the initial nozzle).

B_{min} occurs when $80(2 - \tan\beta) = 0$

or $\tan\beta = 2.0$

therefore $\beta_{min} = 63.43^{o}$ (1.107 radians)

To find the effective Nozzle Width:-

As shown previously $R + W/2 = Rn + W_{eff}/2$ (3.18)

therefore $W_{eff} = 2\,(R + W/2 - Rn)$ (3.19)

for R = 80mm and W = 30mm

$W_{eff} = 2\,(95 - Rn)$ mm (3.20)

The exit angle chosen for this second nozzle was 75^o. At this, the limiting potential line for curved flow occurs at $= (90-75)^o = 15^o$ (0.2618 radians). The nozzle constants are the follows:-

1) for the water model (X2)

R = 80 mm, Rn = 48.38 mm

W = 30 mm, Weff = 93.24 mm

2) for 2 dimensional steel flow (X1)

R = 40 mm, Rn = 24.19 mm

W = 15 mm, Weff = 46.62 mm

The nozzles were made of 10 mm glass to prevent scratching. Nozzle 1 is shown in fig.3.6. The walls were made of perspex (the same thickness as that used in the tundish to obtain 21.15 mm internal thickness). The polished top glass surface was fitted with a rubber seal for a good connection to the tundish. The nozzle walls projected above the glass surface to allow the nozzle to be inserted accurately and to make the nozzle surface level with the internal base of the tundish. Very accurate measuring, cutting, and polishing were necessary to achieve leak free contacts.

The exit width of the nozzle was 30 mm compared to the 15 mm diameter for the actual Stocksbridge nozzle.

In order to control the water flow rate through the nozzle at a constant tundish head, a separate, adjustable

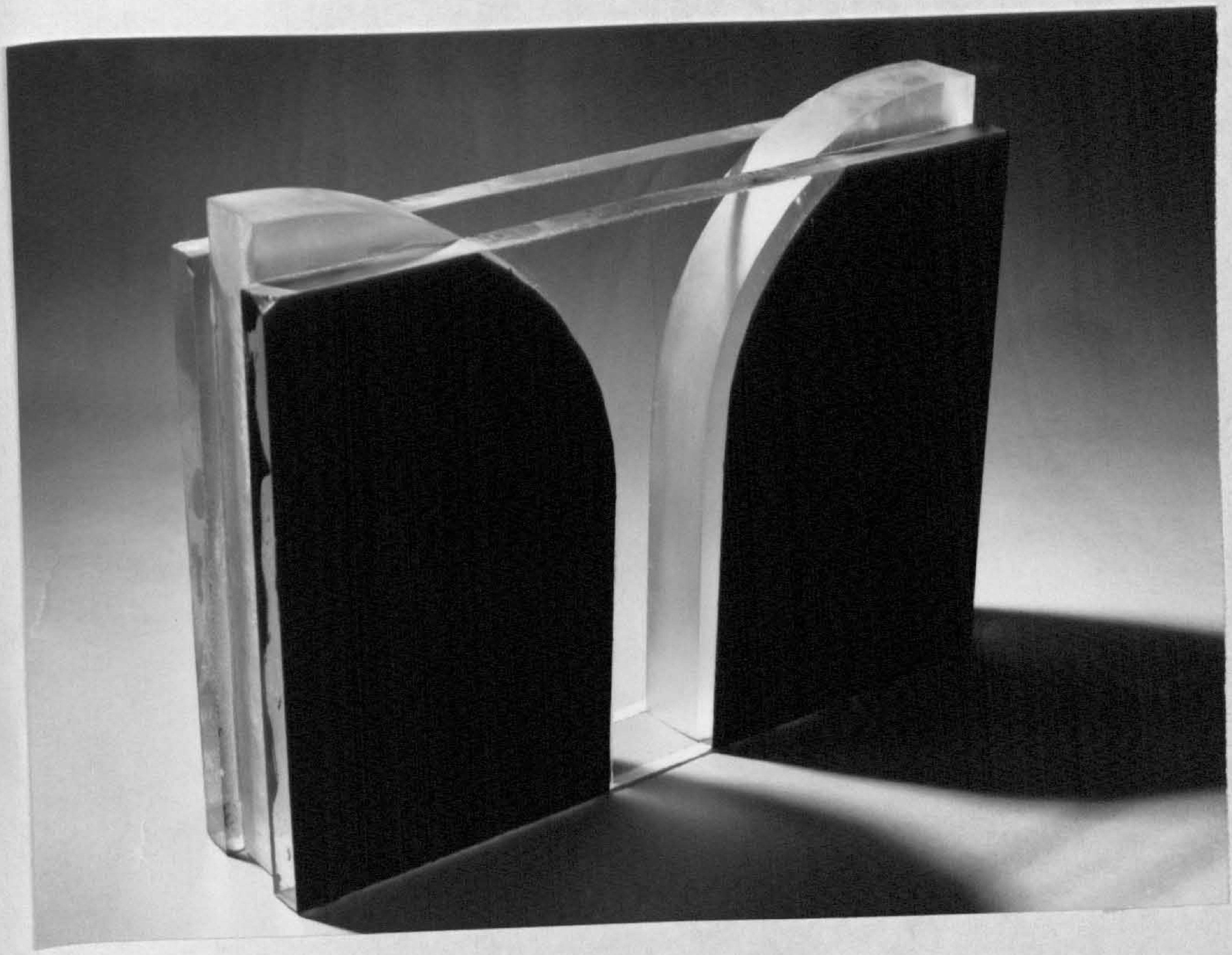

a) nozzle

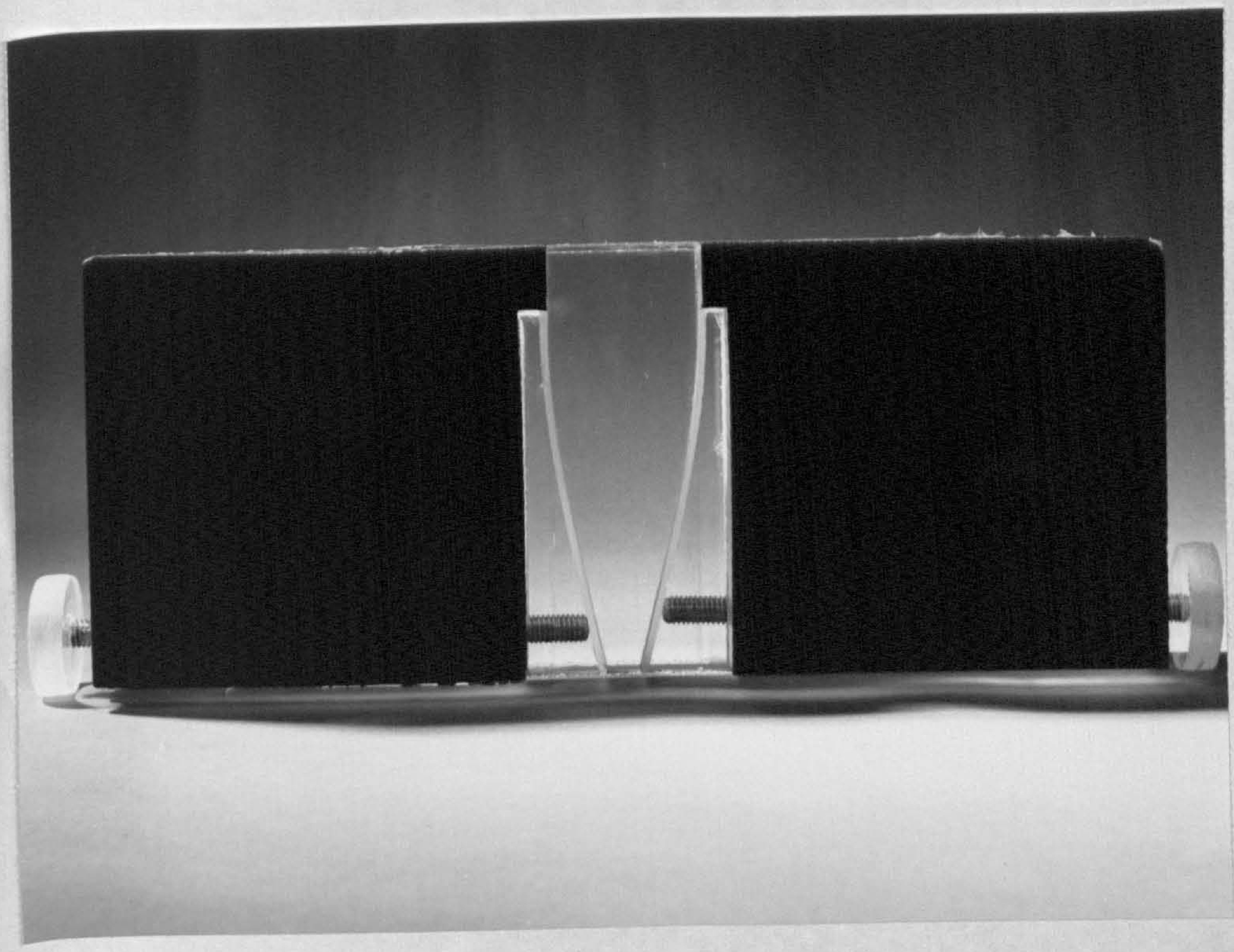

b) flow constrictor

THE DETACHABLE NOZZLE AND FLOW-CONSTRICTOR

FIG. 3.6.

constrictor block (fig. 3.6b) was added to the nozzle. The surface to be connected to the nozzle block was polished and fitted with a rubber seal. Two perspex flaps could be adjusted to any position from 30 mm fully open to almost fully closed. This meant that the water velocity in the parallel exit channel of the nozzle could be controlled. All surfaces of the nozzle and the constrictor except the water viewing section were painted matt black to prevent glare from the lights.

The nozzle and constrictor were connected to the tundish by a 12 mm thick hardened steel base-plate which could be tightened into the beams at the base of the tundish. The whole assembly connected to the tundish is shown in fig. 3.7.

3.1.2.4. COLLECTOR TANK

A plastic dustbin of 650 mm height and 500 mm diameter was used to collect the water from the nozzle. The volumetric flow rate was measured by a 1.128 m tall by 145 mm diameter tube in the dustbin. The system is shown in fig.3.8. In normal running, water from the nozzle passed out of the tube through a 100 mm x 50 mm exit valve at the base of the tube. The door of the valve (fig.3.9a) was kept open by a string passing up the inside of the tube and held firmly in position near the top of the tube on the outside. When the string was released the door closed and the water moved up the tube. When water was at the top of the tube the hydrostatic pressure prevented the door being opened by the string alone. Therefore a lever operated cam (fig. 3.9b) was added to open the door partially to allow the water level to

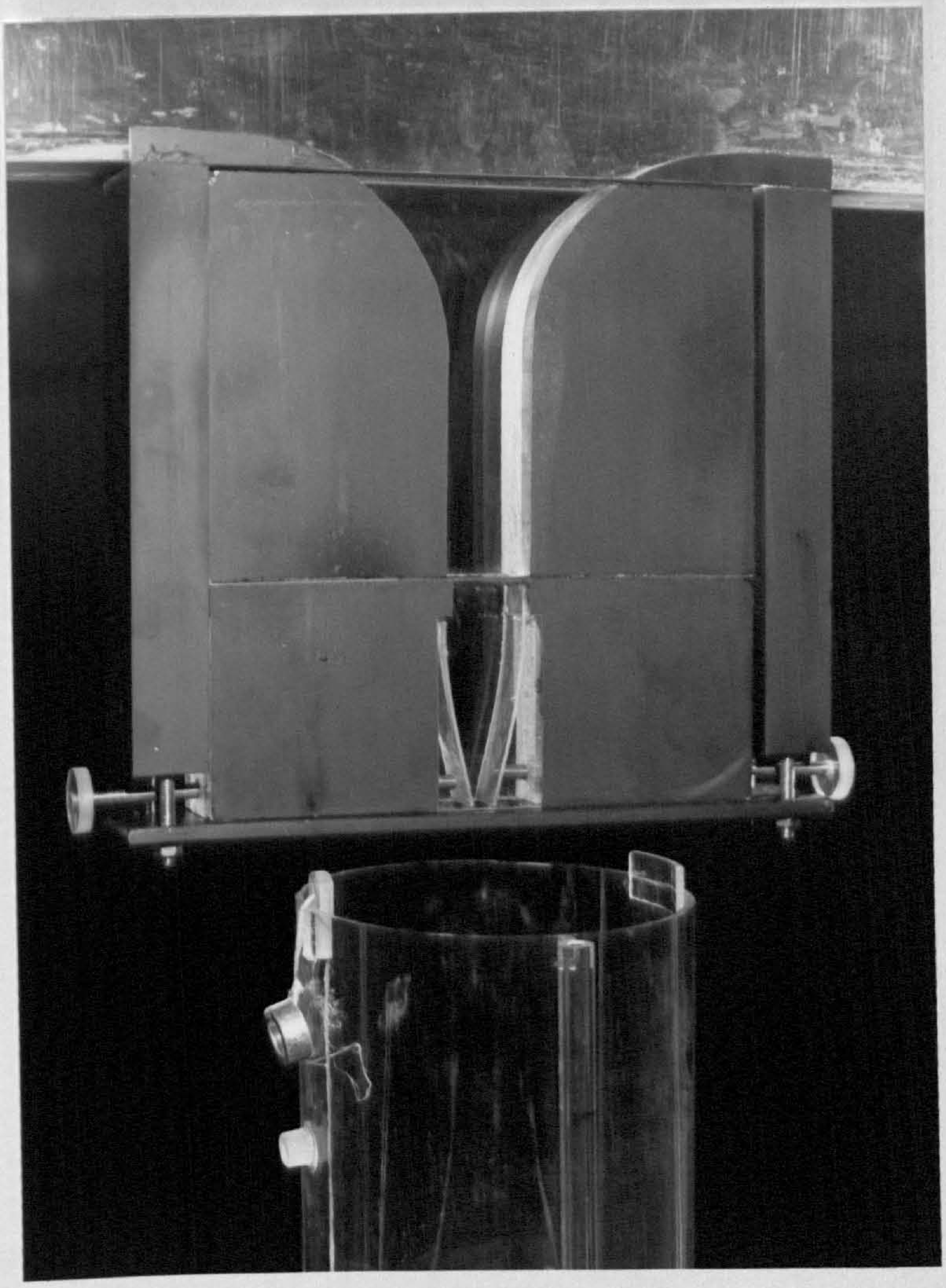

THE NOZZLE AND CONSTRICTOR IN POSITION ON THE TUNDISH

FIG. 3.7.

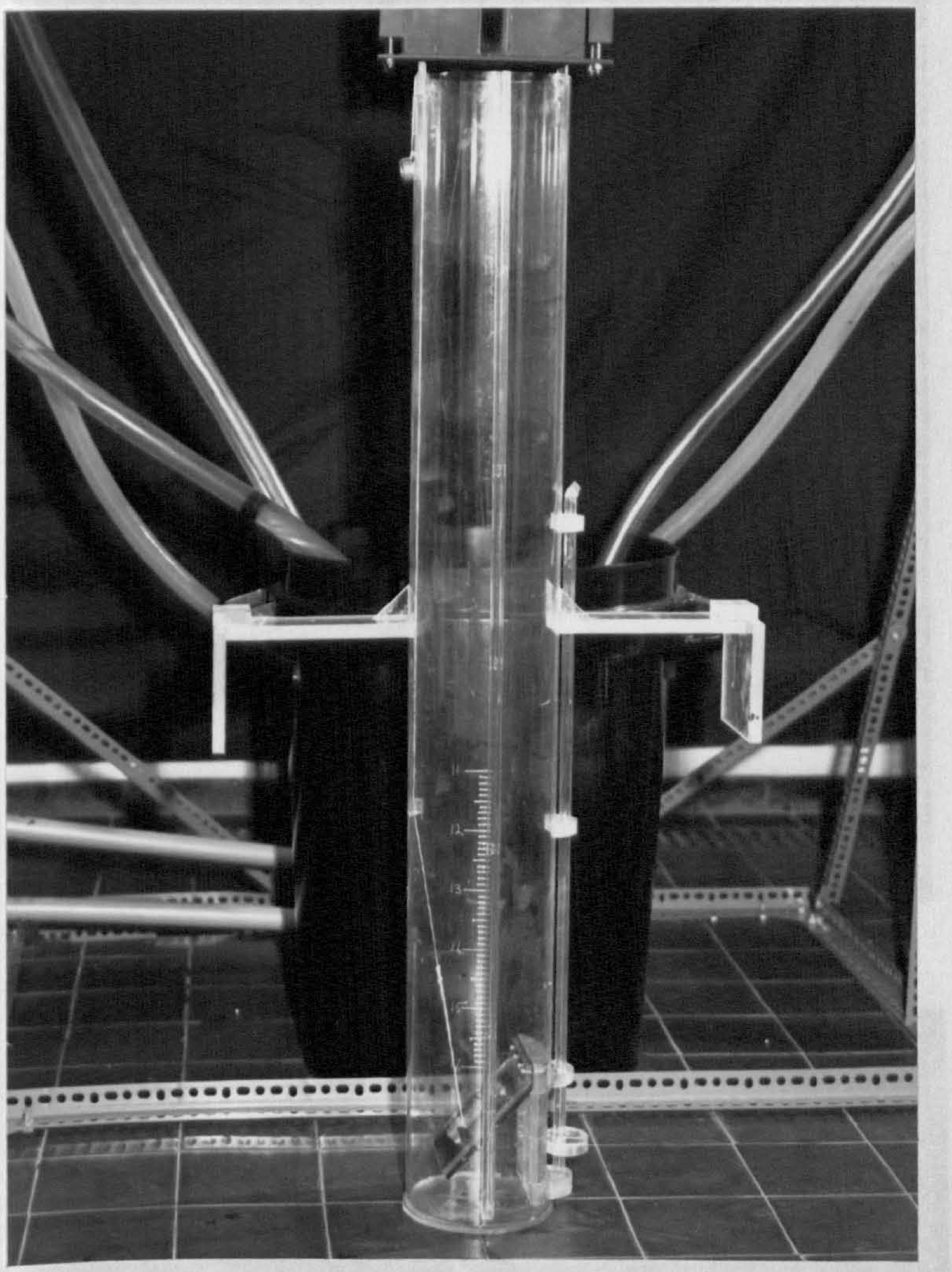

THE COLLECTOR TANK, AND CALLIBRATED CYLINDER FOR FLOW MEASUREMENT

FIG. 3.8.

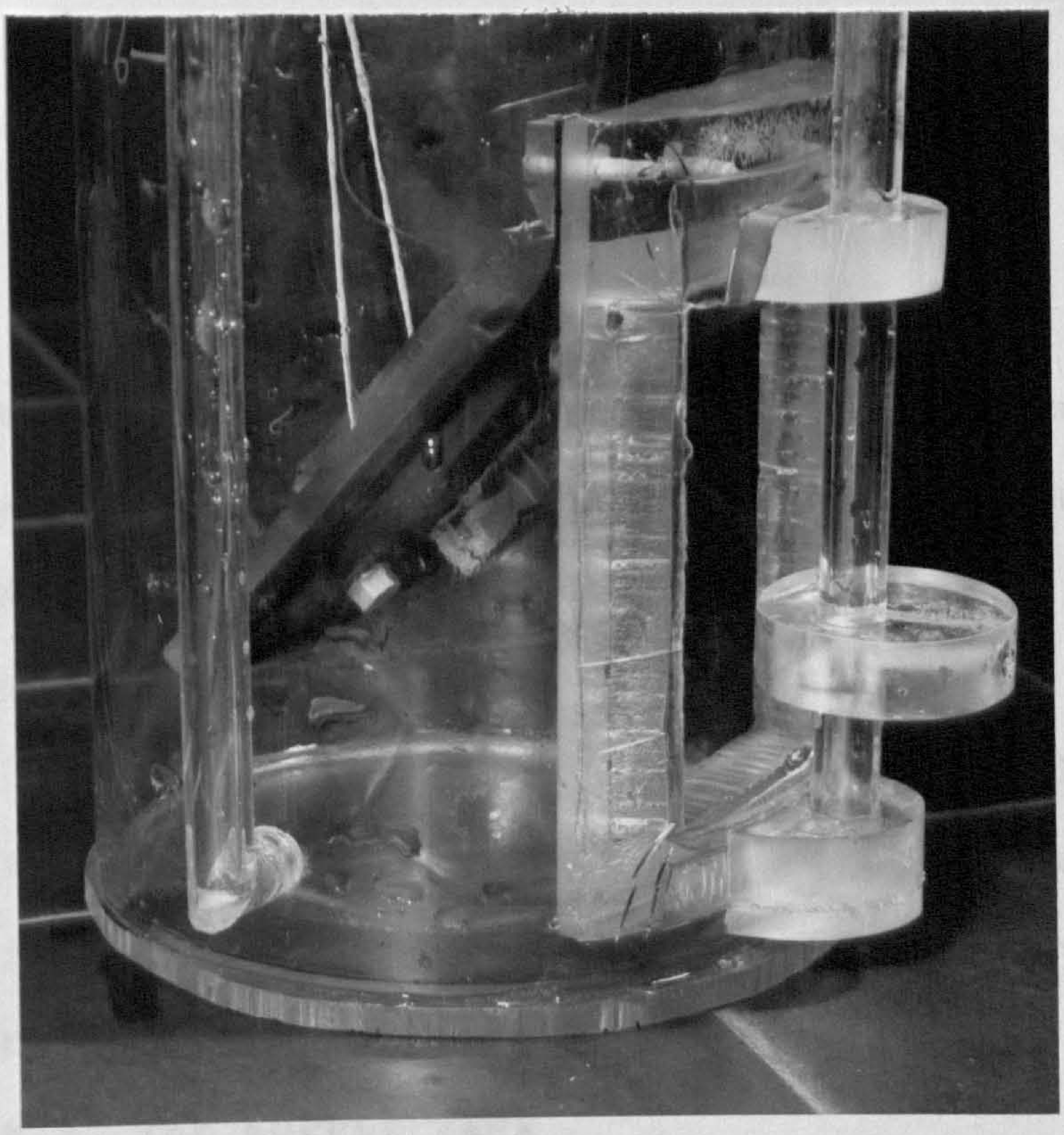

a) fully open

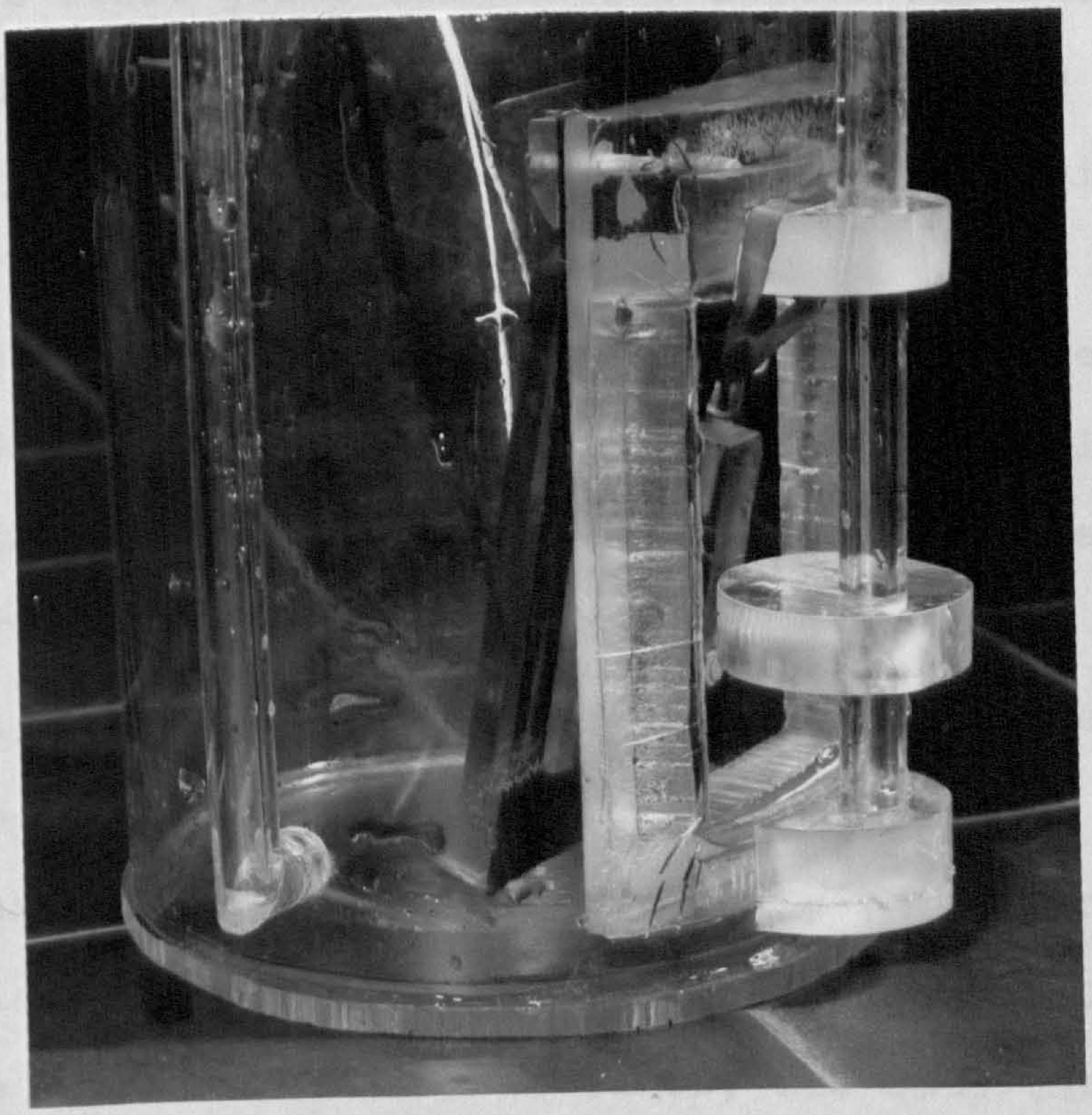

b) partly opened
with the cam

THE DOOR IN THE MEASURING CYLINDER

FIG. 3.9.

fall sufficiently for the door to be again opened fully with the string.

The collector tube was calibrated at 8 litres and 10 litres positions, but because of the high turbulence and excessive air entrainment, the water level was recorded on a manometer tube of 6 mm internal diameter at the side of the collector tube.

Connected to the collector tank was a balance tank (fig.3.10) which enabled a level of water to be maintained in the collector tank sufficient to prevent any air entrainment at the outlet pipe feeding the pump.

3.1.2.5. THE SUPPLY TANK

A fibre-glass tank of 900 litres capacity supplied water for the experiments from four brass taps and four flexible exit pipes. For the purposes of these experiments the quantity of water in the tank was 700 litres (0.7 m^3). Two pipes supplied the distributor tank, one pipe supplied the collector tank, and one pipe supplied the balance tank. The maximum flow rate could be achieved with the flow from two fully open taps, (C and D in fig. 3.2). For lower flow rates taps C and D were gradually closed. Therefore taps A and B required opening to maintain the level of water in the collector tank. The flexible tubing was colour coded at the inlet and outlet ends. In addition to these, two flexible tubes from the tundish overflow, fed into the collector tank. All flexible tubing was 27 mm internal diameter and 3.5 mm wall thickness.

A submerged tube 340 mm in diameter surrounded the

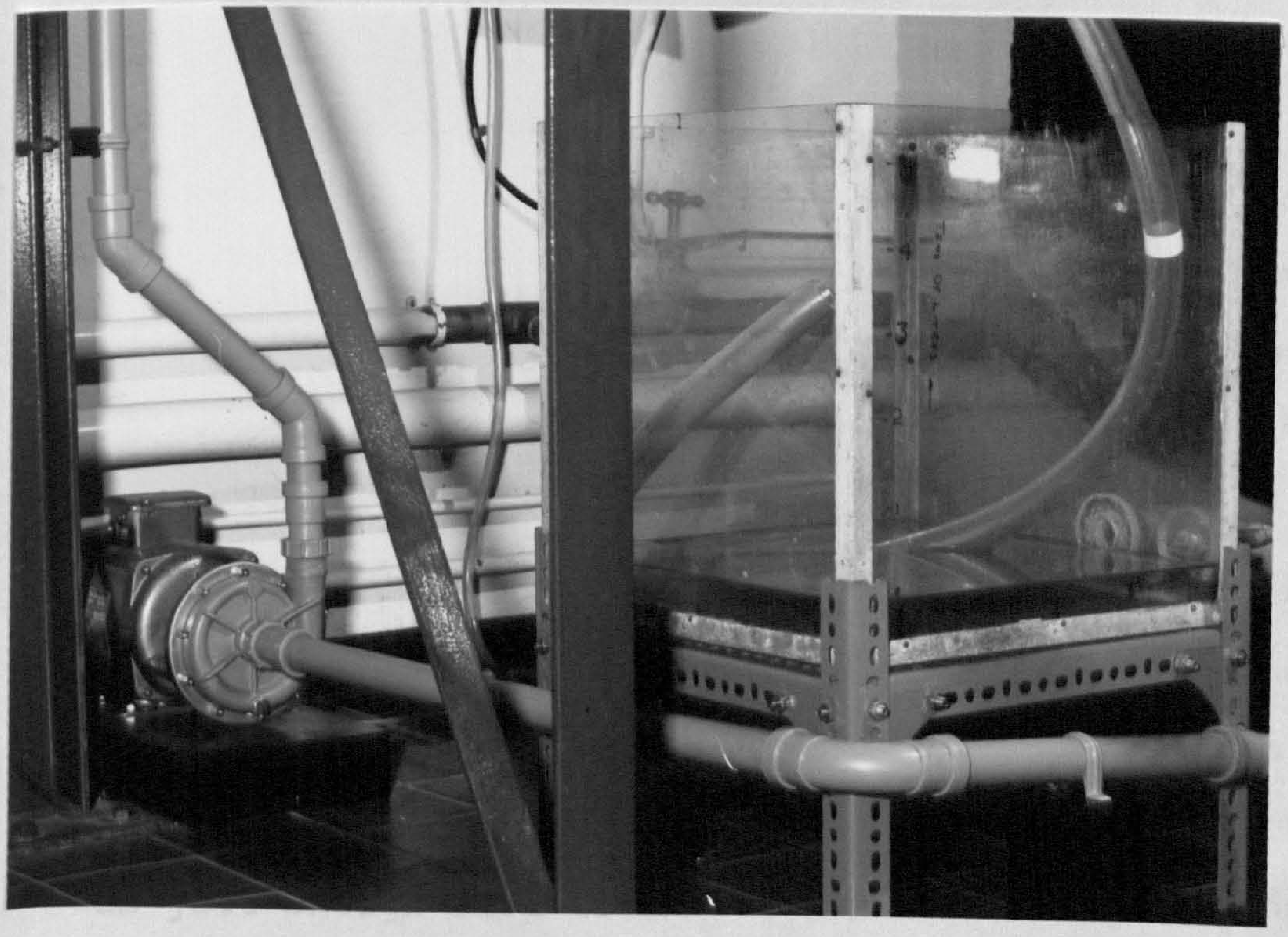

THE PUMP AND BALANCE TANK

FIG. 3.10.

outlets from the supply tank to limit the turbulence and prevent air entrainment. It also prevented any surges of water causing waves in the tank.

The water level in the supply tank was approx. 3.5 m above the pump height.

Tap water was added to the system through a filter to minimise the amount of suspended particles in the water. Sodium sulphate was added as a concentrated solution to the tank and pumped through the system to homogenise its concentration within the recirculating water at 0.15 g/litre.

3.1.2.6. THE PUMP

Water was recirculated by a Beresford PV101 pump, seen in (fig. 3.10) of capacity 50 galls/min (38×10^{-4} m^3/s) at a total head of 4 m. This compared with a maximum expected flow rate through the model of 23×10^{-4} m^3/s. The casing was made of cast iron, but the internal moving parts were made of polypropylene for corrosion resistance. The inlet to the pump was directly from the base of the collector tank, and the outlet was to the supply tank through a filter bag.

3.1.2.7. DESIGN FOR THE ELECTRICAL CONNECTIONS

Electrical connections to the model were made by drilling holes in the rear of one side of the nozzle, as seen in fig.3.11 a and b. For the anode a 3 mm hole was drilled through the glass to the perspex nozzle surface so that there was just enough room to insert a 0.75 mm wire to the interior of the nozzle. The anode wire was then positioned in the corner of the nozzle. The cathode connection was made by first drilling a 3 mm hole at an upward angle through to the

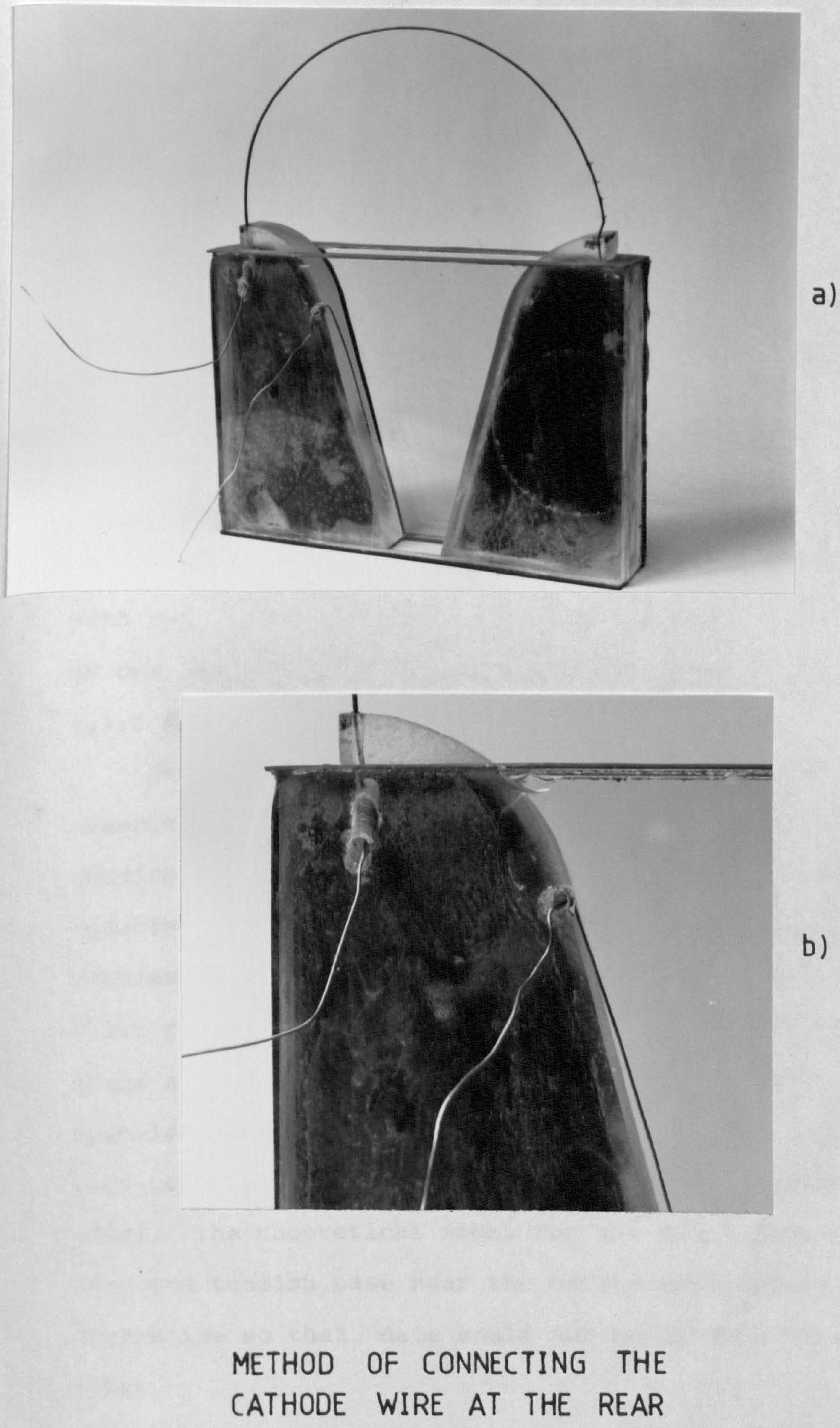

METHOD OF CONNECTING THE CATHODE WIRE AT THE REAR OF THE NOZZLE

FIG. 3.11.

perspex. A 0.75 mm hole from the top of the nozzle near the fixture with the tundish section met the 3 mm hole. The cathode wire of 0.75 mm was pushed through. This wire was then bent in the form of a semi-circle, (corresponding to the assumed start of curved flow through the nozzle), and pushed into a shallow 0.75 mm hole on the other side of the nozzle. The holes were positioned in such a way that the cathode wire was almost touching the rear surface when the nozzle was inserted on to the tundish. Wires to be used for experimental purposes were then soldered on to the semi-circular wire and parts not required were fully insulated with two layers of high voltage insulating varnish followed by one layer of matt black paint.

3.1.3 REMOVAL OF PRE-EXISTING TURBULENCE

Evidence from the prototype model showed the difficulty associated with separated regions and turbulence in the tundish. A crucial part of the design was to find a means of reducing the tundish turbulence to a level where hydrogen bubbles could be clearly observed over the entire length of their paths from the cathode wire to the nozzle exit. A wire gauze at the free water surface reduced the surface turbulence in the prototype so various types of gauze systems were used to establish turbulence free flow in the final model. The theoretical model for the fluid flow had assumed that the tundish base near the nozzle entry would be a fluid streamline so that dams could not be used to divert the flow.

The strategy followed in designing the flow system was to restrict turbulence in the model tundish to regions near the inlet ports. A single gauze was first inserted into the groove nearer the nozzle, and next to this on the entry side a corrugated gauze was inserted. In addition, a semi-circular gauze above the nozzle was found to be important. The set-up is shown in fig. 3.12.

The system was tested by injecting black ink through a capilliary with a syringe; the capilliary being soldered to the support wire. The reduced turbulence obtained is shown for nozzle 1 in the figs. 3.13 to 3.17. Without the gauzes pronounced turbulence existed even at Re_{exit} values as low as 3200, (0.87×10^{-4} m^3/s). With the gauzes there is no evidence of turbulence up to a flow rate of 3.5×10^{-4} m^3 /s ($Re_{exit} = 13500$). Even at 18.9×10^{-4} m^3/s ($Re_{exit} = 74000$) the observed streakline is distinct in the nozzle exit section. A similar trend was seen with nozzle 2.

3.2. FLOW VISUALISATION

3.2.1. HYDROGEN GENERATED IN STILL WATER

A diagram of the apparatus for studying hydrogen bubble generation and visualisation is shown in fig. 3.18a and a photograph in fig 3.18b. This apparatus consisted of of an open perspex tank 305 mm x 51 mm, and 178 mm tall. Holes for the electrodes were drilled above the required level of water.

A direct current was obtained by conversion from the mains with a rectifier. This was then amplified to a possible maximum of 350 V for electrolysis. With a

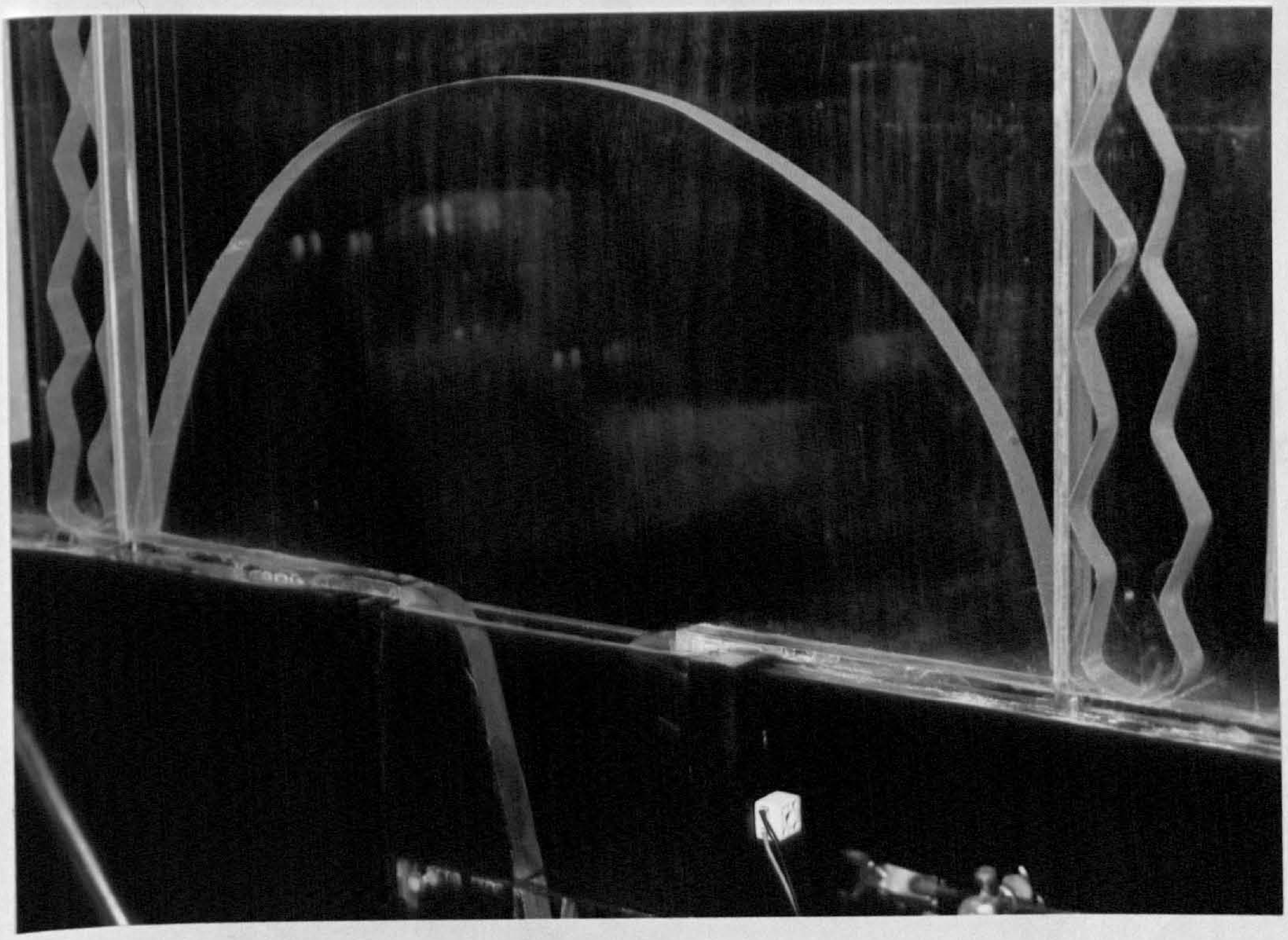

THE GAUZE SYSTEM USED TO CONTROL TURBULENCE

FIG. 3.12.

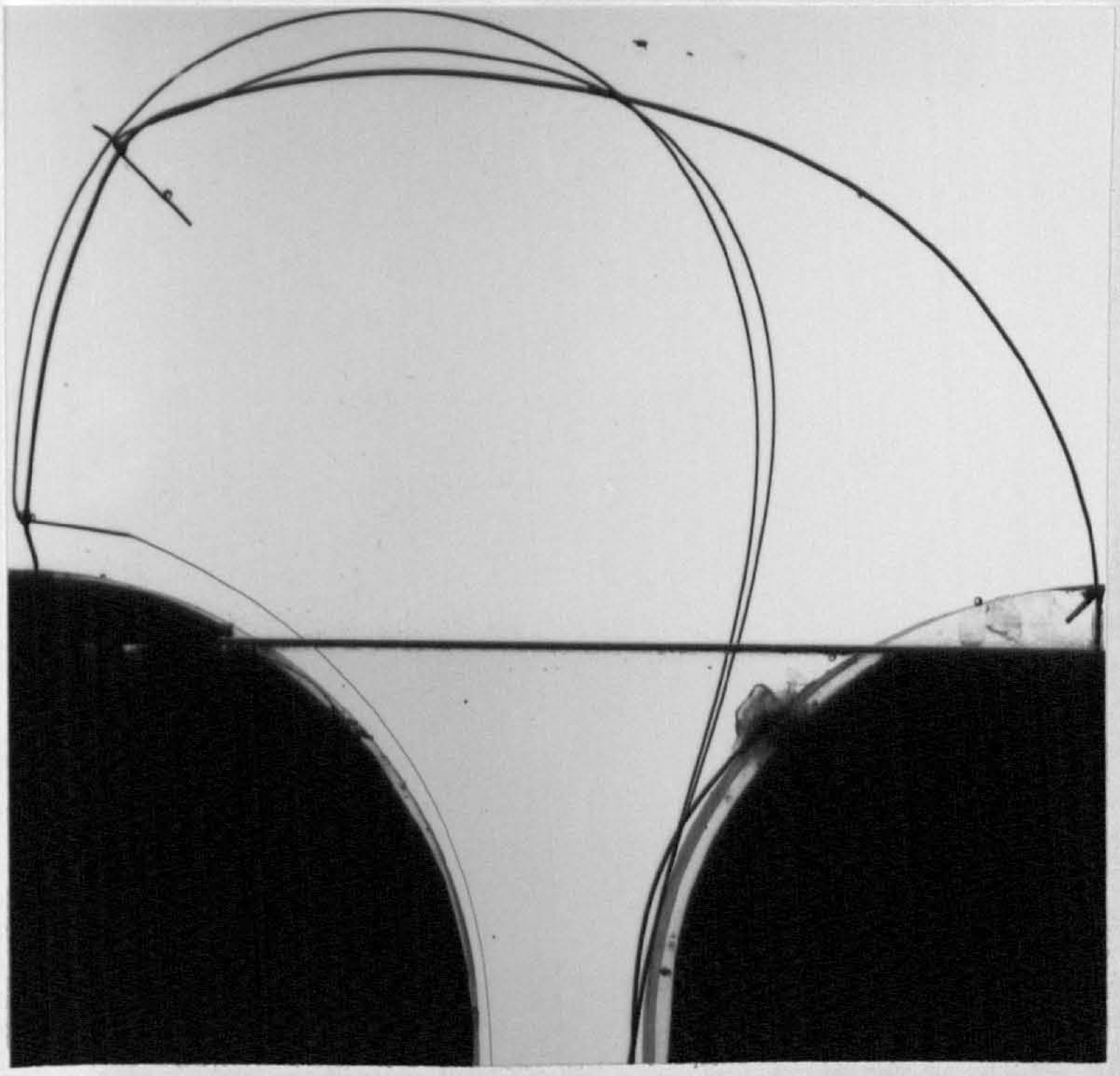

a) with
gauzes

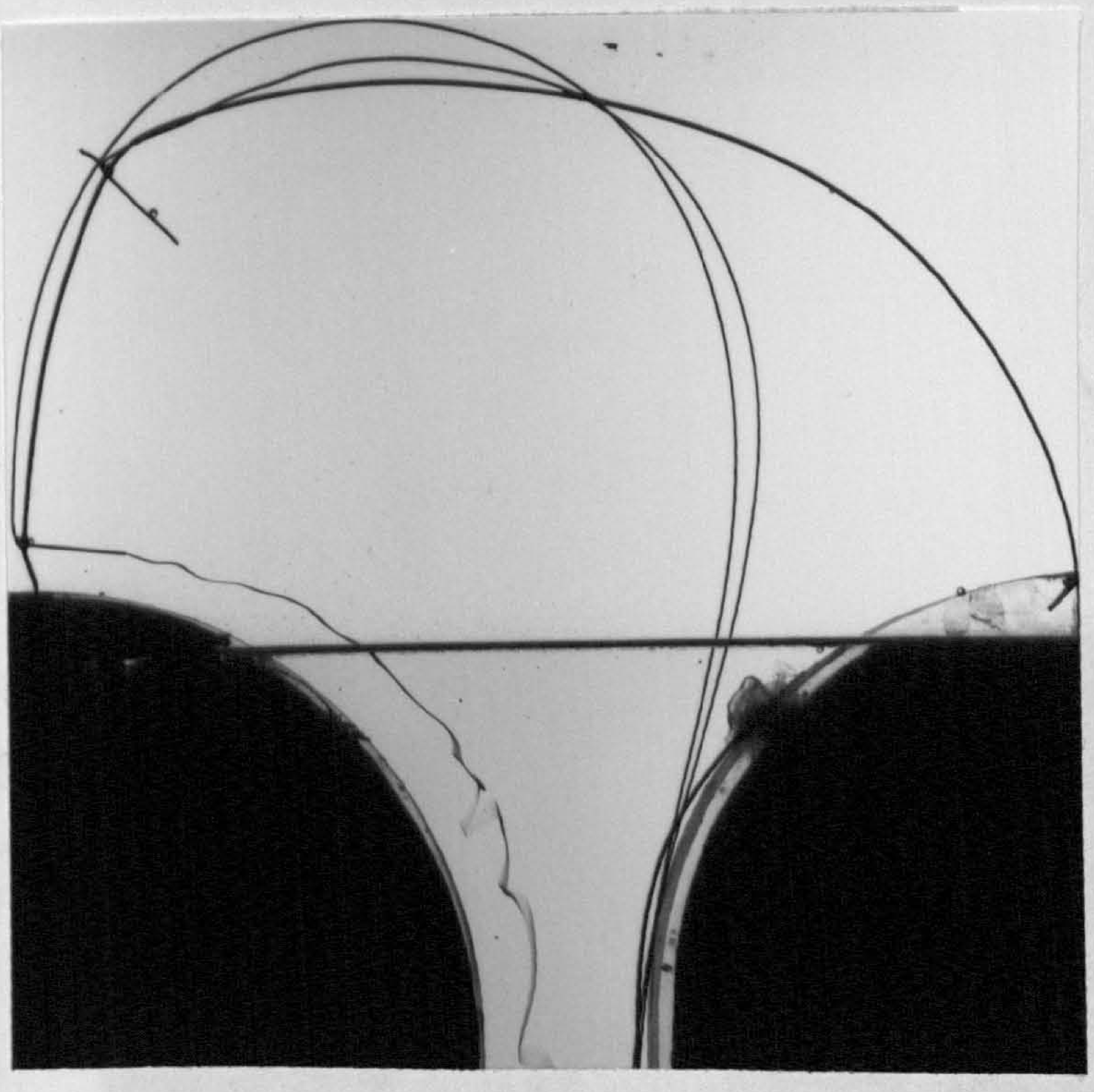

b) without
gauzes

FLOW THROUGH NOZZLE 1 OBSERVED WITH INK INJECTION, (EXIT R_e = 3200)

FIG. 3.13

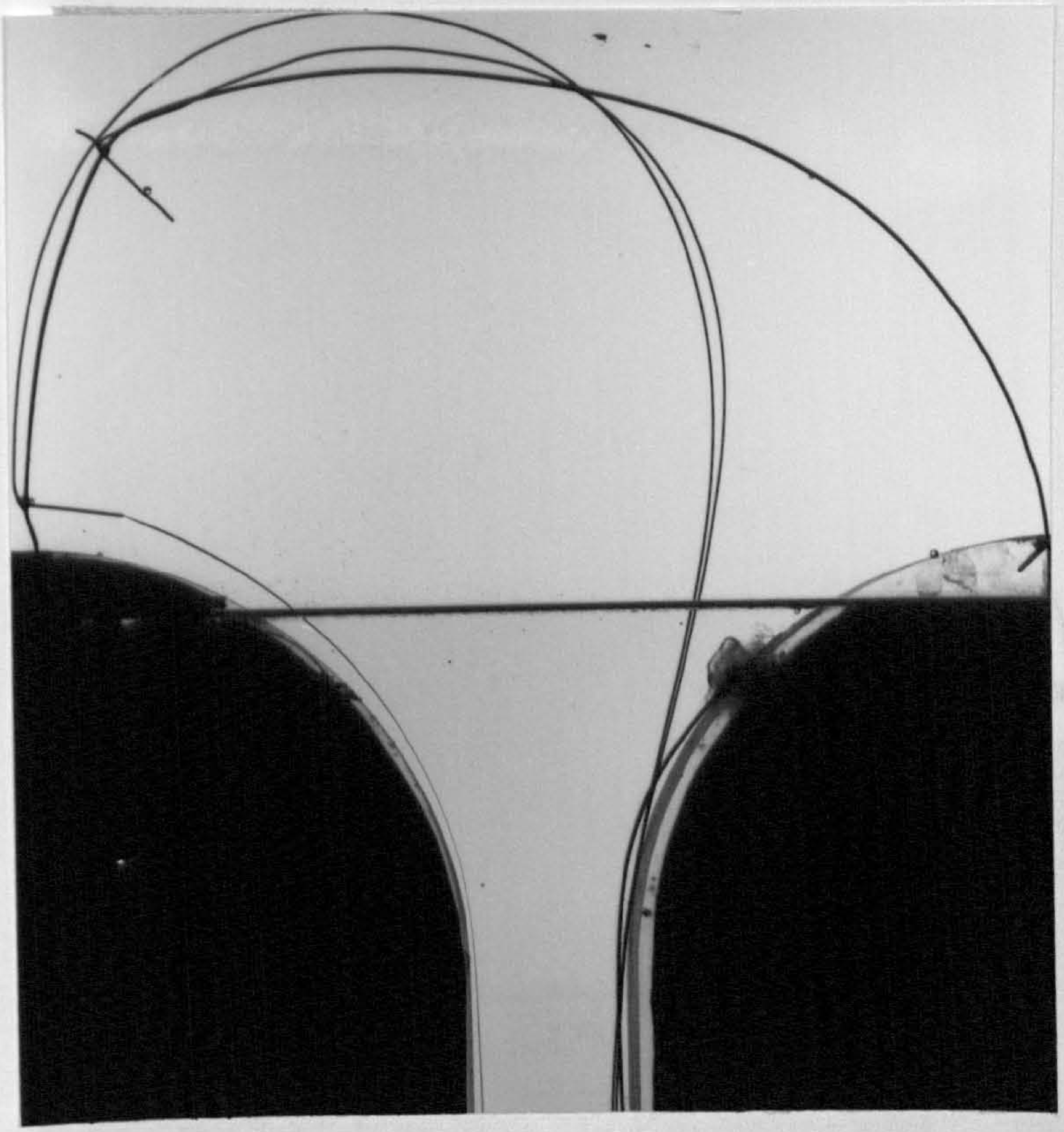

a) with gauzes

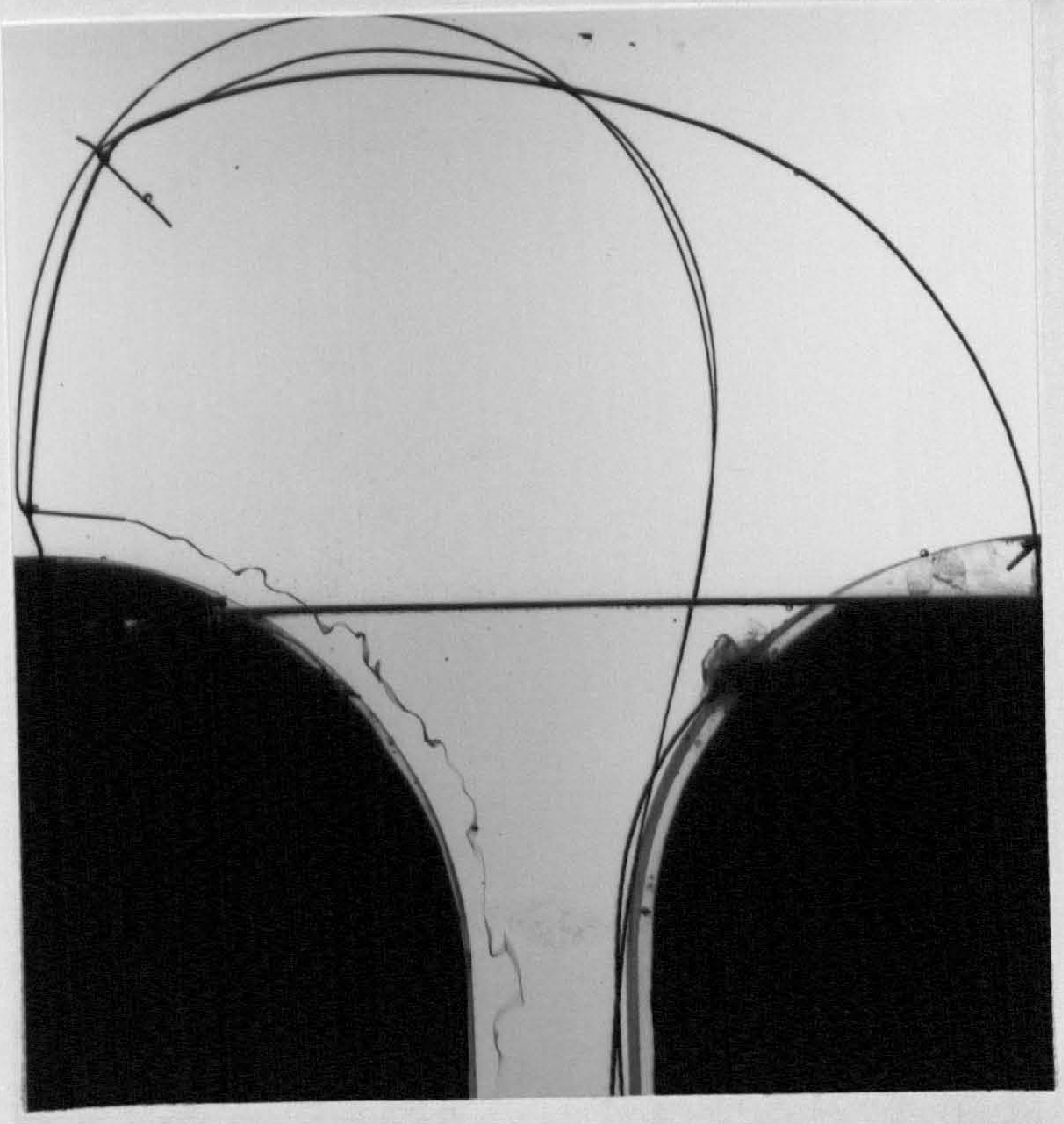

b) without gauzes

FLOW THROUGH NOZZLE 1 OBSERVED WITH INK INJECTION, (EXIT R_e = 13534)

FIG. 3.14

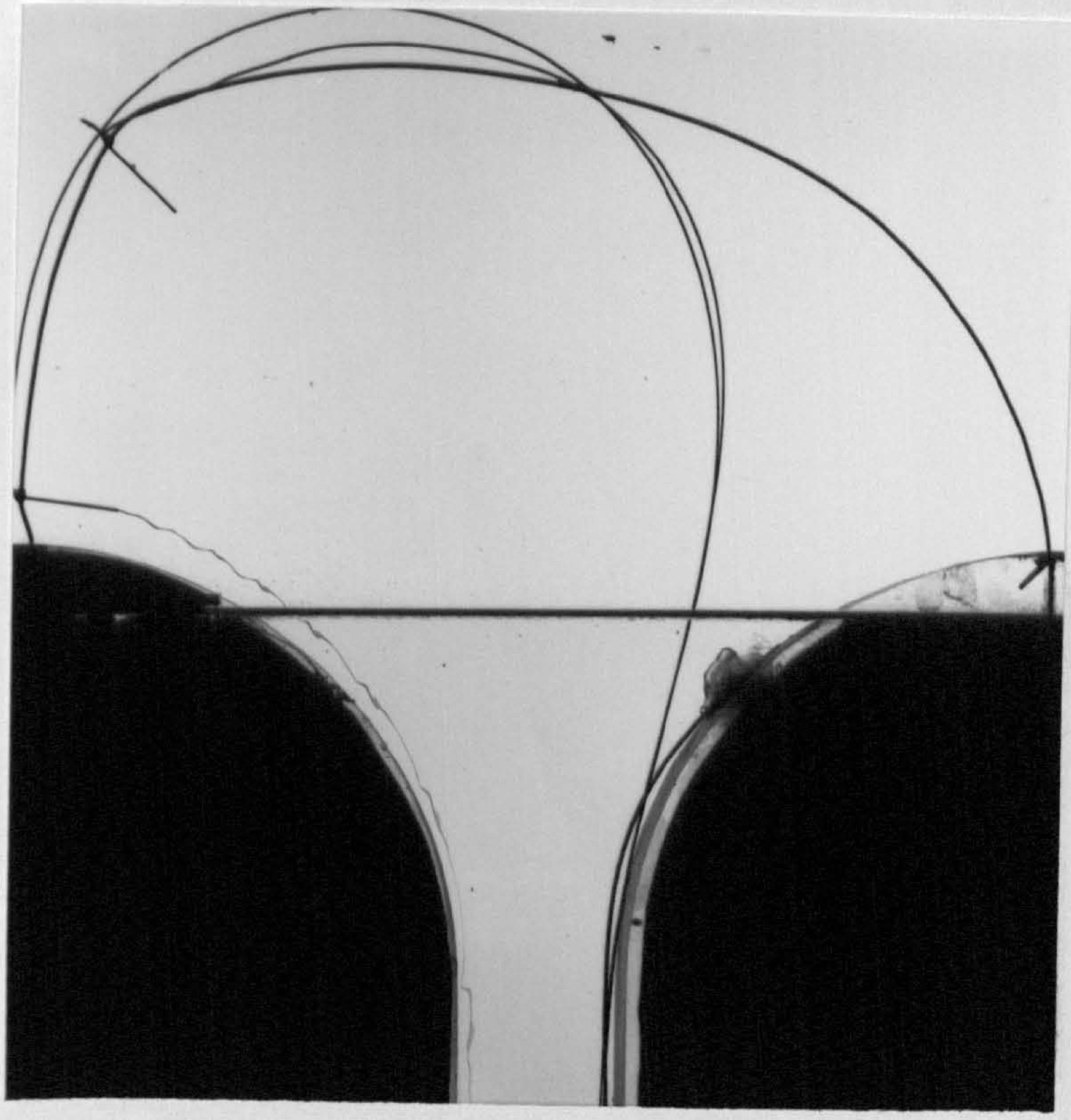

a) with
gauzes

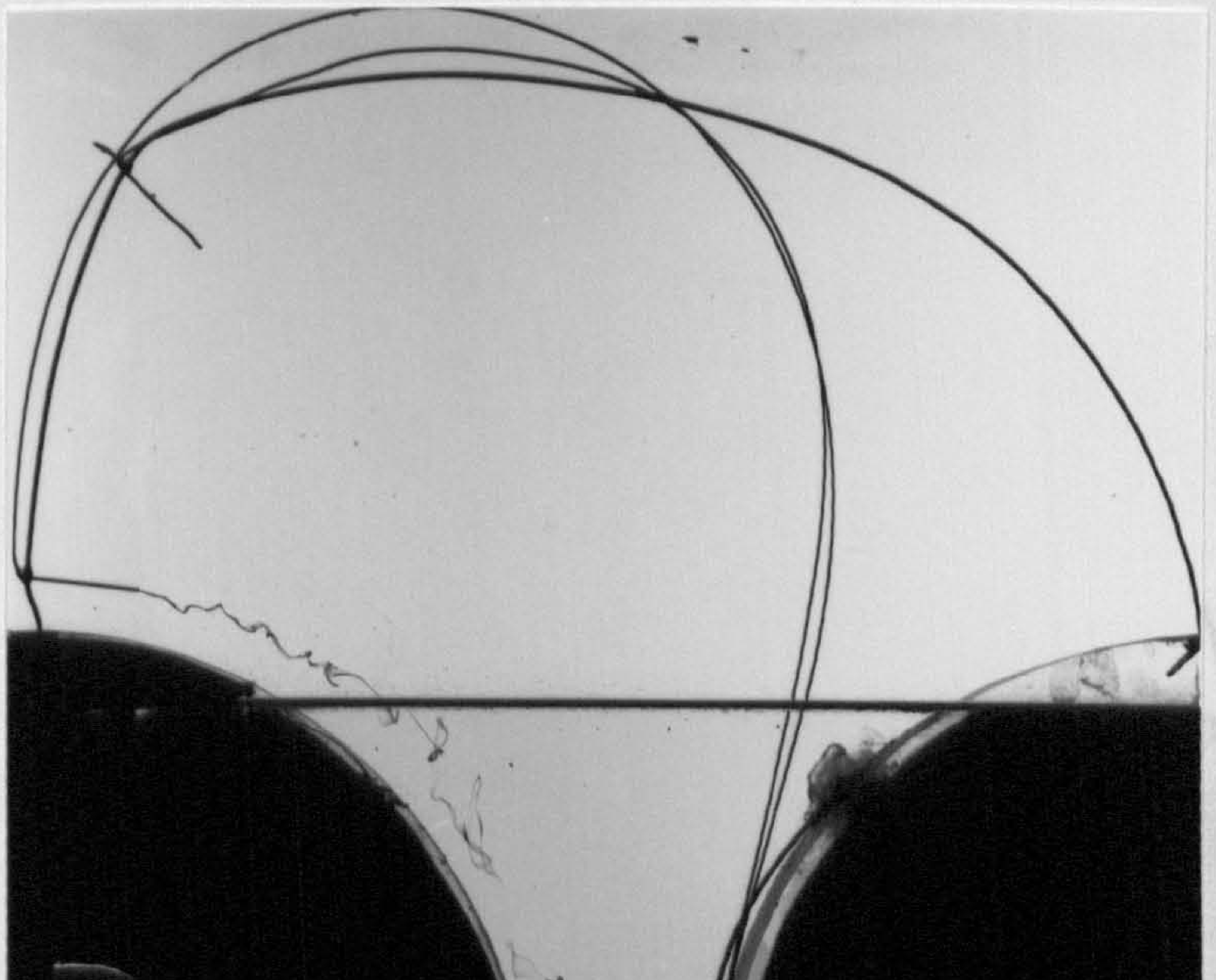

b) without
gauzes

FLOW THROUGH NOZZLE 1 OBSERVED WITH INK INJECTION, (EXIT R_e = 24610)

FIG. 3.15

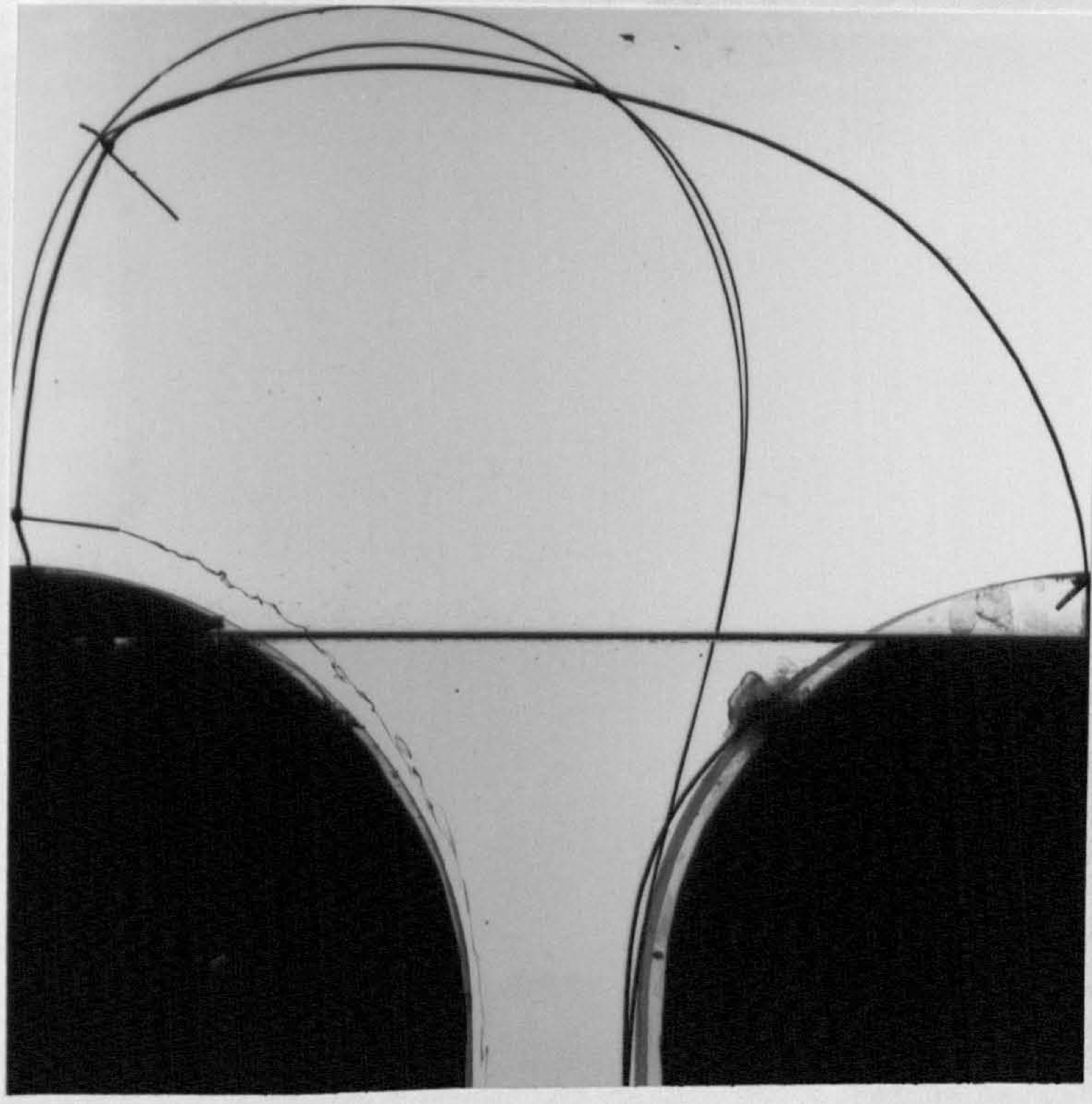

a) with gauzes

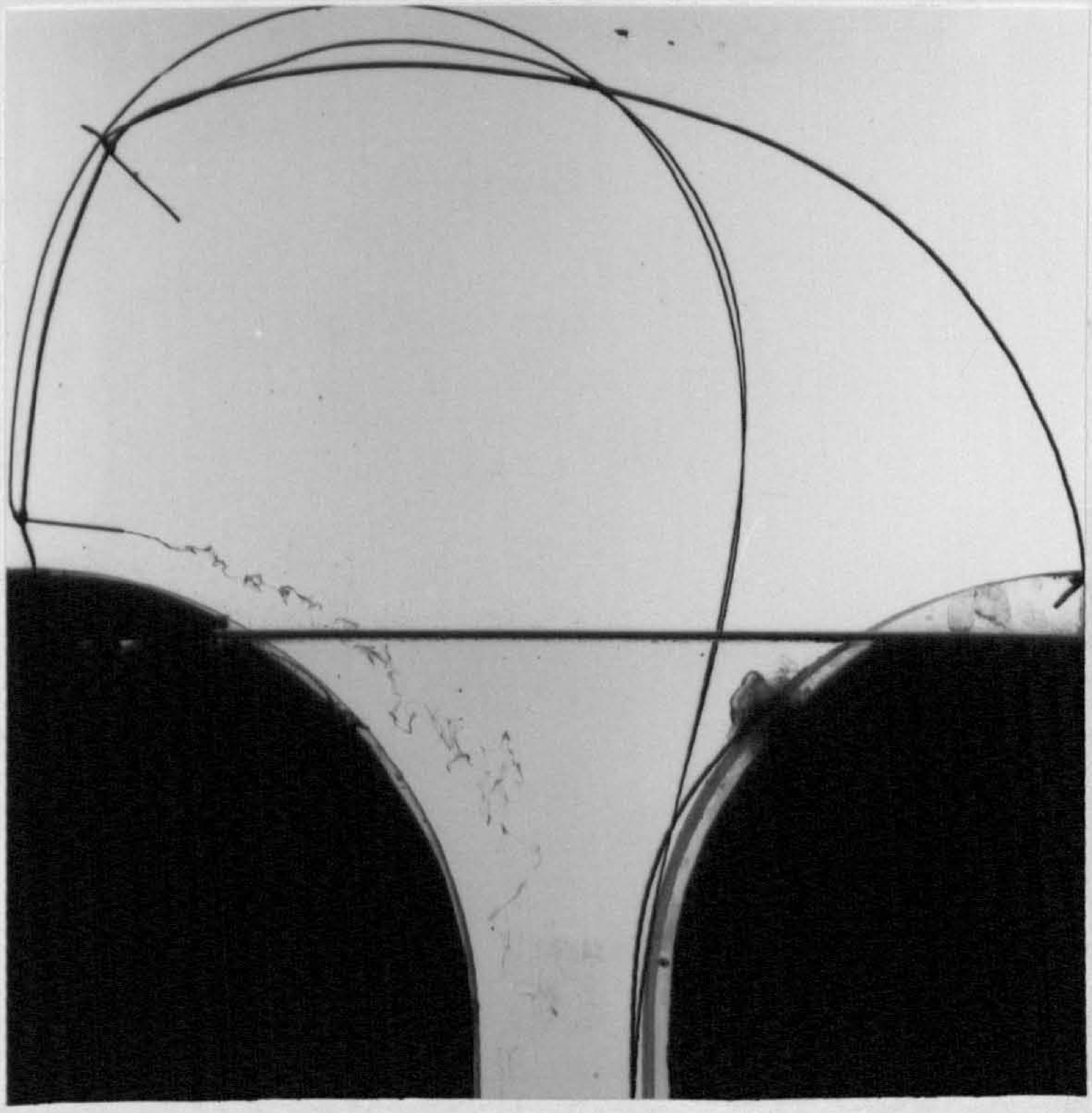

b) without gauzes

FLOW THROUGH NOZZLE 1 OBSERVED WITH INK INJECTION, (EXIT R_e = 47738)

FIG. 3.16

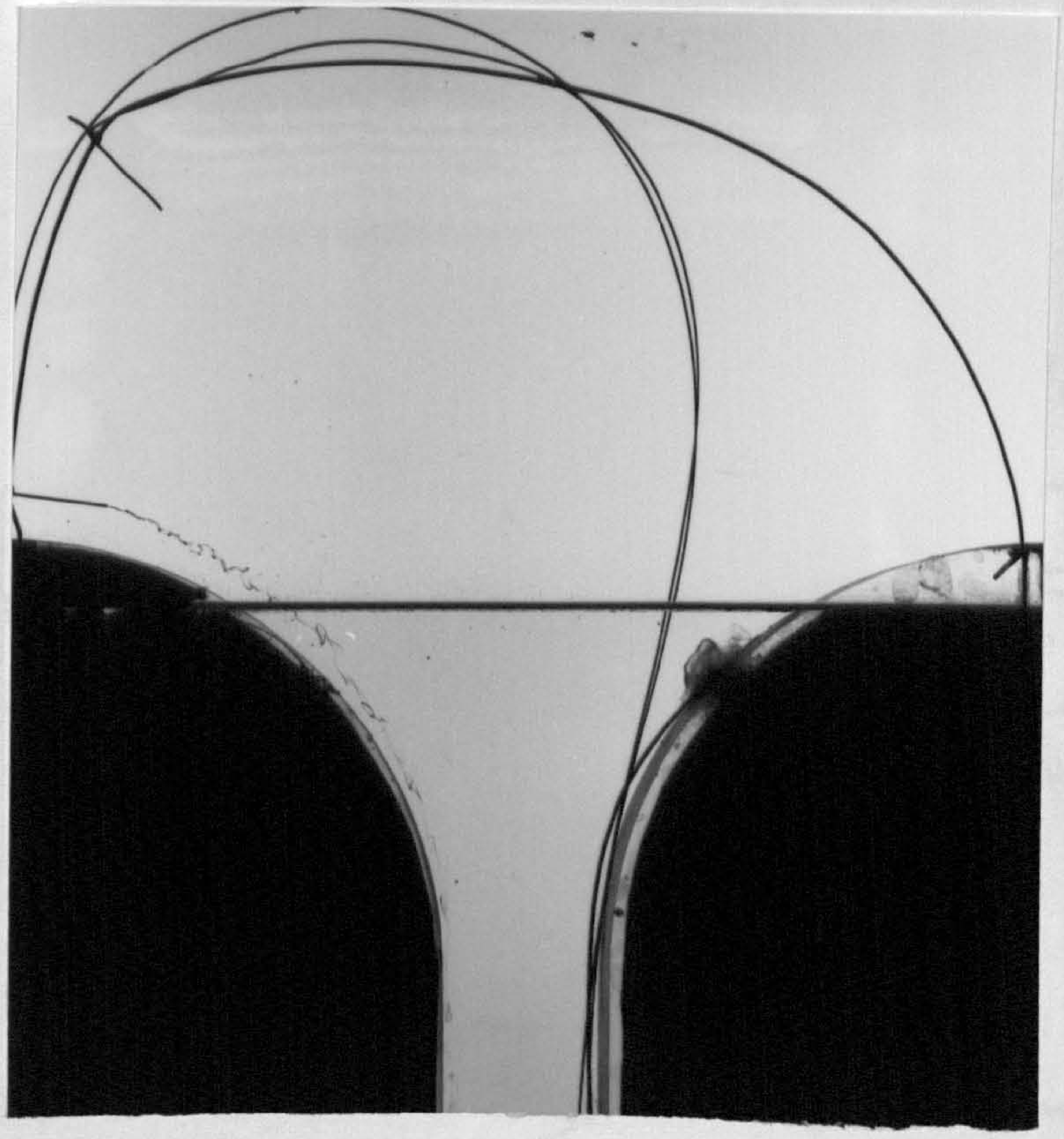

a) with gauzes

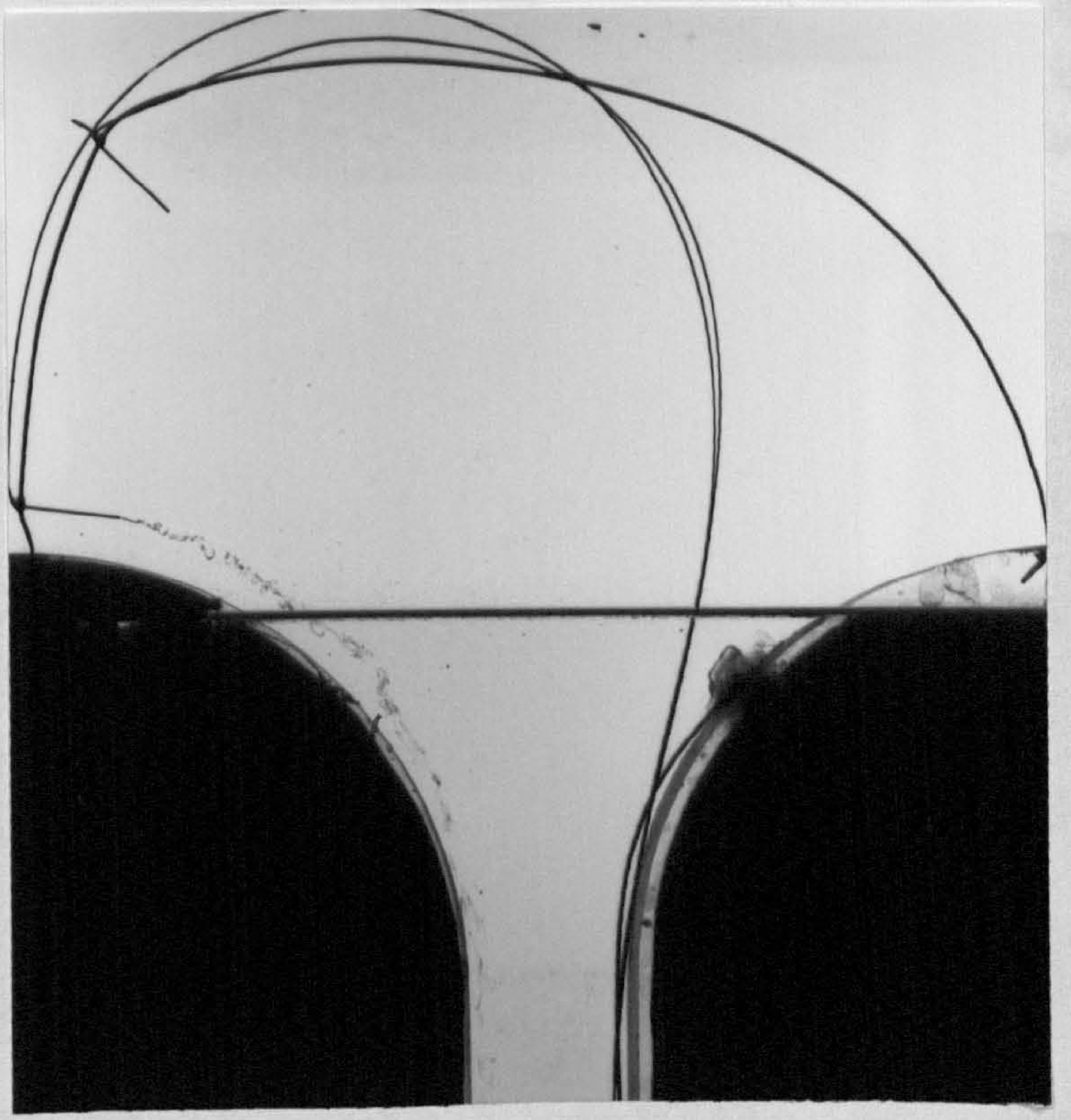

b) without gauzes

FLOW THROUGH NOZZLE 1 OBSERVED WITH INK INJECTION, (EXIT R_e = 74000)

FIG. 3.17

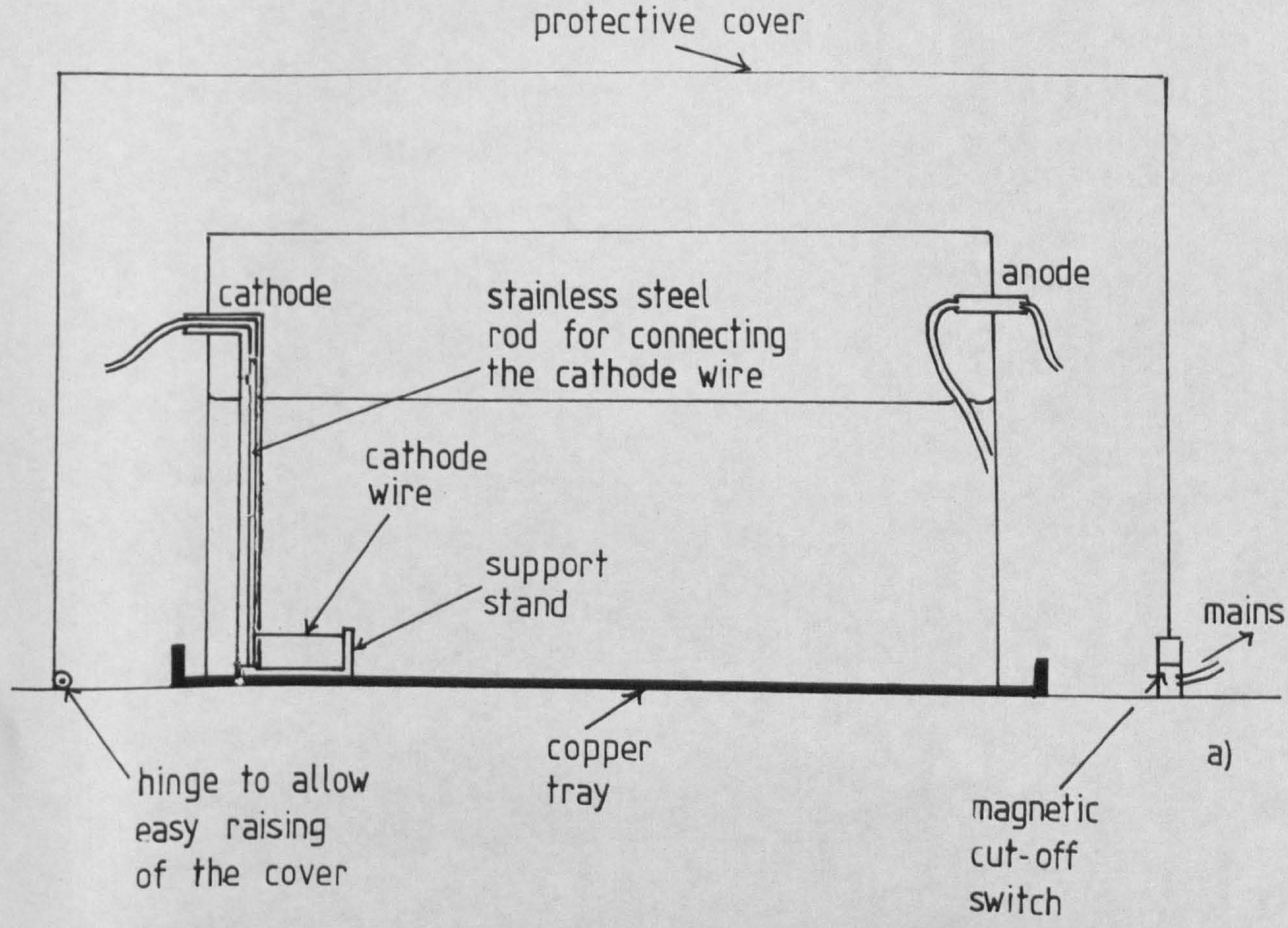

a)

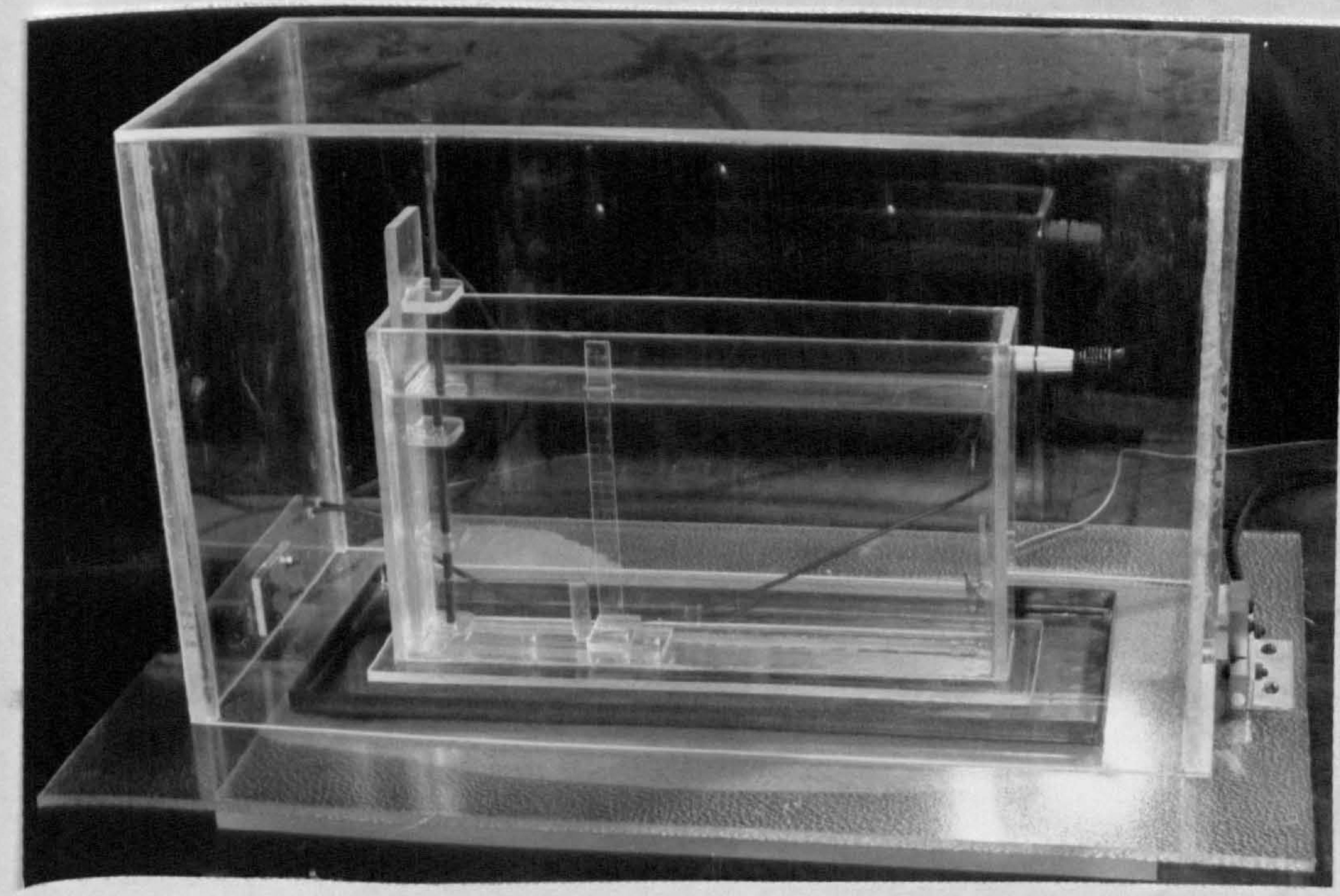

b)

THE APPARATUS FOR GENERATING HYDROGEN BUBBLES IN STILL WATER

FIG. 3.18

specially built pulse generator, high frequency pulses, (10 to 200 Hz), at 2.6 or 2.8 mS widths, or low frequency (.01 to 1.0 Hz) at pulse widths 25 mS to 540 mS were obtained. A continuous current could also be produced.

The cathode consisted of a stainless steel rod insulated with shrink sleeving. The cathode wire either platinum or stainless, was wound round the base of the rod and pushed firmly into the perspex base plate. The other end of the wire was placed in a hole in a perspex rod on the base plate and rotated to stretch the wire. The whole cathode assembly was detachable so that it could be set up outside the model. The anode was a stainless steel wire at the opposite end of the box. Previous work had indicated the possible need to use a solute such as sodium sulphate to allow efficient bubble generation. Initially, then, tests were carried out to study the effect of sodium sulphate additions on the conductivity of water. The results are shown in fig. 3.19. The conductivity of tap water was nearly doubled by the addition of 0.15 g/l of sodium sulphate.

When experiments were carried out with pure deionised water no bubbles were released from a 200 µm platinum wire below a voltage of 300 V, (with a corresponding cathode current of 5 mA). Even at this voltage very few bubbles were released. With sodium sulphate added at a concentration of 0.15 g/l bubbles were produced at 20 V. At 250 V the cathode current was 18 mA with a consequent increase in the number of bubbles. There was considerable variation in the sizes of the bubbles produced, (about 50 µm to 300 µm diameter), this

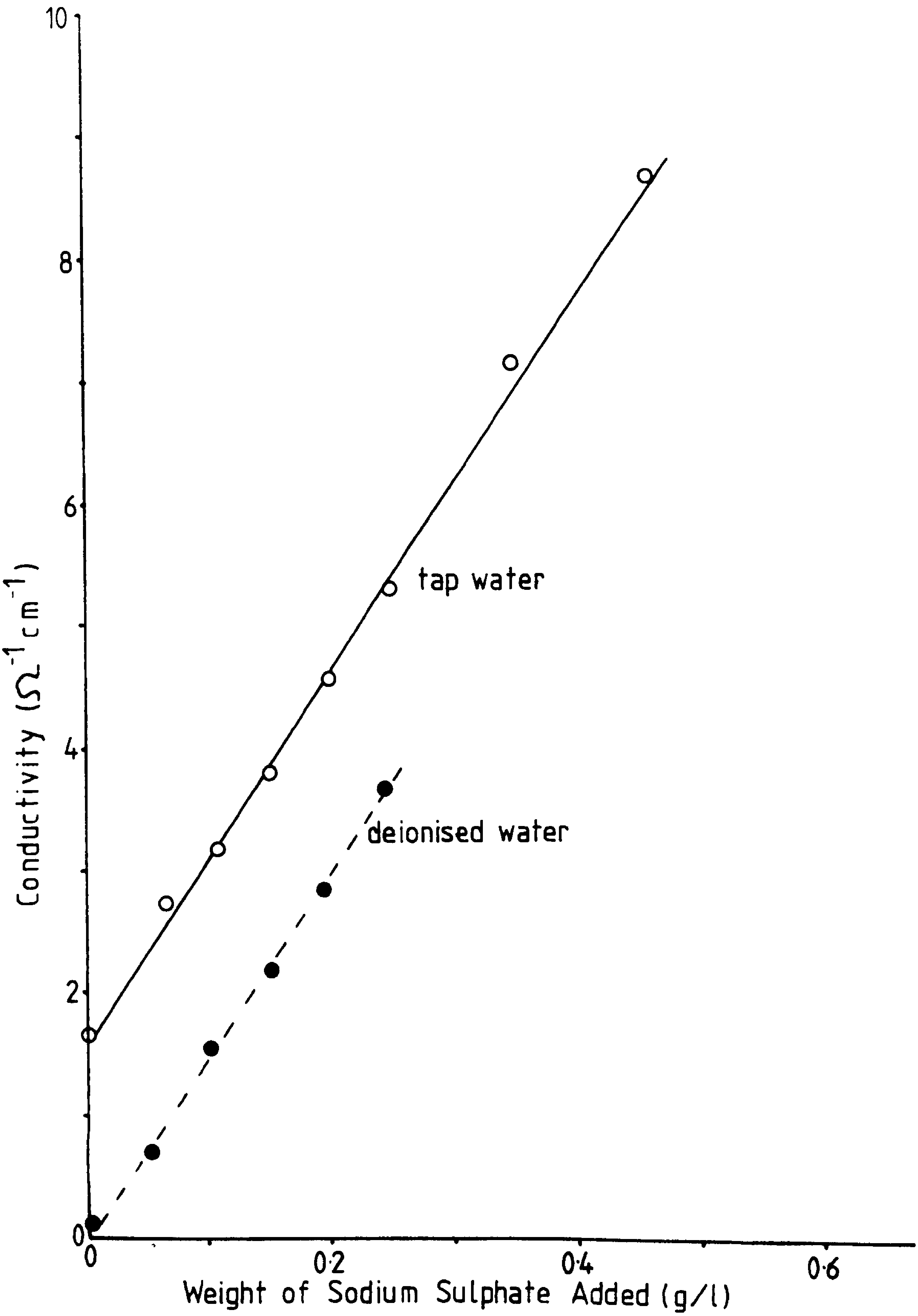

EFFECT OF SODIUM SULPHATE
ON THE CONDUCTIVITY OF WATER

FIG. 3.19

variation being manifest in the different rise rates indicated in fig. 3.20, by expansion in the bubble clouds.

The effects of electrical conditions were studied using a 50 μm stainless steel wire. At a constant frequency the bubble size increased with increase in pulse width, (fig. 3.21). Again there was a large variation in bubble sizes. There was an increase in bubble size with increased frequency at constant pulse width, (fig. 3.22). In general, as the time in the current cycle for which the current was on increased, the bubble size increased.

3.2.2. HYDROGEN GENERATED IN THE PROTOTYPE

Tests carried out with the prototype model necessarily used tap water. The experimental conditions are shown in table 3.1. It can be seen that with a continuous current even at low flow rate the cathode current was 24 mA. This compared with 60 to 70 mA in the still water experiments at 300 V. Velocities of the water at the position of the cathode and at the nozzle exit above the constrictor section are shown in table 3.2. Also shown is the water Reynolds Number at exit and the Reynolds Number associated with the cathode wire.

The clearest streakline picture was obtained at low flow rate, (1.29×10^{-4} m/s) with a continuous current, as seen in fig. 3.23. Distinct and identifiable bubbles are seen from each wire apex. There was a shadow near the nozzle edge caused by reflected light at the internal nozzle surface.

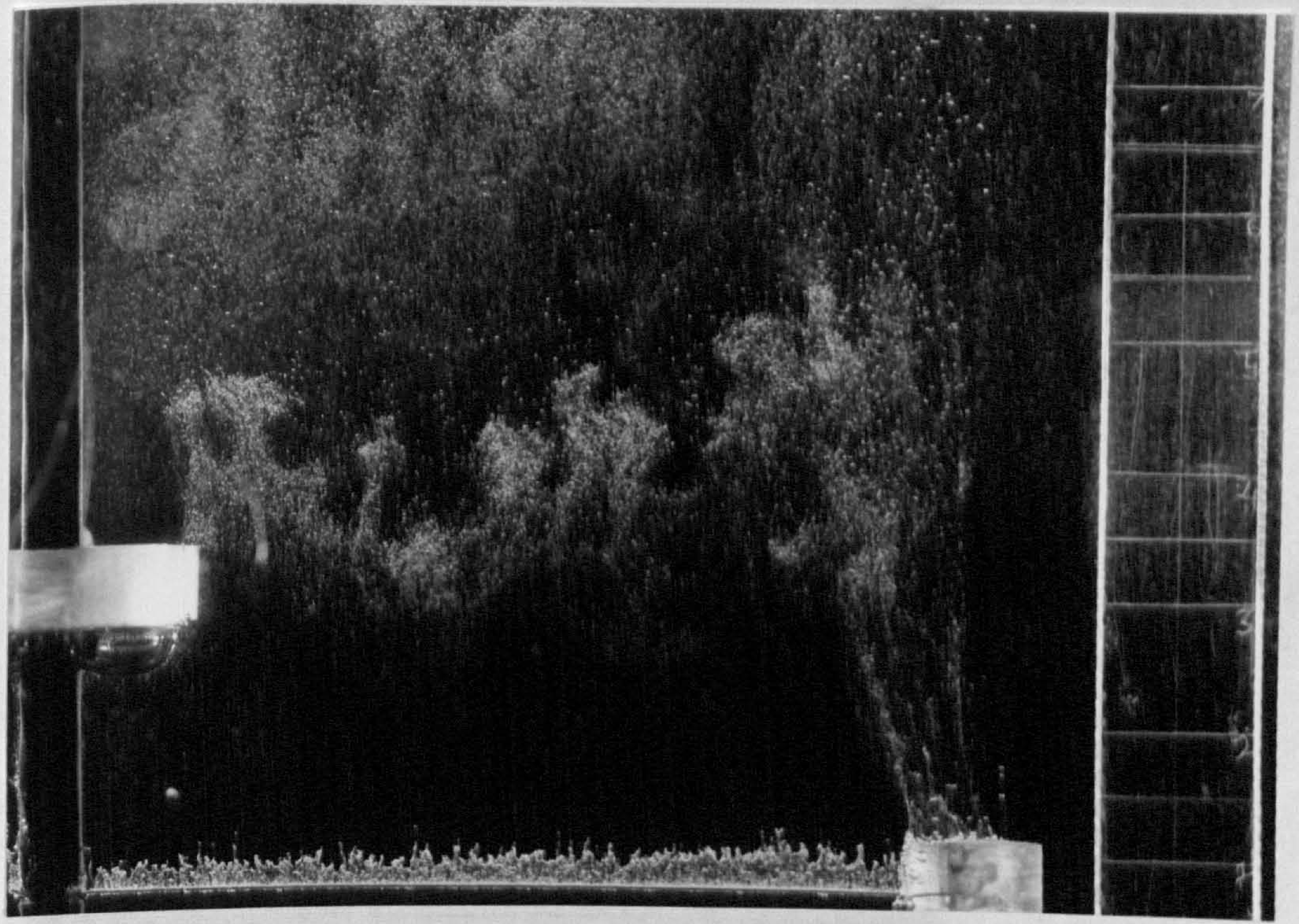

VARYING SIZES OF HYDROGEN BUBBLES GENERATED FROM A 200 μm PLATINUM WIRE SHOWN BY THE DIFFERENT RATES OF RISE.

FIG. 3.20

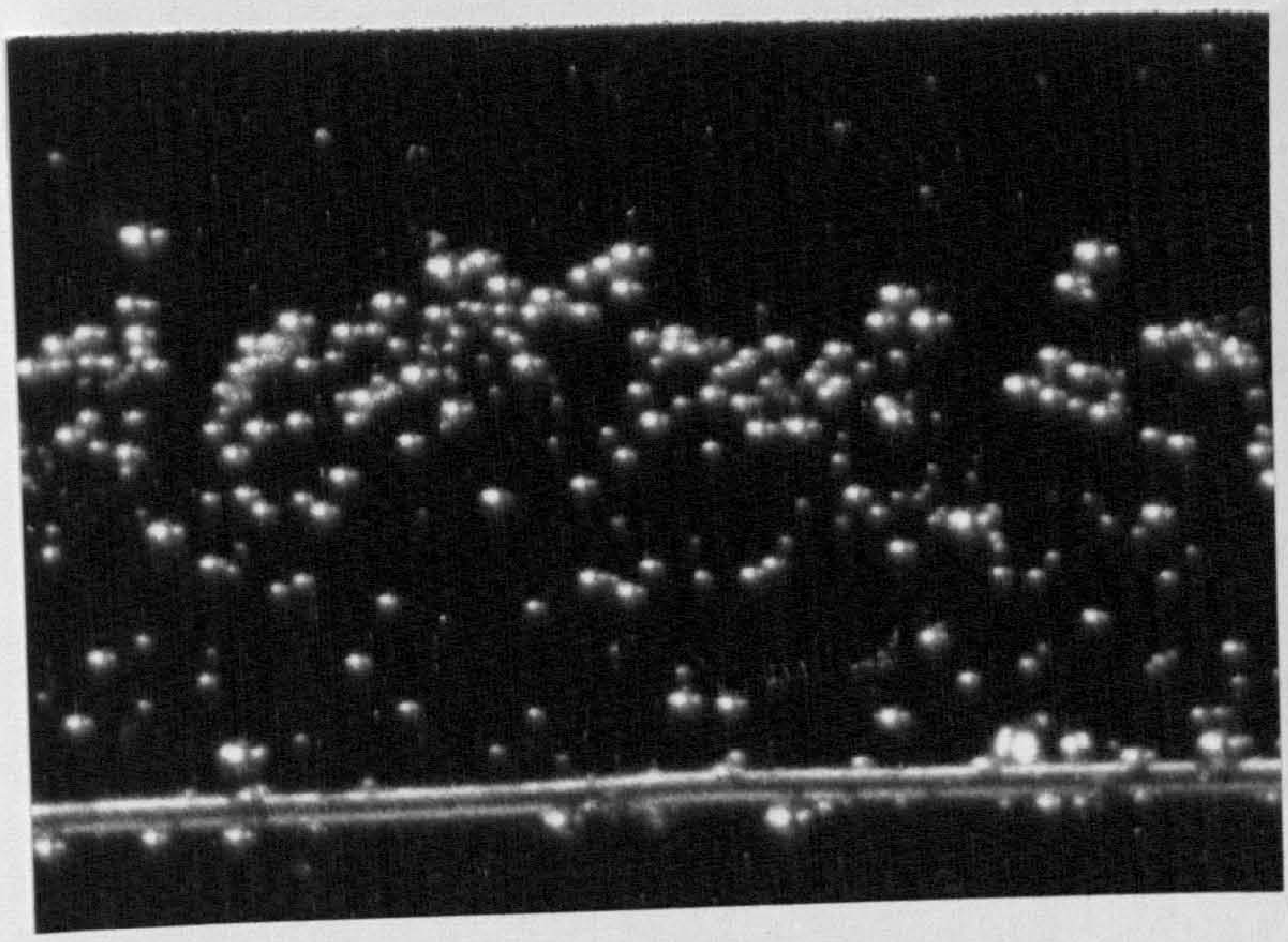

a) 250 V
112 mA
pulse width = 25 mS
frequency = 1 Hz
mag. x48

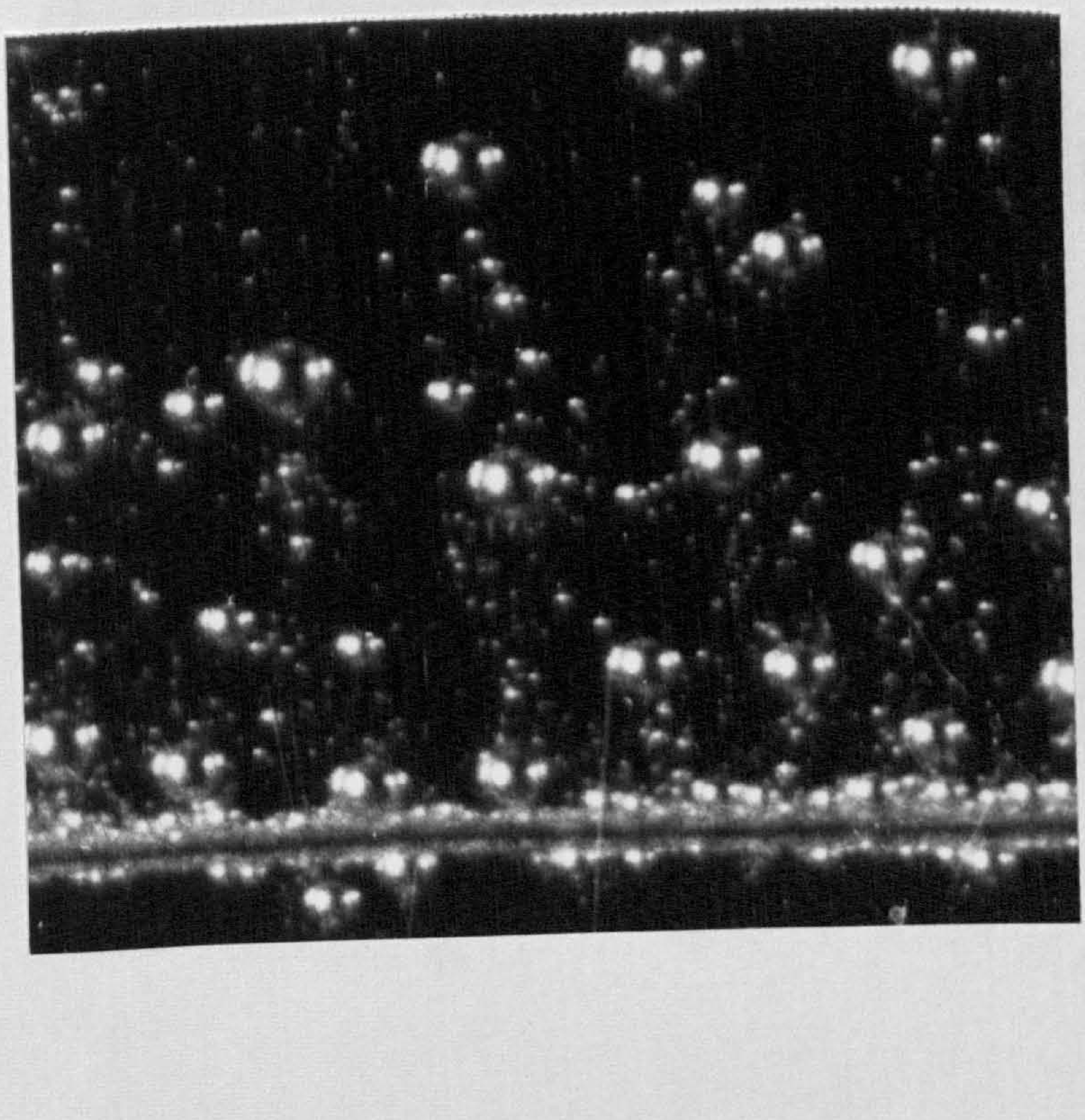

b) 250 V
112 mA
continuous current
mag x48

EFFECT OF PULSE WIDTH ON THE SIZE OF HYDROGEN BUBBLES GENERATED IN STILL WATER BY A 50 μm DIAMETER STAINLESS STEEL WIRE

FIG. 3.21

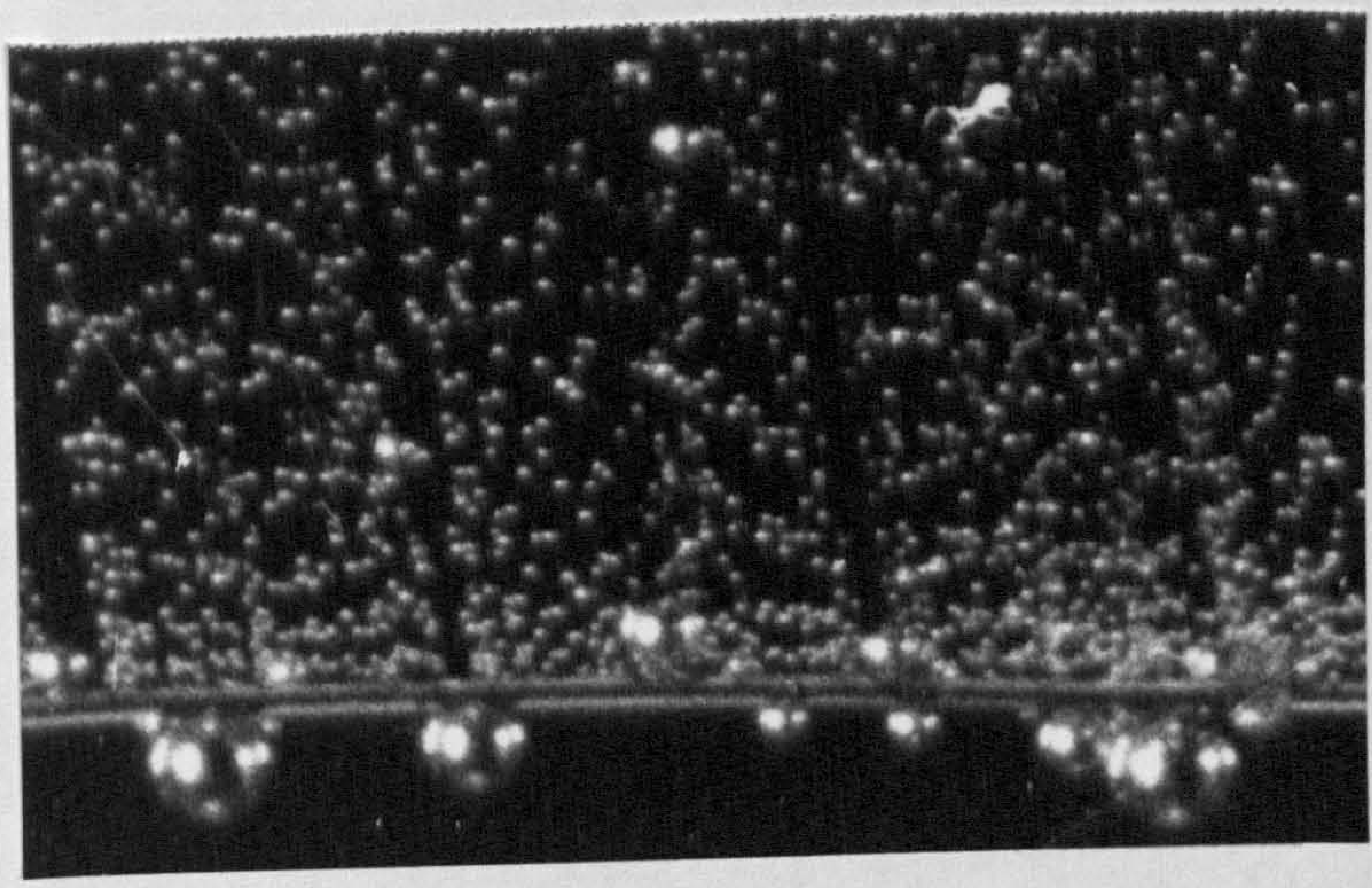

a) 250 V
112 mA
pulse width = 2·8 mS
frequency = 11·3 Hz
mag. x48

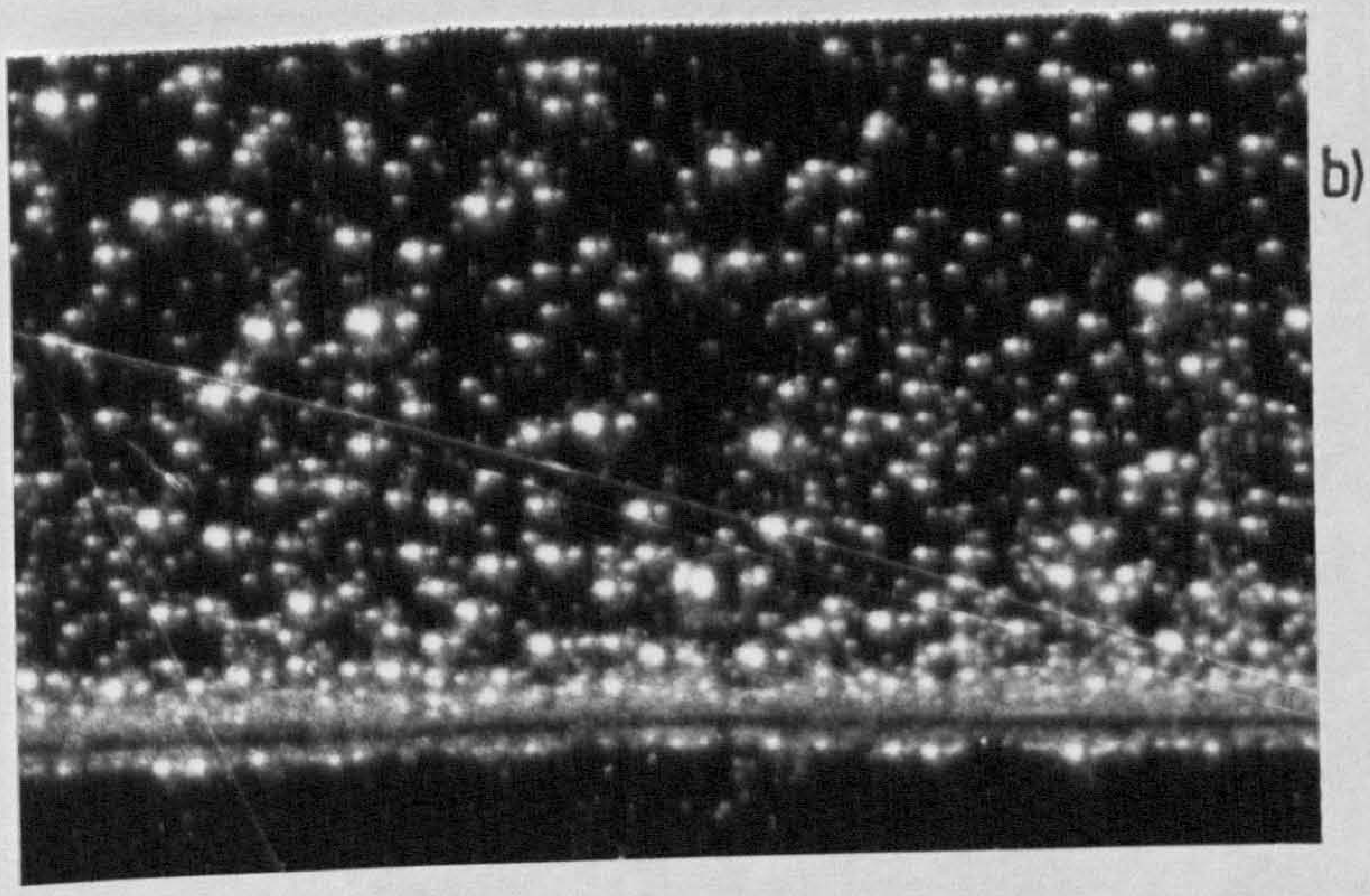

b) 250 V
112 mA
pulse width = 2·8 mS
frequency = 178 Hz
mag. x48

EFFECT OF FREQUENCY ON THE SIZE OF HYDROGEN BUBBLES GENERATED IN STILL WATER BY A 50 µm DIAMETER STAINLESS STEEL WIRE

FIG. 3. 22

water flow rate /(10^{-4} m^3/s)	exit vel. /(m/s)	head of water /(mm)	theor. exit vel. /(m/s)	observed cathode current (mA)					
				freq./(Hz)	cont.	185	164	55.5	26.3
				pulse width /(ms)		2.8	2.8	2.6	2.8
1.29	2.87	440	2.94		24	14	13	6	4
2.49	2.76	445	2.95		24	13	12	6	3
5.15	2.54	425	2.90		35	13	12	6	3

TABLE 3.1 EXPERIMENTAL CONDITIONS FOR THE STILL PHOTOGRAPHY OF FLOWING HYDROGEN BUBBLES

flow rate /(10^{-4} m^3/s)	mean vel. V_w at the wire/(m/s)	mean vel. V_{exit} at the top of 15mm x 15mm exit section /(m/s)	wire dia. /(um)	wire Reynolds No. (Re_w)	Reynolds No. at exit
1.29	0.2	0.6	100	19.9	8937
2.48	0.3	1.2	100	29.8	17875
5.15	0.7	2.9	100	69.5	43198

where $Re_w = v_w \cdot d / \nu$

$Re_{exit} = v_{exit} \cdot D / \nu$

d = wire diameter

D = channel hydraulic diameter

ν = kinematic viscosity of water

TABLE 3.2 FLUID VELOCITIES AND REYNOLDS NUMBERS DURING WORK ON THE PROTOTYPE MODEL

300 V,
24 mA,
continuous current,
exit velocity
= 0 54 m/s

HYDROGEN BUBBLES GENERATED IN TAP WATER FLOWING AT $1{\cdot}29 \times 10^{-4}$ m^3/S

FIG. 3.23

As the frequency of pulsing decreased the visibility of bubbles decreased. Fig. 3.24. shows the effects of pulsing at 55.5 Hz with a low flow rate. At this frequency the pulse width of 2.6 ms meant that the current was on for about 15% of the cycle. Individual bubbles were more identifiable than with a continuous current. The photograph shows no clear indication of the pulsing, probably because the bubbles flow down the wire to the apex from where they were released when the current is off.

Streaklines were only discernable at higher flow rates near the wire, (fig. 3.25), indicating the need for increased electrolyte conductivity.

There were some photographs showing a crossover of two adjacent streaklines, (fig. 3.26). This could be an effect of fluid rotation when bubbles move out of the central plane, since streaklines can not intersect in the same plane in two dimensional flow.

The bubbles that were released from the apexes varied in diameter from 15 µm to 90 µm. This confirms previous reports that, in flowing water, electrolytically generated hydrogen bubbles are approximately half the wire diameter.

3.3 DESIGN OF THE BUBBLE GENERATION SYSTEM

3.3.1 RANDOMLY DISTRIBUTED GAS BUBBLES

Prior to work with electrically generated bubbles both air bubbles and nitrogen bubbles were used in the prototype model. Air bubbles were injected into the feeder box by simply squirting water with a consequent air entrainment.

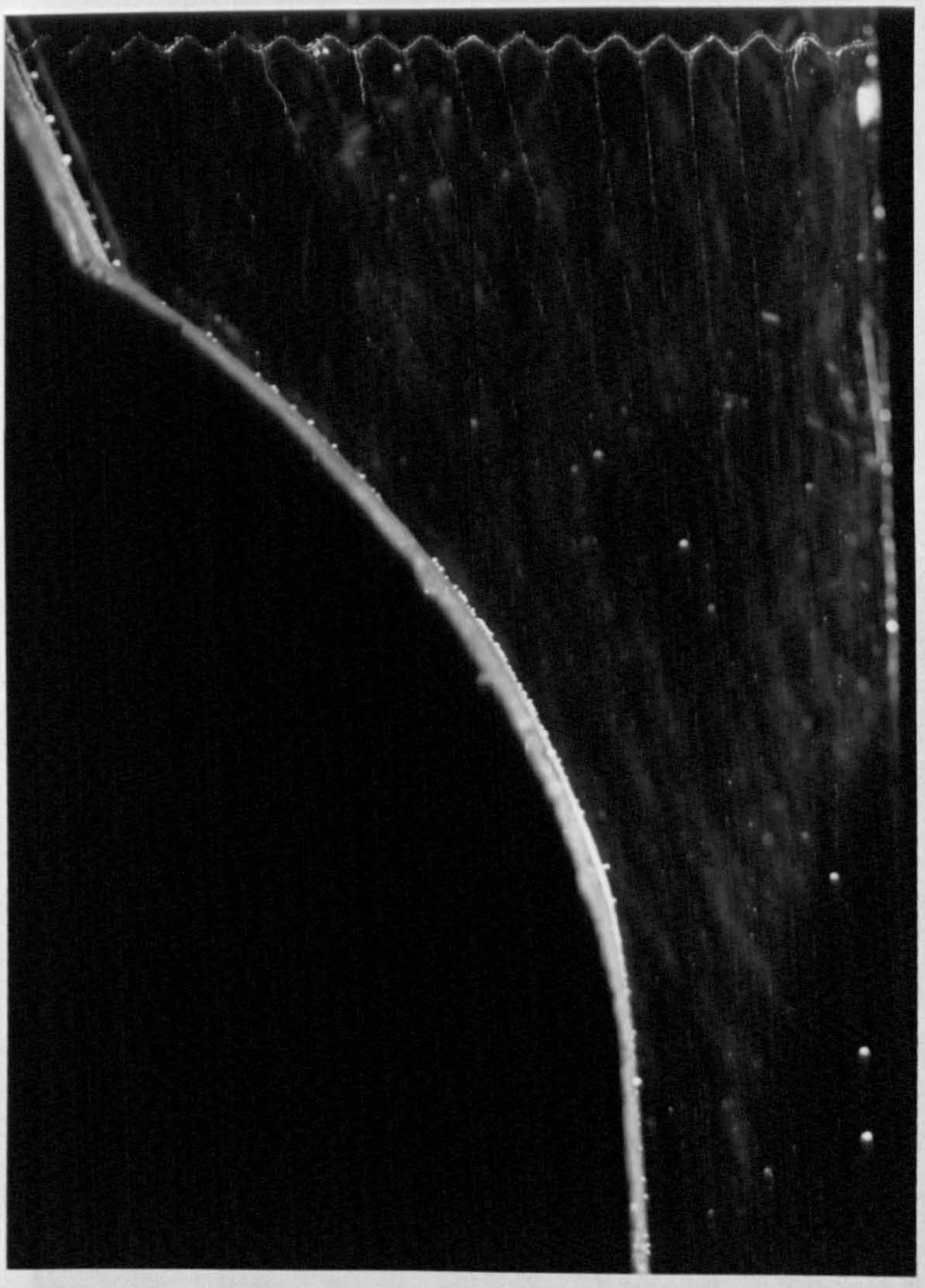

300 V
6 mA
pulse width = 2·6 mS
frequency = 55·5 Hz
exit velocity
= 0·54 m/s

HYDROGEN BUBBLES GENERATED IN TAP WATER FLOWING AT $1{\cdot}29 \times 10^{-4}$ m^3/s WITH LOW FREQUENCY CURRENT

FIG. 3.24

300 V
13 mA
pulse width = 2·8 mS
frequency = 185 Hz
exit velocity
= 2·14 m/s

HYDROGEN BUBBLES GENERATED IN TAP WATER FLOWING AT $5{\cdot}15 \times 10^{-4}$ m^3/s, BEING ONLY DISCERNIBLE NEAR THE WIRE

FIG. 3. 25

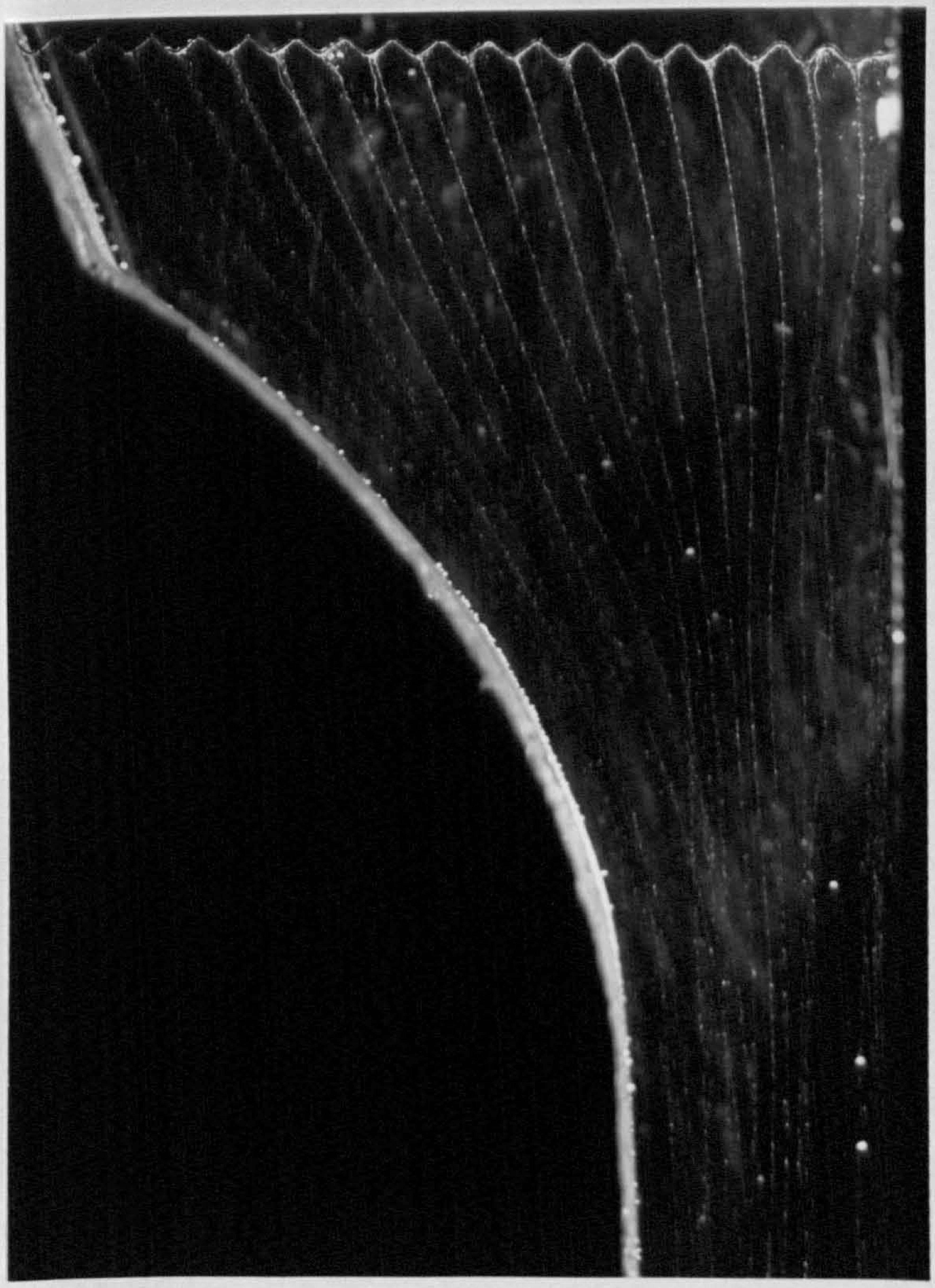

300 V
13 mA
pulse width = 2 8 mS
frequency = 164 Hz
exit velocity
= 0 54 m/s

CROSSOVER OF BUBBLE STREAKLINES INDICATING ROTATION OF THE FLOWING WATER

FIG 3.26

The quantity of bubbles produced was, however, very small. A better method was to inject nitrogen from a pressurised cylinder. The nitrogen flow could easily be controlled to produce a given quantity of bubbles. The turbulence in the feeder box and entry ports ensured the bubbles were relatively small (< 1000 µm diameter). The lighting system was designed by studying the nitrogen bubbles.

This method of introducing gas bubbles had the disadvantage that it introduced bubbles onto more than one plane of the model thickness. Furthermore, bubbles were not generated from a single controlled position.

3.3.2 INJECTED AIR BUBBLES

One system studied to produce bubbles from a known position was a thin capilliary tube connected to a syringe. The tube was 0.711 mm outside diameter and 0.508 mm inside diameter. Bubbles of approximately 1000 µm diameter were produced.

The tube was coiled to a diameter equal to the internal thickness of the model. This did not completely prevent the movement of the tube tip but some information was gained of the flow visualisation, and movement of bubbles to the nozzle surface as seen in fig. 3.27.

3.3.3 ELECTROLYTIC GENERATION OF BUBBLES

The electrical supply to the final model was the same as that used in the experiments with still water. However, the current was supplied through a Claude Lyons pulse generator. This had a range of freqencies from 1 Hz to 10 MHz, and a

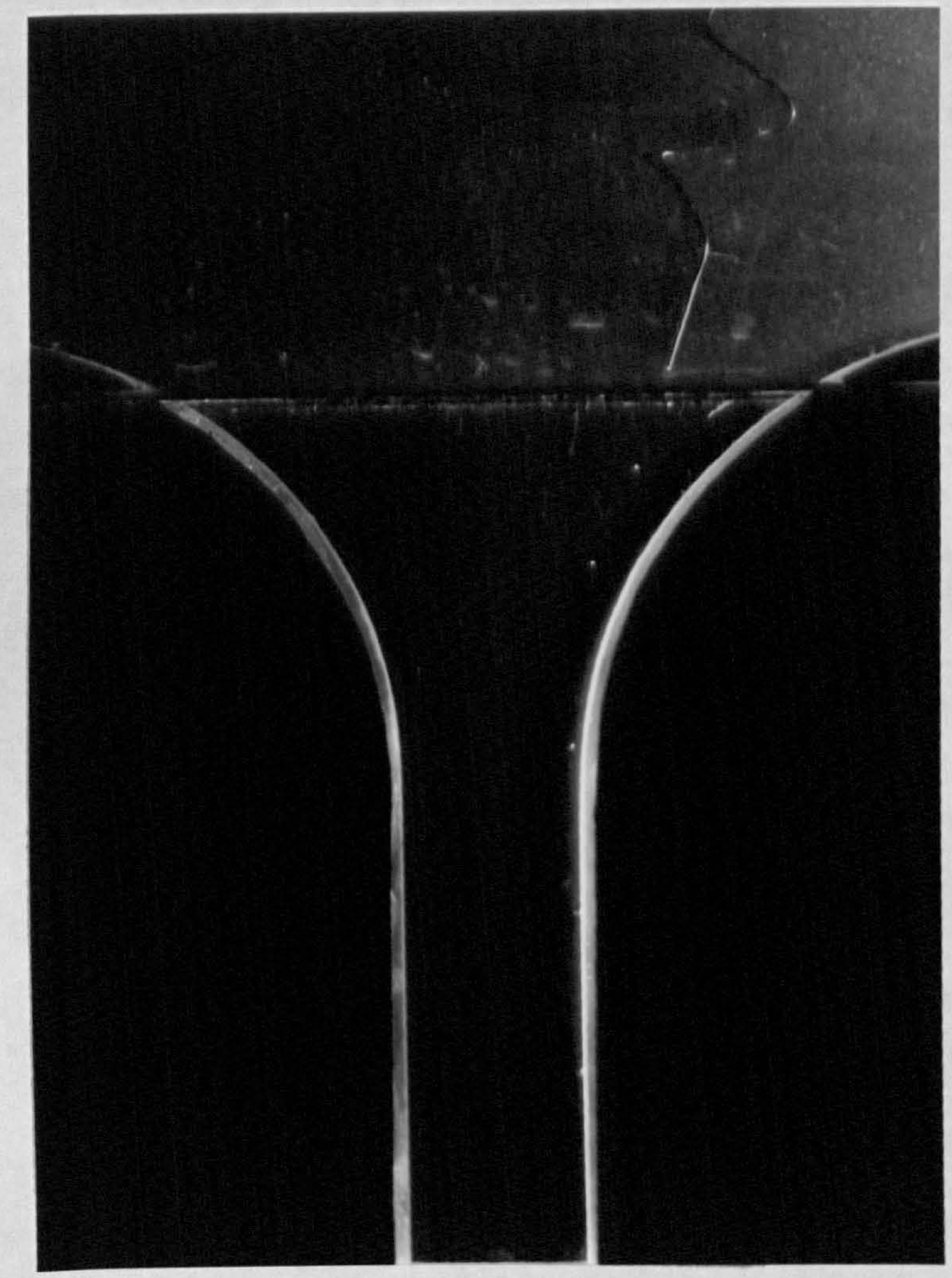

flow speed
= $9{\cdot}09 \times 10^{-4}\,m^3/s$
exit velocity
= 3·8 m/s

AIR BUBBLES FORMED FROM A CAPILLIARY TUBE SHOWING BUBBLES MOVING TOWARDS, AND HITTING THE NOZZLE SURFACE

FIG. 3.27

range of pulse widths from 0.03 µS to 20 mS. The frequency and pulse widths could be varied independently.

3.3.3.1 WIRE MATERIAL

Since platinum was the most popular material used in previous work, this was used initially on trials with still water. Platinum, however, is an expensive metal and is only readily available in diameters of 200 µm and 500 µm. Other sizes could be obtained but at even greater expense. Stainless steel was therefore chosen for more extensive tests, this being available in the annealed and hardened condition in sizes from 50 µm upwards.

3.3.3.2 WIRE CONFIGURATIONS

The form of the cathode used in all the previous work was either straight, (insulated in parts or not), or kinked to produce a line of bubbles from a specific starting point. These forms were used successfully in the prototype model. To study the movement of bubbles through the whole flow field in the final model, bubbles had to be generated in a semi-circular arc of radius 190 mm, corresponding to the assumed start of curved flow. Different configurations were used with varying degrees of success. Every form used a 750 µm diameter stainless steel wire in the 190 mm entry arc as a support for the particular cathode wires.

3.3.3.2.1 KINKED WIRE

To produce the kinked wire a standard bolt or a specially machined brass thread was used to make an impression in thermoplastic. Soft cathode wire was then pressed between the metal thread and the cooled hard plastic impression, (fig. 3.28a). An attempt was made to use wire coiled round a thin metal rod, (fig. 3.28b). This, however, generated bubbles outside the central plane of the wire and from two position on the wire apex.

In the final model the necessary position of the cathode made it impossible to use a kinked wire in lengths greater than about 10 mm. Work in the final model was therefore confined to the use of straight wire.

3.3.3.2.2 STRAIGHT WIRE

At first a ladder type cathode was used with an additional support wire, (fig. 3.29.). The rungs of the ladder were soldered to the supports. All parts, except the central portion of the rungs, were insulated. The problem with this set-up was the difficulty it caused when inserting the nozzle assembly into the tundish without scratching the insulation off the wire, particularly at the soldered joints. To overcome this problem the second support wire was removed and the experimental cathode wire was bent then soldered to the support wire in two positions. This assembly was easier to insert into the tundish. More important, however, the wire could be insulated in one of two ways; first, with the uninsulated section parallel to the viewing direction for observing streamlines, as in fig. 3.30a, or second, perpendicular to the viewing direction, (fig. 3.30.b), so that planes of bubbles could be seen and their sizes measured.

A simplified version of the straight wire is shown in

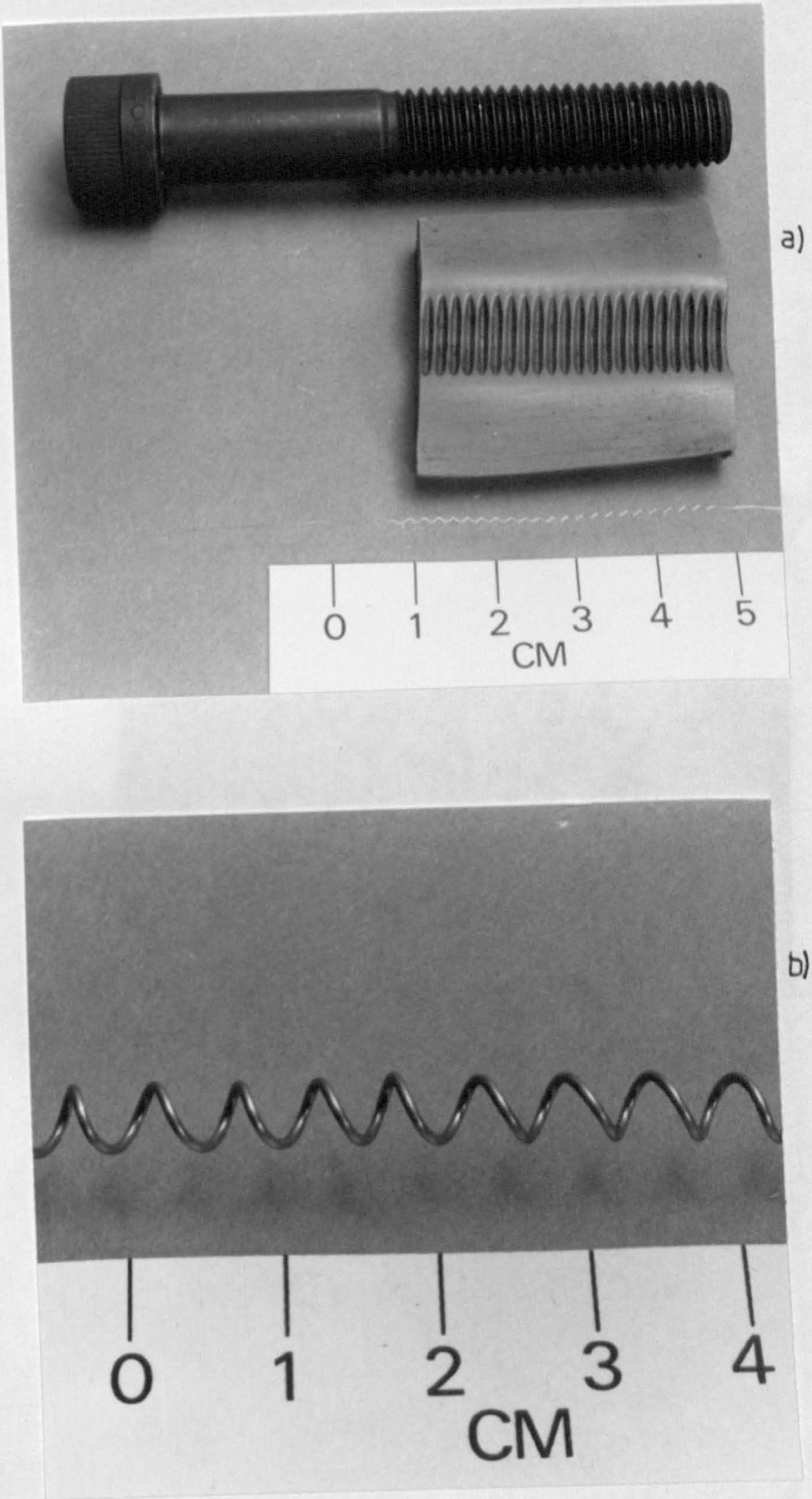

a) pressing of wire between bolt thread and moulding

b) wire formed by coiling round a thin shaft

TWO METHODS OF PRODUCING KINKED WIRE FOR THE CATHODE

FIG. 3.28

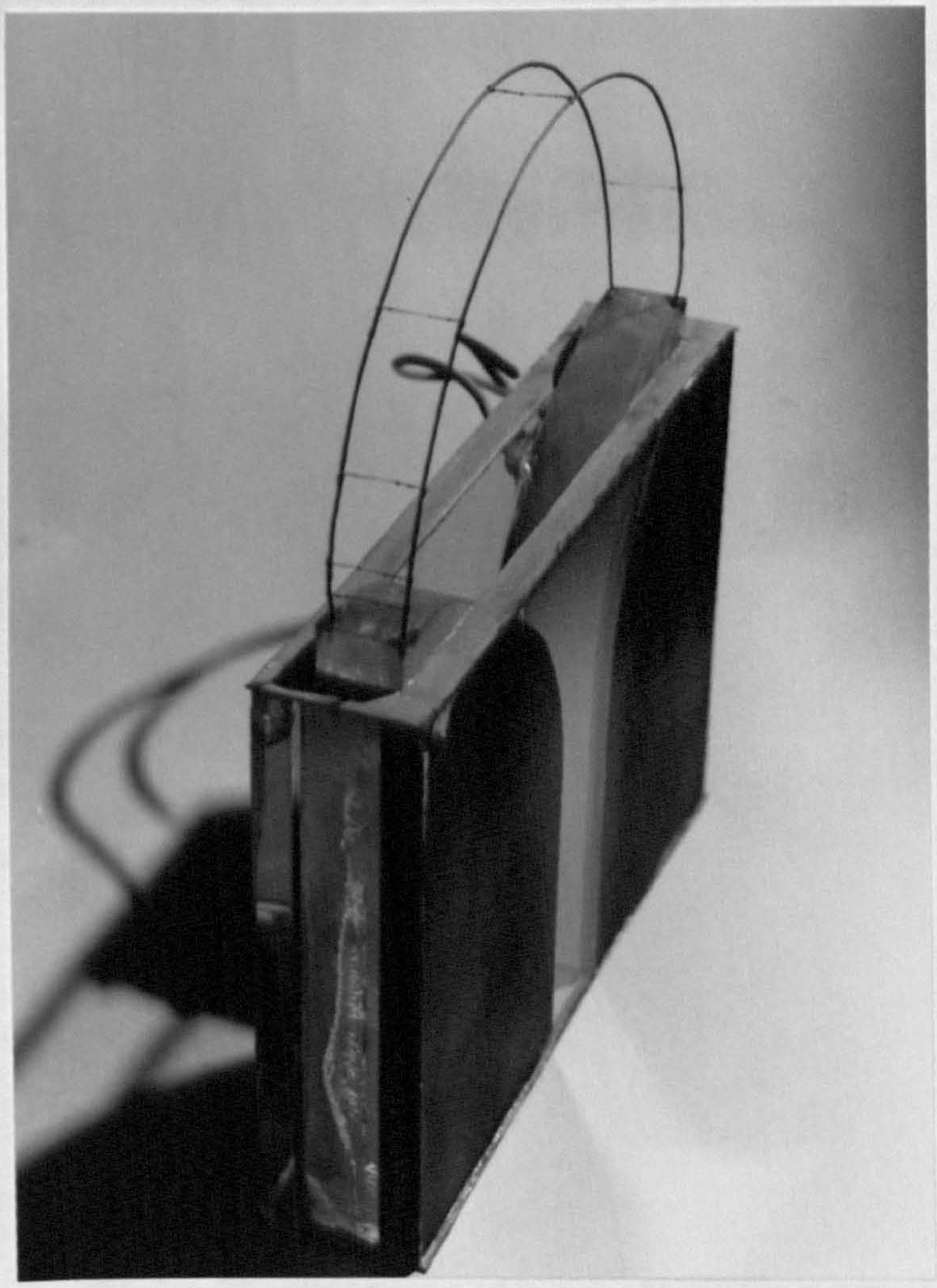

LADDER TYPE CATHODE

FIG. 3.29

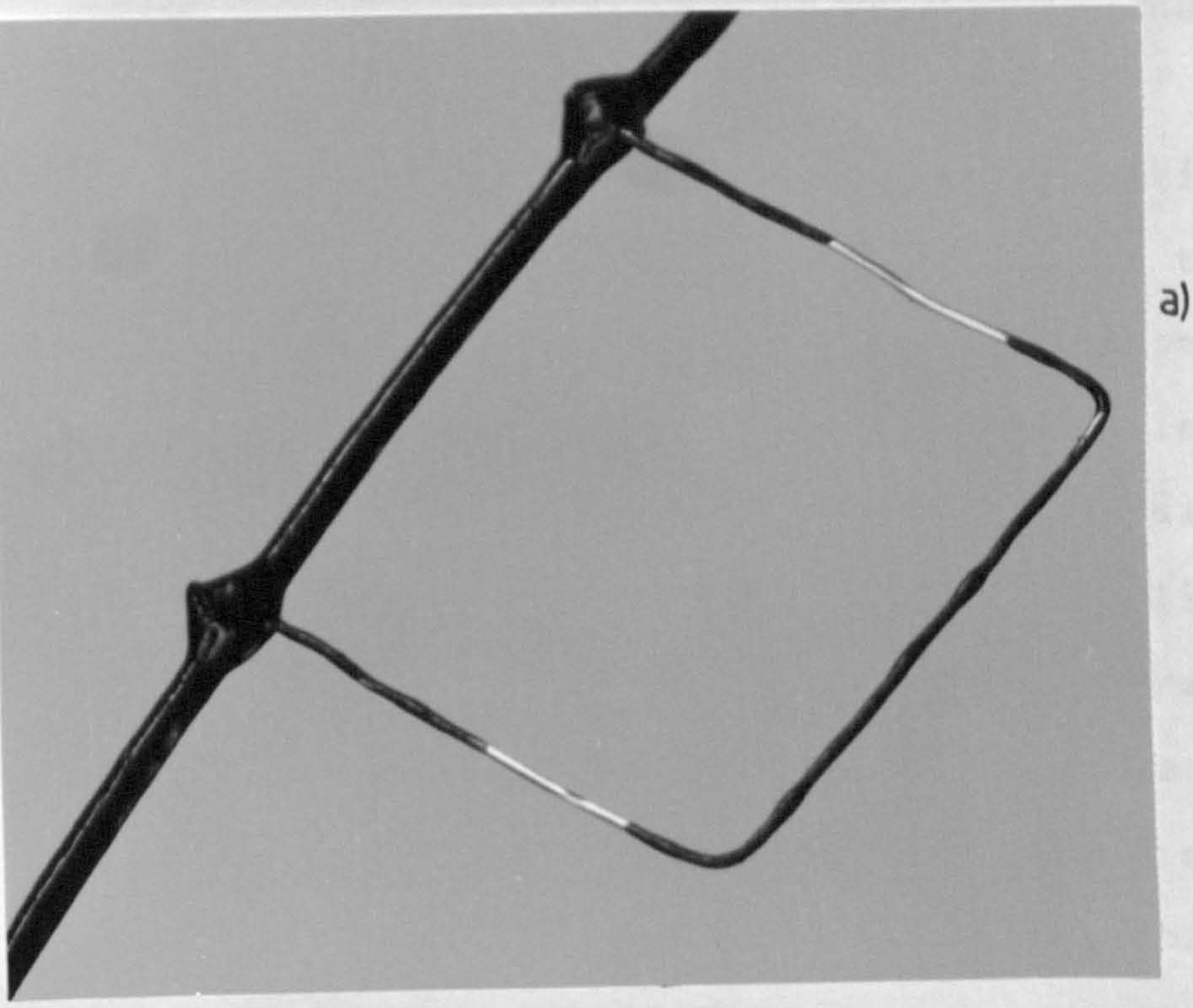

a) parallel to the camera axis

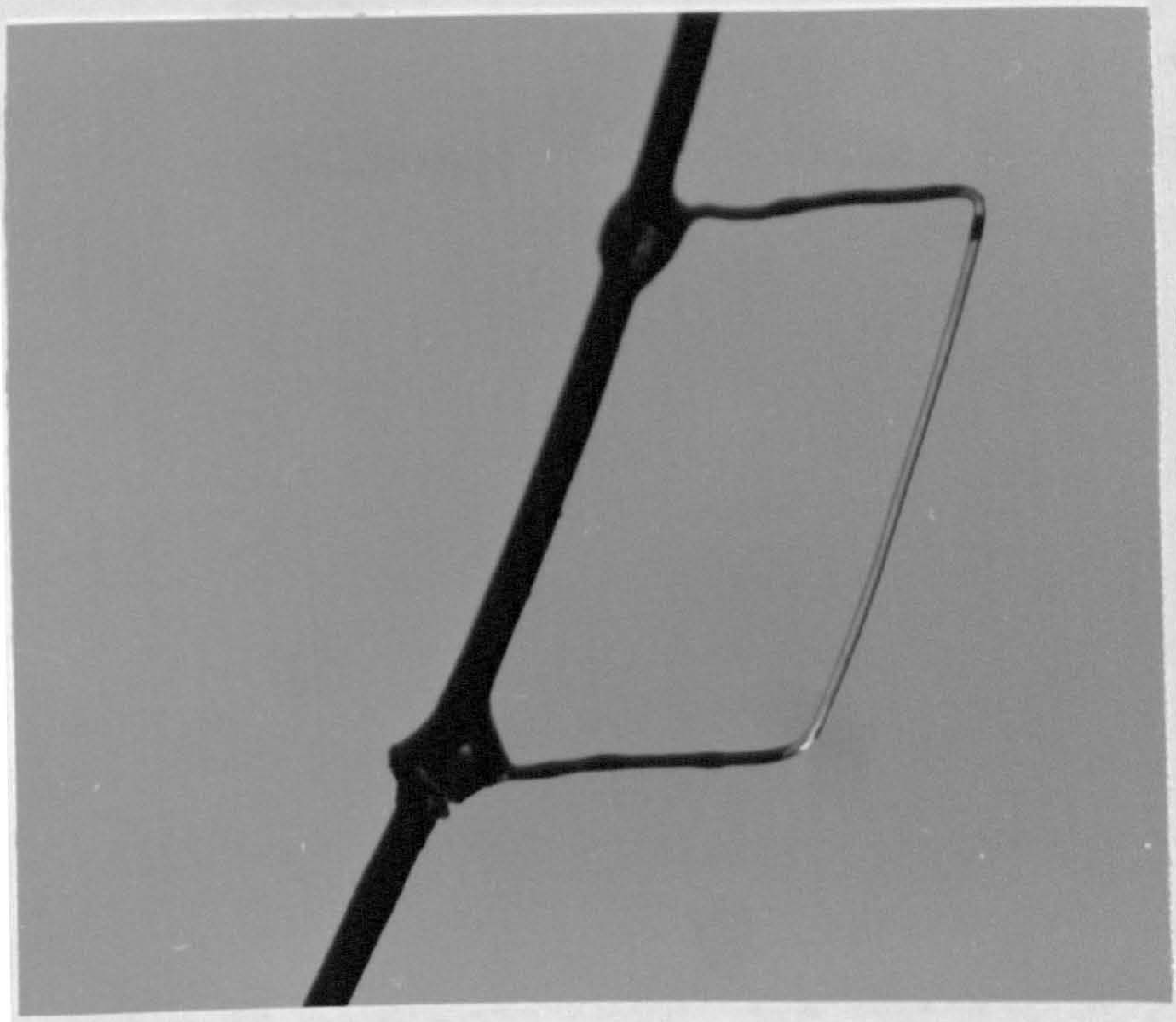

b) normal to the camera axis

TWO USES OF A STRAIGHT CATHODE WIRE PLACED NORMAL TO THE WATER FLOW DIRECTION

FIG. 3.30

fig. 3.31a. This is uninsulated in the section parallel to the water flow direction. In this, as with the other forms of straight wire, the bubbles produced are removed from the wire by the hydrodynamic forces of the flowing water, giving limited opportunity for growth above a certain size. A successful method of overcoming this limitation was to insulate all parts except the tip of the wire, as seen in (fig. 3.31b). The bubbles produced at the tip are protected from the flowing water and are able to grow. Bubbles as large as 1 mm were obtained by this method.

3.4. PHOTOGRAPHIC TECHNIQUES

Photography was an integral part of the experimental procedure. It was only by examining photographs that the following crucial results could be obtained:-

a) sizes of tracer particles,

b) radial movement of tracer particles through the nozzle,

c) velocity of tracer particles through the nozzle and therefore of the fluid velocity.

Many of the details of the camera settings and procedures used were influenced by local conditions such as external lighting and reflections from other equipment. Also the positioning of of the equipment was restricted by the size and layout of the room.

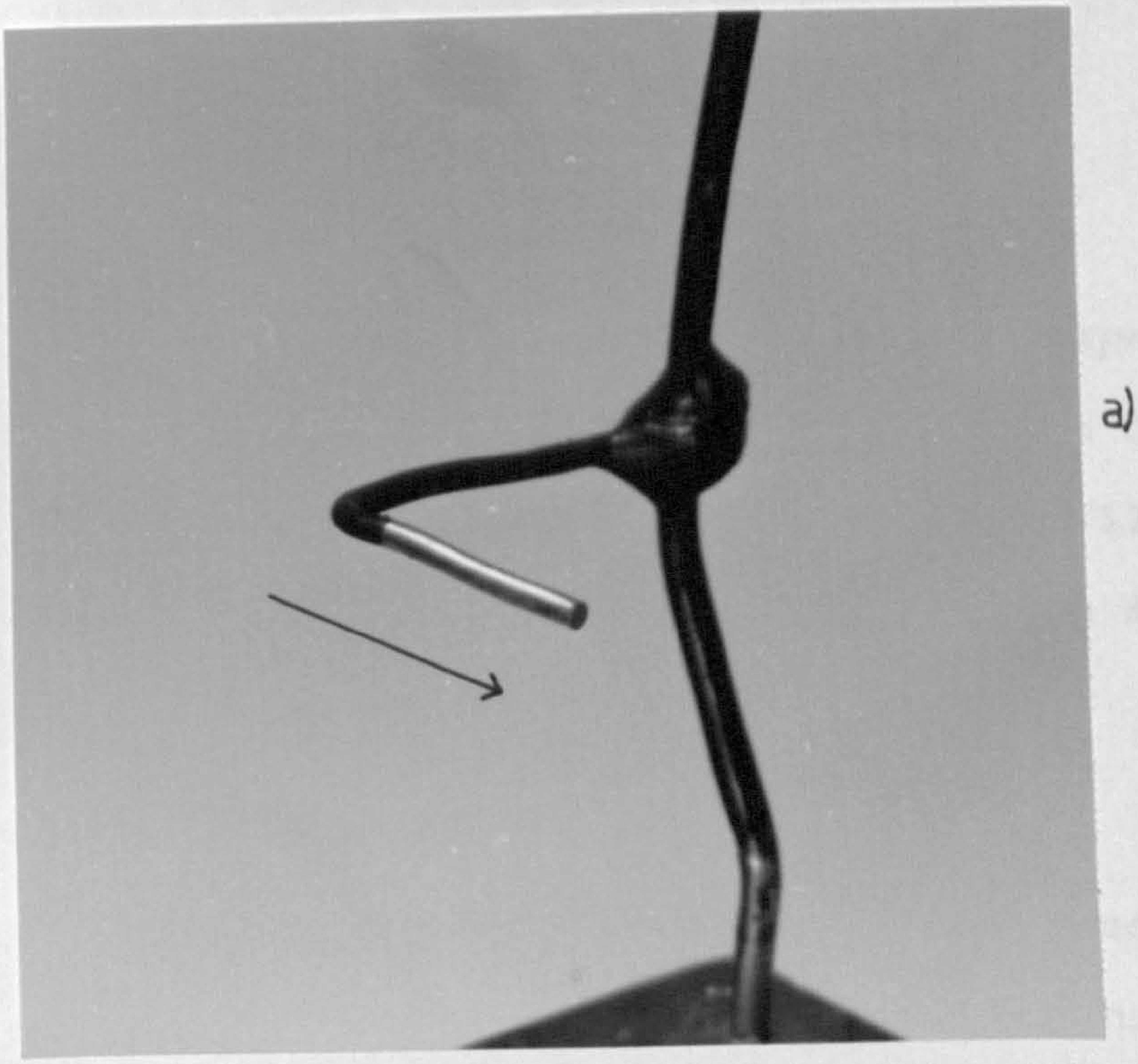

a) uninsulated, to produce a stream of fine bubbles

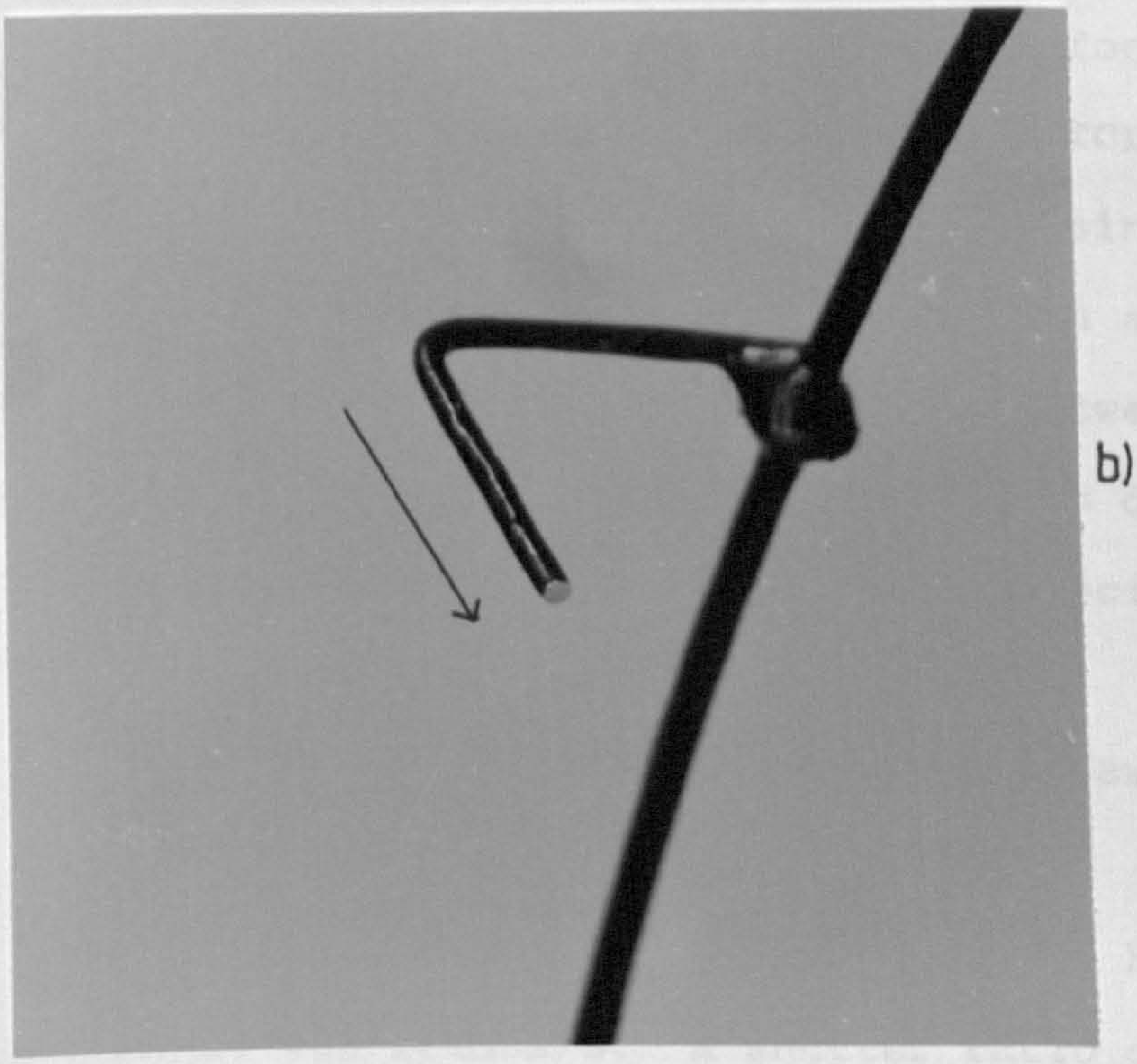

b) uninsulated only at the tip, to produce larger bubbles

SINGLE WIRE CATHODE PARALLEL TO THE WATER FLOW DIRECTION

FIG. 3.31

3.4.1 THE CAMERAS FOR STILL PHOTOGRAPHY

3.4.1.1 FULL NOZZLE VIEWS

When photographing the full experimental nozzle or general views of the apparatus a Bronica GS1 camera was used. This had a 6 cm x 7 cm format on a 120 film. A 110 mm focal length macro lens was fitted which had a maximum opening of f4.

3.4.1.2 CLOSE-UPS

A Nikon F3 35 mm camera was used for close-up photography of tracer particles. The lens used was 135 mm fitted with a bellows extension to achieve the highest magnification consistent with accurate focussing.

3.4.1.3 PHOTOGRAPHY OF ISO-DENSITY PARTICLES

For examination of flow patterns using iso-density particles the 35 mm camera was used with a 55 mm lens. Repeated exposures at shutter speeds between 1/30 and 1/125 s were taken to ensure that there was good discrimination of adjacent areas with different local velocities.

3.4.2 CINE CAMERAS

The film chosen was 16 mm and two cameras of different film speeds were tried during the work.

a) The faster camera was a Hadland Hy-Speed that ran at a nominal 400 frames/s. A shutter ratio of 1 : 2.5 gave an exposure per frame of approximately 1/1000 s. A 55 mm focal length f5.6 lens was fitted. A timing light from a L.E.D. produced 100 pulses/s which at 400 frames/s would give one pulse every 4 frames. Examining the timer marks showed that the film accelerated to 400 frames/s in less than 20 frames. Therefore no results were taken from the first 20 or the last 20 frames of a particular run in the cine film.

b) A Bolex H16 camera ran at a nominal speed of 64 frames/s. The lens fitted was a 25 mm f1.4. The nominal for each frame was 1/540 s. Pulses from an L.E.D. therefore gave one pulse every 6 frames. With this camera the final film speed was achieved almost insantaneously. A photograph of the cine camera and the 35 mm camera in position is shown in fig. 3.32.

3.4.3 LIGHTING

The continuous lighting needed for the cine photography was provided by two 650 W quartz-halogen lamps. These were also used when shutter controlled exposures were taken with either of the still cameras.

Flash-lights were used with the 35 mm camara for close-up photography of tracer particles. A Metz Mecablitz 60 CT was the main unit. Accompanying this was a Metz Mecatwin 60/40. These operated by computer control of the exposure at a given camera aperture setting. The minimum possible flash duration was approximately 1/25,000 s. The camera shutter speed setting was then irrelevent.

3.4.4 MICROFLASH PHOTOGRAPHY

After many photographs with the 35 mm camera with both high shutter speeds and flash control, the most reliable method of measuring the particle sizes was found to be the use of a high a speed microflash. This was a Pulse Argon Jet

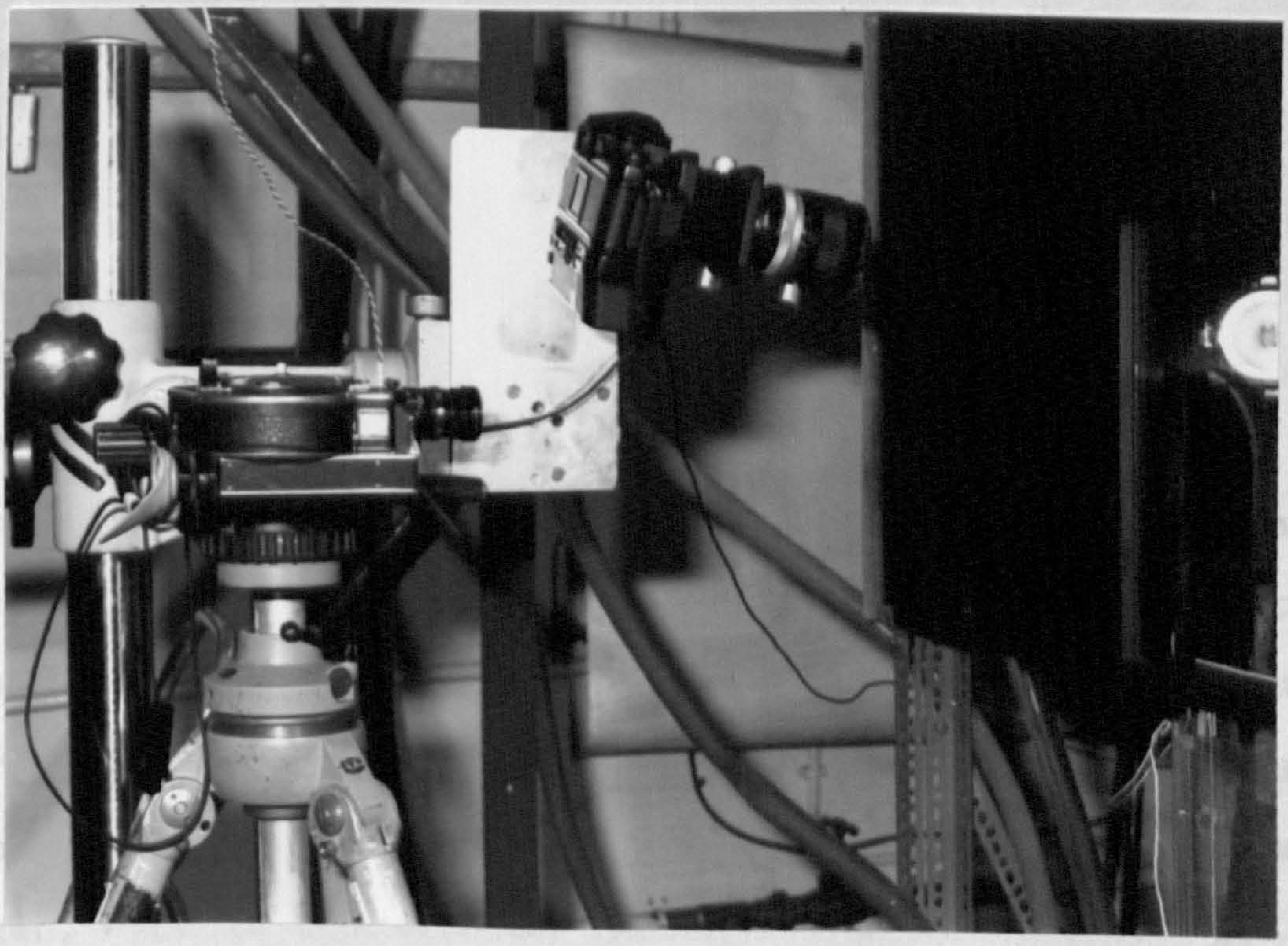

POSITION OF THE CINE CAMERA AND 35 mm CAMERA AT THE FRONT OF THE MODEL

FIG. 3.32

which gave a flash of approximately 0.3 s duration at a 2.5 J output, (fig. 3.33). A spark discharge from a 10 mm source was focused through a 180 mm focal length condenser lens on to the lens apperture of the 35 mm camera. The result was a sharp black circular image on a white background, (fig. 3.34)

There was insufficient space to carry out photographs with the microflash during a cine run because the microflash at the rear would have been in view of the cine film. To obtain representative photographs of hydrogen bubbles in the cine film, the filming was not begun until bubbles were being generated in a predictable manner. A black card was placed between the model and the microfash but not interfering with the rear lighting. After the cine run the black card was quickly removed and a series of microflash photographs were taken. A note was made of any observable changes in bubble size or of the rate of bubble production during the switch from cine to microflash. Results were rejected if changes occurred. Any future experiments carried out on the model should, however, attempt to modify the experimental layout so that the microflash could be used during the cine run. The light from the microflash would be seen on a single frame of the cine film, when it might be possible to identify individual bubbles, of which the size is accurately known. Then, even if the size of generated bubble varies, significant results can be obtained.

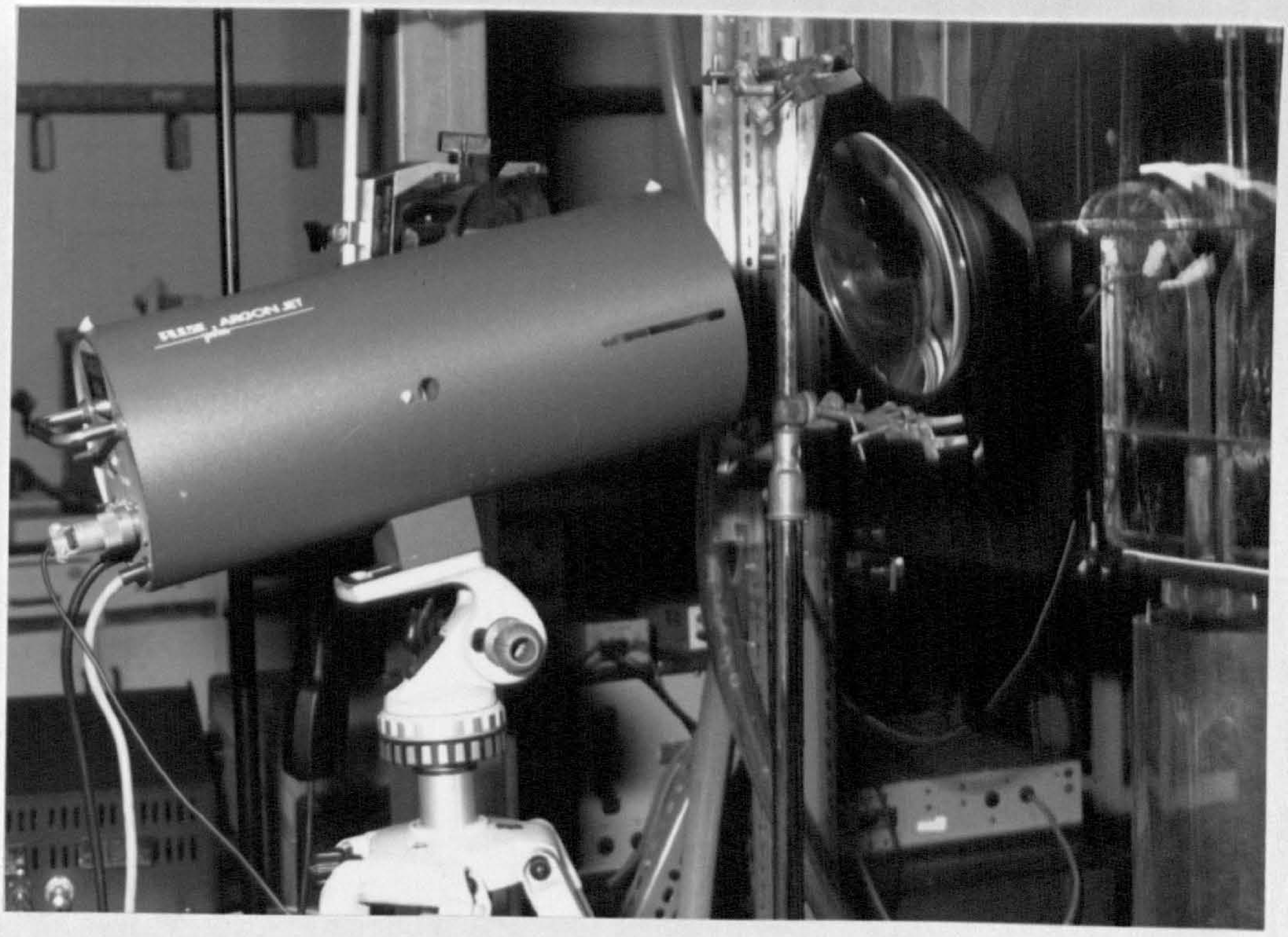

THE MICROFLASH UNIT WITH THE CONDENSER LENS AT THE REAR OF THE MODEL

FIG. 3.33

QUALITY OF PRINTS PRODUCED BY MICROFLASH

FIG. 3.34

3.4.5 POSITIONING OF THE CAMERAS AND LIGHTS

Although previous work suggested that rear lighting at an incident angle of 65° was best. This was generally provided by a parallel beam illuminating a particular part of the flow. In the present experiments an area of approximately 350 mm x 250 mm was being illuminated. With the light from the standard 650 W lamps there was little difference in the observation characteristics of the gas bubbles when using camera angles of between 30° and 60°. It was found that rear illumination at 45° was satisfactory for gas bubbles and for other tracer particles.

Fig. 3.35 shows a diagram of the photographic arrangement using two rear lights. Occasionally a third was used at an angle of 45° from above the model at the rear to show better the shape of larger gas bubbles. All the lights were mounted on a fixed bar at the rear of the model so that when moved they could be easily returned to the original position. The photograph in fig. 3.36 shows the final photographic set-up in relation to the electrical equipment.

3.4.6 PROJECTOR

To examine the cine films a Lafayette projector was used. A frame adjust mechanism allowed single frame movement for frame by frame examination, or continuous movement at 2,4,8, or 16 frames/s, all in either forward or reverse mode. Initial work was carried out by projecting the image on to a screen on the wall to give an image magnified to x 4.3. However, it was more convenient to reflect the image on to a horizontal surface, adjusting accurately to the given nozzle

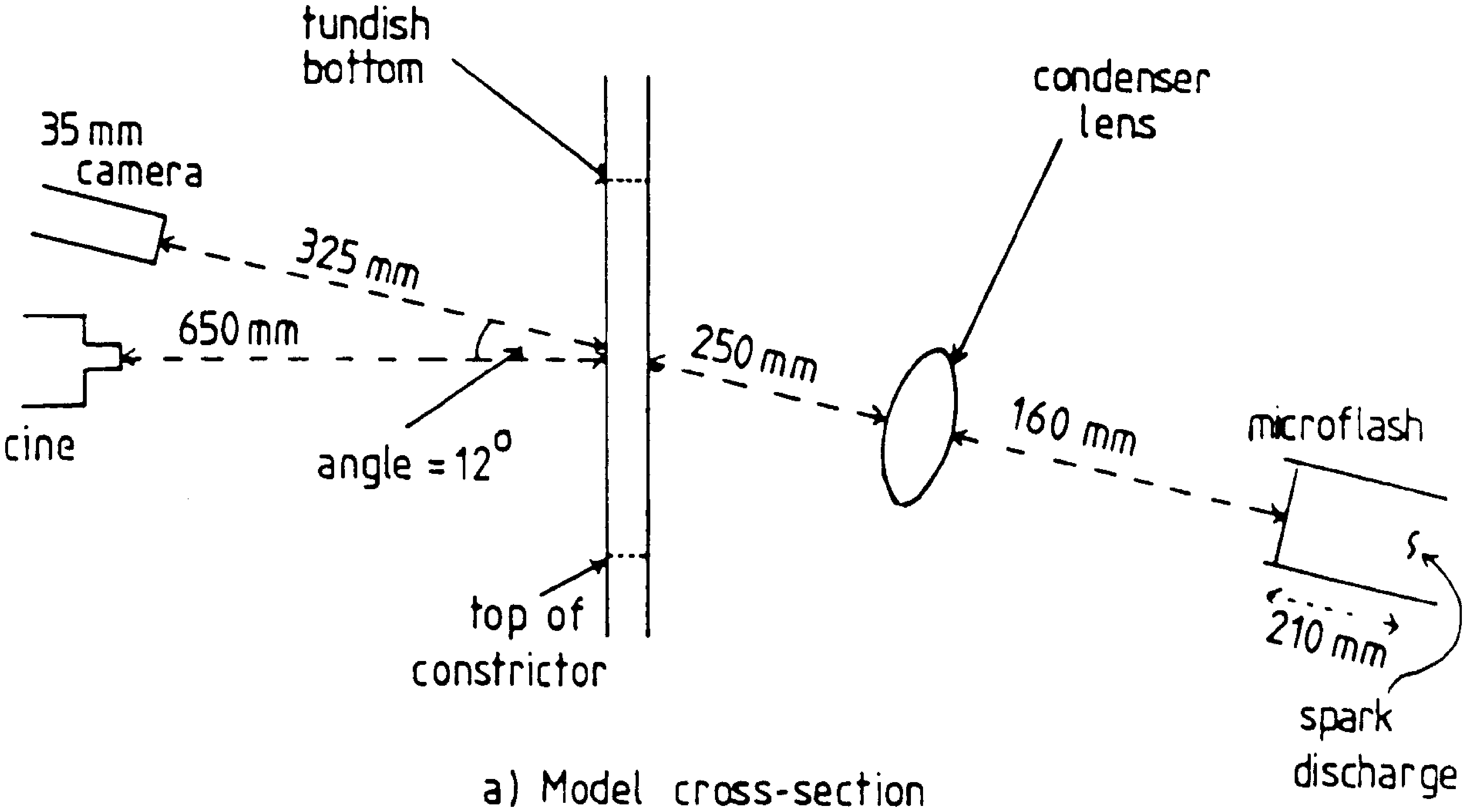

a) Model cross-section

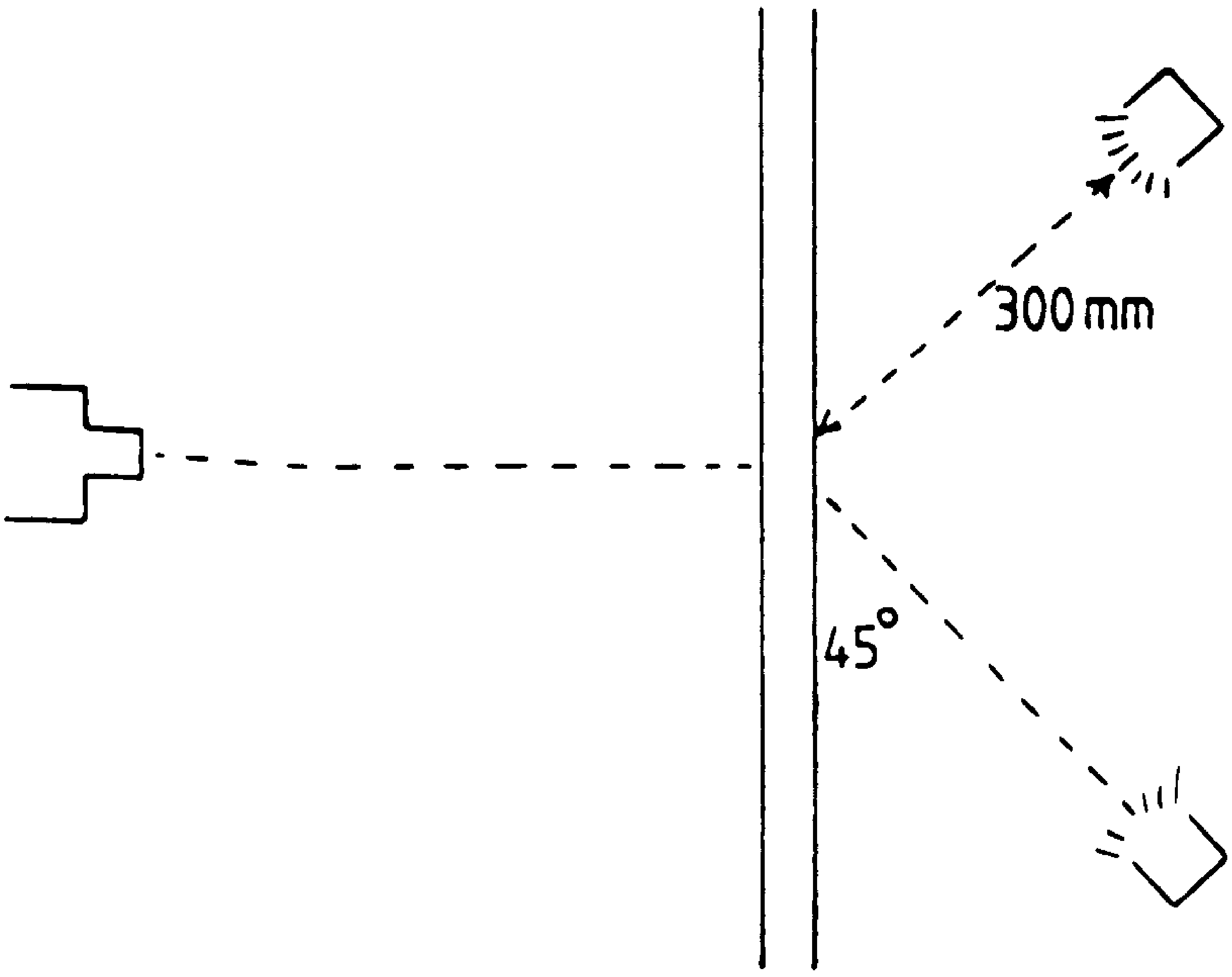

b) Plan of the lighting

THE ARRANGEMENT FOR CINE AND MICROFLASH PHOTOGRAPHY

FIG. 3. 35

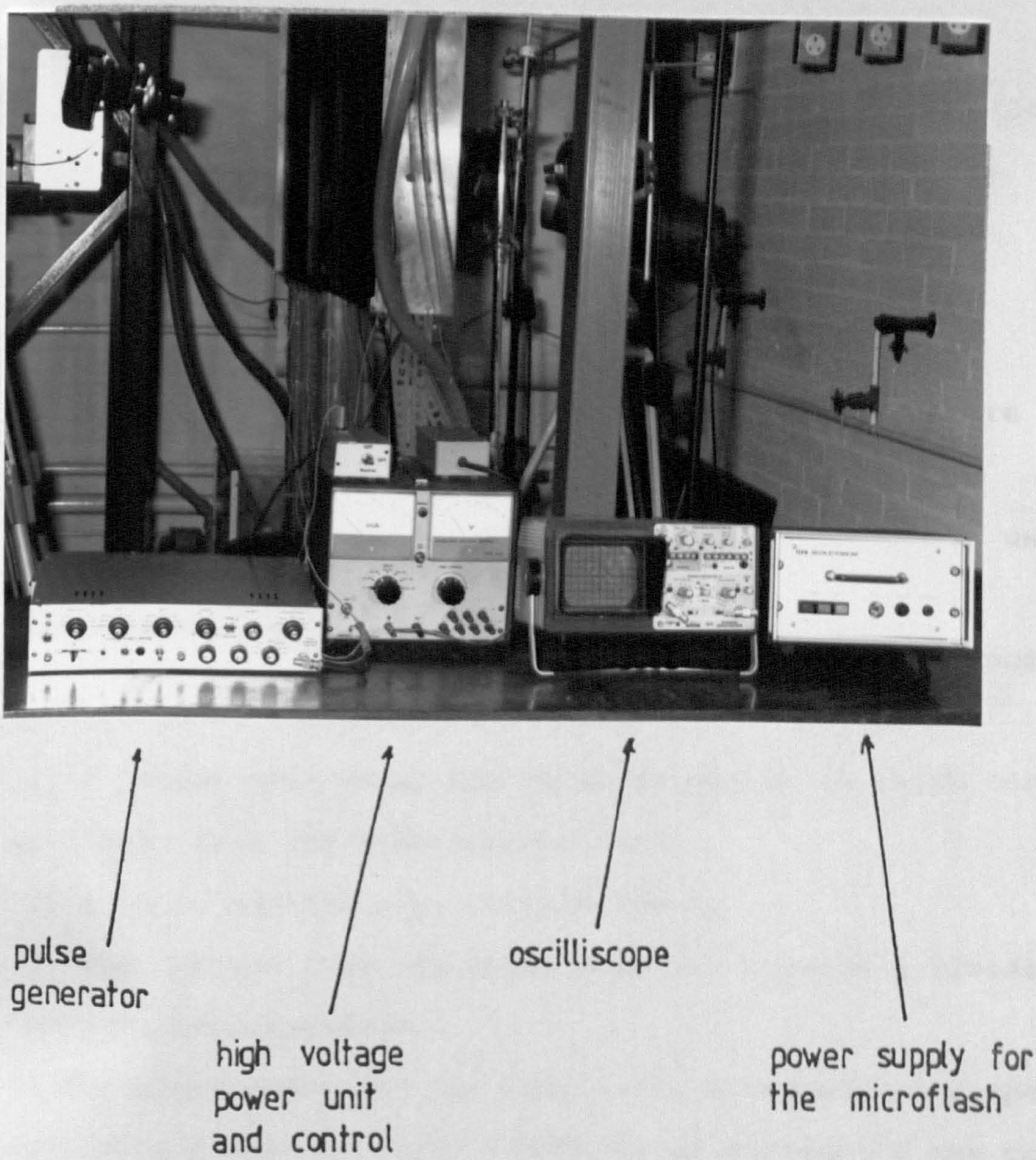

THE FINAL LAYOUT OF THE MODEL

FIG. 3.36

surface profile without magnification, (fig. 3.37). Flow paths were then traced directly on to a drawing of the nozzle.

3.5. SAFETY

Because of the high d.c. voltages (up to 350 V), stringent safety precautions and operating methods were incorporated into the experimental design. The box experiment for generating hydrogen in still water was used to develop the most suitable procedures.

All the safety devices that were necessary are indicated in fig. 3.10. In detail these are:-

1) A copper tray under the model to act as an earth for any spillages from the electrolysis tank.

2) a fully earthed high voltage supply.

3) The current from the mains supplied through a residual-current-curcuit-breaker.

4) A perspex cover for the model with a magnetically operated switch to allow the rapid discharge of current if the cover is lifted with the current still on.

The temporary nature of the prototype model meant that safety precautions could not be met with the rigour required in the final model. All sections containing water were earthed, however, and particular care was taken during the experiments that no-one touched any part of the model.

In the final model, the same principles were applied with the following modifications:-

1) Since the model could not be completely contained, earthing in the event of spillage was supplied by two copper

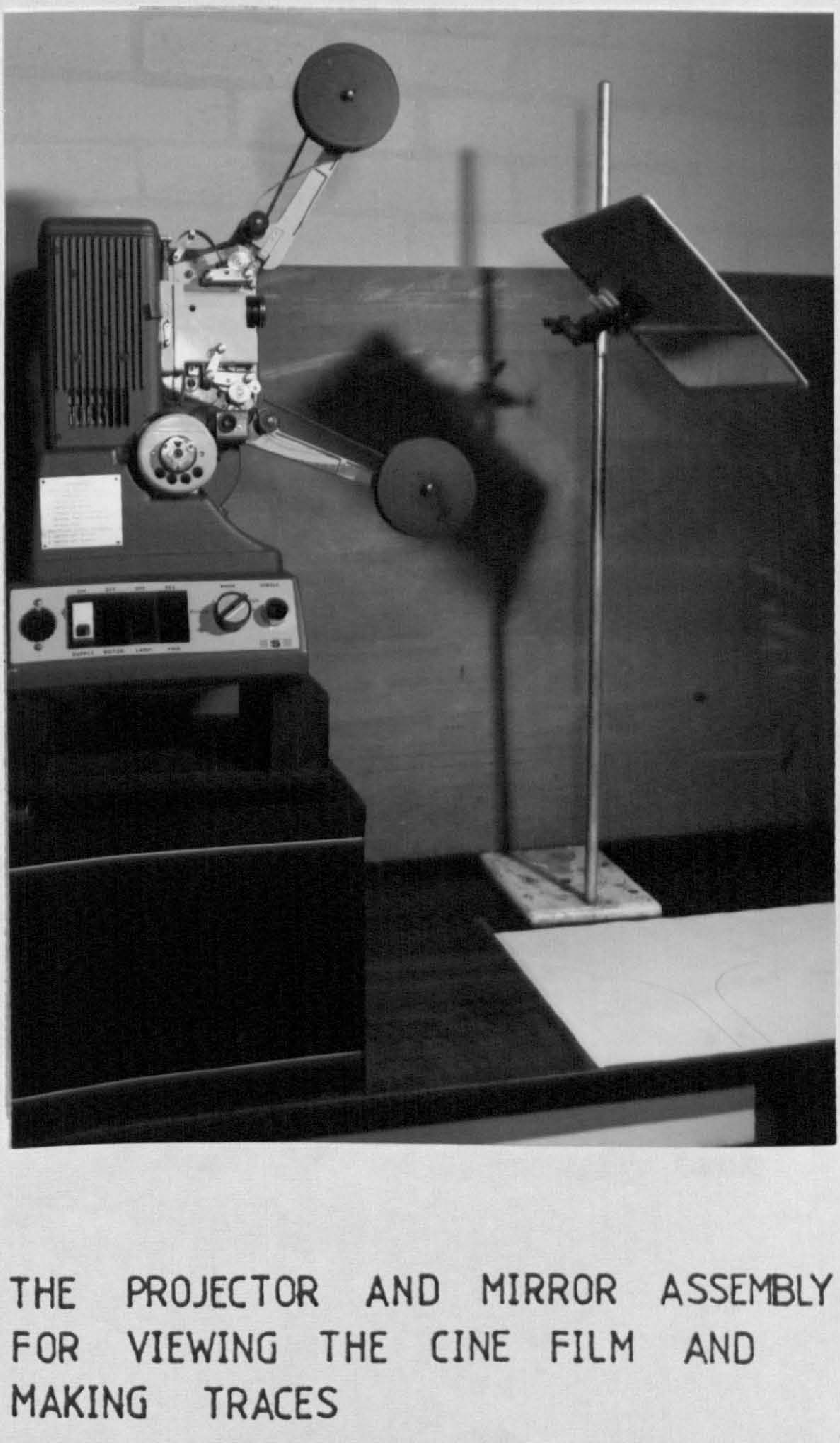

THE PROJECTOR AND MIRROR ASSEMBLY
FOR VIEWING THE CINE FILM AND
MAKING TRACES

FIG. 3.37

sheets on each side of the tundish.

2) The switched safety cover was limited to the front of the model to prevent any physical contact with the tundish or nozzle during the experiments. A glass window in the safety cover allowed easy viewing of the nozzle. No-one was allowed behind the model during an experiment.

3) The switch to the water pump was mounted on the framework holding the supply tank, where it was easily reached for turning on and off quickly.

4) The pulse generator, and the other electrical instruments were kept close together to the side of the model, as far away as was practically possible. The table containing the equipment was positioned to prevent anyone walking behind the model whilst it was operating.

5) All switches needed during the experiment were easily accessible in front of the model. This was particularly important with the rear lights which were turned on and off frequently during the course of an experiment.

6) The room was arranged to exclude anyone other than those directly involved in the experiments.

7) All parts of the system were earthed, that is:-

a) collector tank and measuring tube

b) tundish inlets

c) tundish top

d) framework of the supply tank

e) water pump.

4. EXPERIMENTAL PROCEDURE

4.1. OPERATING THE MODEL

Whenever the model was operated the water flow systems were tested for stability before any electrolysis was started. Similarly the electrical systems were turned off before the model was closed down.

4.1.1. START-UP

With the nozzle in position and the constrictor almost fully closed at about 2 mm, taps C and D are turned on gradually so that water slowly filled the tundish section. The taps are then turned full on until all the air had been removed from the distributer tank, during which time there was a large, noisy overflow from the tundish. When all the air was removed (approx. 2 mins) taps C and D were turned down to provide slightly more water than that required to maintain the full tundish head at the particular nozzle flow rate. Under these conditions, there was only a slight trickle of water from the overflow tubes.

4.1.2. ADJUSTMENT OF FLOW RATE AND MEASUREMENT

The normal procedure was to start at a low flow rate and increase the flow rate in steps.

The protective front cover was removed, then the constrictor opening was increased. The water level in the tundish fell but was brought back to the full head as before by opening taps C and D further. At the same time taps A and B were closed slightly to maintain the same level of water in the collector tank.

When the flow had stabilised the flow rate was measured at least three times. The 10 litre mark was 60 mm from the top of the measuring tube, and at very high flow rates the turbulent water with large quantities of entrained air causes an overflow from the tube before a measurement could be taken. Therefore at constrictor openings of 20 mm or more (about 16.0 x 10^{-4} m^3/s) the 8 litre mark was used for volume measurement.

The water supply was not sufficient to maintain an overflow from the tundish at high flow rates and there was sometimes a tendency for the tundish level to fall by up to 5 mm below the normal level.

The range of flow rates achievable are shown in fig.4.1. There was a possible variation of 2 x 10^{-4} m^3/s in flow rate obtained with the same constrictor opening. The effects of the flow rate on the exit velocity and on the exit Reynolds Number are shown in fig.4.2.

Discharge coefficients through the nozzle were calculated as follows:-

The theoetical flow rate $Q_T = v_{exit} \times A_{exit}$ (4.1)

where A_{exit} is the channel exit area at exit.

The discharge coefficient is then given by:-

$$C_D \; Q = Q_t / Q_A \qquad (4.2)$$

where Q_A is the actual measured flow rate.

The effect of constrictor width is shown in fig. 4.3. There is a reduced discharge at higher flow rates that is also seen in the change in slope in fig.4.1

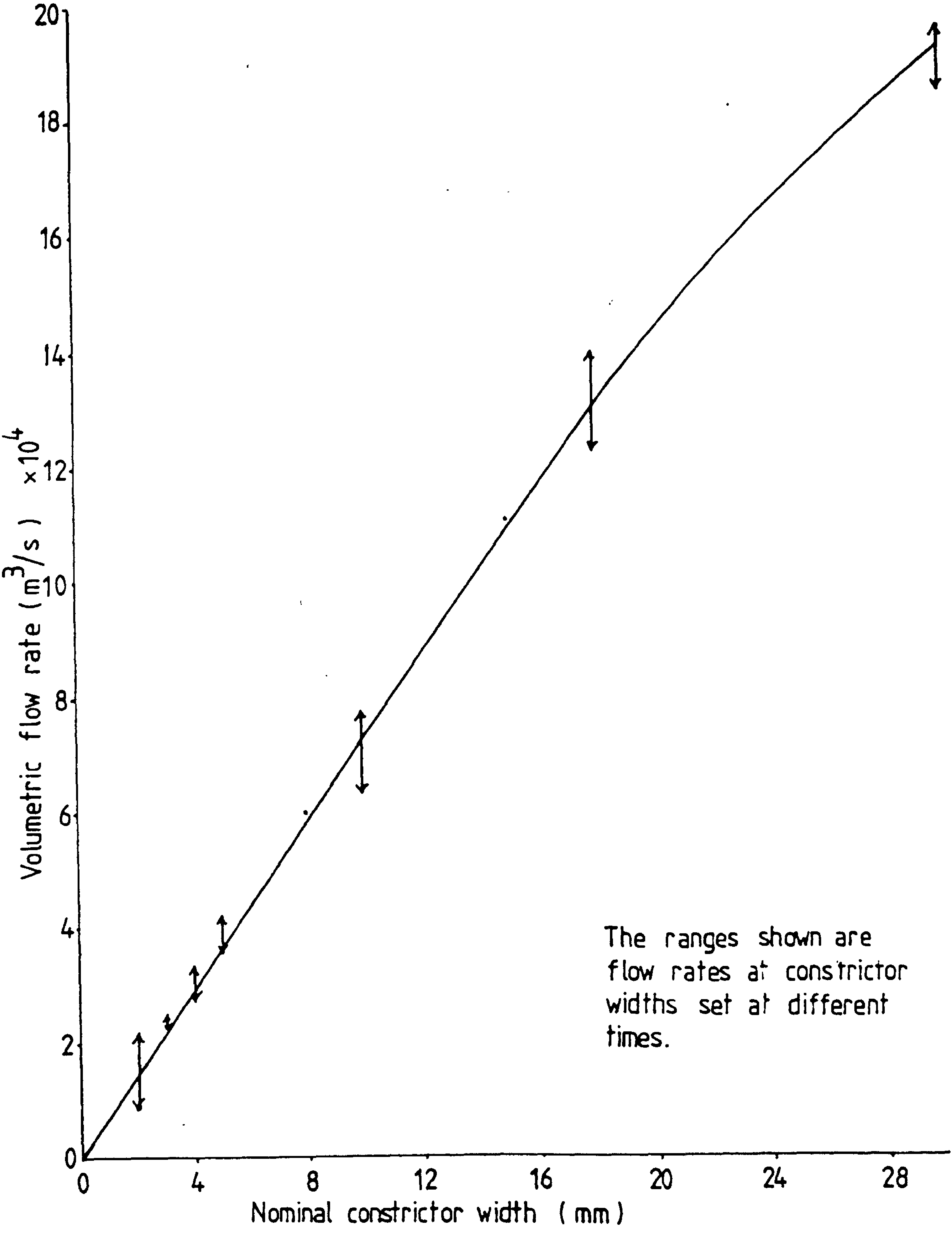

EFFECT OF CONSTRICTOR WIDTH ON THE VOLUMETRIC FLOW RATE

FIG. 4.1

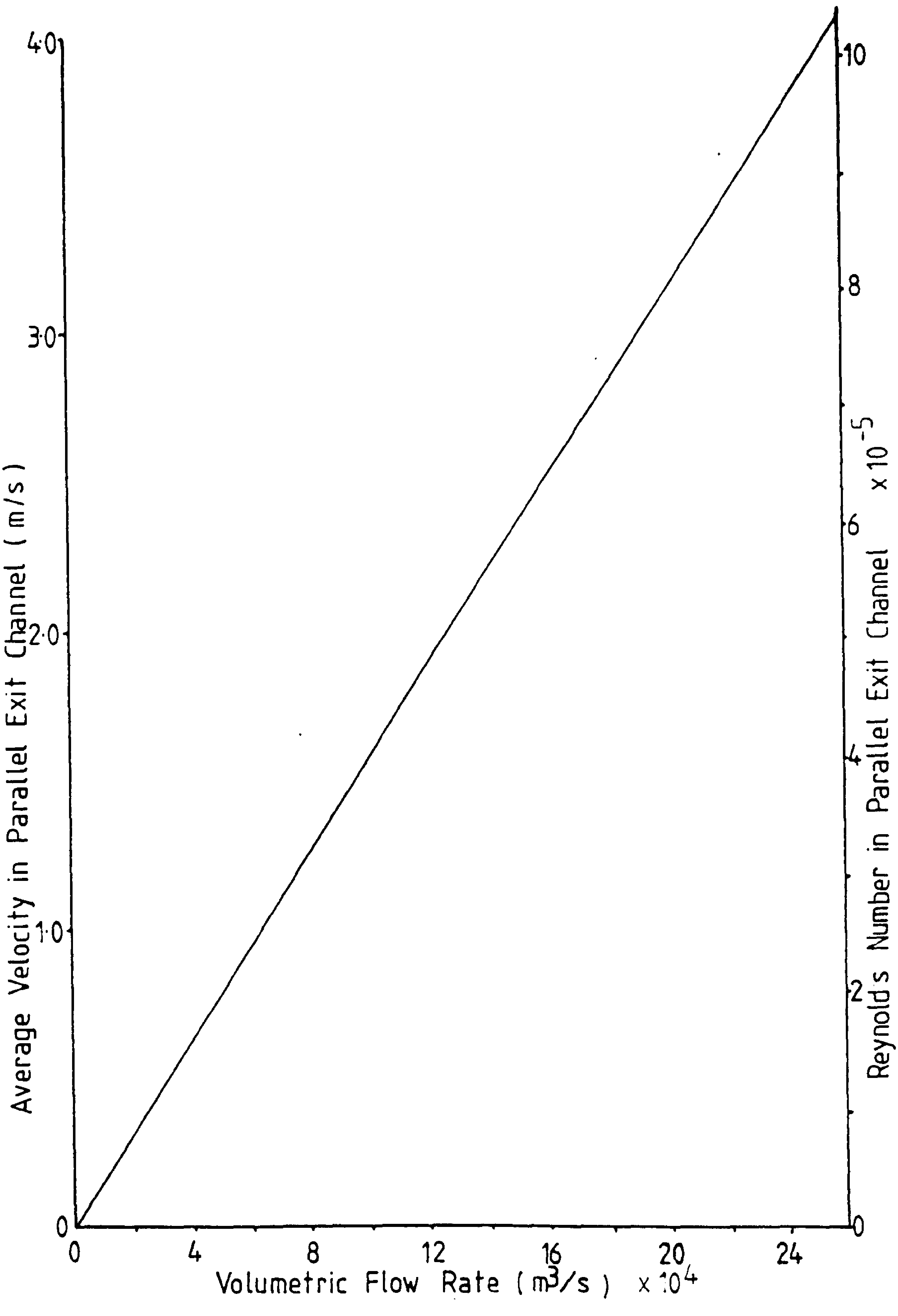

EFFECT OF VOLUMETRIC FLOW RATE
ON THE EXIT CHANNEL VELOCITY
IN THE FINAL MODEL

FIG. 4.2

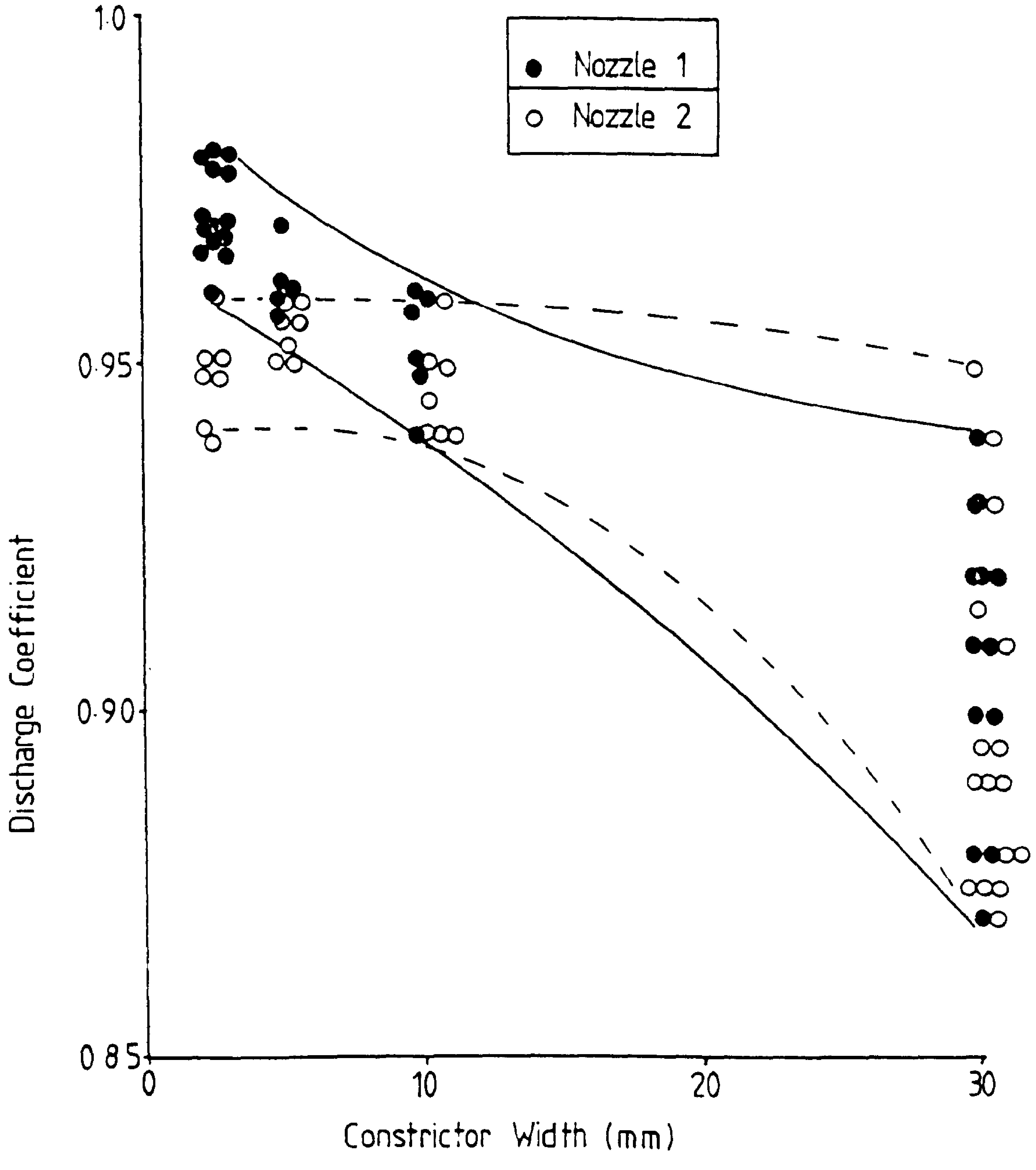

EFFECT OF EXIT CONSTRICTOR
WIDTH ON THE NOZZLE
DISCHARGE COEFFICIENTS

FIG. 4.3

4.1.3. CLOSE-DOWN

All four water taps from the supply tank were fully turned off. Whilst there was still water in the tundish, a bleed plug was taken out of the distributer tank to let in air thus equalising the pressure in the system. The pump was turned off before the water in the collector tank reached the outlet pipe to prevent air being sucked into the pump.

4.2. DETERMINATION OF THE PARTICLE TRACKS

Traces of particle paths were made from the projected image. A number of different methods could be used to record the traces.

1) If very fine hydrogen bubbles were produced from a single point, individual bubbles could not be identified. streamlines at a single frame were then the only means available. This could be carried out from still photographs or from cine film.

2) When a single bubble could be identified the pathline of the bubble was traced frame by frame on the cine film as it moved down the nozzle.

3) In the prototype model a random distribution of particles was present. Traces could be made of those particles that made contact with the surface of the nozzle. However, a semi-quantitative method of measuring the surface hits was devised. The film was run at 2 frames/s or manually frame by frame. The particles that hit the surface on each side of the nozzle were counted by tally counters. At intervals of about 250 frames the total counts were recorded. at the same time the number of particles in an area 100 mm x

100 mm on the projected image were recorded.

The particles hitting the surface were expressed as a proportion of the total number of particles flowing.

$$\text{Volumetric fluid flow rate} = V \ \text{m /s}$$

$$\text{Particle quantity at x4.3 mag.} = p \ / \ 100\text{mm} \times 100\text{mm}$$

$$\text{actual particle quantity} = \frac{p}{.1/4.3 \times .1/4.3} \qquad (4.3)$$

$$\text{actual particle quantity} = 1849\,p \quad \text{particles/m}^2$$

$$\text{planar fluid flow rate} = \frac{V \ (\text{m /s})}{\text{model thickness (m)}} \qquad (4.4)$$

$$= \frac{V}{0.015} \quad \text{m /s} \qquad (4.5)$$

$$= 66.7\,V \quad \text{m /s} \qquad (4.6)$$

$$\text{Rate of particle flow} = 66.7\,V \times 1849\,p \ \text{per second} \qquad (4.7)$$

$$\text{If the total hits} = y\ /\text{sec}$$

the percentage of particle hitting the surface

$$= \frac{y \times 100}{66.7\,V \times 1849\,p} \ \% \qquad (4.8)$$

4.3. MEASUREMENT OF VELOCITY FROM THE CINE FILM

With the cine run at a known speed the movement of a single particle between successive frames was measured from traces of the bubble path.

If v_{cine} is the cine framing speed,

then

$$t = \frac{1}{v_{cine}} \qquad (4.9)$$

where t is the time interval between successive frames.

Therefore the mean velocity of the particle between the two frames is given by:-

$$v_p = \frac{s_p}{t} \qquad (4.10)$$

where s_p is the distance between successive particle positions taking into account the possible image magnifcation.

This method was conveniently used to plot the velocity profile through the nozzle.

Information of velocity profiles could also be obtained by observing timelines. These are lines of bubbles generated at the same time from a straight wire. If the wire is suitably pulsed, discrete lines of bubbles are produced which move in time dependent on the local velocity of fluid.

4.4. DETERMINATION OF BUBBLE SIZES

Ordinary 35 mm close-ups or microflash photographs could be used to measure bubble sizes but as indicated previously the microflash is far superior. Most of the work therefore was carried out using the microflash. For each different set of experimental conditions a number of photographs were taken. If a large number of small bubbles were produced two or three photographs were sufficient. With large bubbles produced at longer time intervals up to 12 photographs may be necessary. Even so, it was increasingly difficult to catch the bubbles on a photograph during their passage between the cathode wire and the nozzle exit. The bubble size was measured from the photograph using a x4 magnifying eyepiece fitted with a scale divided into 0.1 mm. Fig. 4.4 shows a typical series of well produced bubbles.

SERIES OF WELL PRODUCED BUBBLES

FIG. 4.4

5. EXPERIMENTAL RESULTS

5.1. PARTICLE SIZES

Hydrogen bubbles are generated from the cathode wire in two characteristic ways. From the curved surface of the wire either parallel to or normal to the water flow direction, very small bubbles, (less than 50 µm diameter) are produced. At the tip of the wire parallel to the flow direction larger bubbles are produced. This effect is shown most clearly in figs. 5.1 and 5.2, where bubbles from the curved surface and the wire tip can be seen. There was no noticeable bubble production at cathode currents below 5 mA. Above 5 mA the quantity of fine bubbles increased with increase in current but the size of bubbles remained below 50 µm diameter. The size of the bubbles produced from the wire tip did increase with increase in current as seen in fig. 5.1. When the cathode wire was not exactly parallel to the flow direction a wider band of fine bubbles was produced, (particularly noticeable in figs. 5.1 a and b. The lower flow rate tended to produce larger bubbles from the wire tip but local conditions of flow, wire size, insulation and wire surface condition also contributed.

Bubbles produced only from the wire tip are shown in figs. 5.2, 5.3, and 5.4. Measurements of the individual bubbles along with those from fig. 5.1 c are shown in table 5.1. The standard error of the mean is for the 95% confidence level and is described in more detail in section 7.1.

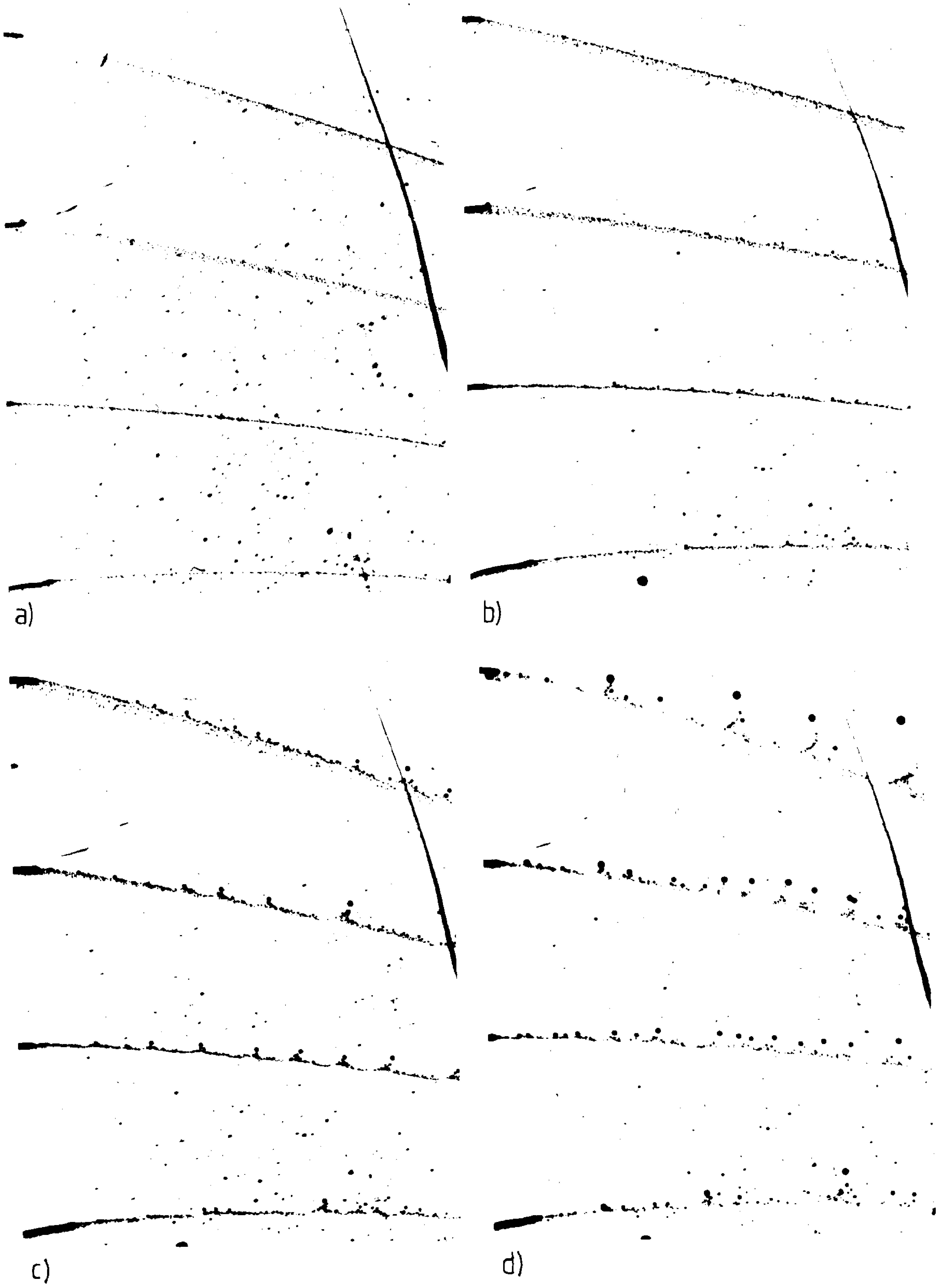

a)

b)

c)

d)

BUBBLES PRODUCED FROM THE CURVED SURFACE AND THE TIP OF A 90 μm DIAMETER STAINLESS STEEL CATHODE PARALLEL TO THE WATER FLOW DIRECTION

5.2

FIG. 5. 1

frequency
= 16·39 Hz

pulse width
= 16 mS

mag. = ×2·9

BUBBLES PRODUCED FROM THE TIP OF A 200 μm DIAMETER WIRE AT $2{\cdot}46 \times 10^{-4}$ m^3/s AND 18 mA

FIG. 5. 2

frequency
= 16·39 Hz

pulse width
= 16 mS

mag. = 2·9

BUBBLES PRODUCED FROM THE TIP OF A 200 um DIAMETER WIRE AT $2 \cdot 46 \times 10^{-4}$ m^3/s AND 54 mA

FIG. 5. 3

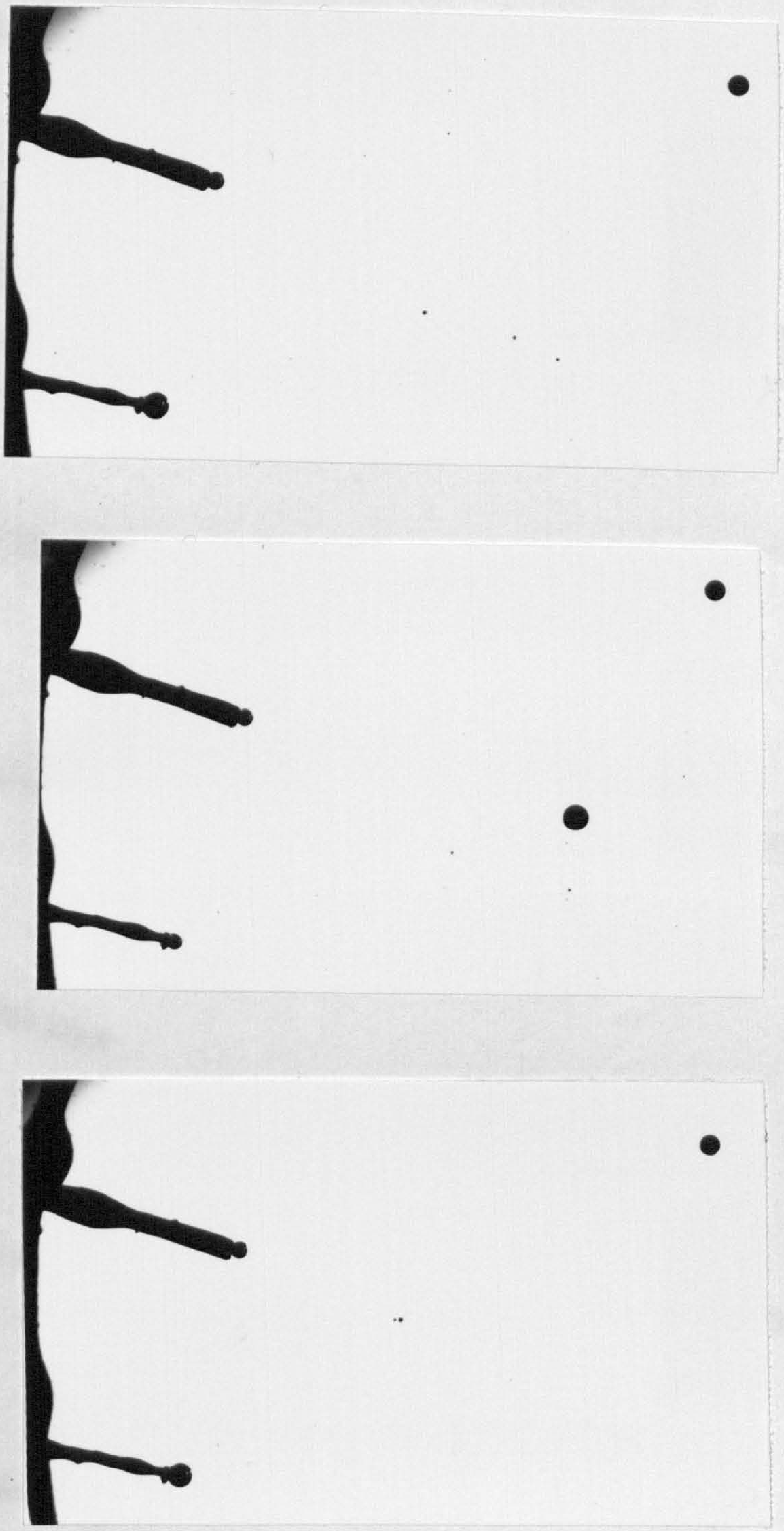

frequency
= 3·64 Hz

pulse width
= 250 mS

upper wire
= 500 μm dia.

lower wire
= 200 μm dia.

mag. = ×2·75

BUBBLES PRODUCED FROM THE TIPS OF TWO WIRES AT $7{\cdot}58 \times 10^{-4}\,m^3/s$ AND 78 mA

FIG. 5. 4

FIG 5 4
(cont.)

	Measured dia. from photos. /(mm)	mag.	actual measurements /(μm)		
			mean dia.	std. dev.	std. error of the mean
fig. 5.1c	6 at 0.25 25 at 0.2 60 at 0.1	x4.4	31	12	2.6
fig. 5.2	0.5 0.5 0.4 0.5 0.5 0.5 0.4 0.5 0.5 0.45 0.4 0.4 0.4 0.4	x2.9	159	16	8.6
	1.6 1.6 1.35 1.6 1.6 1.55 1.3 1.6 1.6 1.5 1.5 1.35 1.3 1.5	x9.6	156	12	6.4
fig. 5.3	0.7 0.75 0.8 0.8 0.7 0.7 0.7 0.75 0.7 0.75 0.7 0.7 0.7 0.7	x2.9	250	13	6.8
	2.4 2.4 2.45 2.4 2.3 2.4 2.4 2.4 2.4 2.4 2.4 2.3 2.4 2.35	x9.6	249	4.1	2.2
fig. 5.4 a,b	2.2 2.2 2.2 2.2 2.2 2.2 2.3 2.1 2.2 (upper wire)	x2.8	786	17	11.2
fig. 5.4 a,b	2.8 2.6 2.5 2.7 2.55 2.5 2.6 2.65 (lower wire)	x2.8	933	34	22.8

TABLE 5.1 DETAIL OF THE BUBBLE SIZE MEASUREMENT

Full details of the bubble sizes produced at the wire tip with different experimental conditions are shown in table 5.2. The cathode current varied with d.c. voltage as shown in fig. 5.5, 130 mA being obtained at 300 V. There was more variation in current in the experiments using only the tip of the wire, (fig. 5.6). Bubble size increased with increase in cathode current as shown in fig. 5.7. The different symbols in fig. 5.7 refer to particular experiments. For most experiments the bubble diameter (d) varied such that;

$$d\ (\mu m) = 8 \times \text{cathode current (mA)}$$

5.2. PARTICLE TRACKS

5.2.1 SMALL BUBBLES (FLOW PATHS)

Water flow paths were most accurately approached by small bubbles generated from the surface of a 90 um diameter wire parallel to the flow direction. Two separate experiments with a total of five wires were carried out. The results from slow flow rates, (approximately 7×10^{-4} m^3/s), are shown for nozzle 1 in fig. 5.8 and for nozzle 2 in fig. 5.9. This gives a Reynolds Number of 27,000 at exit. At this flow rate there was no discernable oscillation of the pathlines in either nozzle. The traces were made from a single frame on the cine film, since the bubbles were too fine and close together to be separated for frame to frame measurements.

With increase in flow rate there was some lateral movement of the pathlines. Figs 5.10 and 5.11 show the

flow rate $(10^{-4} m^3/s)$	voltage /(V)	current /(mA)	bubble dia. /(µm)	nozzle	wire dia. /(µm)
2.46	40	18	150 +28	1	200
	130	54	250 +12		
3.01	80	35	172 +4		
	180	76	243 +6		
3.02	220	92	302 +10		
	220		322 +50		
	300	62	281 +38		
18.8	350	55	403 +40		
18.6	100	38	330 +12	2	200
	150	55	607		
	200	72	772 +70		
18.3	100	37	357	1	200
	150	53	439 +12		
	200	71	704 +60		
19.2	80	28	259 +16	2	500
	120	41	331 +26		
	160	53	404 +14		
	200	68	435 +32		
	260	87	600 +21		
7.46	100	50	421 +82		
	200	93	561 +26		
	300	142	522 +52		
18.8	80	28	286 +20	1	500
	120	42	395 +52		
	160	56	504 +26		
	200	70	516 +26		
	260	89	602 +20		
	340	122	668 +42		
7.35	100	47	723 +60		
	300	132	527 +28		

TABLE 5.2 SIZES OF BUBBLES PRODUCED FROM TIP OF A STAINLESS STEEL WIRE

flow rate (10^{-4} m^3/s)	voltage /(V)	current /(mA)	bubble dia. /(µm)	nozzle	wire dia. /(µm)
7.58	40	14	143 +10	2	500
	80	36	262 +34		200
	120	52	487 +32		500
	180	78	786 +10		200
	40	14	171 +16		500
	80	36	390 +36		200
	120	52	583 +12		500
	180	78	993 +24		200
12.9	120	52	430 +30	2	500
	180	79	742 +18		200
	120	52	589 +6		500
	180	79	653 +12		200
7.33	80	38	271 +14	1	500
	120	57	431 +20		200
	180	84	681 +16		500
	250	118	814 +12		200
	80	38	421		500
	120	57	494 +20		200
	180	84	548 +20		500
	250	118			200
13.1	120	48	412 +16	1	500
	180	72	677 +70		200
	250	101	905 +20		500
	350	135	988 +162		200
	120	48	438 +62		500
	180	72	663 +20		200
	250	101	786		500
	350	135	1167		200

TABLE 5.2(cont.)

flow rate $(10^{-4} m^3/s)$	voltage /(V)	current /(mA)	bubble dia. /(µm)	nozzle	wire dia. /(µm)
19.6	50	17	195 +14	2	100
	70	25	117 +28		
	90	32	132 +12		
	100	34	345 +98		
	130	43	354 +44		
	160	52	667 +166		
	180	60	385 +48		
	200	63	491 +52		
19.7	50	18	196 +18	1	100
	70	25	232 +26		
	80	28	476 +38		
	90	32	214 +14		
	120	42	536		
	150	52	324 +20		
	180	62	874 +82		
20.4	80	19	159 +10	2	90
7.38	20	7	97 +10	2	90
	35	11	133 +8		
	50	13	165 +10		
	80	22	201 +20		
20.4	80	20	140 +4	1	90
7.47	35	11	133 +8	1	90
	50	13	138 +16		
	80	21	201 +16		

TABLE 5.2 (cont.)

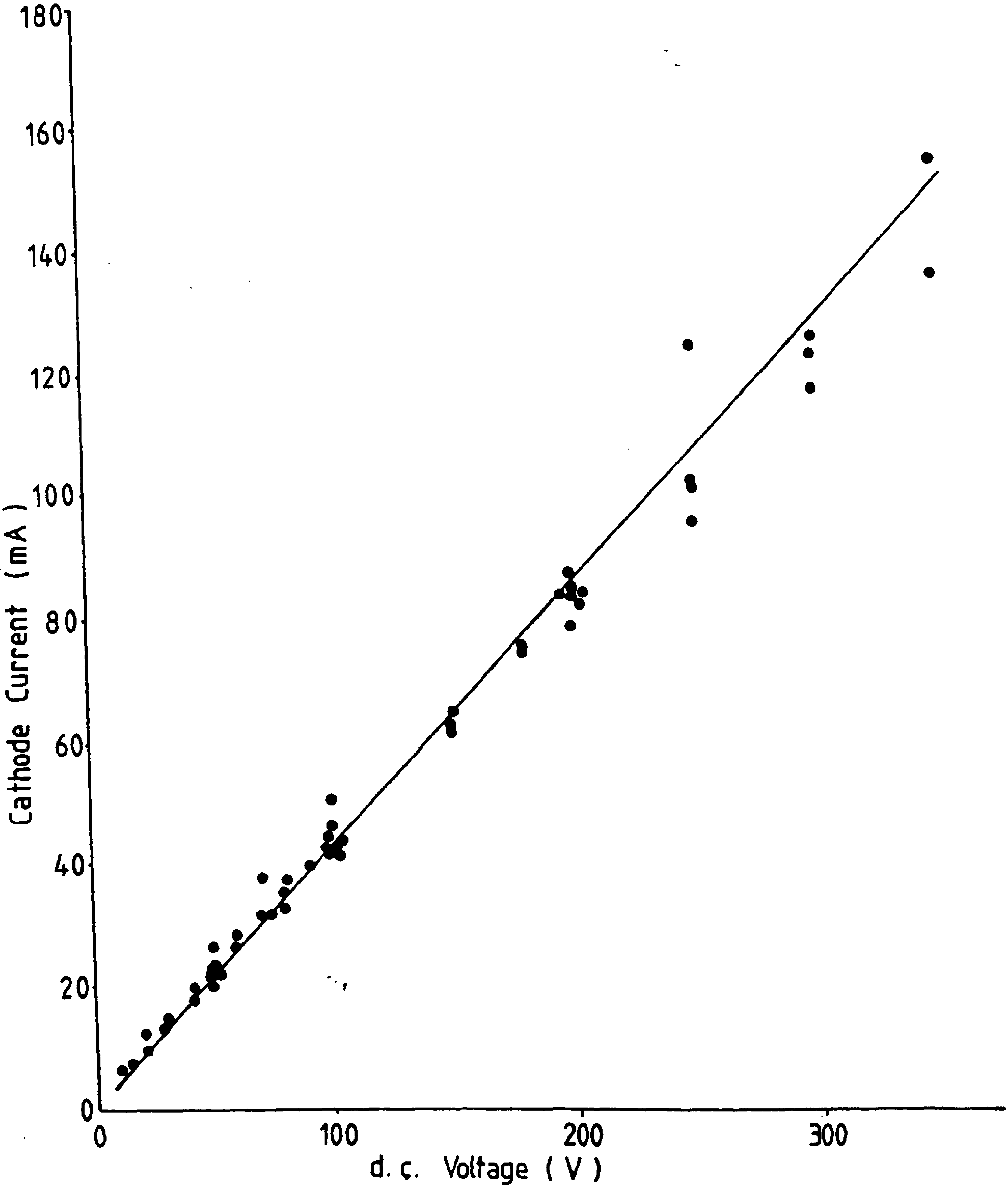

ELECTRICAL CONDITIONS DURING
HYDROGEN GENERATION IN THE
FINAL MODEL

FIG. 5.5

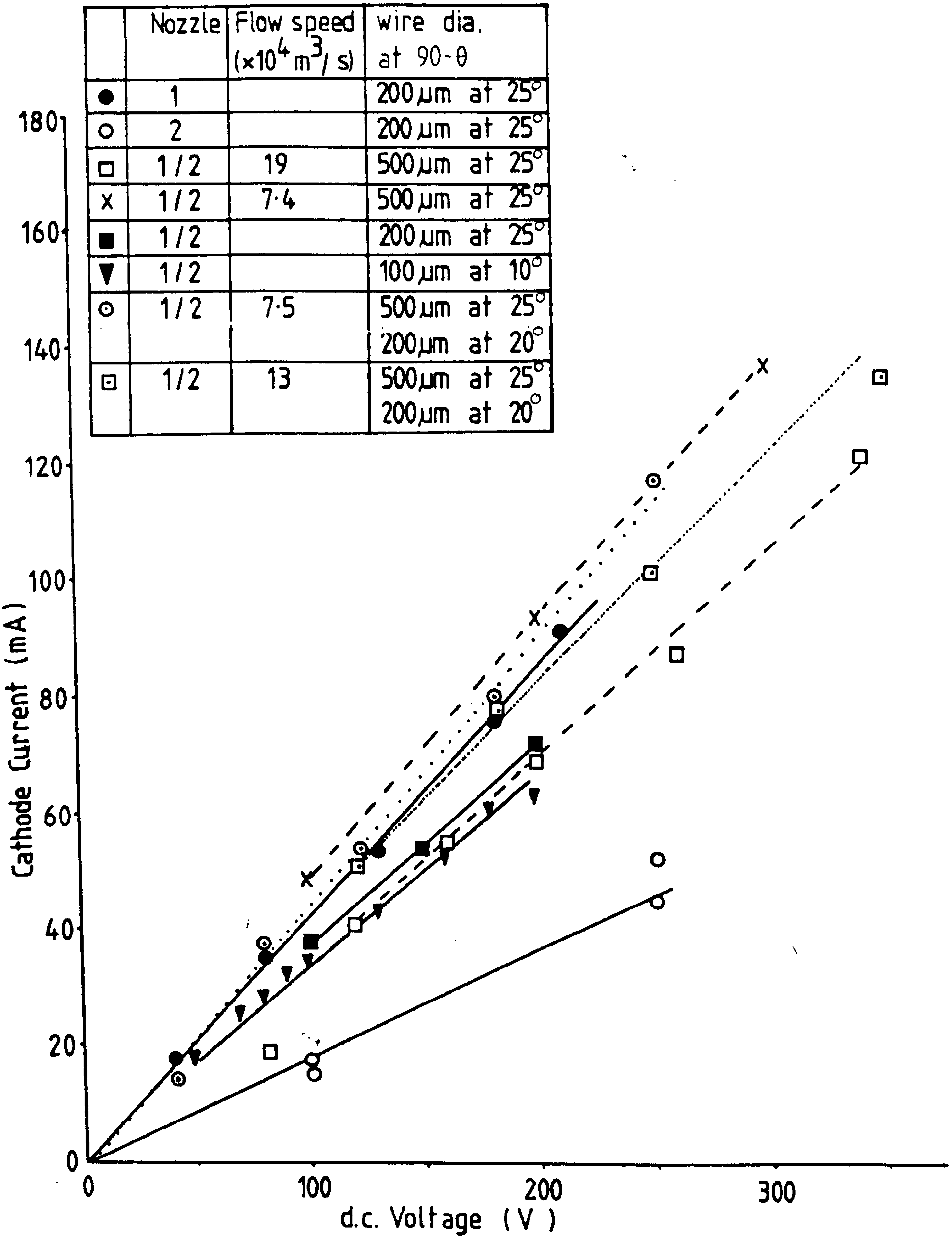

	Nozzle	Flow speed ($\times 10^4 m^3/s$)	wire dia. at 90-θ
●	1		200 µm at 25°
○	2		200 µm at 25°
□	1/2	19	500 µm at 25°
x	1/2	7·4	500 µm at 25°
■	1/2		200 µm at 25°
▼	1/2		100 µm at 10°
⊙	1/2	7·5	500 µm at 25° 200 µm at 20°
⊡	1/2	13	500 µm at 25° 200 µm at 20°

ELECTRICAL CONDITIONS DURING HYDROGEN GENERATION IN THE FINAL MODEL USING ONLY THE TIP OF THE WIRE

FIG. 5.6

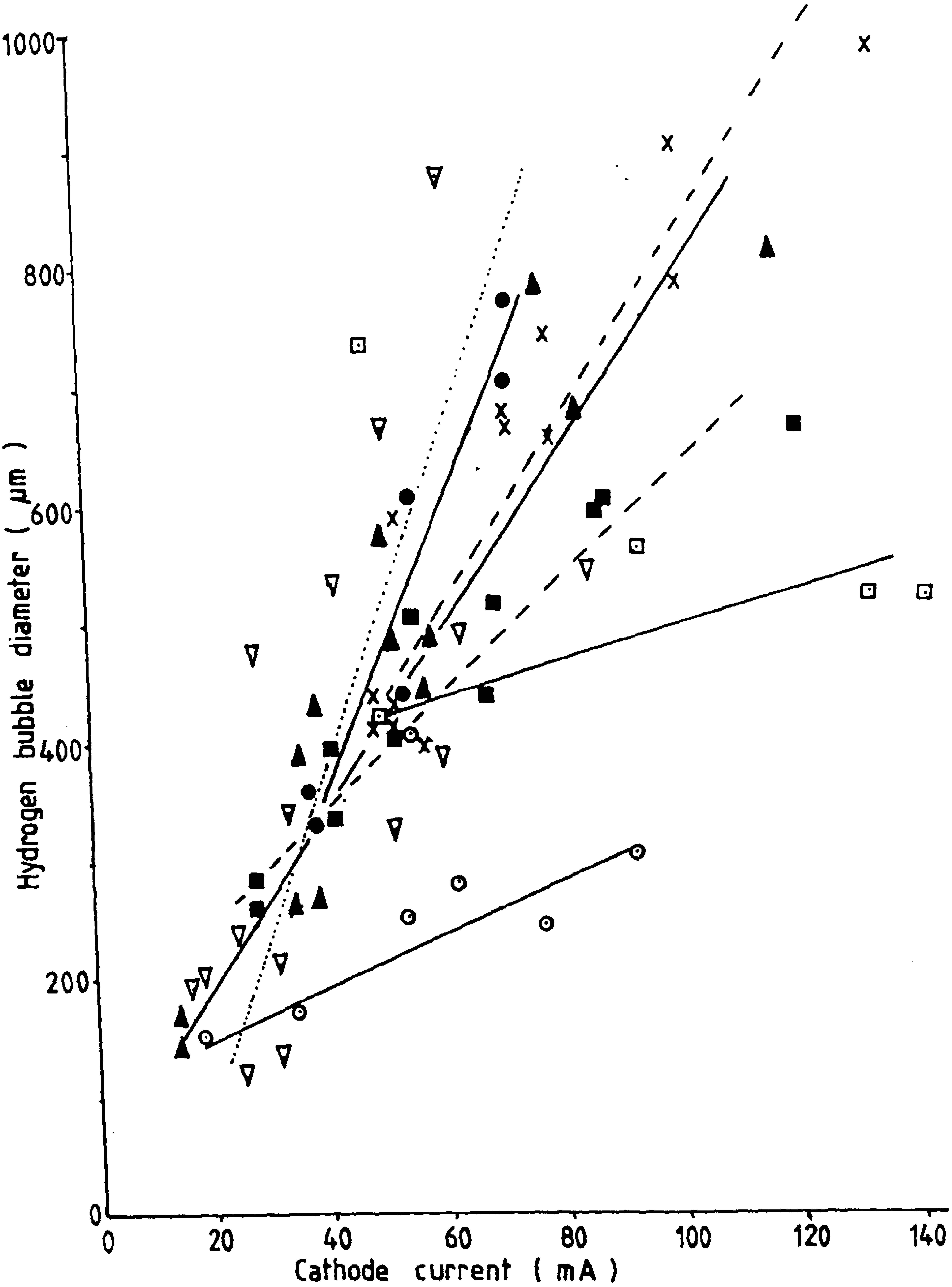

EFFECT OF CATHODE CURRENT ON THE SIZE OF HYDROGEN BUBBLE PRODUCED FROM THE TIP OF A CATHODE WIRE

FIG. 5.7

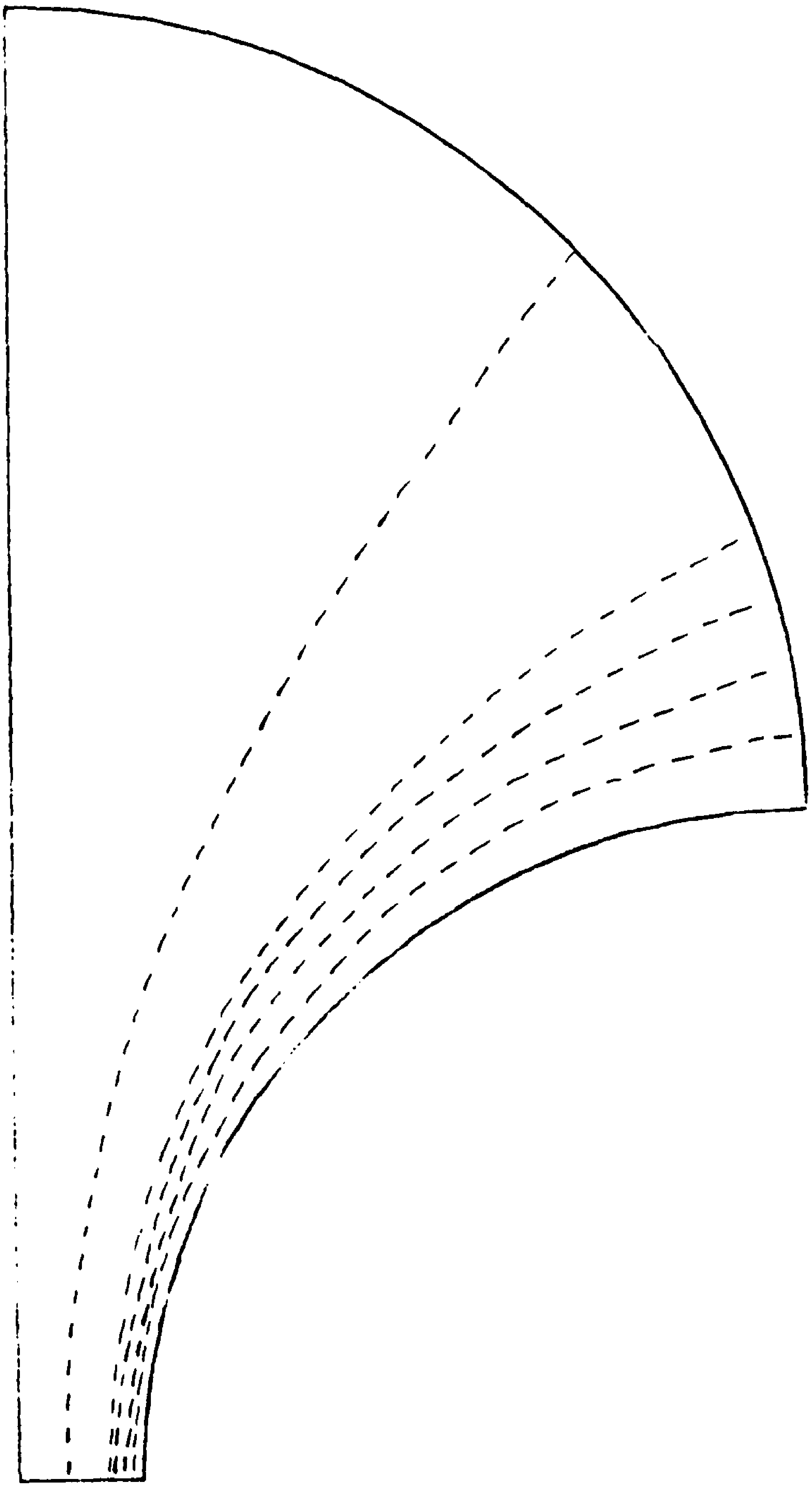

PATHS OF 90µm HYDROGEN BUBBLES IN NOZZLE 1 AT 7×10^{-4} m^3/s

FIG. 5.8

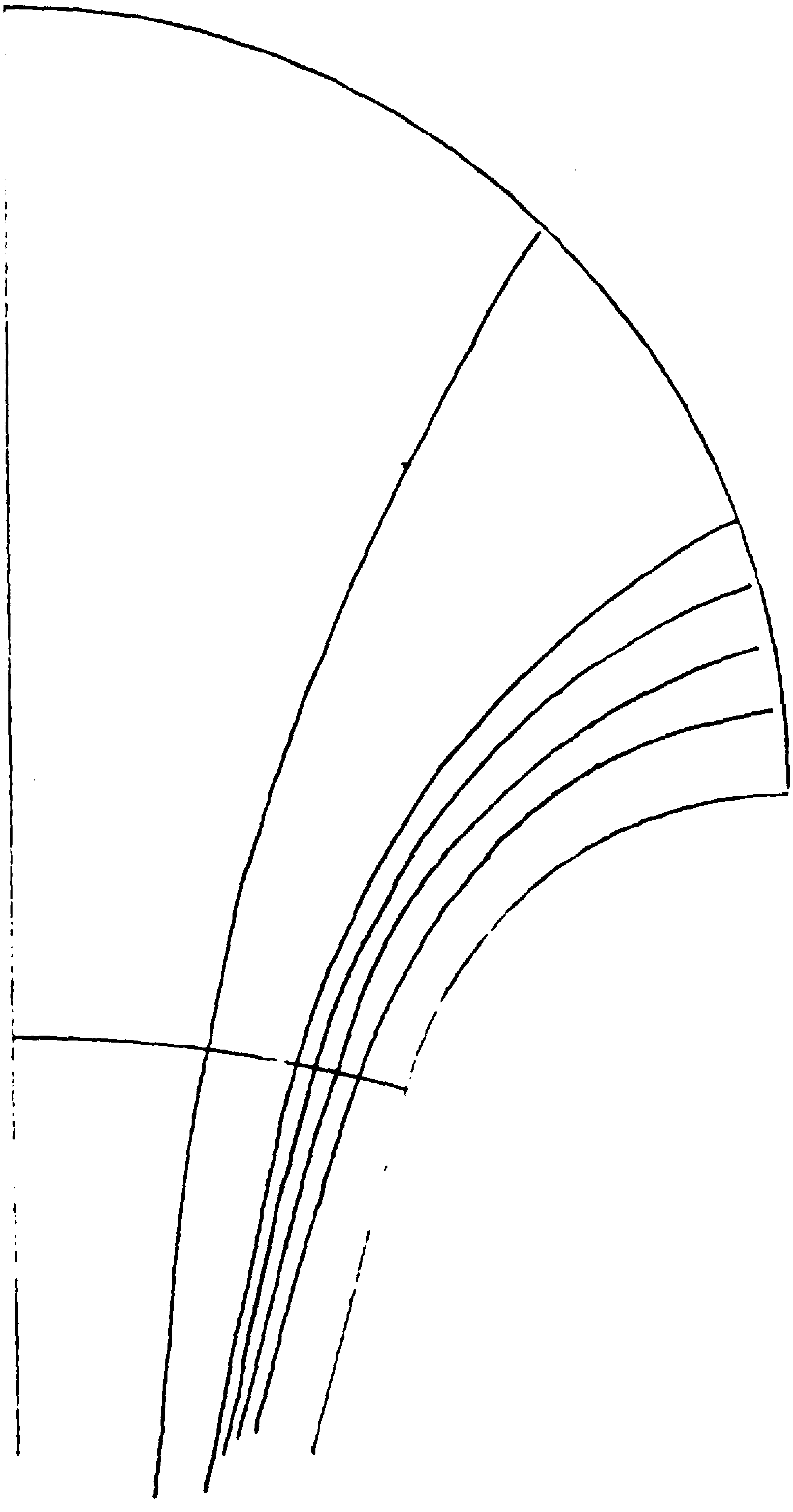

PATHS OF 90 um HYDROGEN BUBBLES IN NOZZLE 2 AT $7 \times 10^{-4} m^3/s$

FIG. 5.9

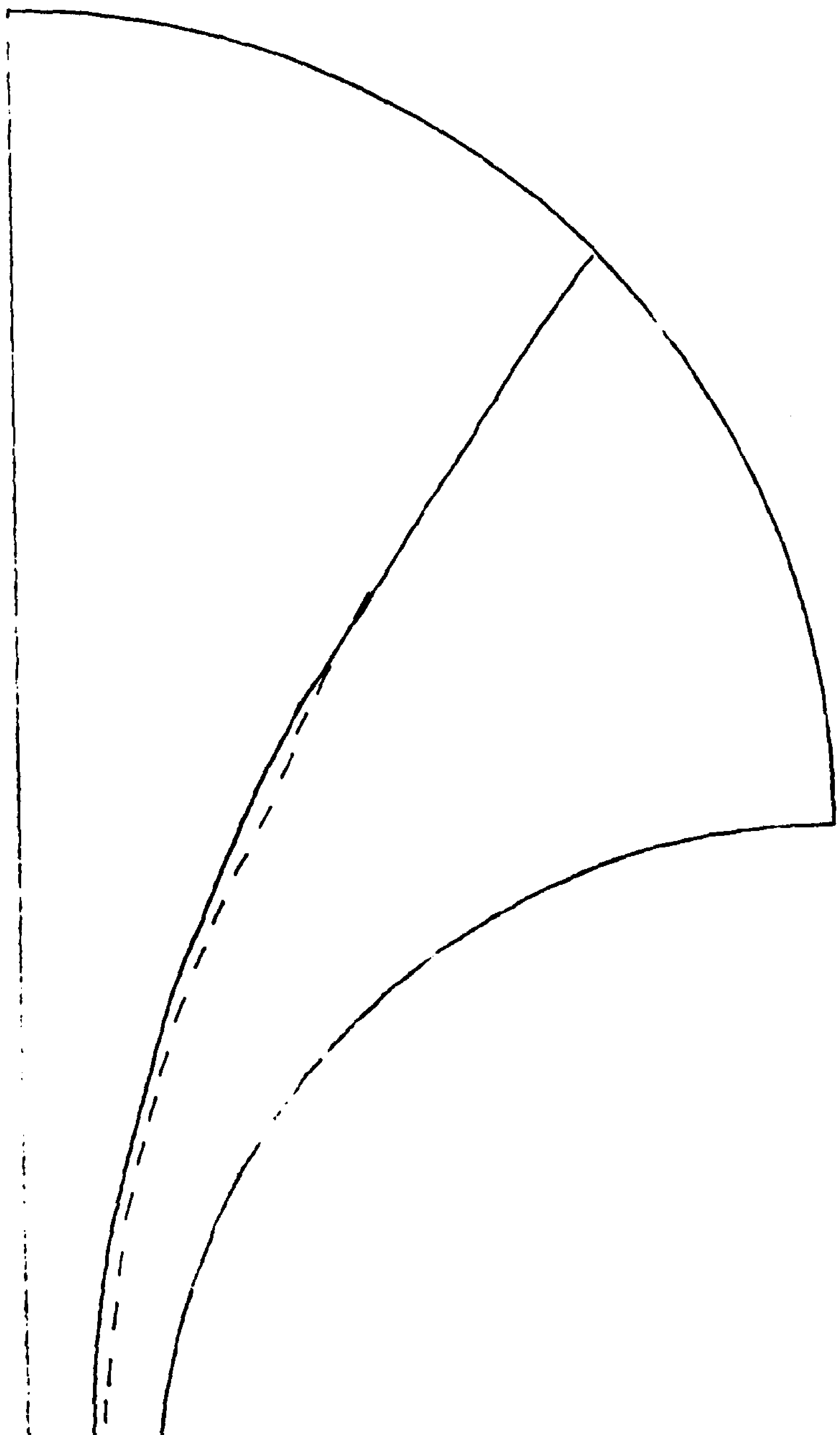

EXTENT OF THE LATERAL MOVEMENT OF PATHLINES IN NOZZLE 1 AT $19 \times 10^{-4} m^3/s$

FIG. 5.10

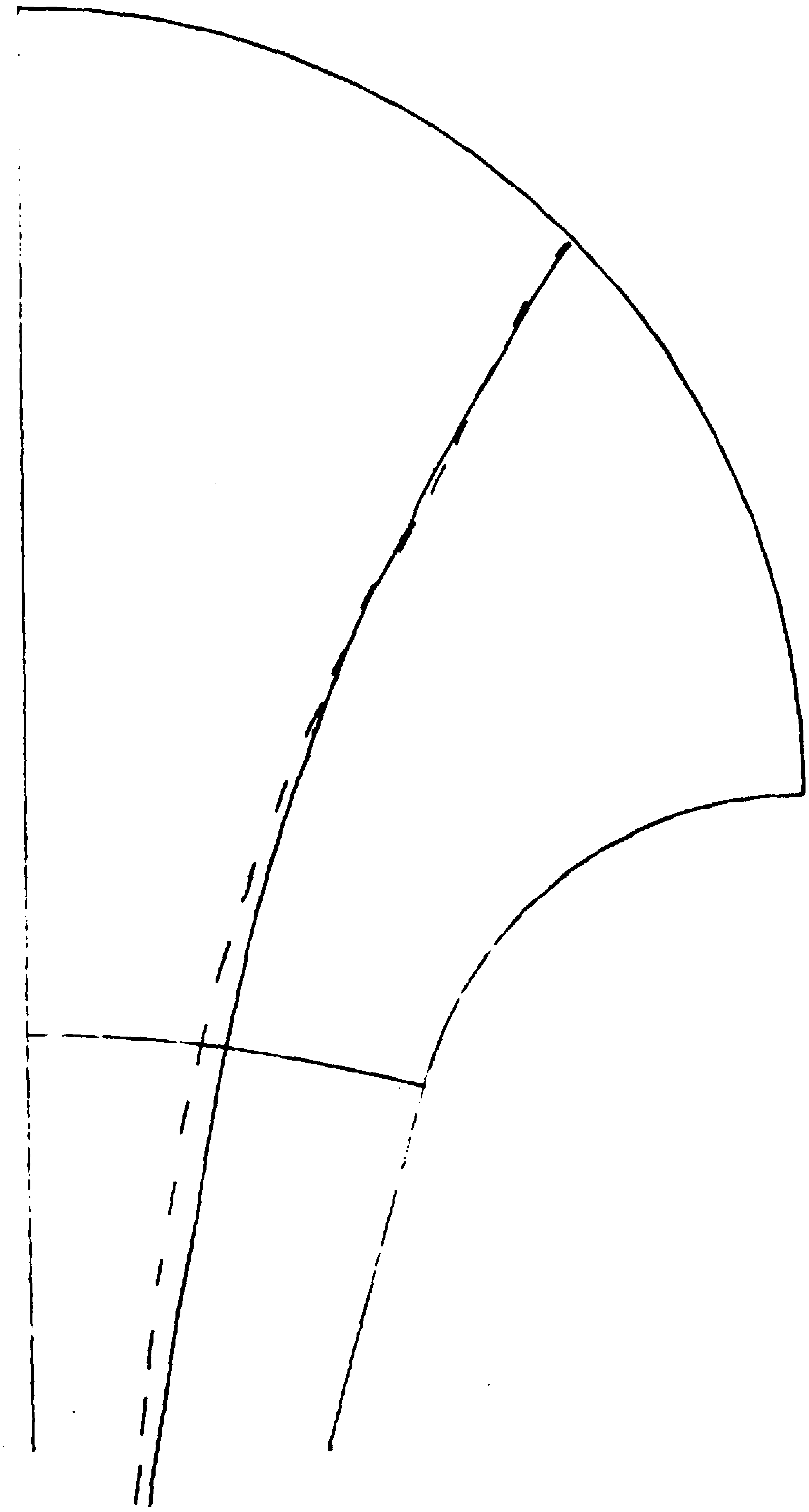

EXTENT OF LATERAL MOVEMENT OF PATHLINES IN NOZZLE 2 AT $19 \times 10^{-4}\ m^3/s$

FIG. 5.11

limits of lateral movement in those pathlines, starting from the 45° position, at 19 x 10^{-4} m^3/s, an exit Reynolds Number of 74,000

5.2.2 FINITE BUBBLES------PARTICLE TRACKS

5.2.2.1 EVIDENCE FROM THE PROTOTYPE MODEL

With the random distribution of nitrogen bubbles it was possible to make traces from the cine films of bubbles seen to hit the surface. typical traces from two different sized bubbles are shown in fig. 5.12. There was no difference in the nature of the traces at the right and left hand side of the nozzle. The bubbles in these traces were quite large as estimated from the cine films, (500 µm to 1300 µm diameter), since smaller bubbles could not be visualised clearly nor followed throughtout their paths.

Given the necessary limitations with this system of bubble generation the percentage of particles hitting the surface was measured as described in section 4.2. For nitrogen bubbles in the approximate size range 500 µm to 1300 µm diameter 6.1% hit the surface. Using the nominally iso-density xylene/dibutyl phthalate particles 4.1% were found to hit the surface.

5.2.2.2 RESULTS FROM THE FINAL MODEL

Since the flow paths of bubbles were studied by traces taken from cine films the most suitable means of displaying the paths was to combine the particle paths from different films on one drawing. In this way the effect of the independent variables could be examined more closely.

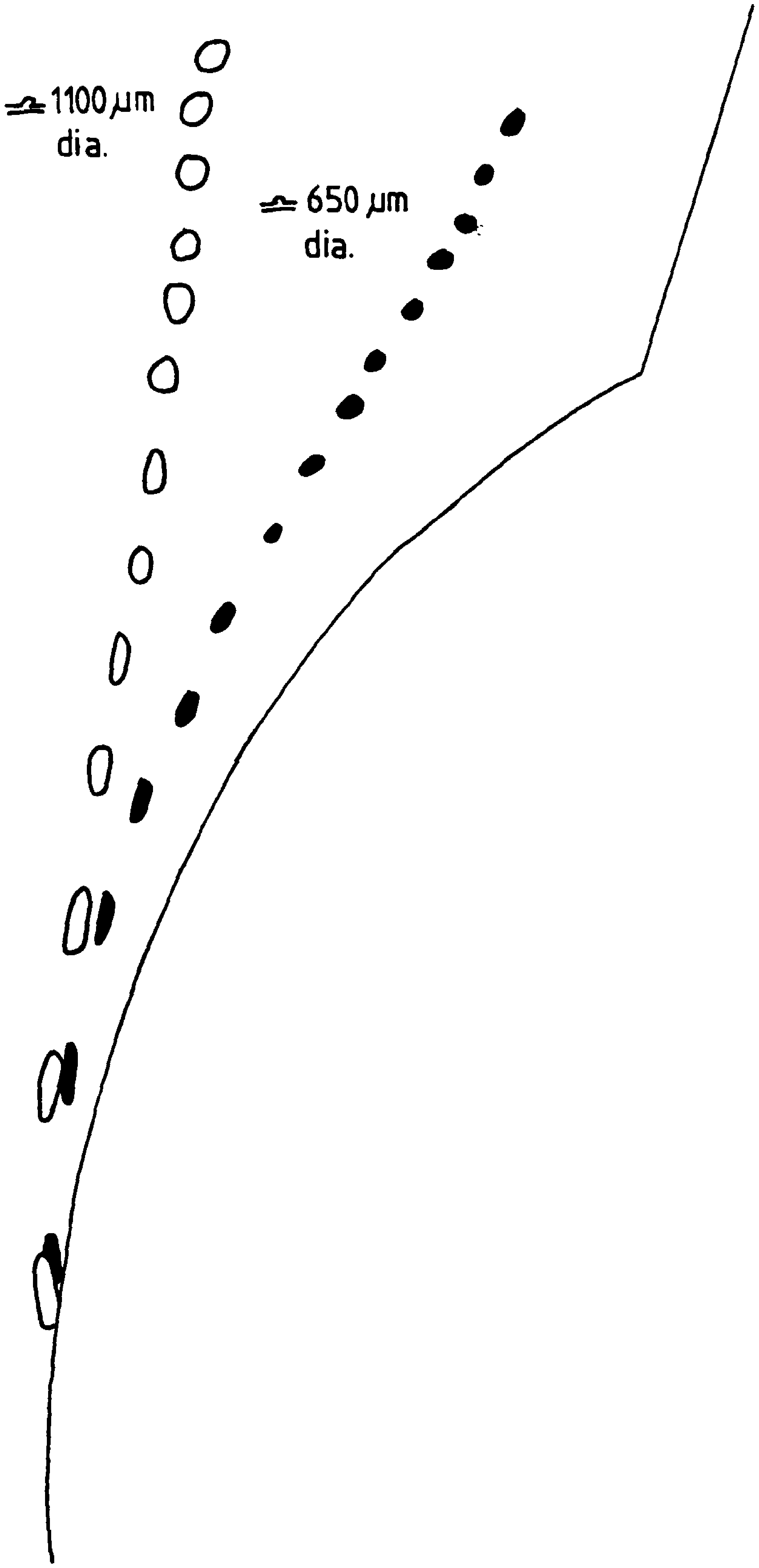

SURFACE HITS OF NITROGEN BUBBLES
IN THE PROTOTYPE MODEL

FIG. 5.12

5.2.2.2.1 THE EFFECT OF PARTICLE SIZE

Fig 5.13 shows combined traces of bubbles from 196 μm diameter to 874 μm diameter in nozzle 1, at a high flow rate and starting at the 80° position. All had very similar flow paths and were seen to hit the surface of the nozzle at or just above the tangent point. A similar combined trace for nozzle 2 at a high flow rate is shown in fig 5.14. Again, the flow paths did not vary greatly with size of bubble, but in contast to nozzle 1 no bubbles were seen to hit the surface.

At a lower flow rate wide variations were seen. Fig. 5.15 shows the paths of bubbles starting from the 65° position in nozzle 1. The paths were influenced most by bouyancy in the upper part of the nozzle. There was an indication that the bubbles of 681 μm diameter and 814 μm diameter were beginning to cross the paths of the smaller bubbles, but they were not seen to hit the surface of the nozzle. Fig. 5.16 shows the result from nozzle 2 at a similar flow rate. Again the dominant influence of buoyancy was seen in the upper part of the nozzle. However, the bubbles retained their separate paths to the nozzle exit without crossing.

5.2.2.2.2 THE EFFECT OF FLUID VELOCITY

To study the effect of fluid velocity at a constant particle size was difficult because changing the flow rate required lengthy adjustments to the water flow system.

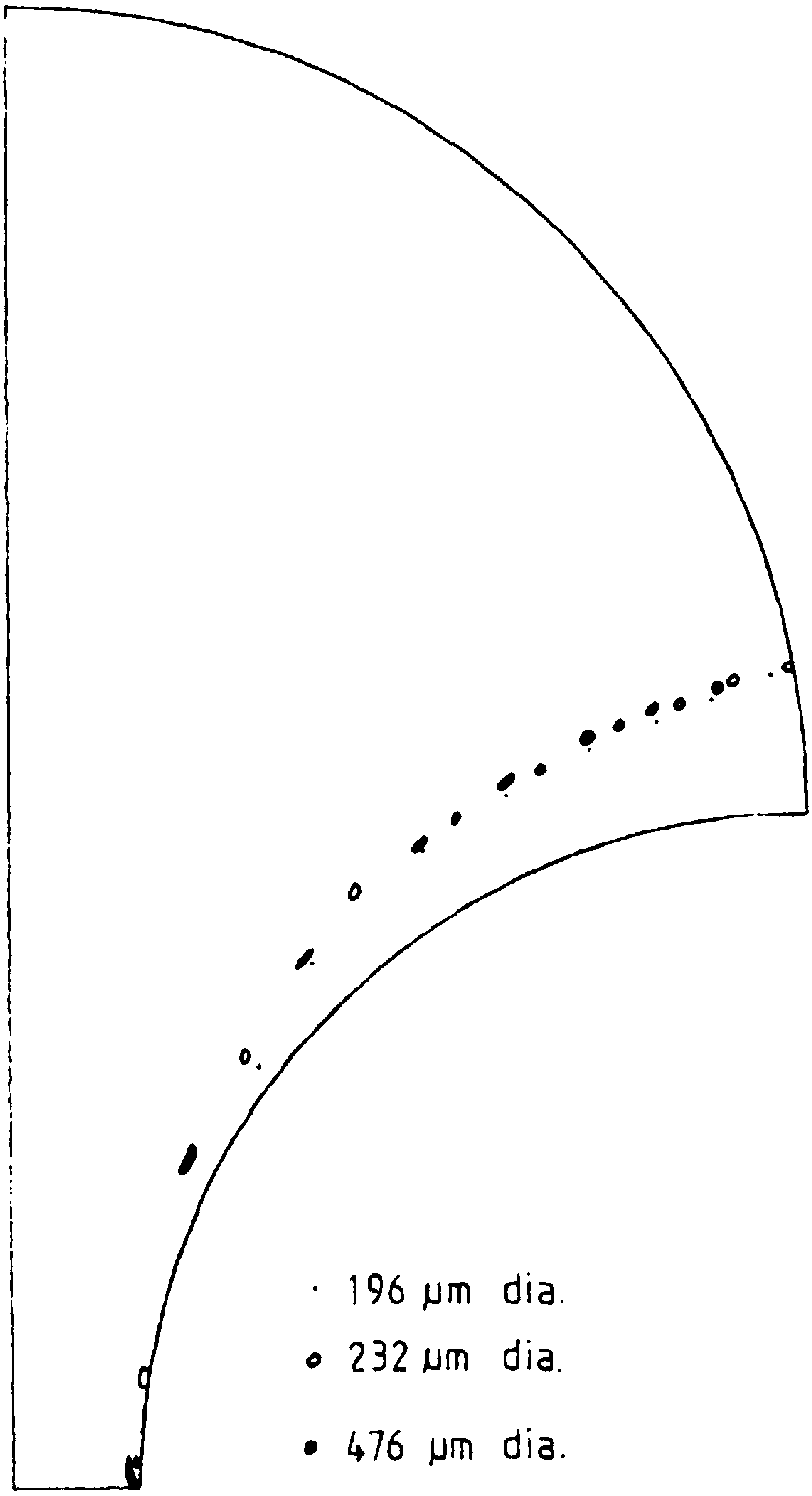

EFFECT OF PARTICLE SIZE ON THE FLOW PATHS IN NOZZLE 1 AT HIGH FLOW RATE ($19{\cdot}71 \times 10^{-4}\,m^3/s$)

FIG. 5.13

EFFECT OF PARTICLE SIZE ON THE FLOW PATHS IN NOZZLE 2 AT HIGH FLOW RATE ($19{\cdot}56 \times 10^{-4}$ m^3/s)

FIG. 5.14

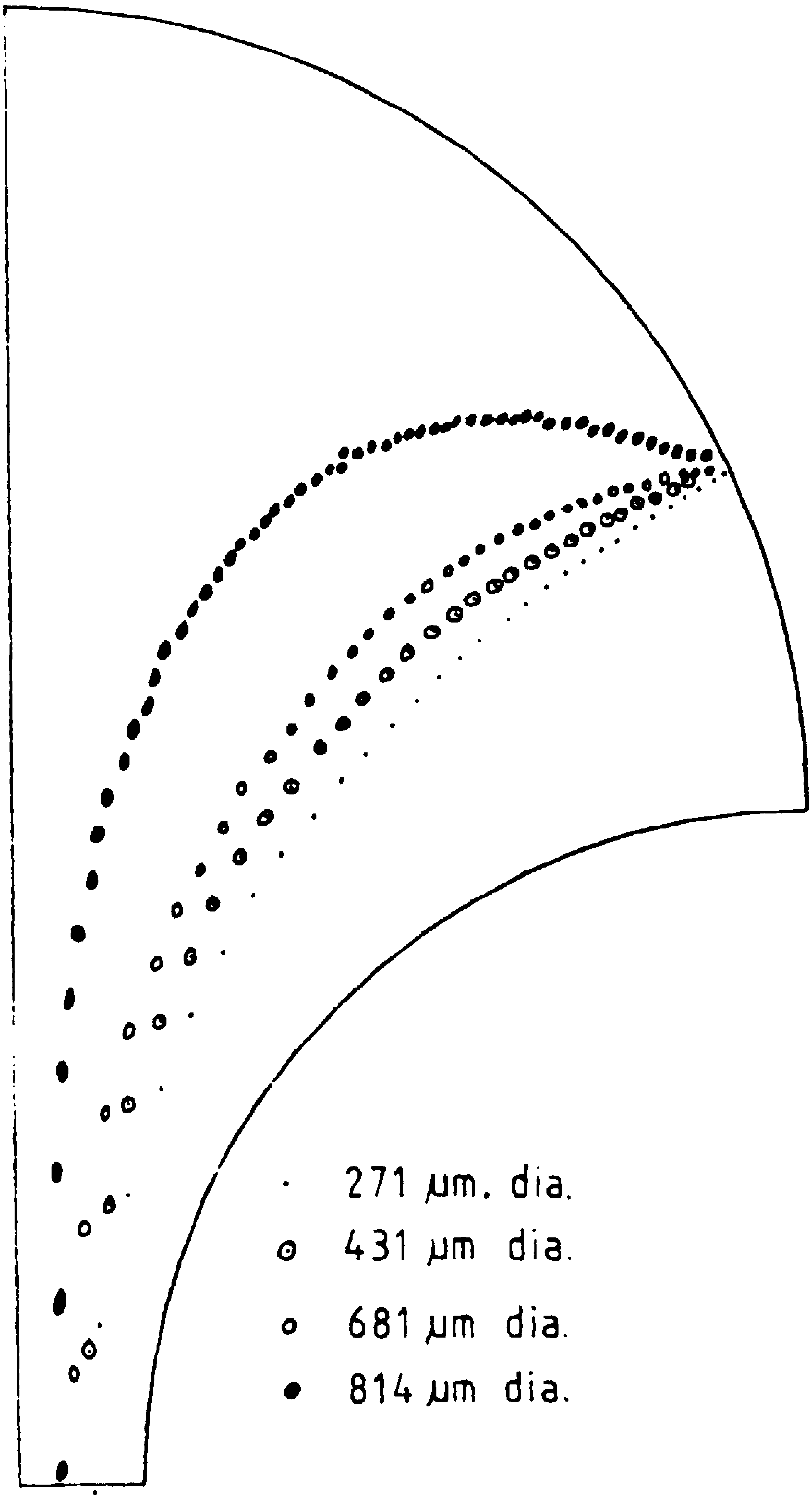

EFFECT OF PARTICLE SIZE ON THE FLOW PATHS IN NOZZLE 1 AT $7{\cdot}33 \times 10^{-4}$ m^3/s

FIG. 5. 15

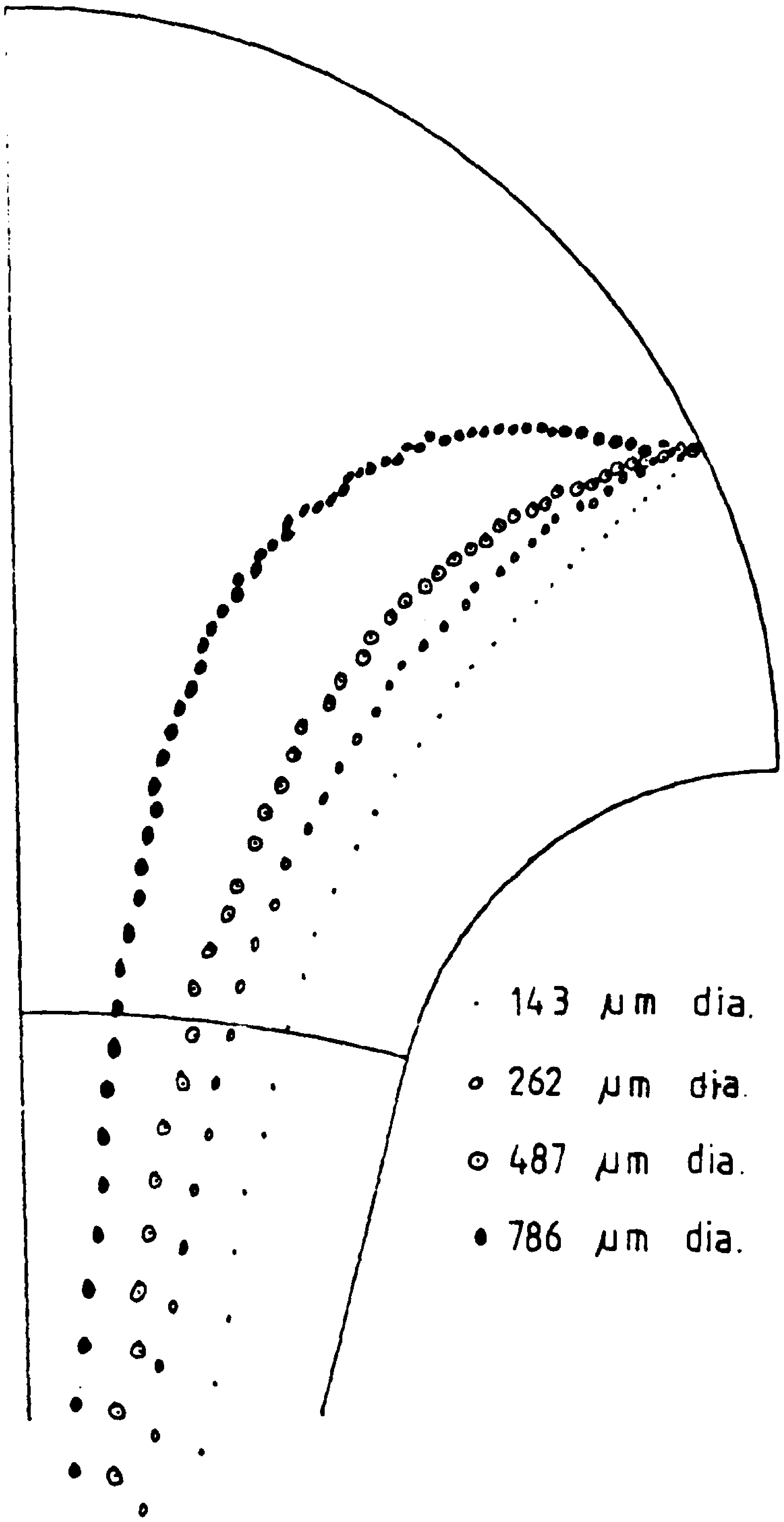

EFFECT OF PARTICLE SIZE ON THE FLOW PATHS IN NOZZLE 2 AT $7{\cdot}58 \times 10^{-4}\,m^3/s$

FIG. 5. 16

Therefore, to see the effect of velocity has involved selecting similar sized bubbles from different experiments. Fig. 5.17 shows the paths of bubbles about 250 μm diameter at three different flow rates, in nozzle 1. The greater the flow rate the nearer was the flow path to the nozzle wall. The same effect was seen from similar sized bubbles in nozzle 2, (fig. 5.18).

At bubble sizes of about 700 μm diameter the flow paths through nozzle 1 at lower flow rates were more distant from the nozzle wall than those at a high flow rate, (fig. 5.19). The results from nozzle 2 were similar except that at a flow rate of 7.58 x 10^{-4} m^3/s the bubbles were seen to rise initially in the upper part of the nozzle, (fig. 5.20).

5.2.2.2.3 EFFECT OF NOZZLE TYPE FOR THE SAME FLOW VELOCITY AND SAME BUBBLE SIZE

Differences between the behaviour of bubbles in nozzle 1 and nozzle 2 have already been indicated. However, a direct comparison is seen by considering the flow, at high velocity of bubbles starting from the 65^o position. In nozzle 1, (fig. 5.21) the bubbles hit the surface near the tangent point. The most marked effect was in the lower part of the nozzle.

In nozzle 2, (fig. 5.22), the bubbles did not hit the surface and the paths in the lower part of the nozzle were almost linear.

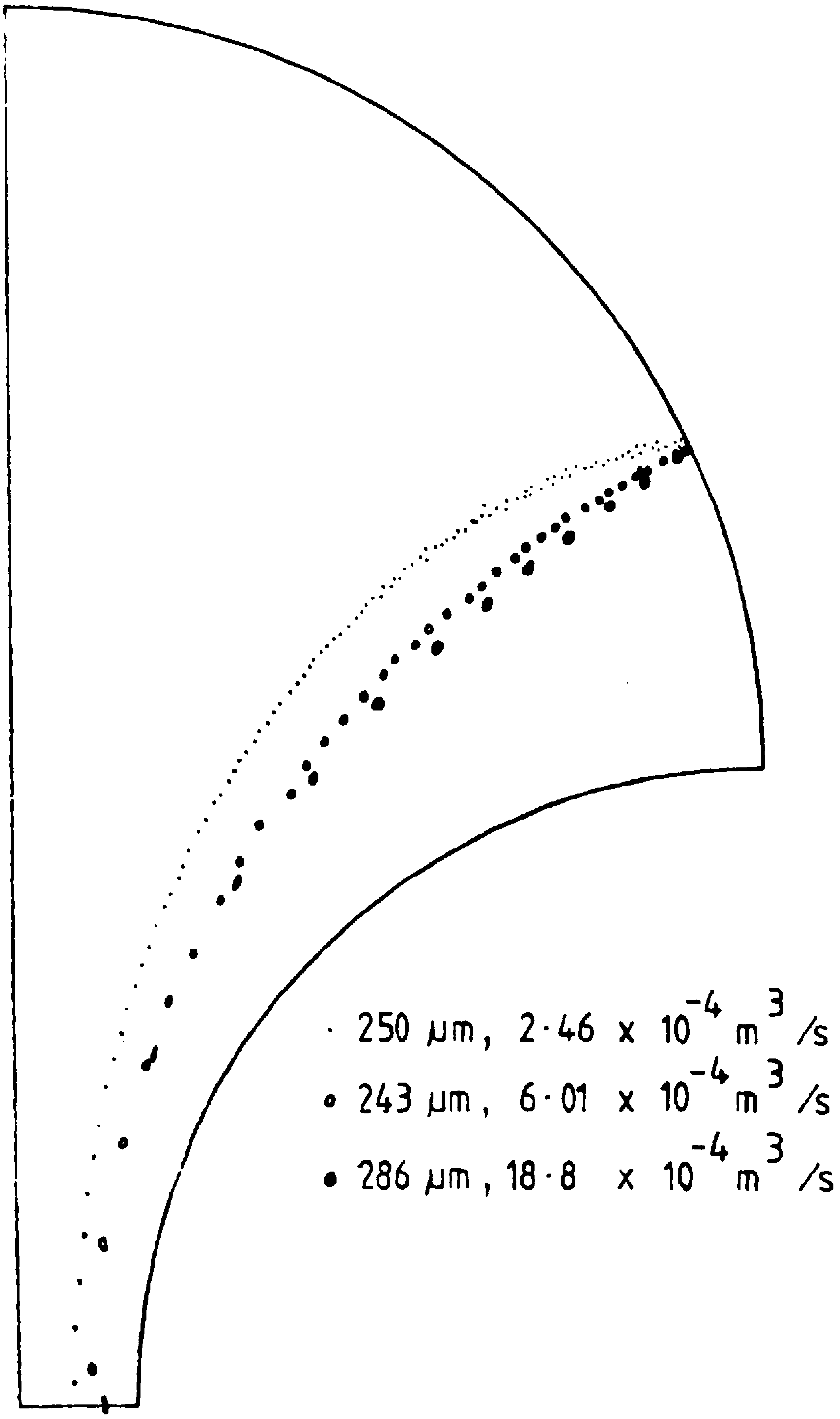

EFFECT OF FLOW VELOCITY ON THE FLOW PATHS IN NOZZLE 1

FIG. 5.17

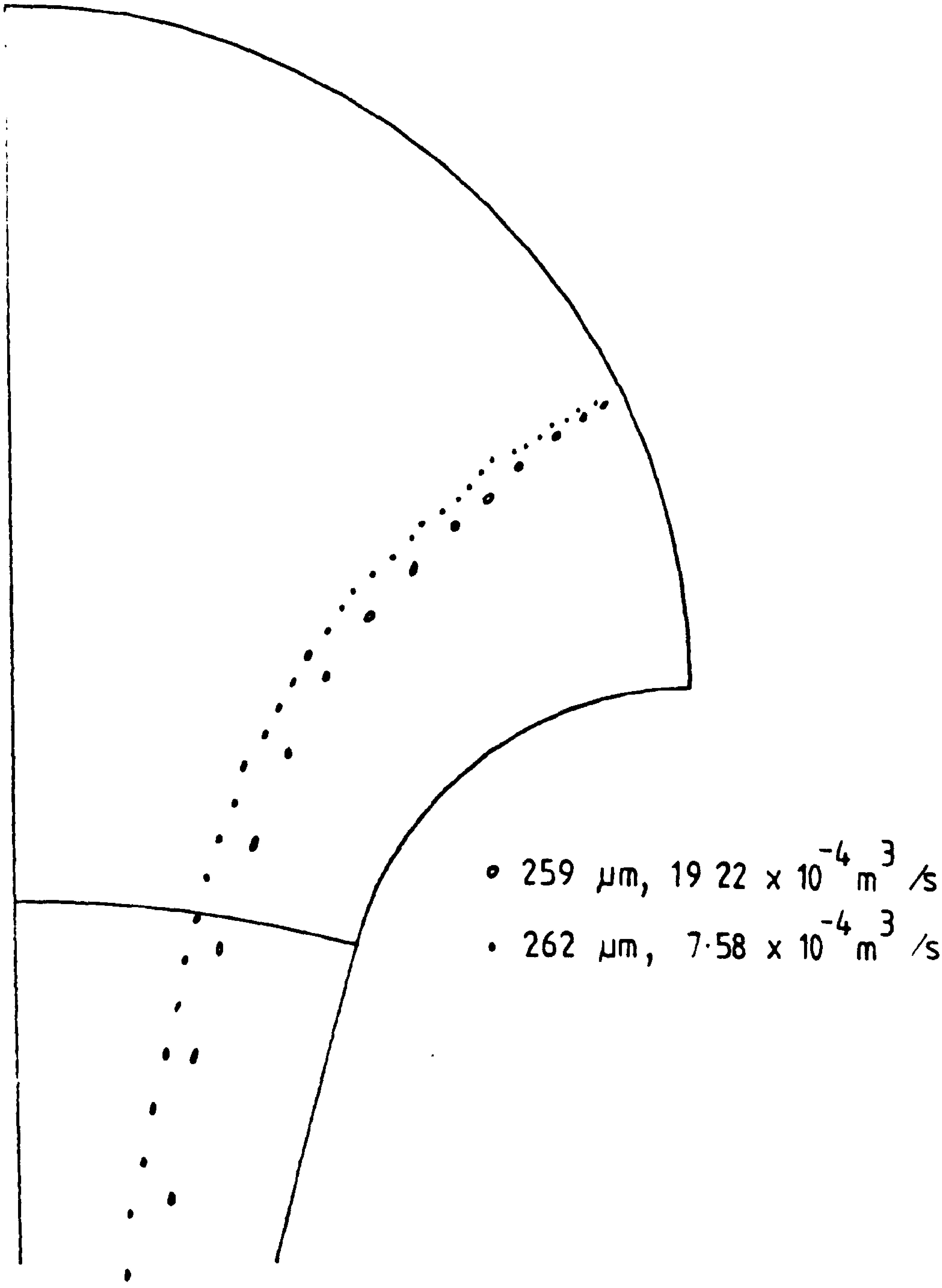

EFFECT OF FLOW VELOCITY ON THE FLOW PATHS IN NOZZLE 2

FIG. 5. 18

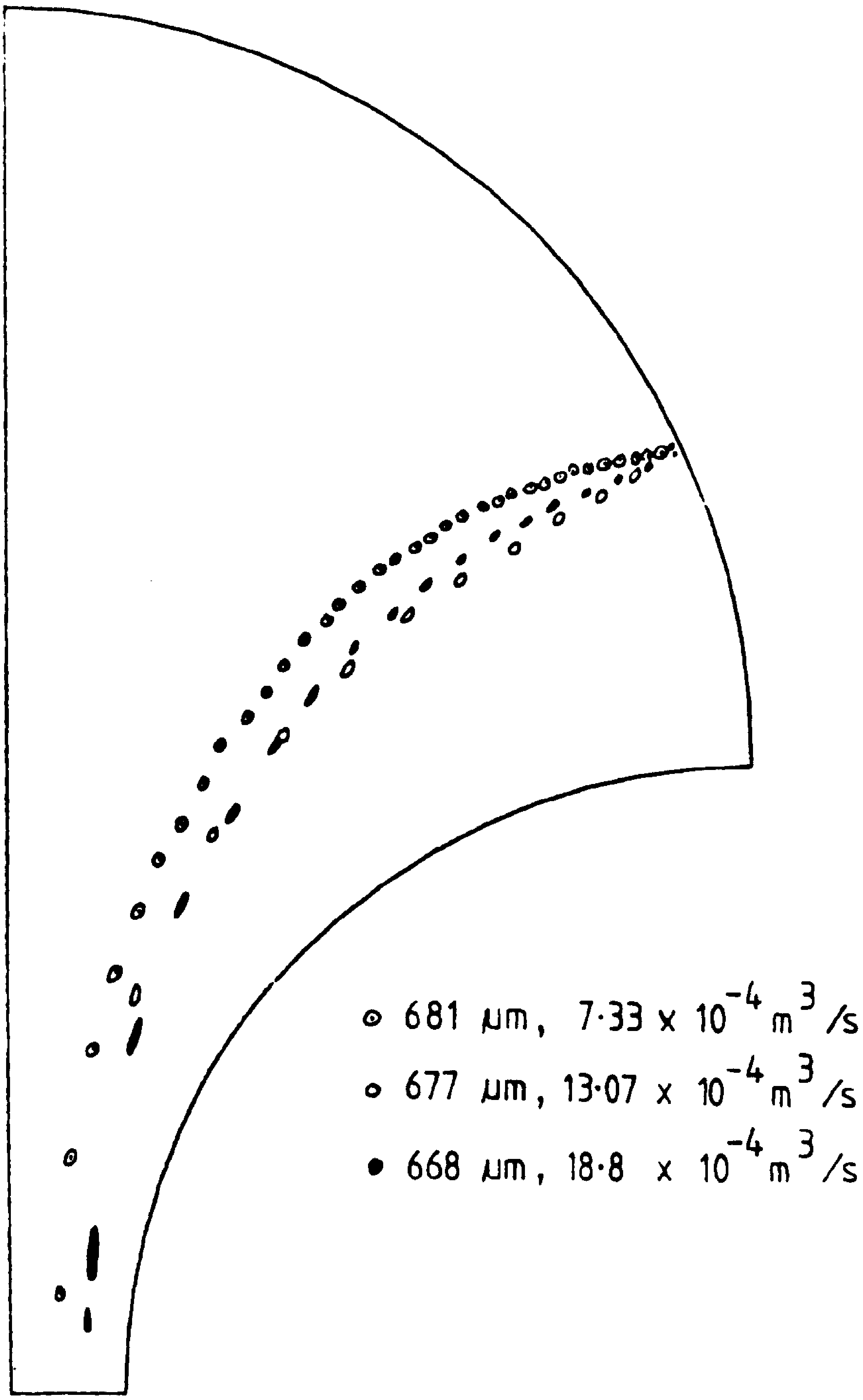

EFFECT OF FLOW VELOCITY ON THE FLOW PATHS IN NOZZLE 1

FIG. 5. 19

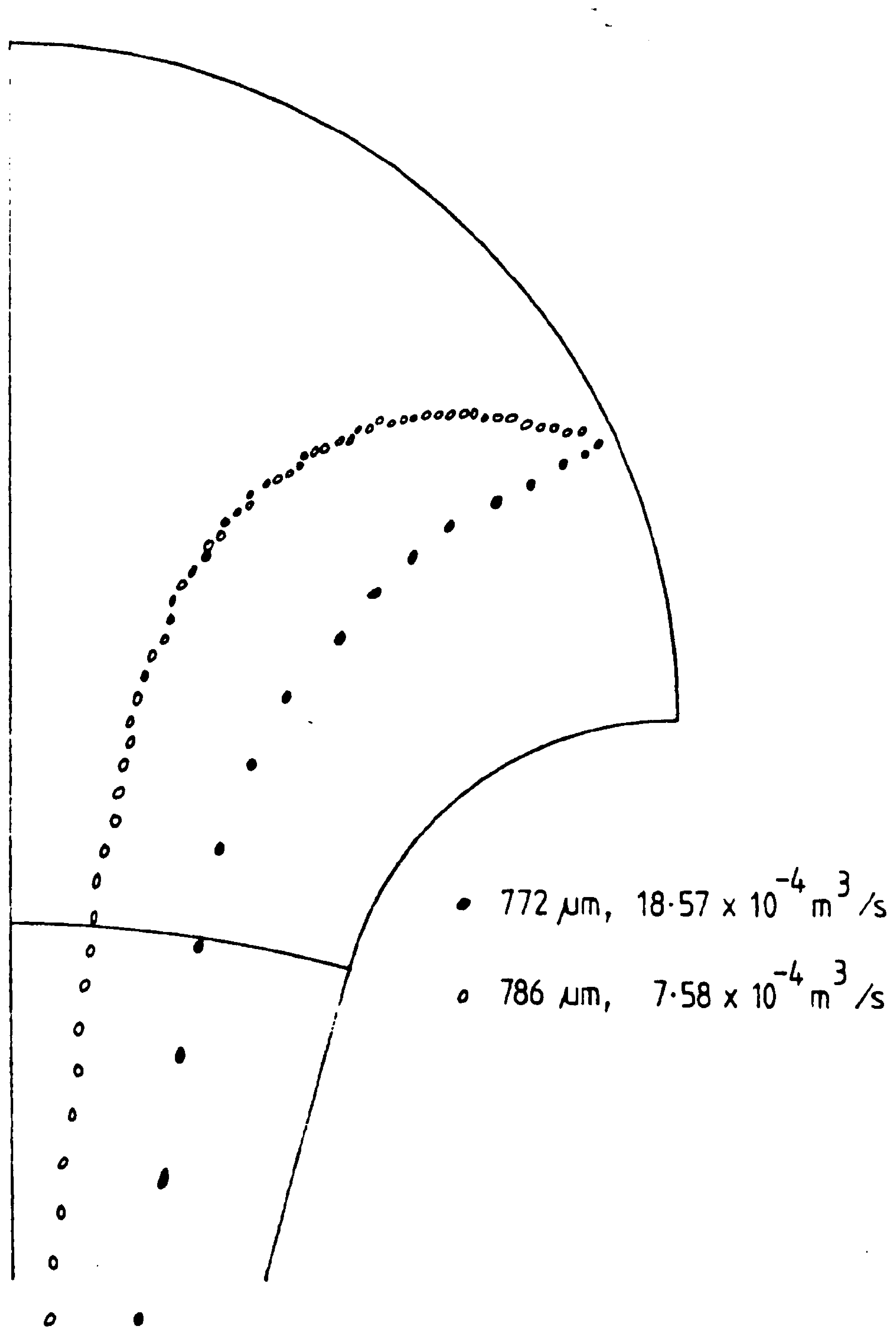

EFFECT OF FLOW VELOCITY ON THE FLOW PATHS IN NOZZLE 2

FIG. 5. 20

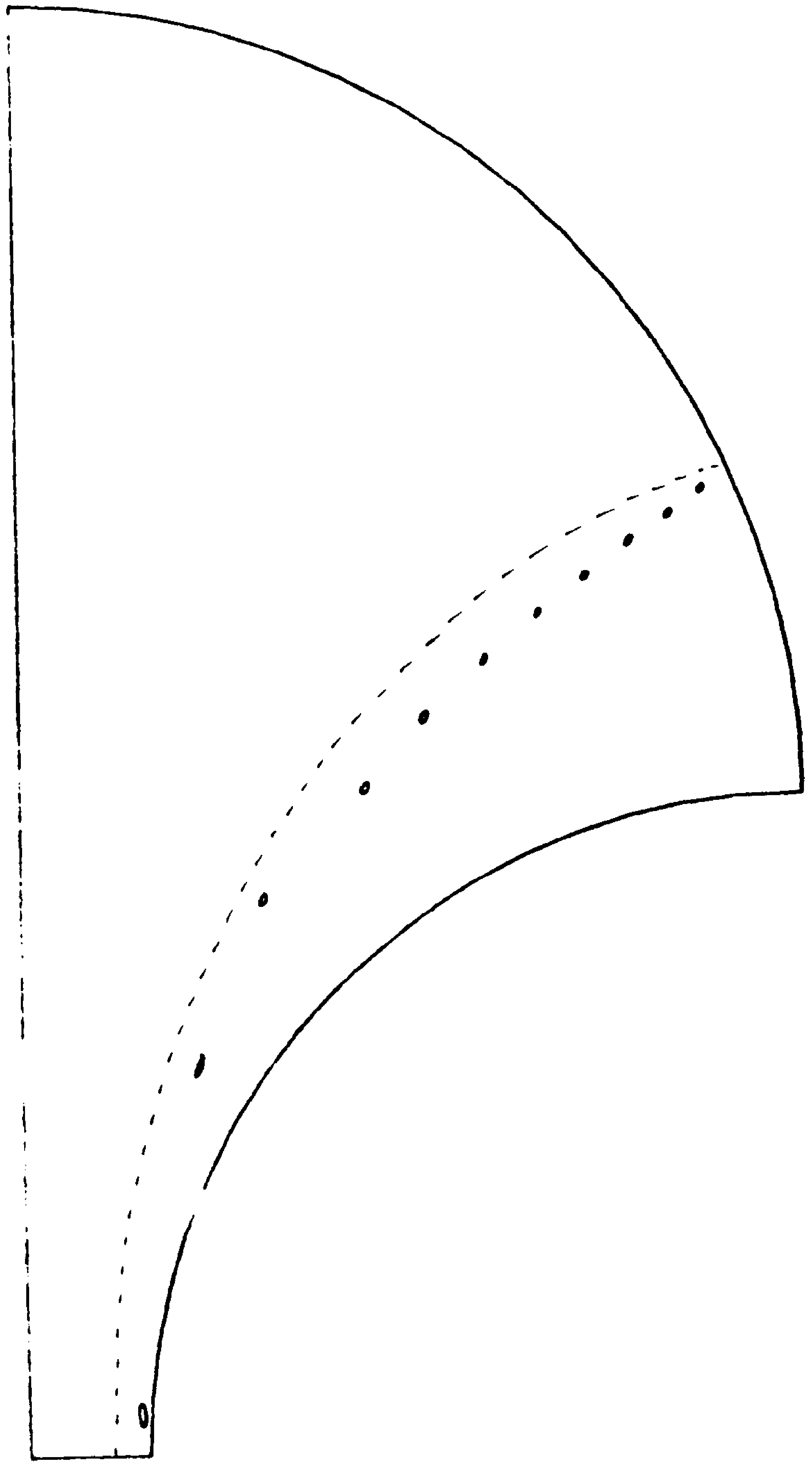

357 µm PARTICLES HITTING THE NOZZLE 1
SURFACE AT 19·32 x 10^{-4} m^3/s

FIG. 5. 21

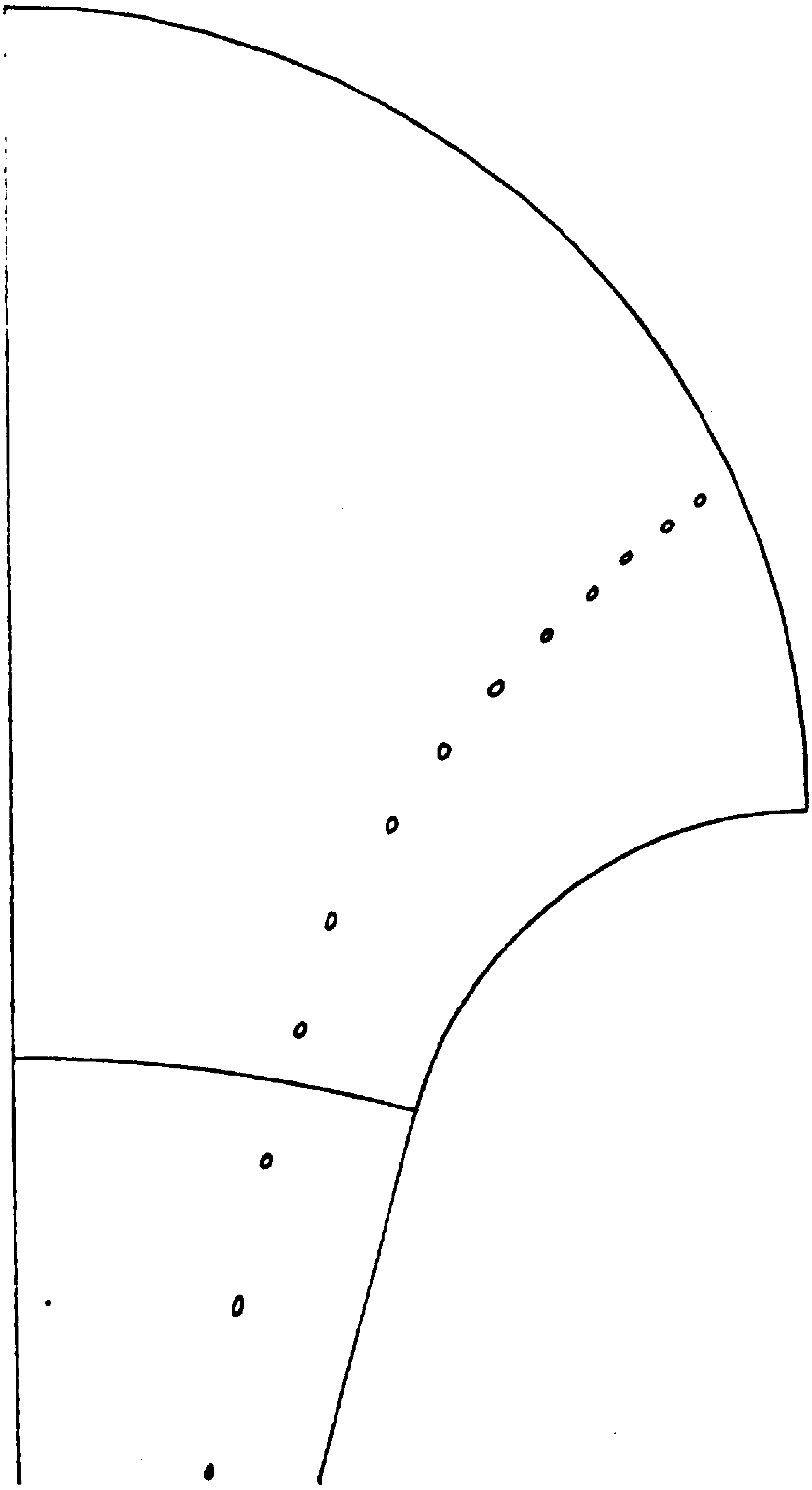

330 μm PARTICLES MISSING THE SURFACE OF NOZZLE 2 AT 18·57 x 10^{-4} m^3/s

FIG. 5. 22

5.3 VELOCITY PROFILES

Experimental evidence of the change in velocity through the nozzles could be obtained from the traces from the cine films. Taking the results from separate experiments with a flow rate of 19 x 10^{-4} m^3/s velocity profiles have been obtained for three different flow paths. Fig. 5.23 shows the profiles for nozzle 1 and fig. 5.24 shows those for nozzle 2. In both nozzles the final exit velocity was 3 m/s but in nozzle 2 the important velocity is that at the end of the curved flow part of the nozzle. This was 0.95 m/s as shown in fig. 5.24.

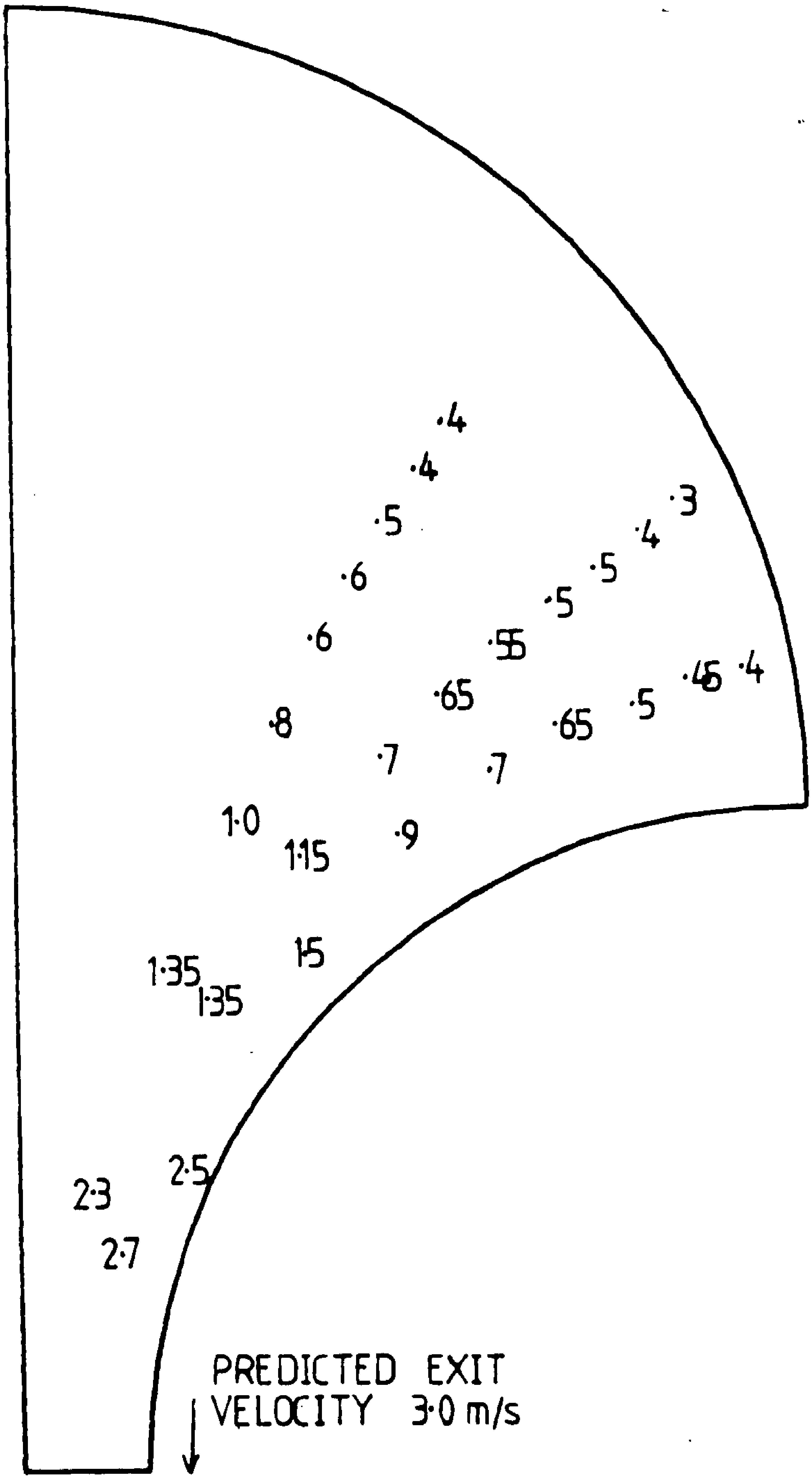

PREDICTED EXIT VELOCITY 3·0 m/s

VELOCITY PROFILES IN NOZZLE 1
(m/s)

FIG. 5.23

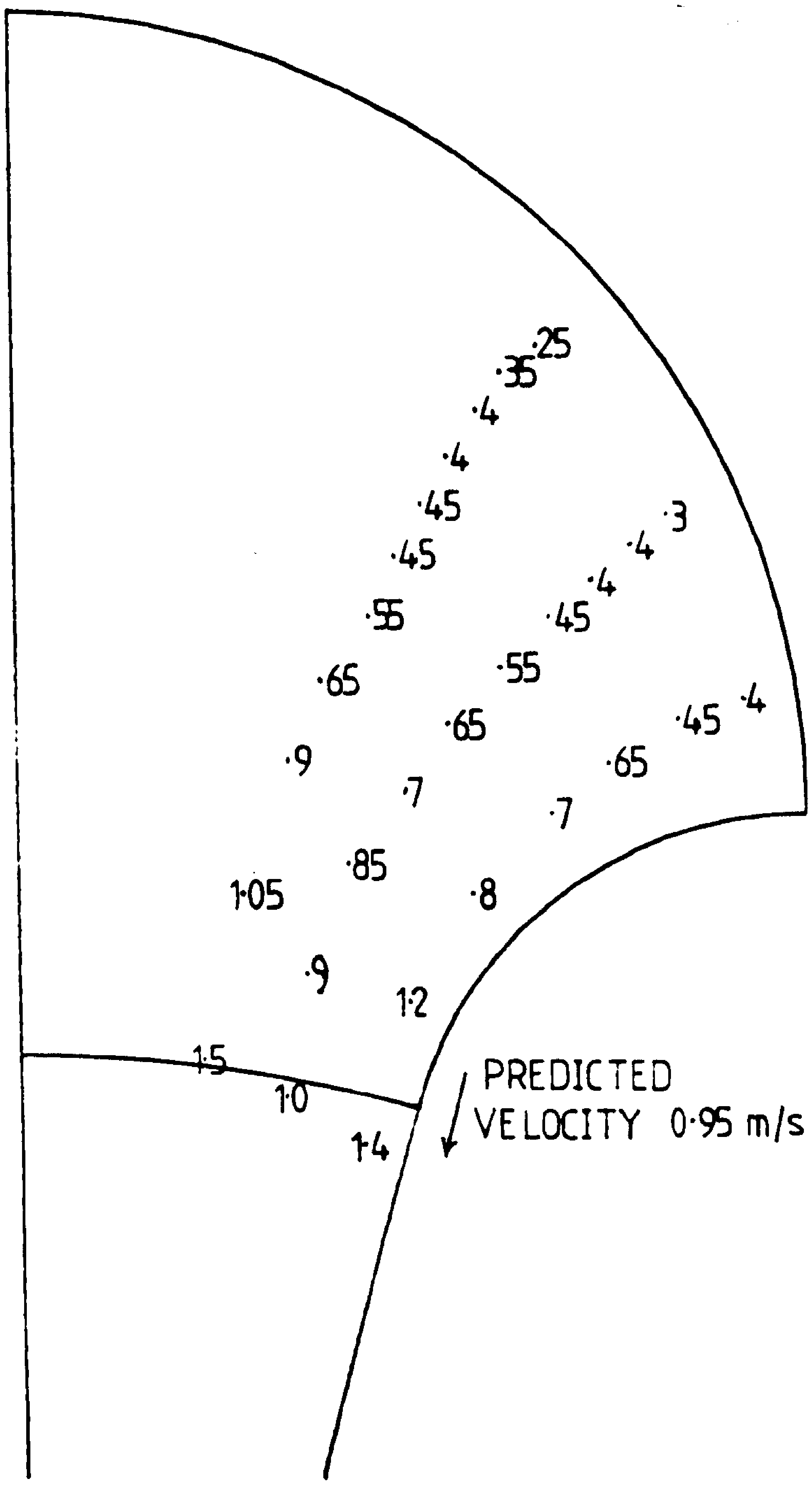

VELOCITY PROFILES IN NOZZLE 2
(m/s)

FIG. 5.24

6. THEORETICAL ANALYSIS AND RESULTS

6.1 POTENTIAL FLOW MODEL

Two dimensional flow through the experimental nozzles is analogous to the electrostatic field generated by two infinitely long parallel filaments of charge. Equipotential lines in such a field are cylindrical surfaces about axes which lie parallel to the lines of charge and in the same plane but at increasing distances from each filament. The basic geometry is discussed by Scott, (ref.92)

Fig.6.1 shows the cross-section of the field with the filaments at (x_o, 0) and ($-x_o$, 0). The field is symmetrical about the plane equidistant from the filaments and two equipotential surfaces - drawn as full lines - are shown in the figure either side of this plane. The radius of the equipotential surface drawn closest to the filament is R. The lines of force in the field lie along cylindical surfaces whose axes lie in the plane equidistant from the filaments such that all the surfaces pass through the filaments. These surfaces are shown in the figure as dashed lines. The surfaces of force and the equipotential surfaces are, of course, orthogonal.

In a similar fashion, the streamlines and the potential lines in the flow of an ideal fluid are orthogonal surfaces. The analogy between the electrostatic field around two filaments and the ideal fluid flow through the experimental nozzles then arises because the curved sides of the nozzles are

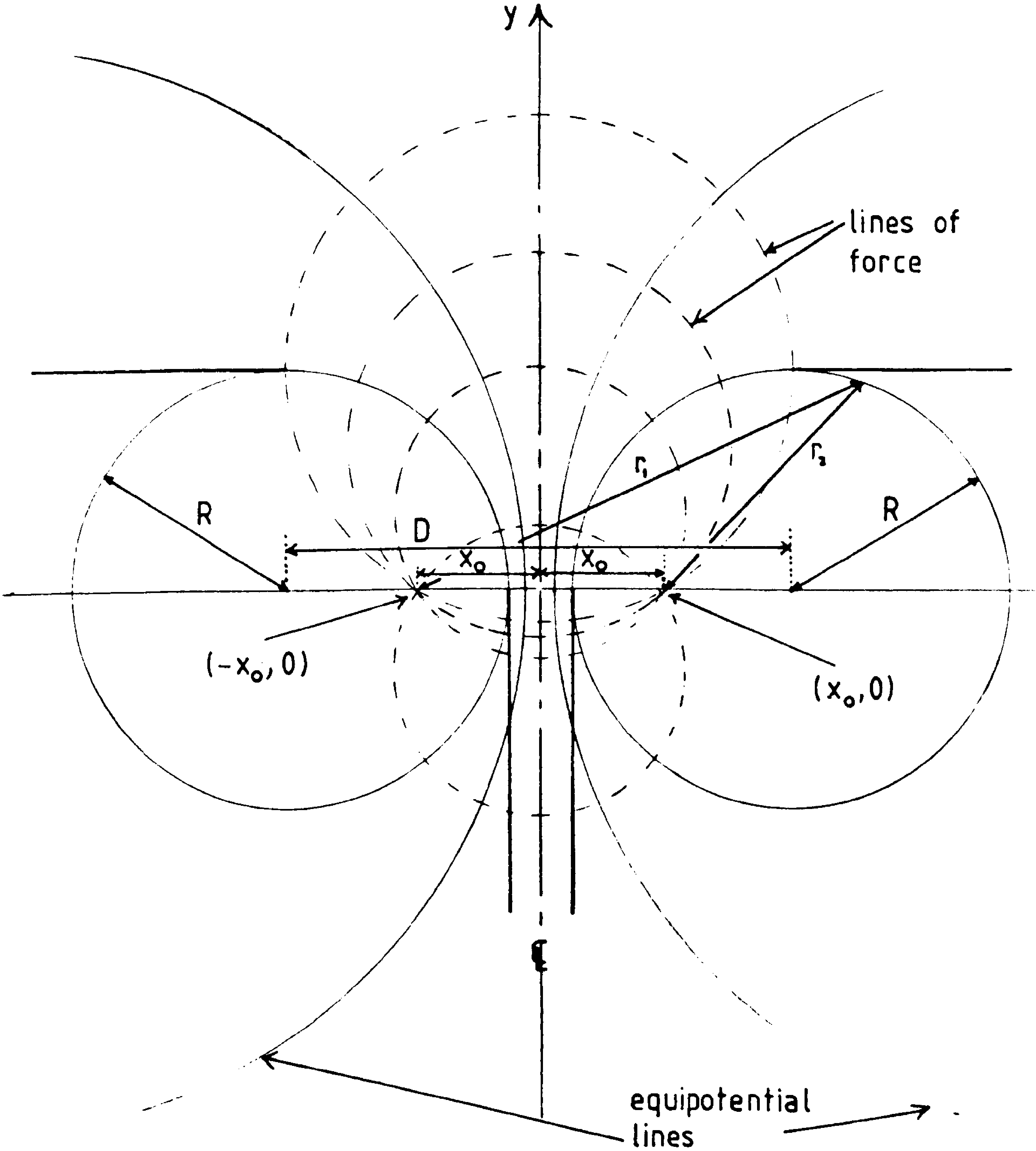

SYSTEM OF EQUIPOTENTIAL LINES AND THE ORTHOGONAL LINES OF CURRENT IN AN ELECTROSTATIC FIELD GENERATED BY TWO WIRES OF RADIUS 'R' (ref. 92)

FIG. 6.1

streamlines of radius R and the symmetry of the nozzle is identical to the symmetry of the field.

The equations derived by Scott for the potential surfaces in the electrostatic field can thus be used to describe the streamlines in the ideal fluid flow. Similarly, the flow area across any equipotential surface per unit length of the 2-dimensional nozzle can be calculated from the length of the corresponding dashed lines of force in figure 6.1 between the electrostatic potential surfaces of radius R.

The following is a summary of the treatment given by Scott for the electrostatic field.

Each equipotential line is specified by defining a constant k such that,

$$\frac{r_2^{\,2}}{r_1^{\,2}} = k^2 - \frac{(x + x_o)^2 + y^2}{(x - x_o)^2 + y^2} \qquad (6.1)$$

$$\text{or} \quad \left\{ x - \left(\frac{k + 1/k}{k - 1/k} \right) x_o \right\}^2 + y^2 = \frac{4\ x_o^{\,2}}{(k - 1/k)^2} \qquad (6.2)$$

The centre of curvature of the potential line is given by:-

$$x_1 = x_o \left(\frac{k + 1/k}{k - 1/k} \right) \qquad (6.3)$$

and the radius of curvature is given by:-

$$r_{curv} = \frac{2\ x_o}{(k - 1/k)} \qquad (6.4)$$

or the curvature ζ as

$$\zeta = \frac{(k - 1/k)}{2\ x_o}$$

When applying this stream function by analogy to fluid flow through a nozzle, fluid streamlines correspond to the calculated equipotential lines, and the potential lines correspond to the lines of force. Further discussion will therefore refer to fluid streamlines and potential lines.

The constant x_o can be found from the known surface geometry. If $D = 2\ x_1 = 2\ R + W$ then,

$$x_o = 1/2\ (D^2 - 4\ R^2)^{1/2}$$

These relationships provide sufficient knowledge for the relevant value of the streamline constant k to be calculated for any given pair of x and y values in the flow field. Once k is determined we can find all the points on the same streamline.

6.1.1 CALCULATION OF Θ, THE ANGLE SUBTENDED BY THE STREAMLINE TANGENT AT THE CENTRE

The common point on all the potential lines is (x_o) so that for any point x, y in fig. 6.2 on page 6.6

$$r_{pot}{}^2 = x_o{}^2 + y_o{}^2$$

therefore $x^2 + (y - y)^2 = x_o{}^2 + y_o{}^2$

therefore $$y_o = \frac{x^2 + y^2 - x_o}{2\ y_i}$$

Also
$$\tan\theta = \frac{x}{y - y_o}$$
from which θ can be calculated.

6.1.2 CALCULATION OF THE ANGLE SUBTENDED AT THE CENTRELINE BY THE INTERSECTION OF A POTENTIAL LINE AT THE NOZZLE SURFACE

From fig. 6.2.
$$\tan\alpha_1 = \frac{y_o}{R + W/2}$$

and
$$\tan\alpha_2 = \frac{R_{pot}}{R}$$

therefore
$$\underline{\underline{\alpha = \tan^{-1}\alpha_1 + \tan^{-1}\alpha_2}}$$

6.1.3 CALCULATION OF THE LOCAL FLUID VELOCITY

All points on a given potential line have the same velocity, which is related to the exit velocity by the ratio of the exit nozzle width and the arc length of the potential line;

$$\text{arc length} = R_{pot} \cdot \alpha$$

If the exit velocity is v_{exit}

then
$$\frac{v_{local}}{v_{exit}} = \frac{W/2}{R_{pot} \cdot \alpha}$$

therefore
$$v_{local} = v_{exit} \cdot \frac{W}{2\, R_{pot} \cdot \alpha}$$

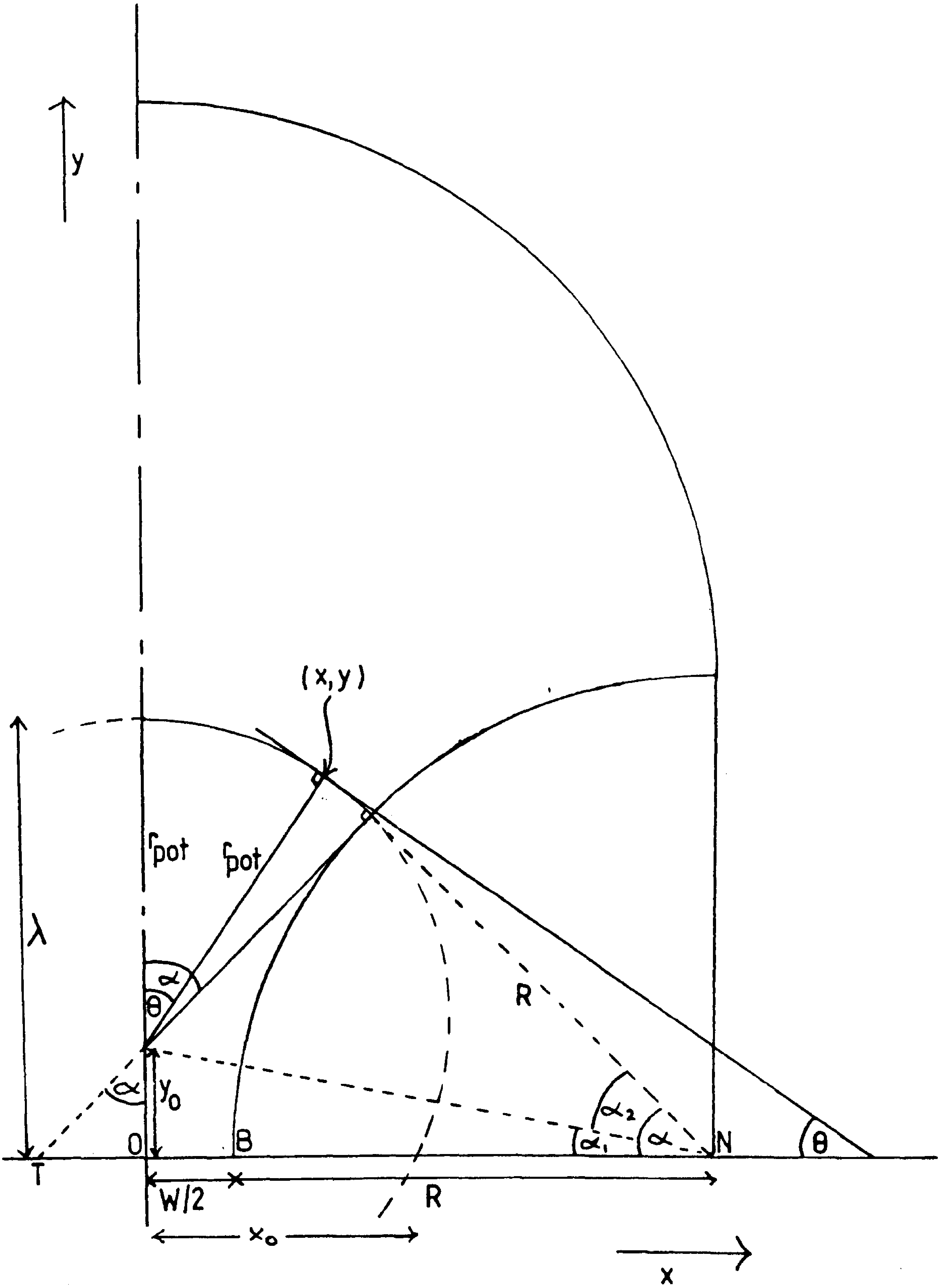

THE GEOMETRY OF A POTENTIAL LINE ASSOCIATED WITH POINT x y IN THE POTENTIAL FLOW FIELD

FIG. 6.2.

6.1.4 CALCULATION OF SUCCESSIVE POINTS ON A STREAMLINE

Knowing all the various constants for a specific streamline, any other point on the same streamline can be found by changing the x value and calculating the new y value. A more consistent approach, however, is to specify an arc length dz along the streamline. A new value of x can be found since,

$$\sin \theta = x/dz \qquad (6.16)$$

after which the new y value can be calculated. This produces a uniform movement along the streamline. A difficulty occurs near the nozzle exit in nozzle 1 at very low values of θ. Here, it is convenient to decrease the y value then calculate the new x value.

6.2 EMPIRCAL NON-TURBULENT FLOW MODEL

The potential flow model adequately predicts the path of small bubbles near the surface of the nozzle, when θ at the entry position is between 80° and 90°. At more distant paths there is a deviation from the potential flow lines. Fig. 6.3 for nozzle 1 and fig. 6.4 for nozzle 2 show the observed paths from the starting position corresponding to θ values of 45°, 70°, 75°, 80°, and 85°. Superimposed on these are the paths of small bubbles predicted by the potential model. The actual paths are nearer the nozzle surface than predicted, the greatest deviation being shown by the pathlines starting from the position $\theta = 45^\circ$.

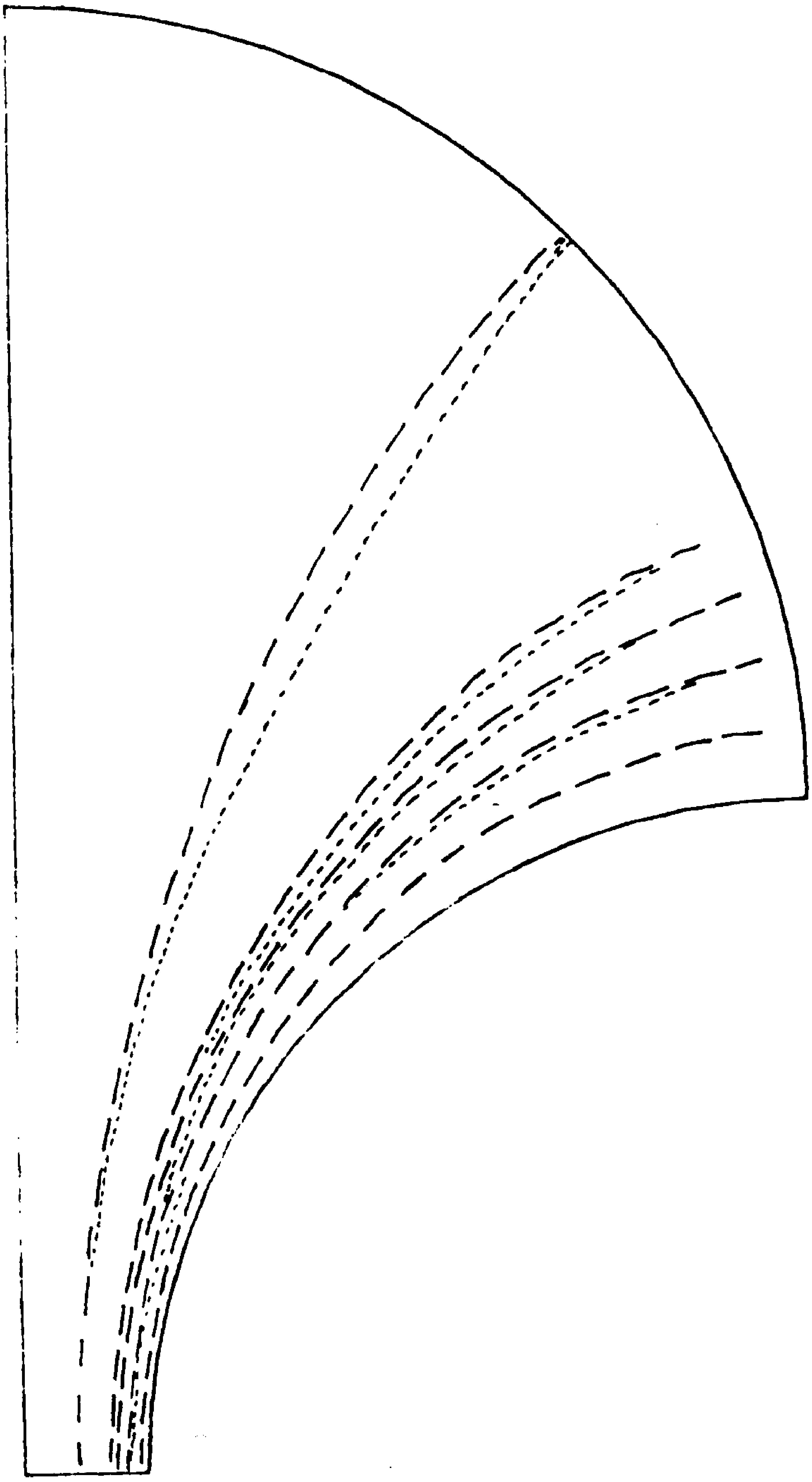

COMPARISON OF POTENTIAL FLOW LINES AND ACTUAL PATHLINES OF SMALL BUBBLES IN NOZZLE 1

FIG. 6. 3

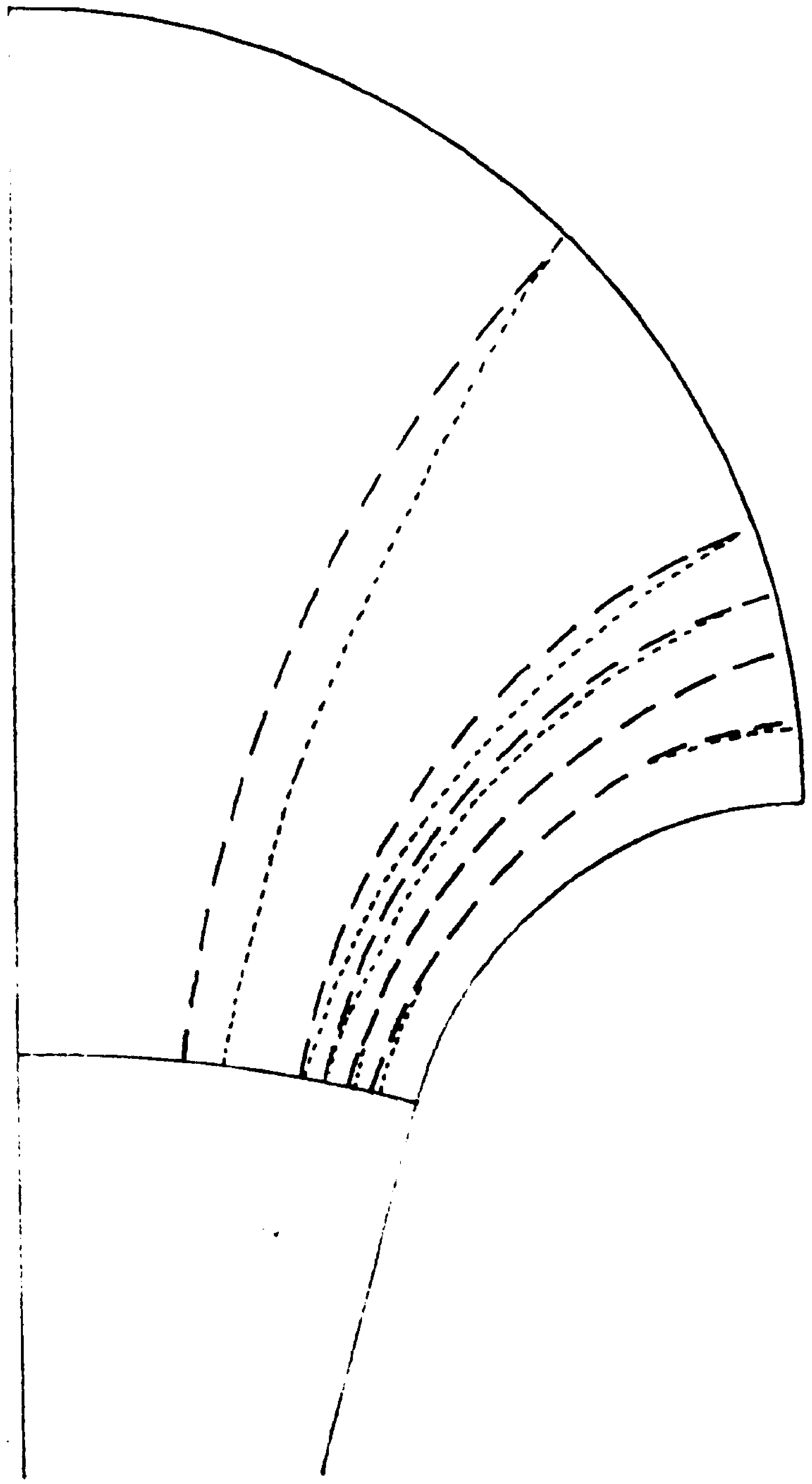

COMPARISON OF POTENTIAL FLOW LINES AND ACTUAL PATHLINES OF SMALL BUBBLES IN NOZZLE 2

FIG. 6.4

The potential model is suitable for studies of nozzle blockage since it is from flow paths near the surface that particles make contact with the nozzle wall. However, a further analysis needs to consider the observed deviations. This can be done by relating the deviation in x value (x_{act} - x_{st}) at a y value associated with the starting position on the entry arc, (y_{entry} - y_{act}). These deviations, measured from fig. 6.3 and 6.4, at a 45° start are shown in table 6.1. similar data from the other starting positions have enabled polynomial curve fits to be produced, giving the predictions for (x_{act} - x_{st}) shown in table 6.2. these formulae can be further used so that the coefficients a, b, and c are related to the streamline constant k at the entry position, k_{entry}. The best fit polynomials are shown in table 6.3. Predicted values of the deviation in x value are shown with the actual values in table 6.1.

Given the above predictions, the track of small particles can be analysed in terms of the potential model. When the potential model at present increases the x value as the particle travels through the nozzle, and then calculates the y value, the empirical model must calculate the x value as follows:-

$$\begin{aligned} x \; = \; & f_1 \text{ (y from the potential model)} \\ & + \; f_2 \, (k_{entry}) \; + \; f_3 (k_{entry}) \; y_{entry} - y_{act} \\ & + \; f_4 \, (k_{entry} \quad (y_{entry} - y_{act})^2 \end{aligned} \qquad (6\ 17)$$

where f_2, f_3, and f_4 are the polynomials predicting

NOZ 1			NOZ 2		
$(y_{entry} - y)$	$(x - x_i)$ act.	pred.	$(y_{entry} - y)$	$(x - x_i)$ act.	pred.
2.18	0.5	2.93	2.18	0.1	0.87
12.18	2.5	2.43	12.18	3.0	2.76
22.18	3.5	2.76	22.18	5.0	4.29
32.18	3.75	3.0	32.18	6.0	5.46
42.18	4.0	3.18	42.18	6.5	6.26
52.18	4.0	3.28	52.18	6.25	6.7
62.18	3.5	3.31	62.18	6.25	6.78
72.18	3.0	3.27	72.18	6.0	6.5
82.18	2.75	3.15	82.18	5.75	5.86
92.18	2.25	2.96	92.18	5.0	4.85
102.18	2.0	2.69	97.18	4.5	4.21
112.18	2.0	2.36			
122.18	1.5	1.94			
132.18	1.5	1.46			
142.18	1.25	0.9			
147.18	1.25	0.6			

TABLE 6.1 DEVIATIONS OF THE OBSERVED PATHS OF SMALL BUBBLES AND THE STREAMLINES IN POTENTIAL FLOW (μm)

NOZ 1

$\underline{45^{\circ}}$

$$x_{act} - x_i = 1.938 + 0.045(y_{entry} - y) - 0.000368\,(y_{entry} - y)^2$$

$\underline{70^{\circ}}$

$$x_{act} - x_i = 2.179 - 0.0232(y_{entry} - y) + 0.00011(y_{entry} - y)^2$$

$\underline{75^{\circ}}$

$$x_{act} - x_i = 2.566 - 0.0499(y_{entry} - y) + 0.000296(y_{entry} - y)^2$$

$\underline{80^{\circ}}$

$$x_{act} - x_i = 0.685 + 0.00937(y_{entry} - y) - 0.000135(y_{entry} - y)^2$$

NOZ 2

$\underline{45^{\circ}}$

$$x_{act} - x_i = 0.414 + 0.215(y_{entry} - y) - 0.00181(y_{entry} - y)^2$$

$\underline{70^{\circ}}$

$$x_{act} - x_i = 1.23 + 0.139(y_{entry} - y) - 0.00264(y_{entry} - y)^2$$

$\underline{75^{\circ}}$

$$x_{act} - x_i = 0.587 + 0.0747(y_{entry} - y) - 0.00137(y_{entry} - y)^2$$

TABLE 6.2 POLYNOMIALS PROVIDING THE BEST CURVE FITS BETWEEN THE STREAMLINES IN POTENTIAL FLOW AND THE OBSEVED PATHS OF SMALL BUBBLES

NOZ 1

$$a = -26.53 + 40.72(k_{entry}) - 14.38(k_{entry})^2$$

$$b = 1.58 - 2.0(k_{entry}) - 0.624(k_{entry})^2$$

$$c = -0.0031 + 0.0033(k_{entry}) - 0.0008(k_{entry})^2$$

NOZ 2

$$a = -2.897 + 3.107(k_{entry}) - 0.635(k_{entry})^2$$

$$b = 0.532 - 0.232(k_{entry}) + 0.0235(k_{entry})^2$$

$$c = 0.0018 - 0.0037(k_{entry}) + 0.0088(k_{entry})^2$$

TABLE 6.3 BEST FIT POLYNOMIALS FOR THE COEFFICIENTS OF SPECIFIC STREAMLINE CURVE FITS constants a, b, and c in table 6.3.

No further analysis of this expression will be attempted here but differentiation will obtain the slope, from which the curvature can be calculated.

6.3 INCLUSION BEHAVIOUR MODEL

6.3.1 MATHEMATICAL FORMULATION

6.3.1.1 STOKES' LAW

The calculation for drag force assumes that the particle Reynolds Number (Re_p) is less than 2 or that the friction factor = $24/Re_p$. This is the creeping flow region where Stokes' Law applies and is only likely to apply at low particle sizes and low flow velocities.

6.3.1.2 NON-STOKES' REGIME

At Re_p values greater than 2 the friction factor is approximately equal to $18.5/Re_p^{0.6}$, (ref.83). The increased friction factor is the result of the turbulent wake behind the particle.

Therefore since $F_{drag} = C_d \times A_p \, (\rho u^2/2)$ (6.31)

where A_p is the projected area of the particle in the direction of flow,

$$F_{drag} = \frac{18.5}{(Re_p)^{0.6}} \quad \frac{\pi d^2}{4} \quad \frac{\rho u^2}{2} \qquad (6.32)$$

$$F_{drag} = \frac{18.5 \, . \, \pi \, . \, d^2 \, . \, \rho \, . \, u^2}{8 \, . \, \left(\frac{d \, . \, u \, . \, \rho}{\mu}\right)^{0.6}} \qquad (6.33)$$

$$F_{drag} = \frac{2.31 \cdot \pi \cdot d^2 \cdot \rho \cdot u^2 \cdot \mu^{0.6}}{d^{0.6} \cdot u^{0.6} \cdot \rho^{0.6}} \qquad (6.34)$$

$$\underline{F_{drag} = 2.31 \cdot \pi \cdot d^{1.4} \cdot \rho^{0.4} \cdot u^{1.4} \cdot \mu^{0.6}} \qquad (6.35)$$

6.3.1.3 HADAMARD'S CORRECTION

Also account must be taken of the possibility of gas circulation in the bubble. This has the effect of reducing the friction in a gas or liquid bubble in a fluid. Using Hadamard's Correction, (ref.93)

$$C_d = \frac{8}{Re_p} \times \frac{(2\mu_f + 3\mu_p)}{(\mu_f + \mu_p)} \qquad (6.36)$$

therefore $C_d = 16/Re_p$

or 2/3 of that for a solid particle in the same flow regime.

Using the friction models described above centripetal velocities have been calculated for hydrogen in water, (fig. 6.5), and for alumina in steel, (fig. 6.6). For solid alumina of course there is no need to consider the Hadamard correction. The increased friction at Re_p values greater than 2 are manifested by reduced centripetal velocties. The evidence from ref.83 suggests that for gas bubble diameters of the order of 1 mm the surface tension forces predominate and the bubble acts as though it was a solid. For this reason Hadamard's Correction was not incorporated into the mathematical model. However, both the Stokes' and non-

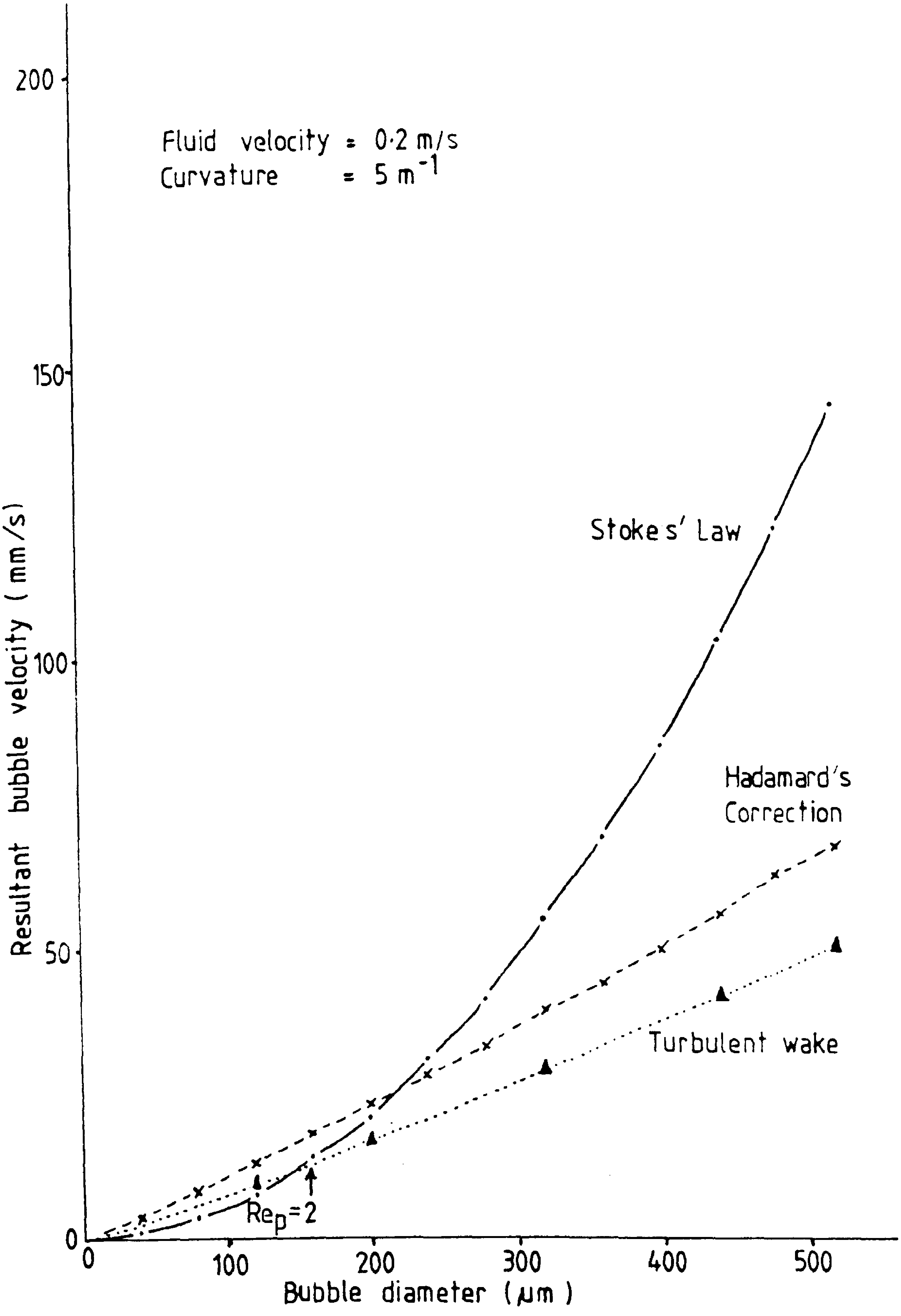

EFFECT OF DIFFERENT FLOW REGIMES ON THE CENTRIPETAL VELOCITY OF HYDROGEN IN WATER

FIG. 6.5

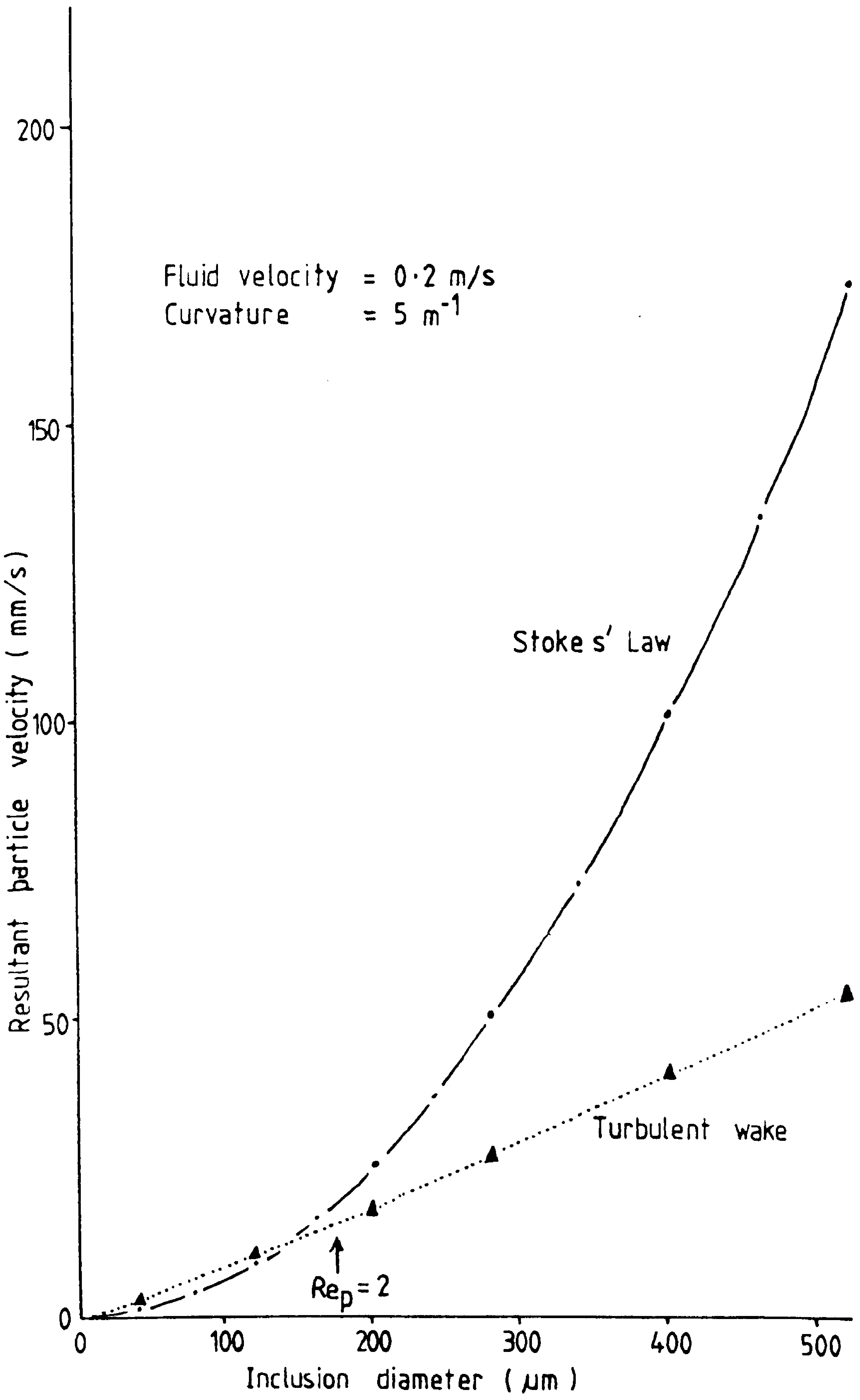

EFFECT OF DIFFERENT FLOW REGIMES ON THE CENTRIPETAL VELOCITY OF ALUMINA IN STEEL

FIG. 6.6

Stokes' friction models were used. In order to determine which friction model to use in the computer calculation the Re_p needed to be calculated from the centripetal velocity which was necessarily calculated from the Stokes' model. The results shown in figs 6.5 and 6.6 do, however, show that there is little difference in the values at low Re_p.

6.3.2 COMPUTER PROGRAMME (NUMERICAL ANALYSIS)

To predict the flow path of a particle through a nozzle a computer programme has been written in FORTRAN. Fluid flow paths have been modelled by the potential flow model. The movement of the particles under the influence of centripetal and gravitational forces has been modelled as described in section 3.5, by a separate subroutine. The Stokes' and non-Stokes' friction calculations have been included in the subroutine. A full copy of the programme for alumina in steel, (SCST), is given in the appendix. A similar programme has been written for hydrogen bubbles in water, (SCH2).

6.3.2.1 FORMAT OF THE PROGRAMME

The programme works with both nozzle 1 and nozzle 2. Variables called for in the input are:-

radius of curvature of the nozzle (mm)
nozzle diameter (mm)
bubble radius (mm)
streamline distance, dz (mm)
exit velocity (m/s).

There are three modes of operation.

1) A plot of the bubble pathline is carried out on a Gould plotter. Only the right hand side of the nozzle flow is plotted for convenience of presentation.

2) A print out of the pathline coordinates not only gives the x, y coordinates of the particle but also:-

a) the total time from the starting position

b) the local fluid velocity

c) the streamline curvature

3) A print out of the limiting θ/α ratio values. This determines the value of θ/α at which a bubble of a specific diameter just hits the nozzle surface at the tangent point.

The programme ends when the region of curved streamline flow ends.

6.3.2.2 NUMERICAL ANALYSIS

Two points on a given streamline are chosen, (x_n, y_n) and (x, y). The arc distance separating them is dz, chosen at the beginning of the programme. Streamline variables from the potential theory are calculated being the same for both points. The fluid velocity, and the resultant velocity of the bubble and its direction are calculated at each point from which average values are the calculated. These are then used to find the new bubble position, (x_c, y_c), which now becomes the new bubble coordinate (x_n, y_n) on a different streamline. Using this Eulerian method there was no significant difference in the bubble pathlines through the nozzle at dz values below 2 mm. Therefore a dz value of 2 mm was chosen for all subsequent work.

The size of the bubbles is taken into account by calculating the angle $\alpha - \theta$ and multiplying by the radius of the particular potential line to find the chord length, (CNTACT in the programme). This is very important at larger bubble sizes.

6.3.2.3 DIFFERENCES IN THE ALUMINA/STEEL PROGRAMME

The programme SCST for alumina in steel is essentially the same as SCH2 but allows a choice of inclusion density and liquid density. This makes it easy to model the movement of other inclusions in steel. Also by changing the liquid viscosity, any liquid, solid or gaseous inclusion in any liquid could be modelled.

Since the actual size of the steel nozzle is half the size of the water model the graphical plot has been doubled for ready comparison with plots from the water model.

6.3.3 RESULTS OF THE COMPUTER PROGRAMME

The format of graphical results from the programme are as shown in section 5.2. The original traces were single plots to avoid any movement of the nozzle axes during multiple plots. Print-outs of the pathline coordinates, streamline velocities and curvatures and of radial velocities provided more information and a typical example is shown in Table 6.4. A number of graphical results are also presented in Chapter 7 in the form of predicted bubble paths.

```
               Nozzle Radius =  80.00 mm
               Nozzle Width  =  30.00 mm
               Exit Velocity = 1.160 m/s
               Bubble Radius =  .2150 mm
               Increment     =  2.000 mm

   Total       Particle           Fluid      Curv.      Radial
   time        position           vel.      (/mm)        vel.
   taken       x          y       (m/s)                 (m/s)
   (s)        (mm)       (mm)

   .017      84.27     120.03     .118     .00754      .0410
   .126      72.10     117.52     .137     .00714      .0409
   .220      60.89     112.91     .159     .00680      .0409
   .300      50.71     106.52     .187     .00650      .0408
   .369      41.59      98.59     .221     .00624      .0407
   .426      33.57      89.35     .266     .00601      .0406
   .473      26.63      78.98     .325     .00583      .0404
   .511      20.78      67.66     .406     .00569      .0403
   .541      16.00      55.53     .517     .00559      .0402
   .565      12.29      42.72     .668     .00555      .0404
   .583       9.65      29.31     .857     .00560      .0418
   .597       8.11      15.30    1.052     .00575      .0453
   .604       7.76       6.97    1.137     .00592      .0482
   .608       7.74       3.39    1.154     .00599      .0491
```

Table 6.4 : Typical output of results from the computer programme for hydrogen bubbles in water.

7 DISCUSSION

7.1 ACCURACY AND QUALITY OF EXPERIMENTAL RESULTS

The purpose of this work has been to discover whether the movement of inclusion towards the centre of curvature in curved nozzle flows makes a significant contribution to the clogging of nozzles used to meter flows in the continuous casting of steel. Before any conclusion can be drawn from the theoretical and experimental work that has been carried out, it is necessary to assess the accuracy of the experimental and theoretical results.

For consideration of experimental errors the following notation will be used:-

the absolute error of variable A = e(A) defined as the difference between the true value A^* and the approximation A,

therefore $e(A) = A - A^*$ (7.1)

the relative error of variable A = r(A) defined as the proportion of the absolute error to the true value A^*.

In practice the approximation A is used so that:-

$$r(A) = e(A) / A \quad (7.2)$$

or the percentage error = $(e(A) / A) \times 100$ (7.3)

The propogation of errors has been calculated as follows:-

If $C = A + B$ or $C = A - B$

$$e(C) = e(A) + e(B)$$

If $C = A \times B$ or $C = A / B$

$$r(C) = r(A) + r(B)$$

7.1.1 BUBBLE SIZE MEASUREMENT

a) By microflash,

$$e(D) = 0.05 \text{ mm}$$

where e(D) is the absolute error as measured on the photograph, (generally at a magnification of x2.8).

Therefore for a small bubble whose image diameter was 0.5 mm, for which the real diameter would be 180 µm, the relative error would be:-

$$r(D) = 0.05/0.5 = 10\%$$

For a large bubble of 1.5 mm diameter (535 µm actual),

$$r(D) = 0.05/1.5 = 3.3\%$$

There is additional to this a variation of the sizes of bubbles generated. This has been taken into account by using the standard error of the estimate (ref. 94):-

$$\text{standard error} = \frac{t\sigma}{\sqrt{n}} \qquad (7.4)$$

where σ is the standard deviation

and n is the number of measurements

t is a factor denoting the level of confidence. (from tables, (ref. 94), t = 2.0 for 95% confidence has been used throughout)

The mean bubble sizes and standard errors tabulated in Table 5.2 on page 5.9 et. sequi. were calculated from the measurements made from the microflash pictures as described in section 4.4. These errors thus incorporate both the error of measurement and the variation in the sizes of bubbles generated. Examination of table 5.2 shows that the variation in measured bubble sizes are about 15% for the smaller bubbles falling to some 5% for the larger. Both these figures are greater than the corresponding assessed measurement error, suggesting that the variations in the sizes of bubbles produced is the predominant error.

There were periods, moreover, were the production of bubbles showed a high degree of instability. These periods were very apparent since a wide variation in bubble paths could be readily observed, with some large bubbles showing significant gravity buoyancy effects. No results, either for bubble sizes or for bubble paths, were taken under these conditions.

7.1.2 MEASUREMENT OF FLOW RATE

$$e(V) = 0.001 \text{ litres}$$

where $e(V)$ is the absolute error in the volume contained in the measuring cylinder, (either 8 or 10 litres). The small volume of water in the measuring manometer tube was included in the calibration to exclude any subsequent error.

Therefore $r(V) = 0.001/10$

or 0.01% in 10 litres,

or similarly 0.0125% in 8 litres.

Converting to m^3

$$10 \text{ litres} = 9.88859 \text{ kg}$$

$$= 9.88859 / 998.2 \text{ m}^3$$

and $8 \text{ litres} = 0.8 \times 9.88859 / 998.2 \text{ m}^3$

therefore $r(V) = 0.01\%$ of $9.90642 \times 10^{-3} \text{ m}^3$

and 0.0125% of 7.925×10^{-3} m^3

$e(t) = 0.1$ s (assessed experimentally)

where $e(t)$ is the absolute error of time measurement.

At 5 s (typical of high flow rate),

$$r(t) = 0.1/5.0 = 2.0\%$$

At 50 s (typical of a low flow rate),

$$r(t) = 0.1/50.0 = 0.2\%$$

Therefore the error in the flow rate V/t is given by,

$$r(V/s) < r(V) + r(t)$$

At low flow rate, where a 10 l volume is used,

$$r(V/s) = 0.01\% + 0.2\% = 0.21\%$$

At high flow rate, where an 8 l volume is used,

$$r(V/s) = 0.0125\% + 2.0\% = 2.01\%$$

7.1.3 MEASUREMENT OF PARTICLE POSITION

The position of particles and the shape of their flow paths were determined by projecting the cine film image down onto a horizontal surface, the height of the projector being adjusted until the image of the nozzle coincided with its traced actual shape on the surface. The following errors were assessed to result from this procedure:-

Error in copy of nozzle shape $e(sh) = 0.1$ mm
Error in setting up for tracing $e(tr) = 0.25$ mm
Error because of frame movement $e(mv) = 0.25$ mm

The error in the frame movement resulted from the mechanical behaviour of the Lafayette projector, no two adjacent images lying directly over one another. These errors applied for all measurements in the vertical direction and to horizontal positions at points removed from the surface. For horizontal position measurements made for points lying close to the nozzle surface, the image of the surface itself provided a more immediate point of reference. Errors due to the setting up of the tracing and to frame movement could be reduced substantially such that the overall accuracy of measurement was of the same order as that for copying the nozzle shape.

7.1.4 CALCULATION OF LOCAL VELOCITIES FROM THE PROJECTED TRACINGS

Errors in the measurement of local velocities along streamlines from the the cine film arise through errors in the position measurement and errors in the time measurement

As shown previously the time between successive frames is the inverse of the frame speed. At 63 fr/s $t = 0.015873$. The error in film speed was estimated as 1 fr/s.

Therefore $e(fr) = 1/63 - 1/64$

$= 0.00025$ s

therefore $r(fr) = 0.00025/0.015873$

$= 1.56\%$

Total error in the vertical distance measurement is given by:-

$$e(dist) = e(sh) + e(mv)$$

$$= 0.1 \text{ mm} + 0.25 \text{ mm}$$

$$= 0.35 \text{ mm}$$

If the distance measurement = 4 mm

$$r(dist) = 0.35/4.0 = 8.8\%$$

If the distance measurement = 40 mm

$$r(dist) = 0.35/40 = 0.88\%$$

Therefore the error in velocity is given by:-

$$r(v) < r(t) + r(dist)$$

If distance is 4 mm $r(v) < 1.56\% + 8.8\% = 10\%$

If distance is 40 mm $r(v) < 1.56\% + 0.88\% = 2.5\%$

7.1.5 CALCULATION OF THE EXIT VELOCITY FROM THE MEASURED FLOW RATE

To calculate the exit velocity the cross-section of the exit channel needs to be measured. This is less accurate than the other measurements because of the slight distortion of the perspex during machining and preparation.

Although the width and thickness were measured to a precision of + 0.01 mm with callipers a more realistic error is + 0.5 mm.

therefore, since area = width x thickness

$$\begin{aligned} r(area) &= r(width) + r(thick.) \\ &= 0.5/30 + 0.5/21.15 \\ &= 0.017 + 0.024 \\ &= 4\ \% \end{aligned}$$

to find the error in exit velocity

$$r(vel) = r(V/s) + r(area)$$

therefore at high flow rate

$$r(vel) = 0.1125\,\% + 4\,\% = 4.1\,\%$$

and at low flow rates

$$r(vel) = 0.02\,\% + 4\,\% = 4\,\%$$

7.1.6 ERRORS IN THE THEORETICAL RESULTS

As stated in Chapter 6, the numerical calculations were carried out using a range of decreasing values of the step length, dz, until predictions with two successive values agreed up to the third significant digit. This represented a computational error of the order of 0.1%, that is very much smaller than the experimental errors.

7.2 BEHAVIOUR OF THE EXPERIMENTAL APPARATUS

7.2.1 ESTABLISHMENT OF SMOOTHED FLOW CONDITIONS

The experimental apparatus was quite successful in creating a smooth nozzle flow in which the behaviour of individual bubbles and streams of similarly sized bubbles could be observed. Examination of Figure 3.23, on page 3:43, and Figure 3.17 on page 3:33, for example, shows that clearly defined stream lines were established in the nozzle even at Reynolds numbers up to 74000.

The existence of smoothed flow at such high Reynolds numbers was due to the presence of the dams and gauzes in the tundish, particularly the semi-circular gauze that can be clearly seen in Figure 3.12 on page 3:28. These removed all the pre-existing turbulence in the tundish so that the fluid entered the nozzle in laminar flow. Insufficient perturbations existed in the subsequent accelerating flow for turbulence to be established during the time that it took the fluid to flow through the nozzle. The fact that the curved surfaces of both the nozzles were smooth and shaped to coincide with ideal flow streamlines were additional contributing factors.

Although the path lines remained clear and distinct, the flow field showed a slight oscillation, particularly at high Reynolds numbers. This is illustrated in Figure 5.10 on page 5:17. This oscillation was the only hint of the onset of turbulence that was observed.

The establishment of such smooth flow conditions in the experimental apparatus was required if relative radial movement due to centripetal effects was to be observed. It could be argued that the absence of turbulence would detract from the validity of comparisons made between the experimental results and plant conditions. A suggestion is made subsequently as to how the effect of turbulence could be included in the theoretical model that has been used. However, the ease with which the onset of turbulence could be suppressed in the experimental apparatus suggests that turbulent conditions actually applying in accelerating nozzle flows will lag some way behind those existing in steady established flow at comparable Reynolds numbers.

Since most of our current knowledge about turbulent intensities in internal flows relates to steady established flow, it is apparent that turbulent flow conditions in nozzle flows will be very difficult to predict. Moreover, the ease with which turbulence could be suppressed suggests that laminar flow could be maintained in operating continuous casting nozzles, possibly leading to some improvements in teeming practice on continuous casting plants.

7.2.2 PRODUCTION OF HYDROGEN BUBBLES OF CONTROLLED SIZES

Limited control only could be excercised over the size of bubbles produced under the flowing conditions in the model. Hydrogen bubbles are normally used for flow visualisation for which bubbles of small diameter are required - small diameter in order to minimise the type of centripetal effects that are central to this investigation. The bulk of the literature surveyed in section 2.2 reports that small diameter bubbles are generated from cathode wires of small diameter placed normal to the flow direction, the bubble diameter being about half the wire diameter. This approximate relationship was found to apply in this work up to wire diameters of some 200 µm.

It was, however, necessary to produce bubbles of larger diameter but when wires of larger diameter were used, the relationship between wire diameter and bubble diameter ceased to apply. Numbers of small bubbles were produced at different points on the surfaces of the such large wires to be swept around its circumference in the boundary layer. These fine bubbles did not coalesce but, at low velocities, left from the back of the wire in a thin axial plane. Neither did they coalesce at high velocities, but moved around the wire to the boundary layer break away point to leave as a thick blanket. As a result of this behaviour, there was no relationship between wire diameter and bubble diameter and it was impossible to produce the large bubble sizes required.

Fine bubbles were also produced on the surfaces of wires placed parallel to the flow direction but bubbles were also produced at the downstream tip. These latter bubbles, being protected from the sweeping action of the flow by the wire itself, were able to grow to larger sizes before being swept away. Even here, however, the previously reported relationship between wire and bubble size did not apply, equation (5.1) on page 5:8 showing that the cathode current had the strongest influence on bubble size for wire diameters in the range from 90 μm up to 500 μm. (See also Figure 5.7).

It would appear that the bubbles have a finite time in which to grow before being swept away, this time being virtually independent of wire diameter and flow velocity. There is however, a wide range of other conditions, such as wire surface condition and the presence of surface active agents in the water, that influence the diameter of the bubbles (ref.61). Figure 5.7 on page 5.14 indicates the degree of scatter in bubbles sizes that were produced. It was, however, normally possible to increase the current, once an experiment had been set up, until bubbles of the required diameter were being produced, although the actual wire diameter imposed a limit on the maximum bubble size that could be achieved in this way.

In experiments where large bubbles only were required, the surface of the wire was coated in order to stop the formation of the fine bubbles along the length of the wire. It was for these coated wire conditions that equation (5.1) was derived and figure (5.7) obtained.

7.2.3 SUPPLY OF BUBBLE FREE WATER

Some of the results presented for the prototype nozzle were for bubbles that already existed in the flow entering the nozzle region, having been entrained into the flow at some previous point. For the more accurate experiments using controlled size hydrogen bubbles, these pre-existing bubbles could not be tolerated. Careful filling procedures were developed to exclude all air from the mixing box so that bubbles could not be entrained at that point. In addition, the vertical gauzes just inside the inlet ports and the low positioning of the inlet ports kept the surface of the water in the slice tundish free of waves thus avoiding a second mechanism for the entrainment of gas bubbles.

7.2.4 DESIGN FOR INTERCHANGEABLE NOZZLES

Considerable effort was required to make the interchangeable nozzle system function. Precautions that were eventually adopted are apparent in Figure 3.6 on page 3.17.

The curved nozzle surface had to protrude above the viewing side plates and all the protruding vertical surfaces had to be ground perfectly flat, as did their mating surfaces on the bottom of the tundish. Thus was necessary to ensure that the flow ran smoothly along the bottom of the tundish and into the nozzle without any turbulence or entrainiment of bubbles. Although the principle water tight seal was provided by a rubber gasket around the upper horizontal surface of the side plates, it was still necessary to achieve a high degree of seal between the protruding vertical surfaces.

Similar precautions, although not so severe, had to be taken over the interface between the nozzle sections and the flow constrictor. Figure 3.6(b) shows the upper ground surface of this constrictor.

Since only two nozzle geometries were examined in this work, hindsight shows that less work would have been involved if integral tundishes, nozzles and flow constrictors had been constructed for each geometry.

7.3 EXPERIMENTAL RESULTS

7.3.1 FINE BUBBLE FLOW PATHS - STREAMLINES

The flow streamlines, as indicated by the paths of fine bubbles, have already been mentioned since they show how effective the apparatus had been in establishing smooth flow conditions in the nozzles. The clarity with which the smoothed flow is shown in figures such as 3.23 demonstrates the effectiveness of hydrogen bubble streams as flow markers. Comparison between this figure and the dye traces, for example in Figure 3.13, show that hydrogen bubble streams are somewhat more effective than dye streams, especially since they more easily show a number of adjacent stream lines. However, the onset of turbulence as laminar flow conditions break up is more easily seen using a dye trace, see Figure 3.16.

On the other hand, the flow oscillations that have already been discussed at high Reynolds numbers could only be seen using the bubble streams. This was because each bubble stream was released from a constant position and retained its identity over an extended period of time. The oscillation of such a stream in relation to the nozzle walls could thus be observed over a number of different cine frames.

Figure 5.10 shows the extent of oscillation for a mid-stream line in the nozzle 1 and Figure 5.11 presents the same information for nozzle 2. The extent of oscillation in nozzle 2 was slightly the greater, perhaps because the smaller degree of convergence in this nozzle provided less damping to lateral motion in the nozzle flow.

7.3.2 MEASUREMENT OF VELOCITY

Local flow velocities could be measured from successive positions of a single bubble on the bubble position tracings made from the projected cine film. Positions were determined relative to the image of the nozzle itself on the projection in order to compensate for the mechanical movement of the frame image. Typical results are presented in Figures 5.23 and 5.24.

An independent check on the accuracy of the velocities measured in this way is provided by the nozzle exit velocity determined from measured volumetric flows. Velocities measured from the cine film in the straight section of the first nozzle are plotted against velocities determined from the volumetric flow rate in Figure 7.1. This figure shows that the cine velocities are fairly consistent in themselves but are some 14% above the velocities measured from the volumetric flow rate.

The difference between the two sets of figures is too great to be explained by experimental error. The accumulated errors involved in measuring velocities from the cine film and in measuring the 'volumetric' velocities amount to no more than 8%. The systematic discrepancy can, however, be adequately explained in terms of the developing velocity profiles.

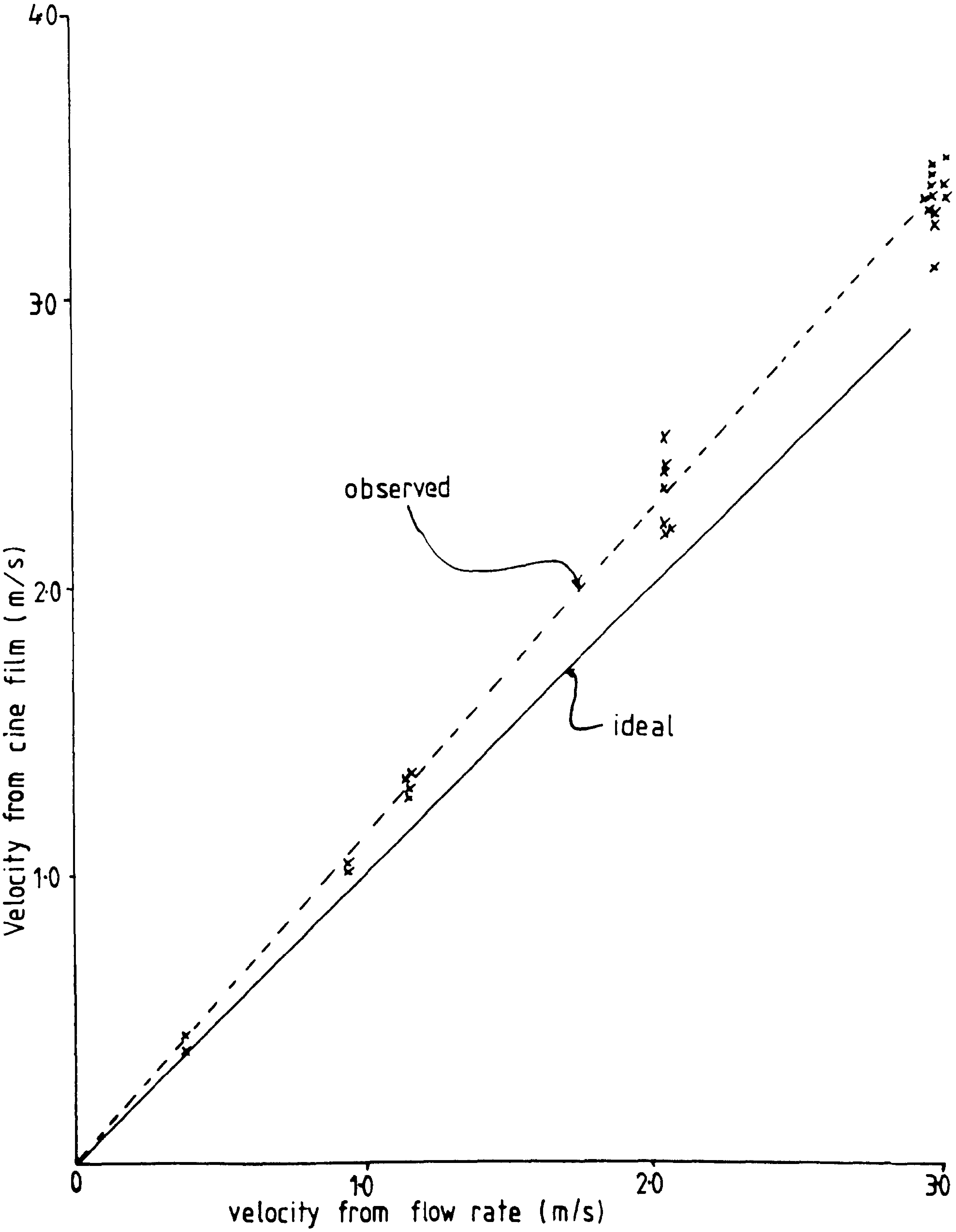

COMPARISON OF EXIT VELOCITIES FROM FLOW RATE AND CINE FILM

FIG. 7.1

Bubbles that can be seen on the cine film sufficiently well for their velocities to be determined are in the main central body of the flowing water. In fully developed turbulent flow, the centre line velocity in a round pipe is 25% greater than the average velocity, and in laminar flow it is 100% greater. The converging nature of the nozzle ensures that such established velocity profiles are not set up, the nozzle operating in an entry length mode with boundary layers developing at the wall. If we assume that the average velocity in the boundary layer is about half the velocity in the central region, a 14% difference between the actual volumetric flow and the volumetric flow corresponds to a boundary layer occupying some 28% of the flow area. Since the flow area in this region of the nozzle is about 30 mm by 21 mm, such a boundary layer would be some 4 mm in thickness, a perfectly plausable value. A similar comparison could not be made for nozzle 2 since no parallel portion exists over which velocity measurements could be made. Boundary layer thicknesses in nozzle 2, as in the converging section of nozzle 1, would be considerably thinner than those in the parallel section of nozzle 1 - certainly no more than 2 mm in thickness.

7.3.4 PATHS OF LARGE BUBBLES

Paths of large bubbles were obtained in the prototype and in the final nozzle. Only very few paths have been included in the thesis from the prototype nozzle because little control could be exerted over the bubbles that were present and the bubble size could not be measured, the micro-flash being unavailable at the time the experiments were carried out. Moreover, the geometry of the prototype nozzle was that of the Stocksbridge which could not be modelled using the theoretical approach adopted.

Figure 5.12 shows the paths of two bubbles that the cine film indicated collided with the nozzle wall. Paths were recorded for injected nitrogen bubbles and for the iso-density particles. The number of surface hits recorded for the bubbles was some 50% greater than the number recorded for the iso-density particles suggesting the centripetal effect sought in this work did have a significant effect. However, the identification of a 'hit' from the cine record was not easily accomplished because the identity of randomly introduced drops and bubbles was difficult to follow from frame to frame and because the lighting system used produced regions of shadow and distortion close to the curved nozzle walls. These lighting problems did not occur in work with the final nozzles because hydrogen bubbles could be accurately placed in the central plane, the lighting system being adjusted to give distortion free illumination of this region.

Bubble paths for the final nozzles have been presented in figures 5.13 through to 5.22. These paths are all recorded for starting points on a semi-circular arc whose centre coincides with the intersection of the plane of the tundish base with the central plane of the slice nozzle and whose diameter is the distance between the nozzle tangent points that coincide with the tundish base. This arc was chosen in the experiments because it coincided with the starting arc used in the theoretical ideal flow analysis.

Separate figures are presented to show the effect of bubble size, flow velocity and differences between nozzle 1 and nozzle 2. The trends shown in these figures can be explained in terms of buoyancy and centripetal effects. In the upper region of the nozzle where flow velocities are relatively low and possess strong horizontal components, buoyancy effects can have a major effect.

In the upper region of the flow, upward motion moves the bubbles away from the surface of the nozzle and thus towards the centre of the flow regime. The effect becomes more clearly marked as bubble size increases and the flow rate decreases, as shown by Figures 5.15 and 5.20 demonstrate. A simple force balance between the buoyancy force and the drag force at the terminal velocity explains the effect of bubble diameter. If we assume that Stokes law applies, we can write this balance as:-

$$\pi d^3/6 \Delta \rho g = 3 \pi \mu v d \qquad (7.5)$$

which gives the terminal velocity due to buoyancy alone as:-

$$v = \frac{d^2 \Delta \rho g}{18 \mu} \qquad (7.6)$$

Thus the relative vertical motion between the bubble and the water flow in which it finds itself increases rapidly with bubble size. The longer the bubble is in the flow region containing significant horizontal components the greater will the separation between the flow of the water and the path of the bubble - thus explaining the effect of low flow rates.

Of course the greater influence of buoyancy on the larger bubbles stems from the effects of size on the relative magnitude of body forces and surface forces. The effect of centripetal forces on the flow paths of bubbles results from a similar balance between a body force and a surface force so that effect of centripetal forces becomes more marked as the particle size increases. This effect has been discussed in the literature survey and is illustrated in 2.11 where the centripetal velocity is shown to increase with bubble size up to a maximum related to the flow velocity. Thereafter, the inertial effect involved in accelerating the virtual mass of the bubble reduces the relative velocity.

Thus the effects of buoyancy and rotating flows on bubble paths both increase with bubble size. It is tempting to imagine that large bubbles might show a highly curved path rising towards the flow centre after their initial release and then curving strongly back to the surface in the lower regions of the flow. Such a bubble path, however, is not possible because the initial buoyancy rise takes the bubble away from the nozzle surface into streamlines of lower curvature, the most curved streamlines being those closest to the surface.

Figures 5.13 and 5.21 show bubbles that hit the wall of nozzle 1 round about the vertical tangent point. Figure 5.13 shows the collision paths of bubbles released from a point on the starting arc relatively close to the tundish bottom. Bubbles of diameters 196, 232 and 476 μm collided with the nozzle wall when released from a point 16.5 mm above the tundish base, the flow velocity exiting from the nozzle being about 3 $m.s^{-1}$. Figure 5.8 shows that the streamline path from this point reaches the horizontal plane at the nozzle exit at a position some 2 mm in from the nozzle wall. The bubbles that hit the wall on this plane have thus moved a distance of 2 mm towards the flow centre in the time the flow has taken to travel from the semi-circular arc to the exit horizontal plane.

Experimentally measured steamline velocities are shown in Figure 5.23 and indicate that the average velocity of the streamline starting 18 mm above the tundish bottom is some 1 $m.s^{-1}$. Since the path length is about 130 mm, the flow time along this streamline is some 0.13 secs. If bubbles released from this point move a radial distance of 2 mm, their average radial velocity is 0.015 $m.s^{-1}$. Fig 2.11 shows that the theoretical radial velocity that would be expected under these conditions is about 0.02 $m.s^{-1}$ indicating a good degree of agreement with the behaviour observed experimentally.

Figure 5.23, also for nozzle 1, shows a bubble of diameter 357 μm hitting the surface, having been released from a point 38 mm above the tundish bottom. Comparable estimates for this bubble show that it must have moved a radial distance of some 4 mm while the stream flow travelled about 140 mm at an average velocity of some 0.7 $m.s^{-1}$. This corresponds to a radial velocity of about 0.02 $m.s^{-1}$, once again directly in line with the velocities indicated by figure 2.11.

These results clearly show that radial motion of lighter particles in a rotating flow, brought about by centripetal forces, can bring the particles into contact with the curved solid surfaces about which the flow is rotating. What is more, the hits that were observed for nozzle 1 all occured at or near the vertical tangent point, the very point at which nozzle blockage is known to occur in steel nozzle flows. Certainly these results give a clear indication that centripetal motion could have an important bearing on nozzle blockage.

Figures 5.14 and 5.22 show comparable bubbles released at the identical positions for nozzle 2 and at the same exit speed. By the time the bubbles have reached the end of the curved flow region, indicated by the lower circular arc in the figures, they have departed very little from the flow streamline as disclosed by the fine bubbles. Subsequently, the streamlines are straight and no movement towards the wall was observed in this section. At no time were surface hits observed for nozzle 2, making observation of expermiments with nozzle 2 somewhat unadventful. The experiments, however, clearly showed that the much straighter streamlines that existed in nozzle 2 reduced centripetal effects to almost zero.

7.4 COMPUTER RESULTS

The computer programme that was constructed from the ideal flow model is presented in Appendix 1, having been referred to in section 6.3.2. Typical tabulated results are presented on page 6.21. The programme could also provide output in the form of flow plots for bubbles of different sizes and a number of typical plots of this nature are presented and discussed in the next section. One version of the computer programme calculated the behaviour of alumina inclusions in steel, and results from this version are discussed in section 7.6.

The computer programme behaved well, numerical solution of the equations behaving in a stable manner in spite of their strongly non-linear nature. The Euler method of numerical solution proved adequate with a step length of 2 mm. The Runge-Kutta method was also used in the early stages of development of the computer programme, and appeared to give stable solutions with a step length of about 5 mm. The greater number of computations involved in each Runge-Kutta step, however, meant that there was little if any advantage over the Euler method.

7.5 COMPARISON BETWEEN EXPERIMENTAL AND THEORETICAL RESULTS

7.5.1 STREAMLINE GEOMETRY

Figures 6.3 and 6.4 show, for nozzles 1 and 2 respectively, comparisons between the experimental flow paths determined for fine bubbles (25 μm) and the predicted ideal flow streamlines. The dashed paths are those predicted theoretically and the dotted paths are the paths observed for the very small bubbles.

The computer model was not able to predict actual potential flow streamlines since it was written to predict the paths of low densitiy particles in the potential flow field. By getting the programme to predict the paths of minute bubbles of 1 μm or less at very low velocities, the difference between an actual ideal streamline and the predicted particle path starting at the same point could be reduced until it was comparable to the computational error. Particle paths predicted in this way are indistinguishable from ideal streamlines and have been taken as equivalent to them throughout this work.

Figures 6.3 and 6.4 show that the streamlines in the slice nozzles, as disclosed by the bubble paths, lie, in the main, extremely close to the ideal potential flow streamlines. They are not, however, identical so that the potential flow model can be taken as a semi-empirical representation of the flow pattern that exists in the experiments. However, the region of greatest discrepancy exists in the central region, especially in nozzle 2, where the curvature of the streamlines is minimal. Close to the nozzle walls the observed streamlines and the potential streamlines are virtually coincident. Thus the potential flow model is of great value in predicting the behaviour of inclusion and bubbles in that region of the flow that is most critical as far as nozzle blockage is concerned. Only particles that start from postions close to the wall can collide with the wall and the potential flow model is particularly accurate in this region.

Should a more accurate flow model be required, say in the central region, an improved empirical model was developed in which the x co-ordinate deviation between the potential streamline and the fine bubble streamline was measured at different y co-ordinates along the path length. Typical values of these deviations are presented in columns 2 and 5 in Table 6.1. These, and similar, deviations have been correlated against second order polynomials which are tabulated in Table 6.2. In order to generalise the flow model, however, further correlations were derived to relate the polynomial coefficients to the k value used to describe the potential flow streamline starting from any given entry position. These correlations, once again in polynomial form, are presented in Table 6.3. It is thus possible to describe the shape of any observed streamline as a function of the k-value at its entry point.

In order to demonstrate the improvement in accuracy that can be obtained in this way, columns 3 and 6 in Table 6.1 present the predicted deviations. Deviations of 3 mm, for example, have been reduced in this way to deviations of no more than 0.27 mm - a 90% reduction in the error.

This more complex flow model was not used further in this work but its availability in this thesis would enable it to be used, should a more accurate prediction of nozzle flow behaviour be required.

7.5.2 STREAMLINE VELOCITIES

The theoretical results discussed in the previous section had been obtained in the form of streamline plots from the theoretical model. In addition, theoretical results can be presented in the form of tables such as that presented on page 6.21. It can be seen that these tables include the velocity of particles along the streamlines and, since the velocities of fine bubbles could also be obtained from the cine film, a comparision between the theoretical and experimental velocities also acts as test of the semi-empirical flow model that was used.

Figures 7.2 to 7.4 shows such comparisions for an experiment involving the maximum exit velocity - 3 $m.s^{-1}$ for three different starting positions - specified in terms of the angle subtended by the arc between the starting position and the nozzle centre line. The experimental values are those shown in Figure 5.33 on page 5.34. Good agreement is

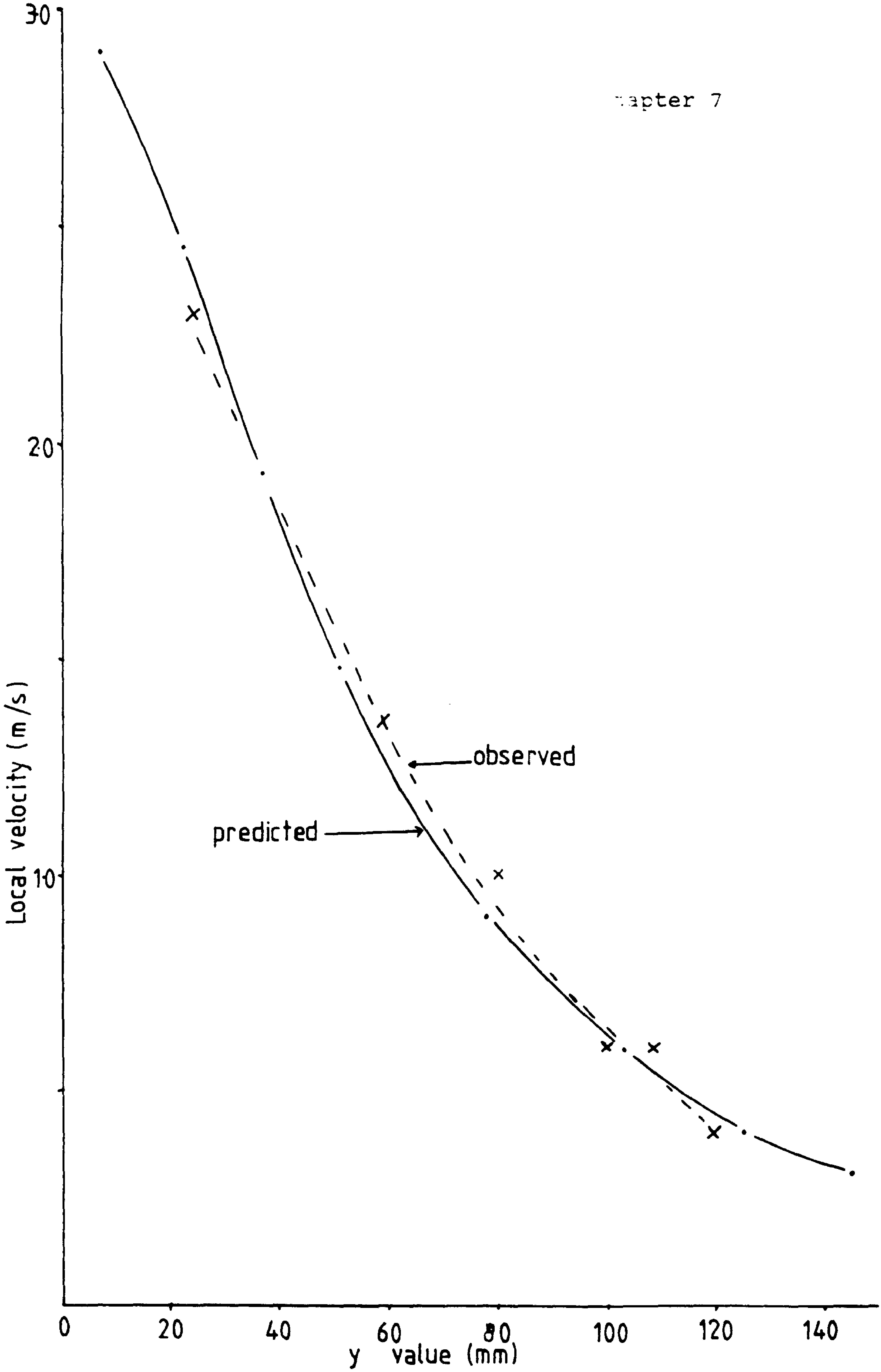

VELOCITY CHANGES THROUGH NOZZLE 1
STARTING FROM THE 45° POSITION

FIG. 7.2

VELOCITY CHANGES THROUGH NOZZLE 1
STARTING FROM THE 65° POSITION

FIG, 7.3

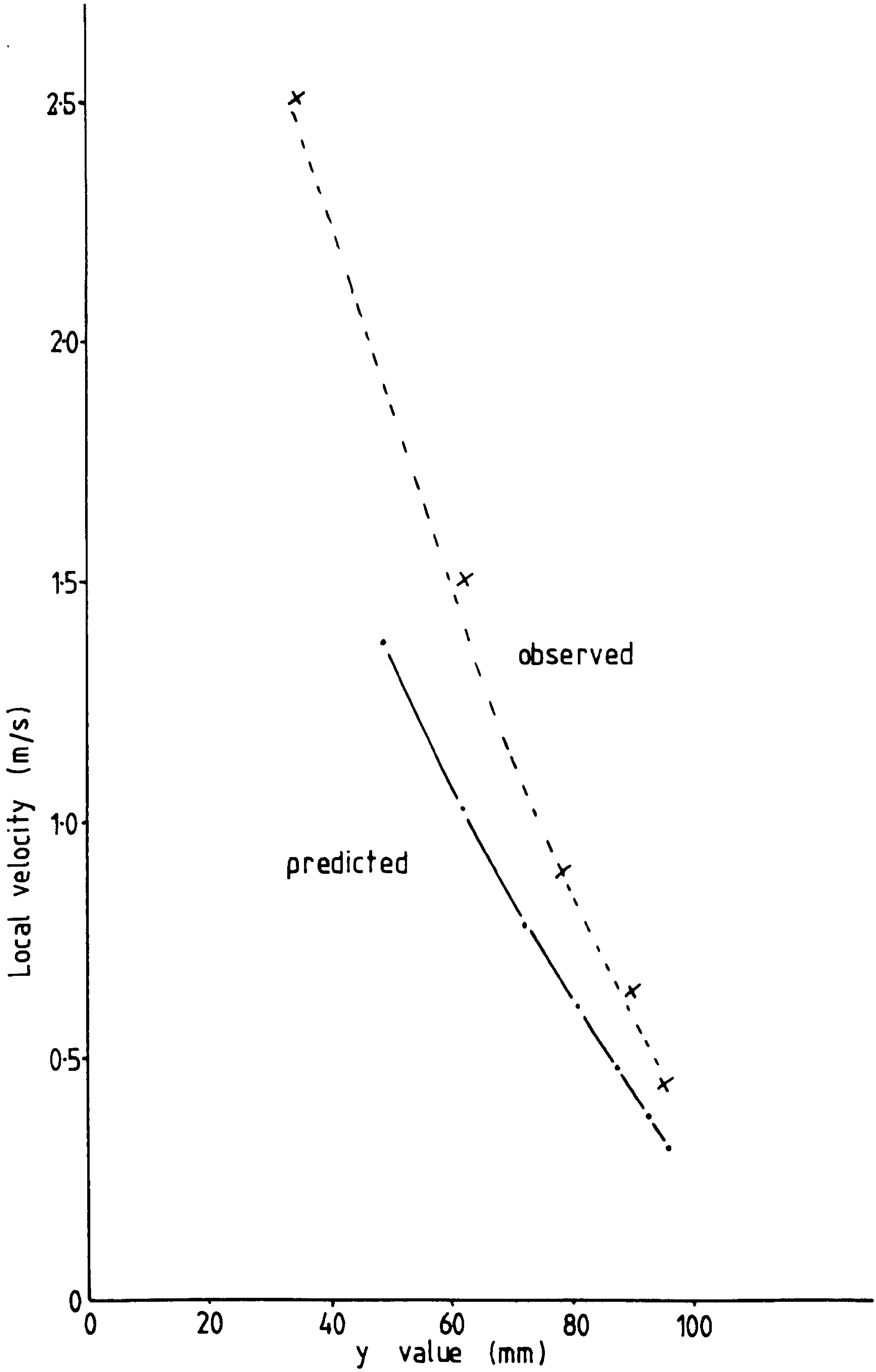

VELOCITY CHANGES THROUGH NOZZLE 1
STARTING FROM THE 80° POSITION

FIG. 7.4

achieved for the streamlines that start in the 45° and 65° positions but the theoretical velocities for the streamline starting at 80° are lower than those measured experimentally.

This discrepancy is in the wrong sense to be explained by the existence of a boundary layer and is possibly due to experimental error in the velocity measurements. The greater degree of curvature in the path of this streamline makes is difficult of place the point on the streamline at which each velocity measurement was made. However, even in this least accurate region, the theoretical and experimental velocities are quite close so that, overall the semi-empirical model based on the potential streamlines presents a good description of both the geometry and magnitude of the flow field.

7.5.3. PATHS OF LARGE BUBBLES

Comparisons between the theoretical and experimental paths of large bubbles are shown in figures 7.5 and 7.6. These comparisons show the effects of gravity and inertia on the bubbles as well as the discrepancies that exist between the shapes of the theoretical and the actual streamlines - as disclosed by the paths of small bubbles.

The effects of gravity and inertia are clearly demonstrated by Figure 7.5 which shows the paths of two bubbles at a low exit velocity. The path of the large bubble, 814 μm in diameter, as determined experimentally, rises above the predicted path. This is due to the twin effects of gravity

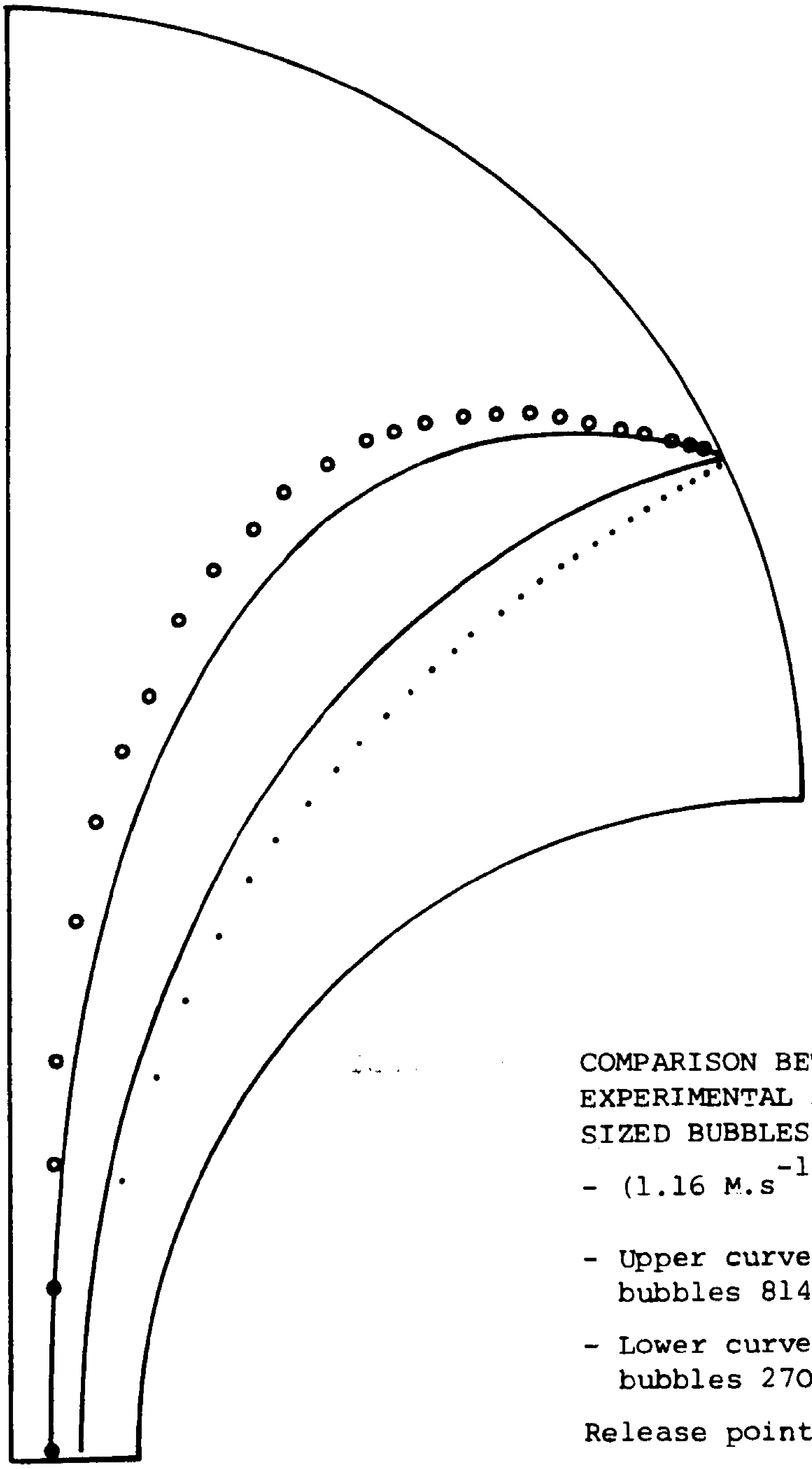

FIG. 7.5

COMPARISON BETWEEN THEORETICAL AND EXPERIMENTAL RESULTS FOR DIFFERENT SIZED BUBBLES AT A LOW EXIT VELOCITY.

- $(1.16\ M.s^{-1}$ or $7.33x10^{-4}\ m^{3}.s^{-1})$

- Upper curve and experimental points: bubbles 814 um in diameter

- Lower curve and experimental points: bubbles 270 um in diameter

Release point 120.2 mm above nozzle exit

- experimental results taken from Figure 5.15

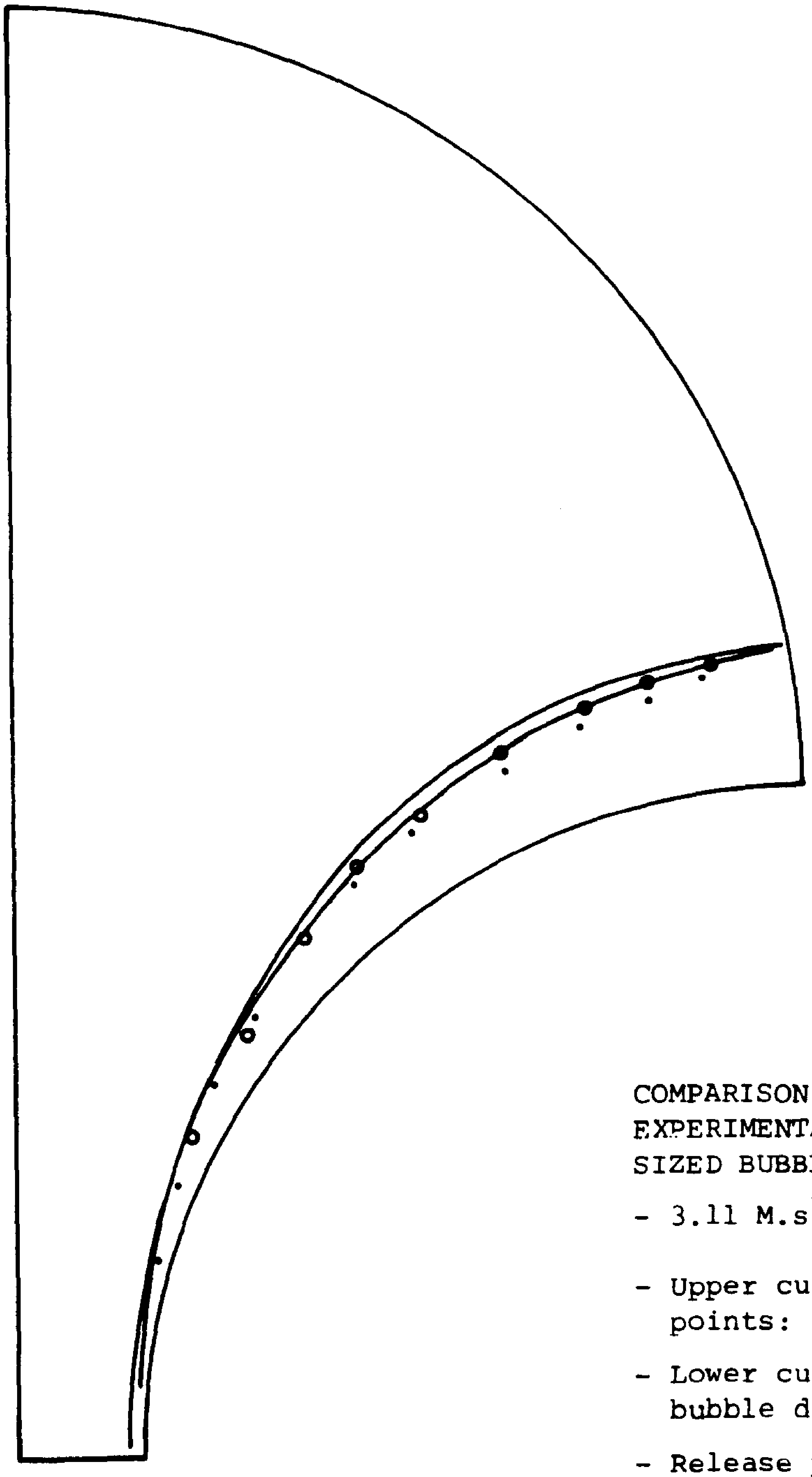

COMPARISON BETWEEN THEORETICAL AND EXPERIMENTAL RESULTS FOR DIFFERENT SIZED BUBBLES AT A HIGH EXIT VELOCITY.

- 3.11 $M.s^{-1}$ or $19.7x10^{-4}$ m^3s^{-1}

- Upper curve and open circle experimental points: bubble diameter = 476 um

- Lower curve and experimental points: bubble diameter = 196 µm

- Release point 96.5 mm above nozzle exit

- Experimental results taken from 5.13

FIG. 7.6

and inertia. The theoretical model ignores the effects of inertia, predicting that a large bubble will accelerate instantaneously to the local streamline velocity. An actual bubble will be lagging behind the streamline velocity so that, in the accelerating flow as the bubble enters the nozzle region, it will move more slowly than the theory predicts. Thus it will spend more time in the slowly moving entry region where the vertical component of the stream velocity is very low indeed. During this time, then, it will be rising under gravity and moving away from the path predicted theoretically. Figure 7.5 shows just this behaviour for the larger bubble with the practical path rising above that predicted theoretically especially in the entry region.

The two paths come together in the lower part of the nozzle flow due to two factors. The flow is converging thus reducing the separation that can be seen between two separate paths. Furthermore, the vertical component of the streamline velocity is becoming dominant in this region so that the effect of gravity will not be seen in the shape of the path, but in the progress of the bubble along the path.

The path of the smaller bubble shown in Figure 7.5, on the other hand, lies below that predicted theoretically. Much of the discrepancy is due to differences shown in Figure 6.3 between the streamlines geometries assumed in the theoretical model and those disclosed by the paths of small bubbles at low flow rates.

Figure 7.6 shows a similar set of experimental and theoretical results for a high exit velocity and for a starting position that is much closer to the nozzle surface. Gravitational effects have much less time to influence the path of the larger bubble, 476 µm here, and its path coincides more or less exactly with the theoretical prediction. Furthermore, Figure 6.3 shows that the discrepancy between theoretical streamline and the actual streamline is very much less in this region. The experimental path of the smaller bubble in figure 7.6 lies inside the theoretical path by an amount that is almost identical to the discrepancy shown in this region in Figure 6.3 between the shapes of the experimental and theoretical streamlines. The effect that size has on the bubble path is almost identical for the theoretical and experimental results.

7.5.4 BUBBLE HITS AT THE NOZZLE SURFACE

Evidence has been presented to show how accurately the experimental particle paths are predicted by the theoretical model. However, one of the most important features of the theoretical model is its ability to predict the extent to which particles hit the surface of the nozzle. Figure 5.13 has already been referred to since it presents the experimentally determined paths of three bubbles that hit the surface of the nozzle. The paths of the largest and smallest of these bubbles have been predicted theoretically and have been presented in Figure 7.6.

The path predicted theoretically for the largest of these bubbles - bubble diameter 476 µm - intersects the nozzle surface in a position almost identical to that observed in the experiment. It is also interesting to note that the theoretical path for this bubble is more curved than the path for the smallest bubble - diameter 196 µm - and that the two paths cross. These facts stem from the greater effects that gravitational and centripetal forces have on the movement of the larger bubble. Initially, the larger bubble rises more rapidly under gravity and so its path rises above and lies outside the path of the smaller bubble.

Subsequently, centripetal effects also have a greater influence on the path of the larger bubble giving it a higher centripetal velocity and causing it to veer in towards the wall and across the path of the smallest bubble. The theoretical behaviour and experimental behaviour of this bubble are almost identical.

The theoretical and experimental behaviour of the smallest bubble are also very similar except that the theory did not predict that this bubble would hit the nozzle wall. There are two factors that might explain this. Since the path of the bubbles was being followed experimentally using cine film, bubble hits were mainly recorded by inference between frames. In some case, hits would be inferred and thus recorded even though they would have taken place below the nozzle exit. The second factor is the flow oscillation that has already been referred to. The magnitude of this oscillation is illustrated in Figure 5.10, and it can be seen that lateral oscillation of streamlines in the throat region is of similar magnitude to the separation shown in figure 7.6 between the path of the small bubble and the nozzle wall. The periodicity of the flow oscillation seemed to be of the same order as the time taken by a bubble to flow through the nozzle. Thus a large proportion of the bubbles that would otherwise have passed through the nozzle without hitting the walls could be diverted onto the nozzle wall by the flow oscillation. Although not done in this work, some form of random perturbation could be imposed on the theoretically predicted path to replicate this effect.

Figure 5.21 also shows a bubble hitting the nozzle wall although starting from a point much further from the wall than the bubbles discussed above. That figure also shows, as a dotted line, the corresponding theoretical bubble path. The theoretical path remains outside the experimental plot and does not intersect with the nozzle wall. The discrepancy between the theoretical and experimental paths is too great to be explained in terms of the flow oscillation referred to above. However, this bubble is travelling through that region of the nozzle where the experimental streamlines lie inside the theoretical streamlines. This effect, taken together with the flow oscillation, is possibly sufficient to explain how the bubble came into contact with the wall, although entering the nozzle so far away from the wall.

7.5.5 VALIDITY OF THE THEORETICAL MODEL

The discussion in the previous sections shows that the semi-empirical flow field model, based on the electrostatic field between two parallel wires, presents a fairly accurate picture of the geometry and velocity of fluid flow in the two dimensional slice nozzle. The model also allows fairly accurate predictions to be made of the movement of isolated second phase particles in these nozzle flows under the twin effects of centripetal and gravitaional forces. These predictions are made ignoring the inertial effects - they therefore assume that the second phase particles are continuously at their local terminal velocity. The fact that inertial effects can be ignored is well established in the literature (see section 2.3) and the good agreement that has been obtained in this work between theory and experiment is further confirmation of that fact.

7.6 RELEVANCE TO INCLUSION BEHAVIOUR DURING STEEL FLOW THROUGH METERING NOZZLES

As was pointed out in the literatrue study, it is well established that alumina inclusions existing in molten steel, can block metering nozzles and stop further flow of steel entirely. Indeed, before calcium was extensively used to render the alumina inclusions liquid, the flowability of steel was a quoted parameter - being the mass of steel that could flow through a nozzle before the nozzle became blocked.

It is generally agreed that surface tension forces, as discussed in the Chapter 2, are sufficient to bind the particles to the wall, or to other particles already at the wall, and eventually seal the nozzle. The mechanism whereby the alumina inclusions arrive as the wall has, however, been in some doubt.

The theoretical and experimental work presented in this thesis has shown that centripetal pressure present in nozzle flows can drive lighter second phase particles to the nozzle wall. Alumina inclusions in steel are such particles so it is apparent that they will be driven towards the walls of converging nozzles. Before this fluid dynamic process can be considered to be the dominant mechanism bringing particles to the wall, it is necessary to make a critical comparision between conclusions from this work and published data about the blocking of nozzles.

Sets of experiments described by Farrell and Hilty (ref. 8) and by Wilson, Heasom, Nicholson and Hills (ref. 87) provide useful data for this comparision. Molten steel, maintained at a constant head in a tundish, flowed through zirconia nozzles of fixed geometry, 5.6 mm and 6mm in diameter respectively. The steel had been carefully deoxidised before the experiments were carried out and then aluminium was added to the steel prior to its being cast. For each experiment, the time that the steel took to flow through the nozzle and the amount of steel that could be cast were recorded.

Comparison between the amount of alumina required to block the nozzles in these experiments and the amount that this theory predicts would be carried to the wall provides a means of ascertaining the importance of centripetal effects.

A problem arises because the nozzles that were used did not have a curved entry surface but were sharp edged. The flow into such a nozzle does, however, follow a curved path - this is why the vena contracta occurs. Singh(39) reports that fluid flowing into a sharp edged orifice rejoins the wall at a distance downstream approximately double the diameter. The actual diameter of the vena contracta at its narrowest point can be estimated from the coefficient of discharge and these two distances can be used to estimate the curvature of the streamline closest to the nozzle edge.

If D_R is the diameter of the flow at its narrowest point and D_T the actual nozzle diameter, the coefficient of discharge, since it is the real flow over the theoretical flow, is given as

$$C_D = \left|\frac{D_R}{D_T}\right|^2 \qquad (7.7)$$

Thus, as is shown in figure 7.7, the curvature of the streamline that just touches the edge of the nozzle is the curvature of the circle for which a chord of length $2D_T$ lies at a perpendicular distance of $(D_T - D_R)/2$ from the circle.

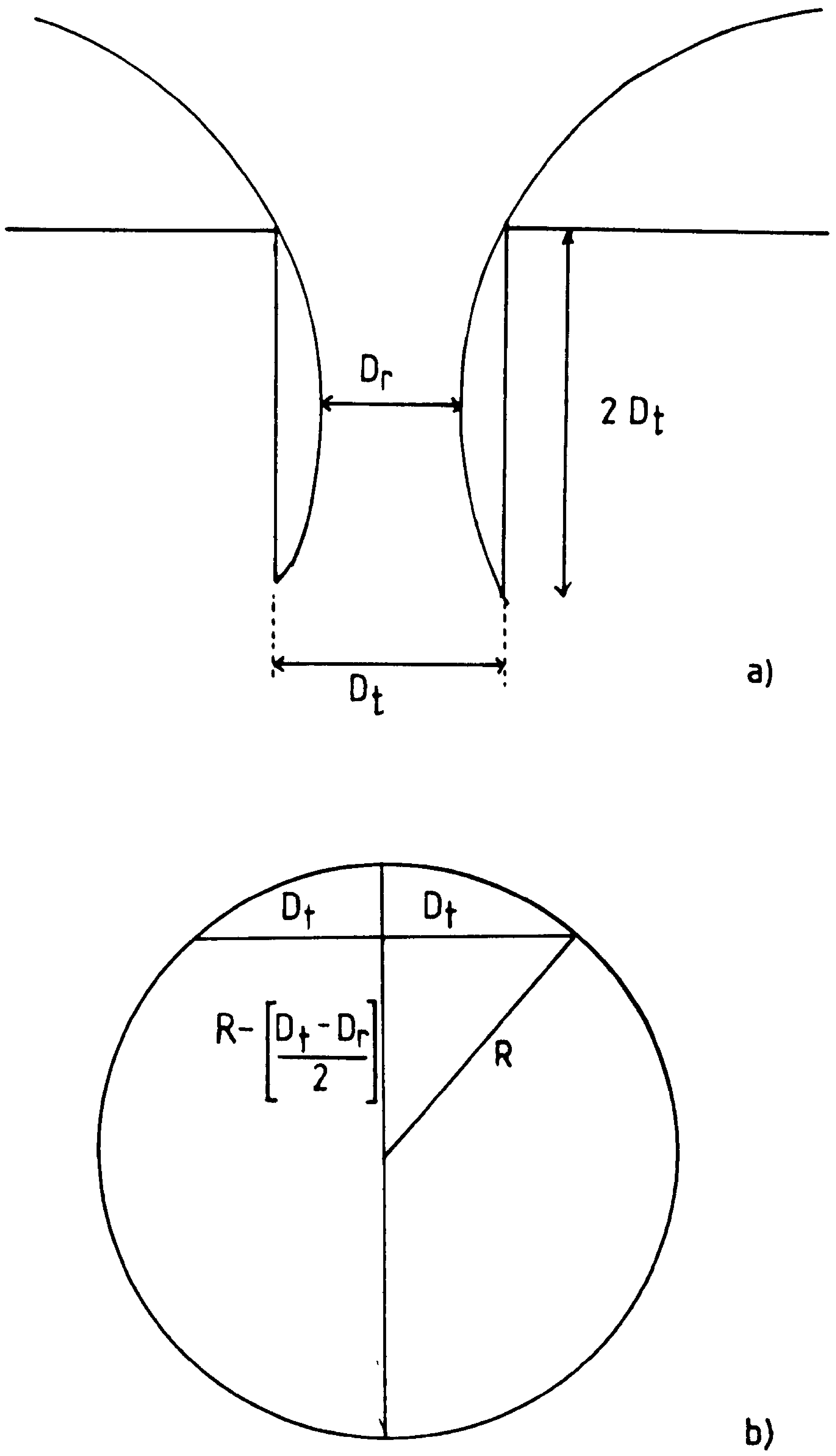

GEOMETRY OF THE VENA CONTRACTA

FIG. 7.7

The application of Pythagoras shows that the radius of this circle is

$$R = \frac{D_t^2 - \left(\frac{D_t - D_r}{2}\right)^2}{D_t - D_r} \qquad (7.8)$$

For the nozzle geometry used in ref. 39 and a discharge coefficient of 0.65 the radius of curvature of the outer streamline in the flow that just touches the nozzle is 30 mm. This streamline will pass through a 'vena contracta' nozzle of diameter 4.5 mm, this 'nozzle' being analogous to the nozzle 1 type treated in this work except that it is defined by a flow streamline rather than by a solid nozzle surface. The model used for the flow of steel into the nozzle is shown in figure 7.8 where R is the radius of the vena-contracta streamline. The nozzle flow regime is assumed to start from a hemispherical surface of radius $R + D_N/2$ whose centre lies on the axis of the nozzle at a height $R - D_N$ above the entrance plane of the nozzle.

The theory developed in this work can then be used to predict the behaviour of an inclusion starting from a typical point marked as A on the hemispherical surface. Inclusions of sufficient size starting from this point will cross the vena-contracta streamline at a point within the nozzle and thus enter the vena-contracta dead zone. These inclusions would be expected to attach themselves to the nozzle wall and contribute to the blockage of the nozzle.

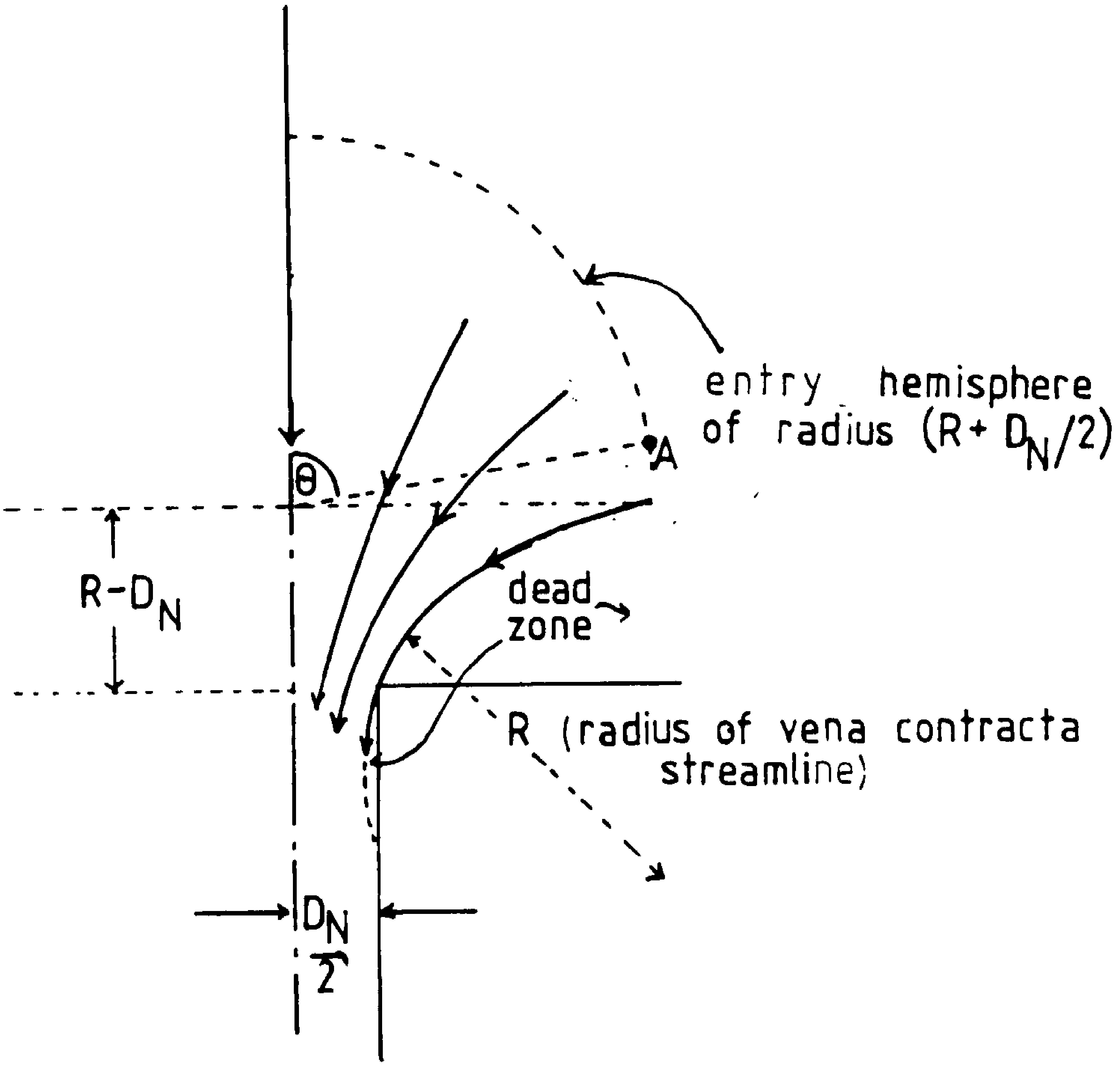

POTENTIAL FLOW MODEL FOR STEEL FLOW INTO A NOZZLE SHOWING THE ENTRY HEMISPHERICAL SURFACE

FIG. 7·8

Figure 7.9 shows the paths of a number of inclusions of different sizes that do this, the caption on the figure showing their sizes. It can be expected that all inclusions of a larger size starting from the same point will also cross the streamline so that the figure shows that the diameter of the smallest inclusion that crosses the vena-contracta streamline is related to the distance from the nozzle entrance plane at which it entered the nozzle flow regime.

Figure 7.10 has been constructed from a number of plots such as those shown in figure 7.9 to demonstrate this relationship in terms of the angle θ subtended by the inclusion's starting position on the starting hemisphere. The figure shows that the minimum diameter can be taken, approximately, as a linear function of the complement of the angle θ:-

$$d_{min} = a(90^{o} - \theta) \qquad (7.9)$$

where the value of a is 27 μm.deg^{-1} when the exit velocity is 3 m.s^{-1} and 40 μm.deg^{-1} when the exit velocity is 2 m.s^{-1}.

Data presented by Franklin (95) from experimental studies of alumina inclusion populations in molten steel is plotted in figure 7.11 to show how the mass fraction of alumina particles of sizes greater than a specified size varies with that size. If we consider the inclusions entering the nozzle flow regime from positions between θ and $\theta+d\theta$, a fraction, $f(d_{min})$ of them will enter the dead zone of the nozzle, where $f(d_{min})$ is the ordinate in figure 7.11 corresponding to the value of d_{min} given by equation (7.9).

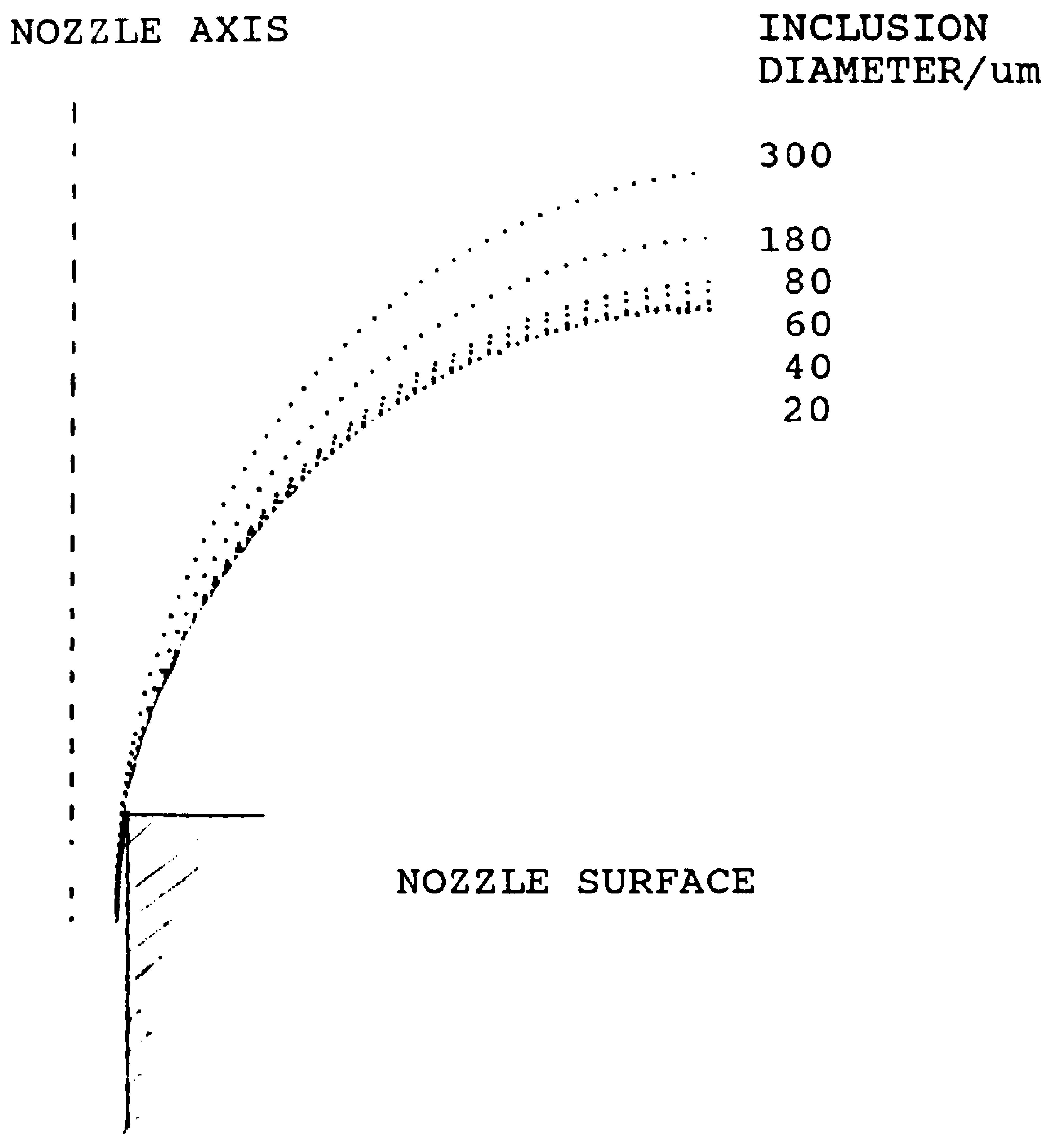

FIGURE 7.9 : PATHS OF ALUMINA INCLUSIONS IN STEEL ENTERING A SHARP EDGED ORIFICE OF DIAMETER 5.6 mm AND CROSSING INTO THE THE VENA CONTRACTA DEAD FLOW ZONE. (EXIT STEEL VELOCITY = 3 m.s^{-1}; SCALE X2)

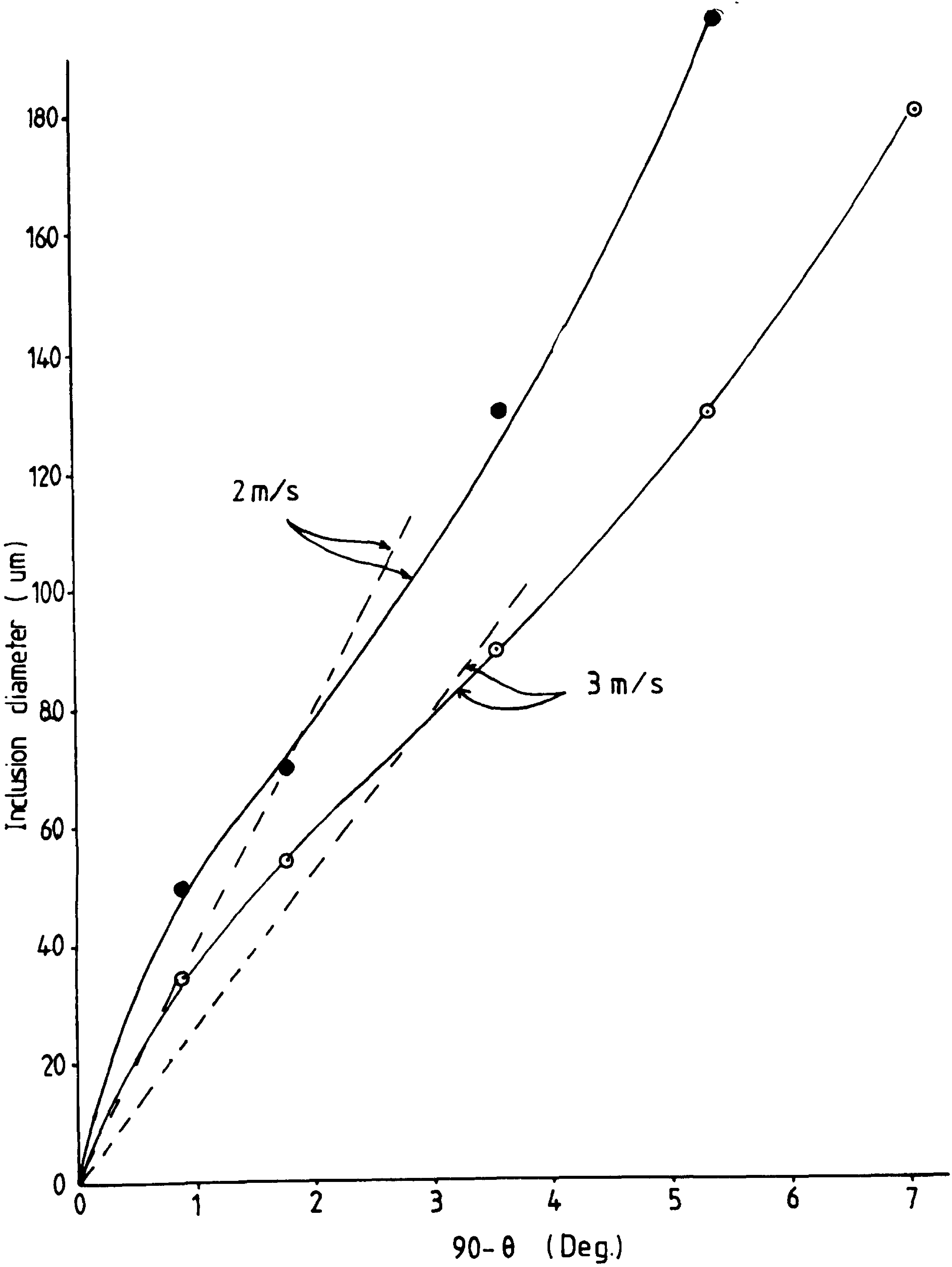

EFFECT OF STARTING POSITION ON THE MINIMUM INCLUSION DIAMETER THAT HITS THE NOZZLE SURFACE

FIG. 7.10

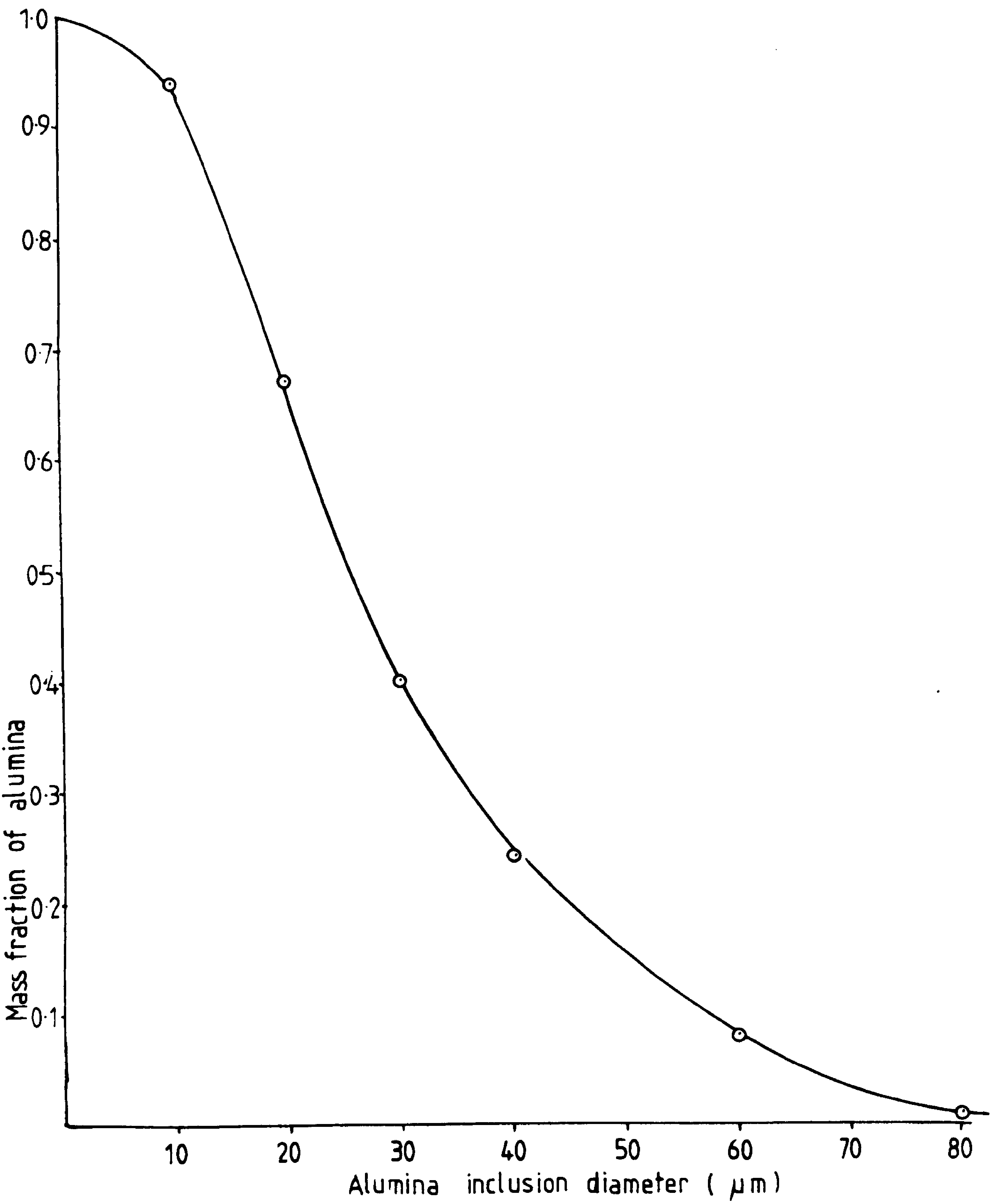

MASS FRACTION OF ALUMINA IN STEEL GREATER THAN A GIVEN SIZE

FIG. 7. 11

The flow velocity across the entry hemisphere is constant so that the fraction of the steel that enters the nozzle flow regime between θ and $\theta+d\theta$ is equal to the fraction of the entry hemisphere's surface that lies between these two angles, that is $\sin\theta \, d\theta$ radians^{-1}. Thus the fraction of the alumina present in the steel as a whole that enters the dead zone as a result of its presence in the steel that enters between θ and $\theta+d\theta$ is

$$f_{d_{min}} \; \mathrm{Sin}\theta d\theta \text{ radians}^{-1}$$

Figure 7.11 shows that virtually none of the alumina present in the steel is in the form of inclusions of diameter greater than 80 µm, so that the total fraction of the alumina in the steel flowing through the nozzle that enters the dead zone is given by:-

$$\left[f_{Al_2O_3} \right] B = \int_{\theta_{80}}^{90^{\circ}} f_{d_{min}} \; \mathrm{Sin}\theta \; d\theta \text{ radians}^{-1} \qquad (7.10)$$

where θ_{80} is the value of θ given by figure 7.10 that corresponding to an inclusion size of 80 µm. The figure shows that the smallest value of θ_{80} is about 87°. Sin θ can thus be set at unity throughout the range of the integration in equation (7.10) and the integration can then be transformed using the relationship shown by equation (7.9). Differentiating equation (7.9) gives:-

$$d\theta = - \frac{d(d_{min})}{a} \qquad (7.11)$$

Thus the fraction of the alumina present in the steel flowing through the nozzle that enters the dead zone is given by:-

$$\left[f_{Al_2O_3}\right]_B = \frac{1}{a}\int_0^{80\ \mathrm{um}} f_{d_{min}}\, d(d_{min})\ \mathrm{radians}^{-1} \qquad (7.12)$$

Graphical integration of figure 7.11 gives

$$\int_0^{80\ \mathrm{um}} f_{d_{min}}\, d(d_{min}) = 26\ \mu\mathrm{m} \qquad (7.13)$$

Since 1 radian = 28.6 deg, equations (7.12) and (7.13) give:-

$$\left[f_{Al_2O_3}\right]_B = \frac{0.91}{a}\ \mu\mathrm{m.deg}^{-1}$$

Substituting the values of a determined from figure 7.11 means that 2.5% of the alumina present in the steel enters the dead zone of the vena-contracta when the exit velocity is 3 $m.s^{-1}$ and 3.6% when the exit velocity is 2 $m.s^{-1}$.

Faulring et alia reported that 16 Kg of steel, deoxidised with 190 ppm of aluminium flowed through the nozzle before it became blocked, and the photographs presented in their experiments suggest that the alumina deposits that blocked their nozzles were about 1 mm in thickness. Since the nozzles were 5.6 mm in diameter, such deposits would amount to some 25 mm^3 of alumina - 0.075 g of alumina.

Under normal deoxidation practice, some 2/3 of the total aluminium added to the molten steel is combined with the oxygen to form alumina. Thus one would expect that 16 kg of molten steel would contain 3.8 g of alumina so that the deposited mass of alumina represents 2% of the alumina present in the metal - a figure relatively near that predicted by this theory.

Wilson et alia measured the times taken to block nozzles of similar shape in their experiments with 'inverted nozles'. The nozzles were 6 mm in diameter and, their photographs suggest, were blocked with alumina discs some 2 mm in thickness. Typically, a zircon nozzle would take 3 min 35 s to block, the steel flow rate through the nozzle averaging 24 kg of steel per minute.

The oxygen contents of their steels were about 35 ppm and, assuming that this oxygen was entirely bound up in alumina, represents some 70 ppm of alumina in the steel. The steel flowing through the nozzle thus contains some 6 gms of alumina. If 3% of this alumina were deposited across the nozzle, it would reprents 0.18 g, or a disc across a 6mm diameter tube of some 1.8 mm thickness. This thickness is entirely compatable with the photographs that Wilson et al present of their blocked nozzles.

Thus, in the case of both of these experiments, the centripetal effect predicts nozzle blockage rates that are compatable with the rates measured experimentally.

7.7 NOZZLE DESIGN

The results of the experimental work with two nozzle designs has shown the advantage of having a linear convergent section, (nozzle 2 shown iin fig. 3.5), over nozzle 1, (also in fig. 3.5), where the curvature extends from the tundish base to the nozzle exit. There are two features of the nozzsle 2 design that are important. First, the fluid velocities in the upper part of the nozzle are much lower than those in nozzle 1 as can be seen by comparing the velocity profiles in fig. 2.16, (nozzle 1), with those in fig. 2.17, (nozzle 2). As a result, in nozzle 2 the dominant bouyant forces allow the larger particles to rise towards the upper surface of the tundish. Second, the linear convergent section produces linear streamlines where there is no centripetal movement of particles.

At the exit of nozzle 2 the streamlines will, of course, curve to produce a vertical stream of fluid. It is likely, however, that this curvature will be mainly confined to the section level with the vena contracta formed just below the exit to the nozzle. The vena contracta should be small because the change in angle is small. The coefficient of discharge will be much higher than that with a 90^{o} change of section. It can be seen in fig. 4.3 that the coefficient of discharge of nozzle 2 is 0.87 and above, even for the high flow rates. This compares with a coefficient of discharge of 0.65 for a nozzle with a 90^{o} change of section. The evidence from other experimental work, (ref.87), using a linear convergent section followed by a parallel section is that the blockage occurs in the parallel section.

Further improvements in the nozzle design could be made in essentially two ways. The radius of curvature of the upper part could be changed, possibly even varied in one nozzle so as to reduce the curvature gradually. The angle of the linear convergent section could be changed depending on the constraints imposed by the design of the plant. The strategy should be to restrict the centripetal movement of particles towards the nozzle wall to the upper wider parts of the nozzle. Here, any deposit on the surface will not cause the same interference to the flow as it would at the nozzle throat.

The results with the single design in this work are sufficiently promising for steel plant trials to be made with the new nozzle.

8. CONCLUSIONS

8.1. It has been established by a review of the literature that nozzle blockage occurs by the deposition of pre-existing alumina inclusions at the narrowest part of the nozzle. Once there, the inclusions adhere strongly at the surface by interstitial forces.

8.2. The most widely used method of combatting the problem is to add calcium to the steel. Liquid calcium aluminate inclusions are formed which do not adhere to the surface of the nozzle.

8.3. A theory has been developed which uses the centripetal, buoyant, and frictional forces to predict the movement of particles in curved flow paths in a fluid. It has been shown that for the size of particles encountered in practice, the effects of inertia can be ignored.

8.4. A two-dimensional prototype water model of the nozzle used at British Steel Corporation, Stocksbridge Works has been built and the movement of gas bubbles to the nozzle surface was observed.

8.5. Based upon the results obtained with the prototype model, a more adaptable two-dimensional water model has been constructed. Means of interchanging nozzles have enabled two types of nozzle to be examined. Nozzle 1 had a full circular arc from the tundish base to the vertical nozzle exit. Nozzle 2 had a circular upper section and a linear convergent exit section.

8.6. Strigent safety procedures have been built into the model to allow experiments to be carried out at a maximum of 350V direct current.

8.7. Turbulence in the model was eliminated by means of dams of coarse gauze. Laminar flow was then achieved in the nozzle, even at exit channel Reynolds Numbers as high as 74000

8.8. Bubbles of hydrogen were generated in the water by electrolysis at a stainless steel cathode positioned in a semi-circular arc at the tundish base. Sodium sulphate was added to the water to increase the conductivity of the water and increase the number of bubbles produced.

8.9. Different diameters and forms of cathode wire have been used. Precise location of the bubble position was achieved by suitable insulation of parts of the wire. The most satisfactory cathode was a 90 um diameter wire parallel to the flow direction. This was insulated everywhere except the tip, at which bubbles of varying sizes could be generated.

8.10. The sizes of bubbles generated at a wire tip were controlled by changing the the cathode current, giving an approximate relationship:-

$$\text{Bubble diameter } /\mu\text{m} = 8 \times \text{cathode current } /\text{mA}$$

8.11. A computer programme has been written in FORTRAN to predict the movement of hydrogen bubbles in water, and of alumina inclusions in liquid steel, using both experimental nozzles 1 and 2.

8.12. The programme for alumina in steel allows for a possible change of inclusion density and liquid density to study other inclusion/liquid metal systems. Graphical output of the flow paths could be produced in addition to data print-outs.

8.14. A comparison of the observed paths of fine bubbles and the graphical plots predicted by the computer programme has shown them to be almost identical close to the nozzle wall. For differences in the centre of the nozzle, a correction procedure has been developed though not used in the present model.

8.15. It has been shown that in the upper part of the nozzle buoyant forces are dominant, especially at the larger particle sizes. Movement of particles is upward, away from the fluid flow path.

8.16. In the lower part of the nozzle 1 centripetal forces are dominant. Movement of the particles tends to be inward towards the nozzle wall.

8.17. The linear convergent section in nozzle 2 prevents the curved flow paths and therefore of any consequent movement of particles towards the nozzle wall.

8.18. It has been shown that in normal operating practice for aluminium-killed steels and with an exit velocity of between 2 and 3 m/s, 3% of the alumina present in the steel will contribute to the deposit at the narrowest part of the nozzle.

8.19. Using the previous result it has been shown that in flows through sharp right-angled nozzles, the dead zone of the vena contracta forms an effective nozzle curved surface. Blocking in these nozzles can be assumed to result from movement of inclusions into the dead zone.

8.20. In a study of nozzle blocking reported in the literature predicted blocking times show good agreement with those reported.

9. RECOMMENDATIONS FOR FURTHER WORK

9.1 Plant trials should be undertaken with nozzles of the same desgn as the experimental Nozzle 2.

9.2 Consideration should be given to a means of imparting a rotation in the nozzle so that inclusions will be directed away from the nozzle wall.

9.3 Turbulence in the tundish should be limited as much as possible. Any such means will have the effect of reducing the turbulence in the nozzle throat. Refractory surfaces used for this purpose will also have the effect of removing inclusions.

9.4 Since this thesis only considered single inclusions in steel, some work should be done to study the movement of alumina clusters. This can easily be done in programme SCST by altering the density and size of the inclusions.

9.5 The presence of turbulence in the tundish should be modelled by adding random perturbations to the computer model. In such a way, different degrees of turbulence can be simulated.

9.6 The polynomial correction procedure described in this thesis should be incorporated into the computer programme.

REFERENCES

1 A. I. Kokin, Stal' 16, (1956), 272-274

2 R. B. Snow and J. A. Shea, J. Amer. Cer. Soc., (1949), vol 32, no. 6, 187-194

3 M. G. Chigrinov et al, Stal' 23, (1953), 215-217

4 J. F. Mignot, CDS Circ., (1976), nos. 7-8, 1645-1653

5 C. Jizhi et al, Iron and Steel (China), (1982), 17, (5), 14-23

6 Z. Suosheng et al, Scand. J of Met. 14, (1985), 175-182

7 S. N. Singh, Met. Trans. Oct. (1974), 5, (10), 2165-2178

8 J. W. Farrell and D. C. Hilty, Elec. Furn. Proc., AIME, vol. 29, (1971), 31-45

9 F. Hoshi and Y. Aoyama, Trans. I. and S. Inst. of Japan, (1978), 18, (7), 429-444

10 M. Hasegawa et al, Steelmaking Proc., vol. 66, Atlanta, April 17-20, (1983), 261-268

11 K. Oki et al, Taikabutsu, (1980), 626-632

12 M. Hasegawa et al, Tetsu-to Hagane, Oct. (1984), 70, (14), 1704-1711

13 I. Takahashi et al, Nippon Stainless Technical Report, (1985), vol.20, 45-56

14 G. A. Irons, Metallurgical Transactions B, vol.18B, March (1987), 105-117

15 Y. Shirota et al, Trans. ISIJ, vol.27, (1987), 18-24

16 N. M. Frolovskii et al, Ogneupory, vol. 35, (1970), no. 8, 22-27, translation HB 8295

17 A. K. Karlit et al, Ogneupory, vol. 35, (1970), no. 7 27-35, translation HB 8363

18 V. P. Schevchenko et al, Ogneupory, (1970), vol. 35, no. 10, 31-33, translation HB 8345

19 D. C. Hilty and J. W. Farrell, AIME, Elec. Furn. Proc., (1970), 31-46

20 Y. Kurashina et al, UK Patent Application GB 2110971 A

21 G. C. Duderstadt et al, J. Metals, (1968), vol. 20, no.4, 89-94

22 I. Ono et al, Taikabutsu, vol. 26, (1974), no. 5, 197, 172-175, translation HB 9283

23 S. K. Saxena et al, Scand. J. of Met., 7, (1978), 126-133,

24 K. Schwertferger, AIME, Elec. Furn. Conf. Proc. (1970) 95-102

25 H. Nakato et al, Tetsu-to-Hagane, vol. 60, no. 11 Lectures 92,113; pages S430,S451, translation HB 9495

26 P. Kozakevitch and M. Olette, Iron and Steel Inst., Int., Conf., Balatonfured, Hungary, (1970), 'Production and Application of Clean Steels', 42-49

27 A. P. Nagornyi et al, Steel in the USSR, (1980), 9, 472-474

28 F. Tomsu and V. Dolezel, Steel Times, Sept. 9, (1966), 344-346

29 D. Bhattacharya et al, 40 Elec. Furn. Conf., Kansas City, USA, Dec. 7-10, (1982), I. and S. Soc./AIME, 145-152

30 A. Spaccarotella, Steelmaking Proc., vol. 67, Chicago, (1984), I. and S. Soc./AIME, 53-61

31 T. R. Meadowcroft and R. J. Milbourne, J. of Metals, June (1971), 11-17

32 K. Okamoto et al, Iron and Steel Engineer, Dec. (1982), 47-52

33 H. Gruner et al, UK Patent Application GB 2111880 A

34 T. Ueda et al, Tetsu-to Hagane, vol. 61, (1975), no. 11, Lecture 121; page S472, translation HB 9803

35 R. Scheel et al, Inst. of Metals, Conf. Proc., London, Oct. 23-24, (1984), 'Secondary Steelmaking for Product Improvement', 61-72

36 B. Sansby, Int. Conf. on 'Continuous Casting of Steel', Biarritz, (1976), 47-48

37 B. Ferry et al, National Open Hearth and Basic Steelmaking Conf., vol. 58, Toronto, I. and S. Soc./AIME, 284-294

38 L. A. Luyckx, Symposium on Deoxidation Practice - with and without Ladle metallurgy, Pittsburgh, April 20-21, (1982), 25-67

39 S. N. Singh, Steelmaking Proc., vol. 62, Detroit, March 25, 28, (1979), TMS/AIME, 3-10

40 G. M. Faulring et al, Elec. Furn. Proc., vol. 37, (1979), 219-229

41 H. M. Pielet and D. Bhattacharya, Met. Trans. B, Sept., (1984), (3), 547-562

42 I. G. Davies and P. C. Morgan, Inst. of Metals, Conf., Proc., London, Oct. 23-24, (1984), 'Secondary Steelmaking for Product Improvement', 153-164

43 A. 1shii et al, XX1Xth Int. Colloq. on Refractories, (Proc. Conf.), Aachen, FRG, 9-10 Oct. 1986, Interceram, 1987, 70-74

44 E. Marino et al, Journees Siderurgiques ATS, (1983), Paris, Dec. 7-8, (1983), Session 6, Continuous Casting

45 A. Ramacciotti and E. Marino, Elec. Furn. Proc., vol. 42, Toronto, (1984), I. and S. Soc., 293-298

46 E. Marino et al, Off. Gaz 28 July 87, Patent No. US4682717 (USA)

47 A. Kolin, Amer. J. of Physics, (1953), vol. 21, 619-620

48 E. W. Geller, J. of the Aeronautical Sciences, Dec. (1955), 22, 869-870

49 F. A. Schraub et al, J. Basic Eng., (1965), Trans ASME, Series D, 87, 429-444

50 W. Davis and R. Fox, J. Basic Eng., (1967), Trans ASME, Series D, 89, 771-781

51 E. O. Macagno, Iowa Inst. of Hydraulic Research, Rep. No.114, Univ. of Iowa, Feb. (1969)

52 J. Hearney and W. Davis, in 'Flow - Its Measurement and Control in Science and Industry', (ed. R. B. Dowdell), vol 1, (1971), 833-842

53 B. R. Clayton and B. S. Massey, J. of Sci. Instrum., 44, (1967)

54 D. W. Clutter et al, Douglas Aircraft Co. Inc., Engineering Dept., Rep. No. ES29075, (1959)

55 T. J. Mueller, in 'Fluid Mechanics Measurements', (ed. R. J. Goldstein), Hemishere Publ. Corp., (1983), 352-375

56 G. E. Mattingly, David Taylor Model Basin, Rep. 2146, (AD 630 468), (1966)

57 D. M. Levins and D. H. Thompson, Inst. Eng. Aust. Mech Eng. Trans. (Australasia), vol.ME-1, no. 1-2, (1978), 22-2

58 D. H. Thompson, Aust. Aero. Res. Lab., Note A338, (1973)

59 T. Asanuma and S. Takeda, Bull. J. S. M. E., vol. 8, no 32, (1965), 8, 599-608

60 A. C. Tory and K. H. Haywood, Fluid Engr. Conf. (Pittsburgh), May 9-12, (1971), ASME Publ., 71-FE-36

61 M. J. Blandamer et al, Nature, vol.26, Nov.25, (1967), 283-284

62 F. R. Hama and J. Nutant, Proc. Heat Transfer and Fluid Mechanics Inst., (1963), 77-93

63 A. A. Fejer, Int. Conf. on Instrumentation in Aerospace Simulation Facilities at C.I.T., Sept. 10-12, (1973)

64 K. P. H. Frey, ASME, Paper 68-FE-34, for meeting on May 9, (1968)

65 E. Kato et al, Proc. of the 2nd Int. Symp. on Flow Visualization, Sept. 9-12, (1980), Bochum, W. Germ., 20 213

66 T. Matsui et al, Proc. Int. Symp. on Flow Visualization, Oct. 12-14, (1977), Tokyo, 215-220

67 H. Yoshida et al, J. Fac. Eng. Chiba Univ. (Japan) vol.32, no. 2, (1981), 7-12

68 P. H. Kemp and A. J. Grass, Proc. of the 12th Congress of I.A.H.R., vol. 2, (1967), 201-209

69 A. J. Grass, J. Fluid Mech., (1971), vol. 50, 233-255

70 S. L. Weinberg and W. H. Heiser, ASME Paper 68-FE-35 for meeting on May 6-9, (1968)

71 W. C. Thomas and J. C. Rice, J. of Applied Mech. vol. 40, no.2, 321-325

72 S. Taneda, Proc. of the 16th Int. Conf. on Theoretical and Applied Mechanics at Lyngby, Denmark, 19-25 Aug. (1984) 399-410

73 H. Bippes, Proc. of the 2nd Int. Symp. on Flow Visualization, Sept. 9-12, (1980), Bochum, W. Germ., 271-276

74 C. R. Smith and R. D. Paxson, Exp. Fluids, vol. 1, no.1, (1983), 43-49

75 W. O. Criminale and R. W. Nowell, AAIA J., (1965), vol.3 1203

76 F. W. Roos and W. W. Willmarth, AAIA J., (1969), vol.7, 1635-1637

77 D. L. Wilkinson and M. A. Willoughby, J. Hydraulic Res., vol.19, no.2, (1981), 141-153

78 G. Birkoff and T. E. Caywood, Journal of Applied Physics, 20, (1949), 646

79 E. Xueqan and L. Minghui, Kexue Tongbao, vol.29, No.11, Nov. (1984), 1442-1446

80 M. Hayashi et al, Kyushu Univ., Technol. rep., vol.59, No.1, Jan. (1986)

81 A. W. D. Hills, unpublished notes

82 H. Lamb, 'Hydrodynamics', Camb. Univ. Press, 6th Edition, (1932), 597-602

83 J. Szekely and N. J. Themelis, Rate Phenomena in Process Metallurgy, John Wiley and Sons. Inc., (1971)

84 Y. Okamoto et al, Bull. J.S.M.E., (Japan), vol.14, no.7 Oct. (1971), 1088-1094

85 I. Ciobanu et al, Metalurgia (Bucharest), (1983), 35, (8) 384-387, BISITS translation 22734

86 D. Langford, Trans. ASME, J. Applied Mech., vol.35 (1968), 683-688

87 F. G. Wilson et al, Ironmaking and Steelmaking, (1987), vol.14, No.6

88 J. O. Hinze, Turbulence, Mcgraw-Hill, 2nd ed. (1975), Chapter 7.11

89 W. Pfenninger, Boudary Layer and Flow Control, vol.2, (ed. G. V. Lachmann), Pergammon Press, (1961), 961-981

90 A. D. Robertson and A. T. Sheridan, J.I.S.I., July (1970) 625-632

91 D. Wilshynsky et al, Fachberichte Huttenpraxis Metallweiterverarbeitung, vol.23, no.4, (1985), 264-272

92 W. T. Scott, The Physics of Electricity and Magnetism, 2nd ed., John Wiley and Sons Inc., (1966), 163-167

93 Hadamard, Compt. Rend. Acad. Sci., (1911), 152, 1735, and (1912), 154, 109

94 M. R. Spiegel, 'Theory and Problems of Statistics', in Schaum's Outline Series, Schaum Publishing Co., New York, (1961)

```
                              PROGRAM SCST
C
C SCST .FOR is based upon the potential flow derived from
C the electrostatic theory in Scott, (ref. H40).  It
C calculates the steel streamline paths in NOZ 1 and NOZ 2
C and the movement of inclusions under the action of bouyant
C and centripetal forces, ignoring inertia.
C The density of steel and the inclusion is asked for in the
C program.  The program is designed for solid inclusions but
C the behaviour of liquid inclusions can be predicted providing
C they are small enough to be considered as solid particles.
C
      COMMON PI,RADINC,DENSAL,DENST,VISCST
     C
C RNOZ is the radius of curvature of the convergent section
C WNOZ (or WEFF for NOZ 2)is the full width of the nozzle at
C exit, (It has nothing to do with the constrictor section.)
C
    5 WRITE(3,10)
      READ(3,11) RNOZ
      WRITE(3,15)
      READ(3,16) WNOZ
      WRITE(3,18)
      READ(3,19) DENSAL
      WRITE(3,20)
      READ(3,21) DENST
      VISCST=0.006
      PI=3.14159
      TIM=0.0
     C
C Input of INCLUSION radius and STEEL exit velocity is
C obvious.  A request for the increment in the streamline
C distance DZED is necessary because the decrease in x
C value will change as the direction of the streamline
C changes.
C
      WRITE(3,30)
      READ(3,31) RADINC
      WRITE(3,35)
      READ(3,36) DZED
      WRITE(3,40)
      DZED1=DZED
      READ(3,41) VELEXT
C
C You can decide here how you want the results to be output:
C         1) single graph plot of the particle pathline,
C         2) single print-out of the pathline coordinates,
C         3) print-out of the limiting values of theta/alpha
C            to determine the effect of particle size.
C
C You can chose for which nozzle the calculation is to be
C done:-
C         1) NOZ 1----first experimental nozzle (type in 4)
C         2) NOZ 2----2nd experimental nozzle   (type in 5)
C
```

```
      WRITE(3,91)
      READ(3,92) NOZTYP
      WRITE(3,50)
C
C For NOZ 2 the given steel velocity at the nozzle exit
C is modified in the program to a lower velocity at the
C effective nozzle width, (WEFF).
C
      WEFF=WNOZ
      IF(NOZTYP.NE.5) GO TO 7
      VELEXT=VELEXT*(15.0/WEFF)
    7 READ(3,51) MODE
      IF (MODE.NE.1) GO TO 3
      IF(NOZTYP.EQ.5) GO TO 93
      WRITE(2,800)
C
C Plot of the NOZ 1 shape at x2 magnification
C (right hand side)
C
  800 FORMAT(1X,'SP1;VS1;PU;PA1500,1500;PD;
     1PA6480,1500;PA6480,1680;AA6480,4080,-90,5;
     2AA4080,1500,90,5,IN')
C
      GO TO 3
   93 WRITE(2,801)
C
C  Plot of the NOZ 2 shape at x2 magnifiaction
C (right hand side)
C
  801 FORMAT(1X,'SP1;VS1;PU;PA1500,1500;PD;
     1PA8500,1500;PU;PA8500,2957;PD;PA6734,3431;
     1AA7235,5300,-75,5;AA5300,1500,90,5;
     1PU;PA6734,3431;PD;AA13939,1500,15,0.1,IN')
    1 CONTINUE
      IF(RADINC.LT.0.4) GO TO 3
      VELEXT=(VELEXT/(15.0/WEFF)-1.0)*(15.0/WEFF)
      RADINC=0.025
      IF(VELEXT.EQ.4.0) GO TO 9999
C
C Headings.
C
    3 WRITE(2,460) RNOZ
      WRITE(2,465) WNOZ
      WRITE(2,470) VELEXT
      WRITE(2,475) RADINC
      WRITE(2,480) DZED
      WRITE(2,481) DENST
      IF (MODE.EQ.3) GO TO 4
      WRITE(2,849)
      WRITE(3,600)
      READ(3,605) YN1
      GO TO 6
C
C YN1 is the initial y value at the zero potential line.
C The corresponding x value XN1 is calculated from the
```

```
C geometry.
C
C To find the limiting flow path for wuich inclusions
C hit the surface, an initial y value is chosen of 90%
C of the distance along the entry potential line towards
C the surface.
C
    4 YN1=RNOZ*1.1
      YMIN=RNOZ+WNOZ/2.0
      YMAX=2.0*RNOZ+WNOZ/2.0
C
    6 XN1SQR=2.0*YN1*RNOZ+WNOZ*RNOZ+WNOZ**2.0/4.0-YN1**2.0
      XN1=SQRT(XN1SQR)
C
C Store of initial starting coordinates.
C
      YN=YN1
      XN=XN1
C
      V=WNOZ/2.0
      P=2.0*RNOZ+V
C
   55 CONTINUE
C
C Variables for a particular Streamline
C (see Scott (ref. H40))
C
      X0=0.5*SQRT(4.0*RNOZ*WNOZ+WNOZ**2.0)
      IF(NOZTYP.NE.5) GO TO 9
      X0=0.5*(4.0*RNOZ*WEFF+WEFF**2.0)**0.5
    9 PATHK1=(XN+X0)**2.0+YN**2.0
      PATHK2=(XN-X0)**2.0+YN**2.0
      PATHK=(PATHK1/PATHK2)**0.5
C
C Circular streamline curvature
C
      SR=(2.0*X0)/(PATHK-1.0/PATHK)
      CURV=1.0/SR
C
C Two points, 1st (xn,yn) and 2nd (x,y), are chosen on the
C given streamline. All the variables for the potential
C geometry are calculated at both points.  The resultant
C particle velocities and directions from the effects of
C bouyant and centripetal forces are also calculated at
C each point.  The average particle velocity and direction
C are used for calculating the particle movement to position
C xc,yc.  Tis then becomes the new 1st point on a different
C streamline.
C The particle velocity is calculated relative to the moving
C fluid, (Lagrangian system of reference).
C
C Specific 1st point variables.
C
      Y01=(XN**2.0+YN**2.0-X0**2.0)/2.0/YN
      R=(X0**2.0+Y01**2.0)**0.5
```

```
      TANZ1A=Y01/(RNOZ+WNOZ/2.0)
      Z1A=ATAN(TANZ1A)
      TANZ1B=R/RNOZ
      Z1B=ATAN(TANZ1B)
      ALPH1=Z1A+Z1B
      VEL1=(VELEXT*1000.0)*V/R/ALPH1
      TANTH1=XN/(YN-Y01)
      TH1=ATAN(TANTH1)
      RAT1=TH1/ALPH1
C
C Call the subroutine VELH to calculate the effects of bouyancy and
C centripetal forces.
C
      CALL VELH(U1,VEL1,CURV,TH1,GAM1)
C
C The step length originally given must be modified as the
C particle nears the exit position or the nozzle surface.
C Proximity to the surface is indicated in both NOZ 1 and
C NOZ 2 by the ratio theta/alpha approaching 1.0.
C
C The exit in NOZ 1 is when y=0 but very low values of y
C give difficulty in the computer calculations.  Therefore
C a limiting value of y=1.5 has been included.
C Because the streamline is nearly vertical at exit the x
C value is reduced by increasingly smaller amounts as the
C exit is approached.
C The end of calculations for NOZ 2 is represented by the
C lowest potential line for curved flow, (alpha = 0.265).
C
      IF(NOZTYP.EQ.4) GO TO 94
C
C Modified decrease in x value for NOZ 2.
C
      IF((ALPH1.LT.0.4).OR.(RAT1.GT.0.99)) DZED=1.0
      IF((ALPH1.LT.0.33).OR.(RAT1.GT.0.999)) DZED=0.5
      DX=DZED*SIN(TH1)
      X=XN-DX
      GO TO 59
C
C Decrease in x value for next point on the streamline,
C modified as x approaches zero in NOZ 1.
C
   94 IF(YN.LT.1.5) GO TO 999
      IF(YN.LT.3.0) DZED=1.0
      IF((YN.LT.10.0).OR.(RAT1.GT.0.99)) DZED=0.5
      DX=DZED*SIN(TH1)
      X=XN-DX
      GO TO 59
   61 X=XN*.999
      DX=XN-X
      DZED=DX/SIN(TH1)
      GO TO 59
   62 X=XN*.9999999
      DX=XN-X
      DZED=DX/SIN(TH1)
```

```
      GO TO 59

C
C Calculation of corresponding y value on the same
C streamline.
C
C
   59 F1K=PATHK+(1.0/PATHK)
      F2K=PATHK-(1.0/PATHK)
      FX=4.0*X0**2.0
      YSQR=(FX/(F2K**2.0))-(X-(F1K/F2K)*X0)**2.0
      Y=SQRT(YSQR)
C
C Calculation of the 2nd point variables.
C
      Y02=(X**2.0+Y**2.0-X0**2.0)/2.0/Y
      RNEW=(X0**2.0+Y02**2.0)**0.5
      TANZ2A=Y02/(RNOZ+WNOZ/2.0)
      Z2A=ATAN(TANZ2A)
      TANZ2B=RNEW/RNOZ
      Z2B=ATAN(TANZ2B)
      ALPH2=Z2A+Z2B
      VEL2=(VELEXT*1000.0)*V/RNEW/ALPH2
      TANTH2=X/(Y-Y02)
      TH2=ATAN(TANTH2)
      RAT2=TH2/ALPH2
      CALL VELH(U2,VEL2,CURV,TH2,GAM2)
C
      UAVE=(U1+U2)/2.0
      VELAVE=(VEL1+VEL2)/2.0
      ALPHA=(ALPH1+ALPH2)/2.0
      THETA=(TH1+TH2)/2.0
      RATIO=(RAT1+RAT2)/2.0
C Step time.
      DT=DZED/VELAVE
C Cumulative time.
      TIM=TIM+DT
      VELF=VELAVE/1000.0
C Average particle velocity.
      UF=UAVE/1000.0
C Direction of the particle movement.
      GAMAVE=(GAM1+GAM2)/2.0
C
C New coordinate in the inclusion path.
C
      XC=X+UAVE*DT*SIN(GAMAVE)
      YC=Y+UAVE*DT*COS(GAMAVE)
C
C
C
C Plotting of inclusion position.  This includes a coordinate
C change to plot the graph in a convenient way.  The plot is
C at x2 to compare with the dimensions of the water model.
C
      IF (MODE.NE.1) GO TO 70
```

```
      XPL=1500.0+2.0*((2.0*RNOZ+WNOZ/2.0)-YC)/0.025
      YPL=1500.0+2.0*XC/0.025
      IXPL=INT(XPL)
      IYPL=INT(YPL)
      WRITE(2,810) IXPL,IYPL
  810 FORMAT(1X,'SP1;VS5;PA'I5,I5';PD;PU;')
C
   70 IF (MODE.NE.2) GO TO 80
      IF(KPRNT.GT.5) GO TO 79
      KPRNT = KPRNT + 1
      GO TO 80
   79 KPRNT = 0
      WRITE(2,850) TIM,XC,YC,VELF,CURV,UF
   80 XN=XC
      YN=YC
C
C Separation of surface hits and misses.
C
C The calculation of surface hits takes into cosideration
C the size of the inclusion.
C
      CNTACT=RNEW*(ALPHA-THETA)
      IF(NOZTYP.EQ.5) GO TO 95
      IF(CNTACT.LT.RADINC) GO TO 990
      IF(ALPH2.LT.0.01) GO TO 995
      GO TO 55
   95 IF(CNTACT.LT.RADINC) GO TO 990
      IF(ALPH2.LT.0.265) GO TO 995
      GO TO 55
C
C Surface hits
C
  990 WRITE(3,500) XN,YN,XN1,YN1
      DZED=DZED1
      IF(MODE.NE.3) GO TO 999
      YMAX=YN1
      YN1=(YMAX+YMIN)/2.0
      YCH=YMAX-YMIN
      IF(ABS(YCH).GT.0.1) GO TO 6
      GO TO 5010
C
C Surface misses
C
  995 WRITE(2,505) XN,YN,XN1,YN1
      DZEDD=DZED1
      IF(MODE.NE.3) GO TO 999
      YMIN=YN1
      YN1=(YMAX+YMIN)/2.0
      YCH=YMAX-YMIN
      IF(ABS(YCH).GT.0.1) GO TO 6
C
C Calculation of the entry flow-path most distant from the
C nozzle surface which results in an inclusion hitting the
C surface.  This of course results in a surface hit at the
C tangent point of the nozzle.
```

```
C
 5010 YLIM=YN1
      XLIM=(2.0*YLIM+RNOZ+WNOZ*RNOZ+WNOZ**2.0/4.0-YLIM**2.0)
     1**0.5
      TANTHL=XLIM/(YLIM-RNOZ)
      THL=ATAN(TANTHL)
      ENTRYR=THLIM/(PI/2.0)
      WRITE(2,510) XLIM,YLIM,ENTRYR
      RADINC=RADINC+0.025
      GO TO 1
C
C
   10 FORMAT(2X,'RADIUS OF CURVATURE OF NOZZLE (mm)')
   11 FORMAT(F5.1)
   15 FORMAT(2X,'NOZZLE DIAMETER (mm)')
   16 FORMAT(F5.1)
   18 FORMAT(2X,'DENSITY OF SOLID PARTICLE
     1 (Al2O3=3810.0 kg/m3) ?')
   19 FORMAT(F7.1)
   20 FORMAT(2X,'DENSITY OF STEEL (try 7210.0 kg/m3) ?')
   21 FORMAT(F7.1)
   30 FORMAT(2X,'PARTICLE RADIUS ? (mm) ')
   31 FORMAT(F8.6)
   35 FORMAT(2X,'WHAT IS THE INCREMENT IN STREAMLINE',
     1/      2X,'DISTANCE, DZED ? (mm) ')
   36 FORMAT(F8.6)
   40 FORMAT(2X,'WHAT IS THE EXIT VELOCITY ? (m/s) ')
   41 FORMAT(F5.3)
C
   50 FORMAT(2X,'IN WHAT FORM WOULD YOU LIKE THE RESULTS:',
     1//2X,' single graph of pathline     (type 1),',
     2/2x,' single print-out of pathline (type 2),',
     3/2x,' limiting theta/alpha values  (type 3),')
   51 FORMAT(I2)
C
   91 FORMAT(2X,'Which nozzle (NOZ 1--type 4 , NOZ 2--type 5 ')
   92 FORMAT(I2)
  460 FORMAT(//15X,'Nozzle Radius = ',F6.2,' mm')
  465 FORMAT(15X,'Nozzle Width  = ',F6.2,' mm')
  470 FORMAT(15X,'Exit Velocity = ',F5.3,' m/s')
  475 FORMAT(15X,'Inclusion Radius = ',F6.4,' mm')
  480 FORMAT(15X,'Streamline Step  = ',F5.3,' mm')
  481 FORMAT(15X,'STEEL viscosity  = ',F6.1,' MM'//)
C
  500 FORMAT(2X,'   HIT AT ',F7.2,2X,F7.2,2X,
     1'starting from ',F6.2,2X,F5.2,3X,'hit')
  505 FORMAT(2X,'NO HIT AT ',F7.2,2X,F7.2,2X,
     1'starting from ',F7.2,2X,F7.2)
C
  510 FORMAT(///14X,'The limiting entry is at x = ',F7.2,
     1         /14X,'                          y = ',F7.2,
     1         /14X,'The ratio theta/alpha       = ',F6.4)
C
  520 FORMAT(//2X,'ANOTHER RUN ( 1 for YES ) ')
  530 FORMAT(I3)
```

```
C
  600 FORMAT(2X,'WHAT IS THE INITIAL VALUE OF  y (mm)')
  605 FORMAT(F7.2)
C
  849 FORMAT(14X,'    Total    Particle
     1       Fluid    Curv.   Radial'
     1,/8X,     '             time     position
     1       vel.    (/mm)     vel.'
     1,/8X,     '             taken          y
     1      (m/s)              (m/s) '
     1,/8X,     '             (s)      (mm)   (mm)')
  850 FORMAT(15X,F6.3,5X,F5.2,2X,F6.2,2X,F5.3,2X,F7.5
     1,2X,F6.4)
C
  999 WRITE(3,519) TIM
  519 FORMAT(5X,'TOTAL TIME TAKEN  = ',F7.4)
      WRITE(3,520)
      READ(3,530) JMORE
      IF(JMORE.EQ.1) GO TO 5
 9999 STOP
      END
               SUBROUTINE VELH(UHILLS,VEL,CURV,TH,GAMMA)
C
C Because the centripetal and bouyant forces are very small
C the numerical values have been increased for ease of
C computing by using the units;
C---------------------------microgrammes
C---------------------------millimetres
C---------------------------seconds.
C A dummy constant has been used for the same reason.
C
      COMMON PI,RADINC,DENSAL,DENST,VISCST
      DUMMY=100000.0*RADINC
      VISC=VISCST*1000000.0
      G=9.81*1000.0
      RHO=DENST-DENSAL
      VELOC=VEL
      CURVAT=CURV
      VOL=(4.0/3.0)*PI*(RADINC**3.0)
      FB=VOL*G*RHO
      FC=VOL*VEL**2.0*RHO*CURVAT
      FRSQR=(FB**2.0+FC**2.0-2.0*FB*FC*SIN(TH))/DUMMY**2.0
      FR=DUMMY*SQRT(FRSQR)
      UHILLS=FR/(6.0*PI*VISC*RADINC)
      RE1=UHILLS*RADINC*2.0*DENST/VISC
C     PAUSE 3
      IF(RE1.LE.2.0) GO TO 310
C
C Calculation of the resultant velocity in the intermediate
C region when Stoke's Law does not apply, (2 < Re < 500)
C
      A1=2.31*PI*(RADINC*2.0)**1.4*DENST**0.4*VISC**0.6
      PW=1.0/1.4
      UHILLS=(FR/A1)**PW
C
```

```
310 SINGAM=(FC/FR)*COS(TH)
    SL=SINGAM**2.0
    CGAMSQ=1.0-SL
    COSGAM=SQRT(CGAMSQ)
    TANGAM=SINGAM/COSGAM
    GAMMA=ATAN(TANGAM)
    RETURN
    END
```